Simulations of adsorption in porous carbons

Yin, You Fa

Award date:
2000

Awarding institution:
University of Bath

SIMULATIONS OF ADSORPTION IN POROUS CARBONS

Submitted by You Fa Yin
For the degree of PhD
Of the University of Bath
July 2000

ProQuest LLC
789 East Eisenhower Parkway
P.O. Box 1346
Ann Arbor, MI 48106-1346

Youfa Yin
IPTME
Loughborough University
Loughborough
Leicestershire LE11 3TU

Dr. Tim Mays
Department of Chemical Engineering
University of Bath
Bath BA2 7AY

1st December 2000

Ref: My PhD Thesis

Dear Tim,

I write to you to confirm that my PhD thesis, "Simulations of Adsorption in Porous Carbons", is NOT restricted and is freely available for consultation.

I am sorry for any inconvenience due to my mistake.

Many regards,

Youfa Yin

Abstract

Activated carbons are well-known adsorbents. Adsorption in these materials occurs in slit-shaped pores that are so small (narrower than 20 Å) that the overlap of adsorbent-adsorbate interactions from opposite pore walls leads to enhanced adsorption compared to non-porous surfaces. By contrast, the more recent carbon nanotubes (first characterised in 1991) contain narrow pores bounded by curved surfaces, where adsorption enhancement is expected to be even greater than in slit-pores. This project was carried out to explore adsorption in carbon nanotubes compared with activated carbons. The method used was Grand Canonical Ensemble Monte Carlo, which is a computer simulation of adsorption based on statistical mechanics. Comparison of simulated adsorption in activated carbons and carbon nanotubes was made for different model pore geometries and environmental conditions. Computer simulations were also used to explore the potential of carbon nanotubes in a practical application, such as fuel gas storage.

Adsorption in activated carbons is sensitive to pore wall structure. Interactions between neighbouring slits have significant effects on adsorption in thin-walled, narrow slit-shaped pores. For nanotubes, an interaction potential between fluid molecules and solid carbon was derived to represent the adsorption potentials both inside and outside the nanotubes. Due to positive pore wall curvature, potentials inside carbon nanotubes are generally more enhanced compared with slits. Saturation nitrogen densities at 77 K inside isolated carbon nanotubes are higher than inside carbon slits. Adsorption of nitrogen in single-walled carbon nanotube arrays is mainly determined by geometrical factors and, in most cases, the adsorbed phase has higher density than bulk liquid nitrogen. Interstitial adsorption can make marked contribution to the adsorption capacity of nanotube arrays. Very high BET surface areas are found for single-walled carbon nanotube arrays with intermediate tube separations. This indicates that arrays of single-walled carbon nanotubes with intermediate tube separations can achieve high adsorption capacity. Nitrogen isotherms of arrays with small tube diameters and tube separations are type I, while those of arrays with larger tube diameters and tube separations are type IV.

At room temperature and up to 200 bar, both carbon nanotubes and activated carbons have similar volumetric capacities for hydrogen adsorption, which are less than 1/3 of the US Department of Energy (DOE) target of 695 (STP) v/v. However, gravimetric capacities of arrays with sufficiently large tubes and tube separations can reach the DOE target of 6.5 wt%. At 77 K with storage pressure of 70 bar and delivery pressure of 1 bar, only a limited array configurations with small tube diameters and intermediate tube separations can give delivered volumetric capacities that are close to the DOE target. Increasing storage pressure will increase the capacities, but the enhancement can be inefficient depending on the array configurations. The gravimetric capacity target is relatively more achievable, but gaps must be introduced between tubes to achieve the target. At 77 K, carbon nanotube arrays close to the optimal configurations have higher hydrogen capacities than activated carbons. As expected, interstitial adsorption in such nanotube arrays plays an important role in hydrogen storage. Trigonal arrays of open carbon nanotubes have higher methane capacities than activated carbons at 298 K and 34 bar. Square arrays yield lower methane capacities than trigonal arrays and appear to be no better than activated carbons for methane storage. Correlations exist between hydrogen and methane capacities and nanotube structural parameters, such as pore volume and surface areas, and may be used to predict or estimate hydrogen and methane capacities of carbon nanotube materials.

Contents

Section 1

Introduction and Background

Chapter 1
Introduction

1.1 Basis of this project

Carbon nanotubes are a newly discovered material comprising graphite sheets rolled into concentric tubes. The properties of carbon nanotubes are thought to be dependent on the tube diameters and the way in which the graphite sheets are rolled. Also the diameters of the tubes are controllable. Thus this material has attracted the attention of both scientists and engineers all over the world in recent years. Tremendous efforts have been made to synthesise, open and purify nanotubes. At the same time, numerous studies have been carried out on the characterisation, mechanism of growth, physical properties and possible applications of this novel material. Nowadays, carbon nanotubes can be made as single walled, multi-walled tubes and as well as aligned nanotube bundles. However, production yield is still very low and this limits experimental work on the properties of this material. Therefore, much more work is needed to fully explore the novel properties of this fascinating material.

The tubular structure of the nanotubes makes the adsorption potential inside of the tube strongly enhanced compared with flat not-porous surfaces. This enhancement is even stronger than that in microporous carbons, where micropores are often thought to be slit-shaped. It is well known that microporous carbons are one of the best adsorbent materials. Therefore, it is natural to think that carbon nanotubes might be a good adsorbent. Dillon and co-workers [Dillon *et al.*, 1997] studied hydrogen storage in carbon nanotubes and they concluded that carbon nanotubes can store more hydrogen than activated carbons. This work stimulated the interest of many researchers on the adsorption properties of carbon nanotubes. However, due to the limited availability of pure high quality carbon nanotubes, only few experimental measurements have been published. Thus molecular simulations, which are computerised experiments, and have been making considerable contributions to the understanding of adsorption properties of carbon nanotubes. However, no systematic studies have been reported and much more work is required.

1.2 Aims of Project

This project is a systematic study of potentials and adsorption in carbon nanotubes using Grand Canonical Ensemble Monte Carlo (GCEMC) molecular simulations, with reference to the better-known porous activated carbons. The main aims of this project are two fold: (1) To establish a full image of the adsorption characteristics of carbon nanotubes, from single isolated carbon nanotubes to aligned carbon nanotube arrays with different configurations, using molecular simulations. (2) To explore the potential of carbon nanotubes as gas storage media, especially for methane and hydrogen.

1.3 Structure of thesis

This thesis is organised as four sections. Section 1, Introduction and Background, includes Chapters 1-2 and gives a general introduction to, and a background of, the project. Section 2, Fundamentals of Adsorption, includes Chapters 3-7. The models used in this study, including adsorption potentials in isolated carbon nanotubes and nanotube arrays, are presented in Chapter 3, together with the model and potentials of carbon slits. Chapter 4 presents new developments in simulations of adsorption in activated carbons. Chapter 5 gives results and discussions of nitrogen adsorption inside (endohedral) and outside (exohedral) isolated carbon nanotubes and simultaneous endohedral and exohedral adsorption of nitrogen in isolated carbon nanotubes. Nitrogen adsorption in single walled carbon nanotube (SWCNT) arrays is presented in Chapters 6 and 7 for trigonal and square arrays respectively. Section 3, Fuel Gas Storage, is divided into four chapters: Chapters 8-11. Chapter 8 gives a general introduction to, and background of, fuel gas storage. Reviews of studies on methane and hydrogen storage are also made here. Chapters 9 and 10 are devoted to hydrogen and methane storage respectively. The correlation between gas storage capacities and some structural parameters of carbon nanotube arrays is presented in Chapter 11. Section 4, Conclusions and Future Work, presents the conclusions drawn from this study and the areas which more study is needed or of interest. References are listed at the end of the thesis as Chapter 14.

Chapter 2
Background

2.1 Porous Carbon Materials

2.1.1 Characteristics of porous carbons

Porous carbons are carbon materials having minute interstices through which liquids or gases may pass. According to this definition, one of the characteristics of porous carbons is their well-developed pore structures, especially pores with nanometer sizes. Based on the experiences of adsorption chemistry, the International Union of Pure and Applied Chemistry (IUPAC) classifies porosity as follows [Sing *et al.*, 1985]:

(1) Micropores width less than 20 Å

(2) Mesopores width between 20 and 500 Å

(3) Macropores width greater than 500 Å.

Micropores provide high adsorptive capacities for small molecules such as gases and common solvents. Mesopores are important for the adsorption of larger molecules, such as colour bodies. It is considered that macropores are normally unimportant for adsorption and that their main role is to provide passages for adsorbate molecules to gain access to mesopores and micropores. Thus, porous carbon adsorbents are mainly microporous with some degree of mesoporosity.

Due to the existence of a large number of pores, the density of porous carbons is low, ~1.0 g/cm^3 or less, compared with 2.267 g/cm^3 for perfect graphite. Also a large portion of the carbon atoms comprising the solid are in the surfaces of the solid material. Thus porous carbon materials have very high internal surface areas. For example, surface areas as high as more than 3000 m^2 g^{-1} have been found for activated carbons [Byrne and Marsh, 1995] and 2400 m^2 g^{-1} for CO_2 activated carbon fibres [Alcaniz-Monge *et al.*, 1996].

The shape of pores in porous carbons is a complicated matter. However, in most cases they can be well represented by slits in activated carbons and as cylinders in carbon nanotubes (sections 2.1.2 and 2.1.3). In addition, activated carbons are a better known

material than carbon nanotubes and have been studied extensively. Therefore, this study will be centred at carbon nanotubes with reference to activated carbons.

2.1.2 Activated carbons

Elemental carbon exists in the two crystallographic forms, that is diamond and graphite. Graphite has a lamellar structure in which each layer is composed of carbon atoms arranged to form hexagons. However, the majority of carbon is found in less ordered structures and is classified into two groups: graphitic and non-graphitic, according to the degree of crystallographic ordering. The latter is further divided into two categories, the graphitizable and the non-graphitizable carbons [IUPAC, 1982; 1983; 1985], also called coke and char respectively. Graphitizable carbons can be converted to graphitic carbon by heat treatment, while non-graphitizable carbon cannot be converted to graphitic carbon solely by heat treatment up to 3500 K under atmospheric or lower pressures. Activated carbons are a non-graphitic form of carbon.

Activated carbons can be regarded as composed of crumpled and defected lamellae [also called lamellar constituent molecules (LCM)] of sizes from 10 Å to 100 Å [Byrne and Marsh, 1995]. These lamellae can be 'bonded' together to form a three dimensional network with isotropic physical properties. The difference in the detail of size, shape, deformation and 'bonding' together of the LCM generated from the individual parent feedstock during pyrolysis and carbonisation result in wide variations in properties of activated carbons. It is the spaces or voids between the LCM which constitute porosity in activated carbons and play important roles in the application of these carbon materials.

Due to their high surface areas, activated carbons have been in use for thousands of years and for a wide range of applications, such as gas or liquid purification and separation, and as catalyst supports. The largest application is gas- and liquid-phase adsorption. The performance of activated carbons as adsorbents is determined by their porosity and its distribution. On the other hand, adsorption experiments provide useful tools to the characterisation of activated carbons and can provide useful information on the pore structure. Thus, adsorption studies of activated carbons are of great interest.

Activated carbons have been developed extensively since World War I. There are two activation processes in the manufacture of activated carbons to increase their porosity and surface area: chemical and physical activation [Derbyshire *et al.*, 1995]. In the chemical activation, compounds such as $ZnCl_2$ are added to the parent feedstock prior to carbonisation. Physical activation refers to gasification of carbon by gases such as carbon dioxide and steam in the temperature range 700-1100 °C. Under certain conditions, these gases will selectively remove carbon atoms and create and open up porosity. Physical activation is now a preferred process due to environmental considerations.

In activated carbons, there exist all three types of pores. Some of the pores are formed during the carbonisation process prior to activation. However, micropores contribute most to the high surface area of activated carbons. Some electron microscopy studies show that the microporosity in activated carbons are slit shaped and the pore walls often contains only a few number of carbon layers [Fryer, 1981; Marsh and Crawford, 1982], as shown in Figure 2-1. Thus, in recent molecular simulations of adsorption in activated carbons, a slit pore model is commonly used [Aukett *et al.*, 1992; Suzuki *et al.*, 1996].

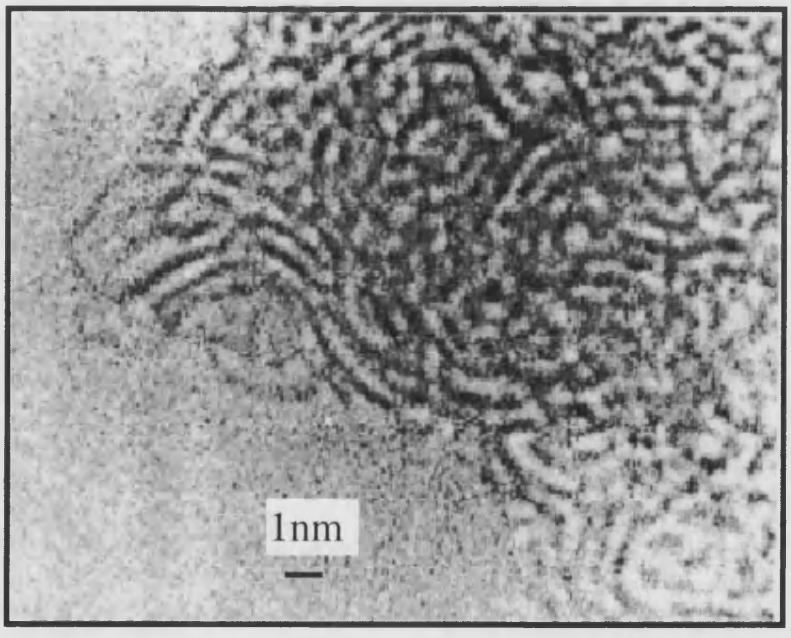

Figure 2-1 Transmission electron microscopy of activated carbon showing slit-like pores with a few carbon layers in pore wall [Fryer, 1981].

2.1.3 Carbon nanotubes

The most recently found carbon material is the fullerene family [Kroto *et al.*, 1985], including the so-called carbon nanotubes [Iijima, 1991]. Since the discovery of multi-walled carbon nanotubes (MWCNT) by Iijima [1991] and single-walled carbon nanotubes (SWCNT) by Iijima and Bethune *et al.* [Iijima and Ichihashi, 1993; Bethune *et al.*, 1993], they have greatly stimulated studies of this novel material in the field of physics, chemistry and materials science. Numerous studies have been carried out on the structure, properties [Dresselhaus *et al.*, 1995; Mintmire and White, 1995; Ebbesen and Ajayan, 1992; Endo and Kroto, 1992; Chopra *et al.*, 1995], and potential applications [Ajayan and Iijima, 1993; Rinzler *et al.*, 1995; Rouff and Lorents, 1995] of this material.

Carbon nanotubes can be thought of as one or more planar sheets of graphite rolled into a cylinder or several concentric cylinders closed seamlessly, as shown in Figure 2-2. This has been supported by TEM studies of carbon nanotubes, as shown in Figure 2-3. These tubes with diameters ranging from less than 10 Å to 200 Å [Ebbesen, 1996] are normally closed at both ends. However, the end caps may be removed [Tsang *et al.*, 1994] by selective oxidation. The exposed hollow channels are mesoporous or microporous depending on the diameters. Also, due to the curvature of the pore wall, adsorption energy in carbon nanotubes is expected to be higher than in porous carbons. Thus, carbon nanotubes may find applications as adsorbents.

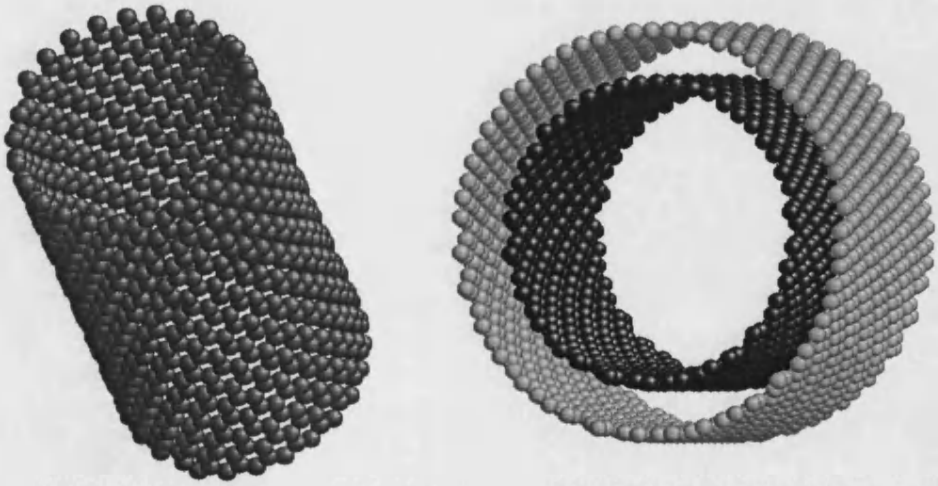

Figure 2-2. Computer generated image of carbon nanotubes. The inner diameters are 20 Å. (a) single-walled; (b) double-walled.

For SWCNTs, the characteristic parameter is the inner diameter, D. For MWCNTs, the number of graphite sheets in the wall, n, and the interlayer spacing between the graphite sheets, Δ, are also important parameters. The interlayer spacing was reported about 3.4 Å [Iijima, 1991], similar to that in graphite. Saito and co-workers [Saito *et al.*, 1993] studied the interlayer spacing in MWCNTs using electron diffraction and the results are Δ = 3.442 Å. However, recently Kiang and co-workers [Kiang *et al.*, 1998] studied three MWCNTs with different inner diameter and number of shells using HRTEM and found that interlayer spacing could vary from 3.4 Å to 3.9 Å and increase with increasing shell diameter. The number of graphene sheets in tube walls can vary from 1 to a few tens.

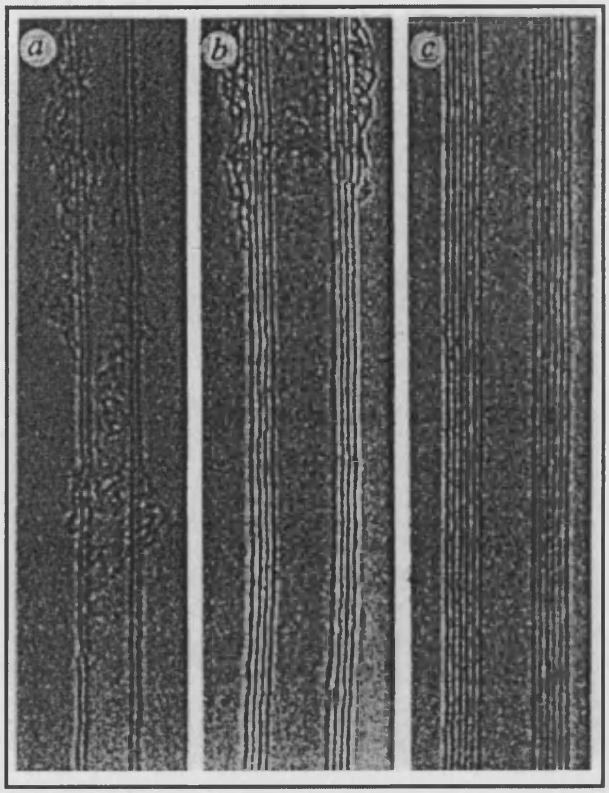

Figure 2-3. Transmission electron microscopy of multi-walled carbon nanotubes [Iijima, 1991].

Carbon nanotubes were first found as the by-products of fullerene production. At present, there are several methods to make them [Ebbesen, 1996; Ebbesen, 1994; Saito *et al.*, 1998], such as carbon arc discharge [Ebbesen and Ajayan, 1992; Ebbesen *et al.*, 1993], catalysed growth [Iijima and Ichihashi, 1993; Bethune *et al.*, 1993], and vaporisation [Ge and Sattler, 1993]. Metal-catalysed laser ablation [Thess *et al.*, 1996; Qin and Iijima, 1997] has been proved to be an efficient method to synthesise SWCNTs, while arc discharge produces the most highly graphitized tubes due to very high temperature (~4000K). The main techniques to synthesise carbon nanotubes may be divided into two groups. One is the vaporisation of graphite, such as the arc discharge and laser ablation. The other is the decomposition of hydrocarbons in the presence of catalysts. This vapour growth method has the advantage of continuous synthesis and

thus the advantage for scale-up and commercial production [Saito *et al.*, 1998]. Nanotubes are often found in bundles or ropes composed of from a few to hundreds of nanotubes [Ebbesen, 1994; Dillon *et al.*, 1997]. Recently, Terrones and Rao *et al.* reported methods to produce larger scale aligned nanotubes [Terrones *et al.*, 1998; Rao *et al.*, 1998].

However, whichever method is used, the nanotubes are always accompanied by nanoparticles, catalysts metals or amorphous carbons and in most cases with their ends closed. There are a number of ways to purify and open carbon nanotubes. One method is to oxidise the nanotube samples by oxygen [Ajayan *et al.*, 1993] or carbon dioxide [Tsang *et al.*, 1993]. In this method, not only the nanoparticles are oxidised, but also the nanotubes, therefore, the yield is very low (~1%). The nitric acid method developed by Tsang and co-workers [Tsang *et al.*, 1994; Dujardin *et al.*, 1998] has higher yields depends on the starting material. The purification and opening of carbon nanotubes are still of great interest and much work has been published in this area [Chen *et al.*, 1996; Hiura *et al.*, 1995; Shelimov *et al.*, 1998].

Purified carbon nanotubes offers the opportunity to study their properties experimentally. Most theoretical and experimental studies published are on the electronic [Yamabe, 1995; Issi *et al.*, 1995; Chauvet *et al.*, 1997] and mechanical properties [Lu, 1997; Sklovsky *et al.*, 1997] of nanotubes. Only limited attention has been paid to the study of adsorption in carbon nanotubes [Mackie *et al.*, 1997]. Work published on the adsorption of carbon nanotubes includes a small number of experimental measurements [Tsang *et al.*, 1993; Dillon *et al.*, 1997; Gaucher *et al.*, 1997], as well as theoretical [Stan and Cole, 1998; Breton *et al.*, 1994] and computer simulations [Maddox *et al.*, 1996; Maddox and Gubbins, 1995]. However, the results of these studies are not in a good agreement. Some of them show that carbon nanotubes might be a promising adsorbent [Dillon *et al.*, 1997; Stan and Cole, 1998], while others show that carbon nanotubes have very low BET surface areas [Tsang *et al.*, 1993; Gaucher *et al.*, 1997; Alain *et al.*, 1999] ranging from 15~300 $m^2 g^{-1}$. Thus, there remain interesting, unanswered questions in this area.

2.2 Adsorption in microporous carbons

When a solid is exposed to a fluid, the quantity taken up by the solid is proportional to the mass of the solid sample, and depends also on the temperature T, the pressure p of the fluid, and the nature of the fluid and the solid. For a certain adsorptive-adsorbent system at a fixed temperature, the amount of fluid adsorbed by the adsorbent is a function of pressure. This relationship is the adsorption isotherm. Most recorded adsorption isotherms can be grouped into six types I to VI [Gregg and Sing, 1982], as shown in Figure 2-4. Microporous carbons will yield type I isotherms, which are characterised by rapid uptake at low pressure followed by a nearly horizontal plateau. Figure 2-5 shows an experimental adsorption isotherm of a commercial microporous carbon that is in good agreement with the type I isotherm. When the carbon is mesoporous, type IV isotherms can be obtained, which are characterised by monolayer and multi-layer formation at low pressures followed by condensation.

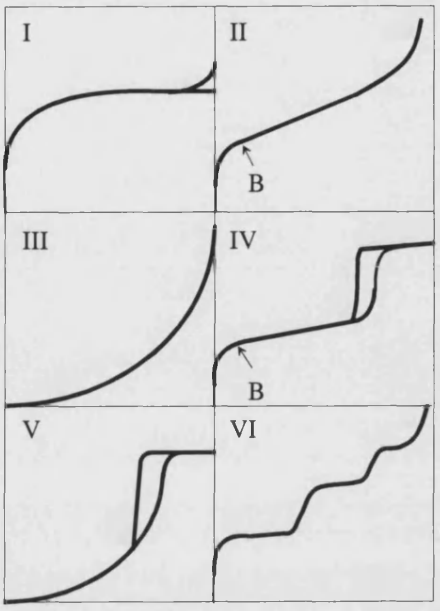

Figure 2-4 Types of adsorption isotherms [Gregg and Sing 1982].

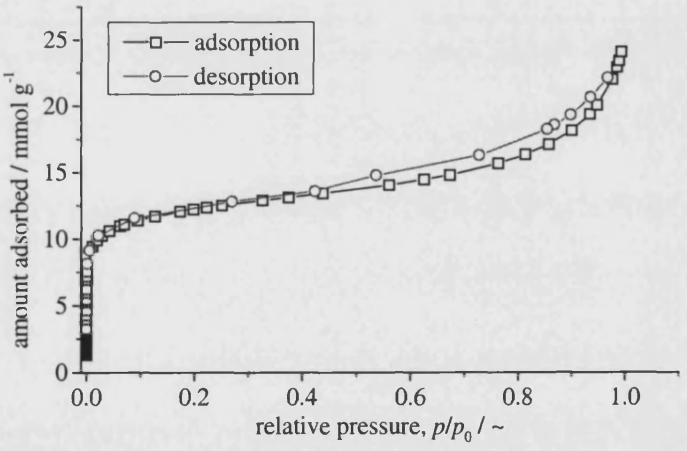

Figure 2-5. Isotherm of nitrogen adsorbed at 77 K in a commercial microporous activated carbon.

The adsorption of a fluid by a solid is determined by the forces between the individual molecules of the fluid and the atoms or ions in the solid. In small micropores, the interaction potential is considerably enhanced due to overlap of adsorption interactions

from opposite pore walls. Consequently, the pore becomes completely full at very low pressures, so that the isotherm rises steeply from the origin. In larger micropores, the enhancement of interaction potentials is relatively small and the increase of adsorption is now the result of a cooperative effect. This gives rise to a rounded knee to the isotherm [Gregg and Sing, 1982]. The micropores that give rise to the first pore filling mechanism are often termed ultramicropores, while those correspond to the second pore filling mechanism are termed supermicropores.

Adsorption has been used extensively to characterise the microporosity in activated carbons [Stoeckli, 1995]. The most useful information can derive from an adsorption experiment includes surface area, micropore volume and pore size and size distributions. In the determination of pore size distributions, none of the established techniques has been accepted as a standard, though there are a number of techniques available [Stoeckli, 1995]. In recent years, other approaches to determine pore size distributions in porous carbons based on molecular simulations have been proposed by a number of researchers [Seaton *et al.*, 1989; Lastoskie *et al.*, 1993]. Thus, there is still continuing interest in the research of adsorption in activated carbons [Zhou and Zhou, 1996; Dillon *et al.*, 1997].

2.3 Molecular simulations of adsorption

2.3.1 Basics of molecular simulations

Molecular simulations of adsorption provide insights into micropore filling mechanisms that are unavailable by other means [McEnaney *et al.*, 1998] and have been proved to be a powerful tool. The main methods of molecular simulations employed in simulations of adsorption are [McEnaney *et al.*, 1998; Cracknell *et al.*, 1995] Grand Canonical Ensemble Monte Carlo (GCEMC), which is based on an equilibrium statistical thermodynamics treatment of the system, Density Functional Theory (DFT), which is an approximate statistical mechanics method and is difficult to apply to complex systems, and Molecular Dynamics (MD), in which laws of motion are applied to ensembles of molecules so as to derive not only equilibrium but also transport properties. However, whichever the method is, the basis of the simulation is to set up a solid pore model and the intermolecular potentials between fluid-fluid and fluid-solid particles. Simulation

results are essentially exact; but their applicability to real materials depends on the validity of the pore and adsorption potential models.

Molecular simulation is a kind of computer experiments that shows the behaviour of a system based on the molecular model of the system. It is now over 40 years since the first molecular simulation of liquids was carried out. Advances in computer technology make it now much easier to carry out molecular simulations and also make it possible to study more complicated systems. Molecular simulations have a valuable role to play in providing essentially exact results for problems which would otherwise only be soluble by approximate methods or might be quite intractable. In this sense, molecular simulation is a test of theories. On the other hand, simulation results may also be compared with those of real experiments. In the first place, this is a test of the underlying model used in the simulation. Eventually, if the model is a good one, the results may offer insights to the experiments and assist the interpretation of new results. Therefore, simulations provide a bridge not only between models and experiments but also between models and theoretical predictions. Simulations also provide a direct route from the microscopic details of the system, such as the position of every molecule, to macroscopic properties of experimental interests, such as density of the system. In some cases, such as adsorption in a single carbon nanotube, it may be very difficult or even impossible to carry out experiments. However, molecular simulations may give useful predictions. Thus, molecular simulations are not only of academic interest, but are also technologically useful.

In molecular simulations of adsorption, the model pore is placed in a virtual tank, which is full of adsorptive and sufficiently large so that the macroscopic properties of the adsorptive, such as pressure and temperature, can be regarded as constant. Then possible movements within the pore-fluid system are simulated and repeated for a large number of times until the system reaches an equilibrium state. Finally, the equilibrium state parameters, such as the number of fluid molecules adsorbed in the pore, can be calculated. By varying the pressure of the adsorptive in the tank, a series of the amount adsorbed in the pore can be obtained as a function of the pressure, that is the result of a real adsorption experiment, the isotherm of the system at a certain temperature. Other parameters, such as adsorption heat, may also be calculated during the simulation.

2.3.2 Grand Canonical Monte Carlo

Monte Carlo is a computerised model sampling experiment that involves the generation of random numbers followed by a limited number of arithmetic and logical operations. The name 'Monte Carlo' was given by Metropolis in 1947 due to the extensive use of random numbers as in gambling [Allen and Tildesley, 1987]. In MC the equilibrium state parameters are evaluated as ensemble averages. The ensemble is a collection of possible microscopic states of the system under certain macroscopic conditions. The following ensembles are in common use: (1) The microcanonical, or constant-*NVE*, ensemble, where the number of molecules N, the volume V and energy E of the system are constants; (2) The canonical, or constant-*NVT* ensemble, where T represents the temperature of the system; (3) the isothermal-isobaric constant-*NPT* ensemble and (4) the grand canonical, or constant-μVT ensemble, where μ denotes the chemical potential of the system. GCEMC is particularly useful for studying inhomogeneous systems such as monolayer and multilayer adsorption near a surface [Whitehouse *et al.*, 1983]. Full details of GCEMC molecular simulations can be found elsewhere [Adams, 1974; 1975; Allen and Tildesley, 1987]. The following paragraphs are devoted to some particular points in the grand canonical ensemble Monte Carlo (GCEMC) molecular simulations of adsorption.

The three movements. In a GCEMC molecular simulation, it is required that a sequence of random states is generated so that by the end of the simulation each state has occurred with the appropriate probability. This is done by set up a Markov chain of states, which is constructed so that it has a limiting distribution of states (A Markov chain is a sequence of trials the outcomes of which belong to the same state space and the outcome of each trial only depends on the outcome of the trial that immediately precedes it). The distribution is proportional to [Allen and Tildesley, 1987]:

$$\exp[-\beta\,(U-N\mu) - \ln N! - 3N\ln\Lambda + N\ln V]$$

where $\beta = 1/k_B T$, k_B is Boltzmann's constant, U is the adsorption potential, V is the

volume and $\Lambda=(h^2/\ 2\pi mk_BT\ )^{1/2}$ is the thermal de Broglie wavelength, h is Planck's constant and m the mass of the fluid molecule. There are a number of methods to generate such a chain, but the commonly used is the original method of Norman and Filinov [Norman and Filinov, 1969]. In this method, there are three trial moves as shown in Figure 2-6 and are introduced below.

(1) *Trial displacement.* By generating a random number, a molecule is randomly selected and then three more random numbers are generated to define the random move of this molecule in X, Y and Z directions respectively. Suppose the interaction potential before the move is U_{old} and the potential after is U_{new}, then the increase of potential is

$$\Delta U = U_{\text{new}} - U_{\text{old}}$$

and the probability of acceptance of this move, P_{on} , is

$$P_{\text{on}} = \text{Min}[1, \exp(-\beta \Delta U)]$$

Where Min represents to take the smallest of the values in brackets. Clearly, if $\Delta U \leq 0$, then $P_{\text{on}} = 1$, the new configuration is accepted and added to the ensemble. If $P_{\text{on}} < 1$, then it is decided by the Metropolis method and will be discussed later.

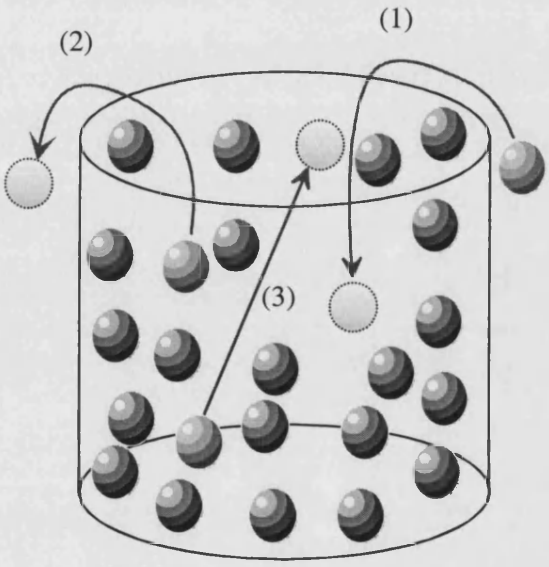

Figure 2-6. Schematic representation of the three possible movements of fluid molecules in molecular simulations: (1) Creation of a fluid molecule inside the model pore; (2) Removal of a fluid molecule from inside the model pore and (3) Random move of a fluid molecule inside the model pore.

(2) *Trial creation.* Three random numbers are generated to randomly locate a position in the pore and a molecule is placed at this position. As in (1), the increase of energy is calculated and the probability is now:

$$P_{\text{on}} = \text{Min}[1, \frac{\exp(-\beta \Delta U + B)}{N+1}]$$

where $B = \beta\mu + \ln V$ and μ is the configurational chemical potential. Whether the configuration is added to the ensemble is then determined in the same way as in (1).

(3) *Trial destruction.* A random number is generated to randomly select a molecule from the previous configuration and it is removed from the system. As above, the increase of energy is calculated and the probability is now:

$$P_{on} = \text{Min}[1, N\exp(\beta\Delta U - B)]$$

and the move is accepted or rejected as above.

Normally, an equal number of trial creations and destructions should be made. Typically, the number is 10 each for a trial move [Aukett *et al.*, 1992].

The Metropolis method. If the calculated probability P_{on} is less than 1, a random number ξ is generated uniformly on [0,1]. If $\xi \leq P_{on}$, then the move is accepted and added to the ensemble; if $\xi \geq P_{on}$, then the move is rejected. This is illustrated in Figure 2-7 for a

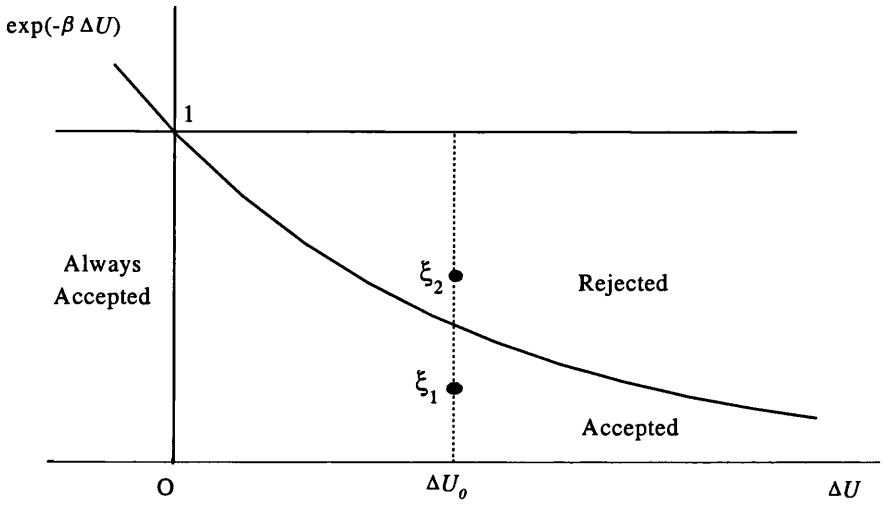

Figure 2-7. Illustration of the Metropolis method.

random move. When a trial move results in an increase of energy of ΔU_0, a random number is generated. If the value of the random number is ξ_1, then the trial is accepted. However, if the number is ξ_2, then the trial is rejected. Because the random number is

uniformly distributed in [0,1], the probability of generate a ξ_1 is $\exp(-\beta \Delta U_0)$. Thus, the resultant probability of accepting uphill moves is proportional to $\exp(-\beta \Delta U)$.

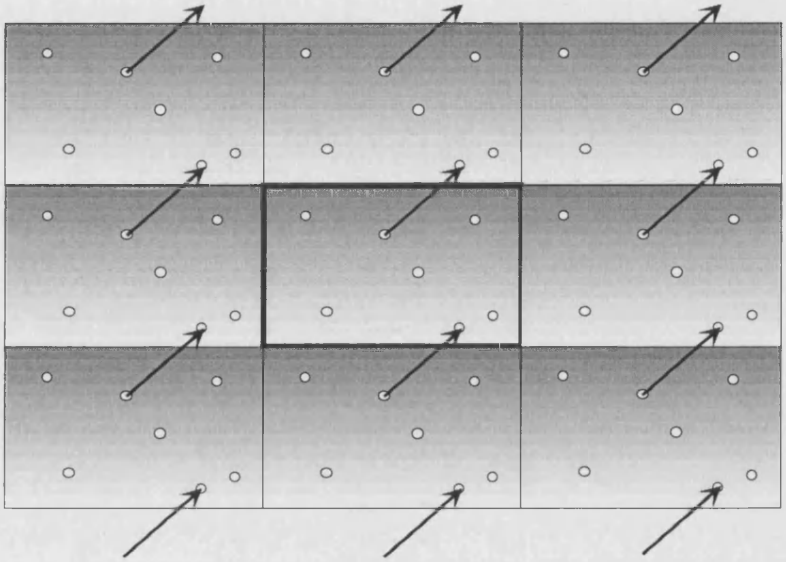

Figure 2-8. Schematic illustration of the periodic boundary conditions.

Periodic boundary conditions. In GCEMC simulations, periodic boundary conditions are commonly implemented to overcome the problem of surface effects. A two dimensional illustration of a periodic system is shown in Figure 2-8. The central simulation box (commonly called the simulation cell in three-dimensional cases) is replicated throughout the surface to form an infinite lattice. During simulations, as a molecule moves in the central box, its periodic image in each of the boxes moves in exactly the same way. Thus, if a molecule leaves the central box, one of its images will enter the box through the opposite side. The number of molecules in the central simulation box is conserved during a trial displacement.

2.3.3 Review of published work

The first step in simulations of adsorption is to establish a pore model of the solid material. Two models are commonly used in simulations of adsorption. One is the cylindrical pore model that is used in simulations of zeolite [Cracknell *et al.*, 1993; Cracknell and Gubbins, 1993] and carbon nanotubes [Maddox *et al.*, 1996; Maddox and Gubbins, 1995]. The other is the slit pore model which is mostly used as a model of micropores in activated carbons and has been studied extensively [Walton and Quirke, 1989; Maddox *et al.*, 1995; Aukett *et al.*, 1992; Suzuki *et al.*, 1996; Yin *et al.*, 1998].

The simulation studies of adsorption in activated carbons cover a wide range of fluids, including argon, nitrogen, methane and water [Maddox *et al.*, 1995; Aukett *et al.*, 1992]. Some studies also have been carried out on binary mixture adsorption [Somers *et al.*, 1996]. In most of these studies, the Steele 10-4-3 gas-solid potential [Steele, 1974] is commonly used. This potential is based on a semi-infinite slab model and excludes the possibility of studying the effects of pore wall structures on adsorption properties. Recently, Mays used another form of fluid-wall potential to study the effects of pore wall thickness and atom density [Mays, 1996]. Suzuki *et al.* studied the influence of interlayer spacing [Suzuki *et al.*, 1996] using the 10-4-3 potential. However, no systematic studies have been published. Also, the effects of input parameters to the simulation are not fully understood, though different values of these parameters are used by different research groups. In addition, pores are treated as isolated slits in common models, while in reality molecules adsorbed in adjacent pores may interact with each other and neighbouring pore walls may also make contributions to the attracting forces to the adsorbate molecules.

Compared with simulation of activated carbons, only a few papers have been published on simulations of carbon nanotubes. Maddox *et al.* studied nitrogen, argon and water adsorption in a single-walled 10.2 Å and a double-walled 47.8 Å nanotubes using potentials that are direct analogues to the Steele 10-4-3 potential for planar graphite surfaces [Maddox *et al.*, 1996; Maddox and Gubbins, 1995; Cracknell *et al.*, 1995; Maddox and Gubbins, 1994]. They found that the small nanotube shows type I adsorption behaviour, while the large nanotube shows layering and condensation hysteresis. They also estimated the specific surface areas for the two tubes, 403 $m^2\ g^{-1}$ for the 10.2 Å single-walled tube and 526 $m^2\ g^{-1}$ for the 47.8 Å double-walled tube. Open-ended nanotubes were also studied and it was reported that the open-ended model give a narrower, more round hysteresis loop. Maddox *et al.* also studied adsorption of binary mixtures of methane, nitrogen and propane in carbon nanotubes and showed that the more strongly adsorbed pure fluid is adsorbed preferentially from an equimolar binary mixture [Maddox *et al.*, 1996]. Recently, Ayappa showed that selectivity of carbon nanotubes is a function of temperature [Ayappa, 1998]. Khan and Ayappa recently reported their study on density distribution of diatoms, such as N_2 and Br_2 in carbon nanotubes using GCEMC [Khan and Ayappa, 1998]. They carried out

simulations for spherical (S), dumbbell (D) and quadruple-dumbbell (QD) models of N_2 and Br_2. They found that the density distribution of N_2 predicted by models S, D and QD were in close agreement and the spherical model adequately describes the density distribution of N_2 in nanopores.

These studies are all concentrated only on endohedral adsorption in isolated nanotubes (adsorption inside tubes). However, carbon nanotubes are much more complicated. Firstly, tube diameters can vary in a wide range. Secondly, the number of graphite layers in tube wall also varies. Thirdly, even for an isolated nanotube, if it is open, the adsorption will not only be endohedral, but also exohedral, that is on the outside of tubes. And in the case of closed tubes, only exohedral adsorption is involved. Finally, as nanotubes are often formed in bundles, adsorption in practical nanotube systems will involve interstitial adsorption between tubes. Therefore, this aspect must be studied before a full view of adsorption in carbon nanotubes can be established. This is the main goal of this project.

2.4 Summary of this study

This project is designed to study the effects of various inputs on the simulation on adsorption in activated carbons and to establish a full image of adsorption in carbon nanotubes using Grand Canonical Ensemble Monte Carlo (GCEMC) molecular simulations. To do this, a new potential is adopted to represent the interaction between fluid and solid carbons in which the pore wall structure can be explicitly modelled. The effects of variations in energy and length parameters in the interaction were also studied systematically. In addition, modelling techniques were developed to model activated carbons as assembles of slit carbon pores rather than single isolated slits. Therefore the interactions between neighbouring slits and adsorbed fluid molecules were included and the effects were studied.

For simulations of adsorption in carbon nanotubes, new potentials between fluid molecules and carbon nanotubes that are applicable to both inside and outside tubes were derived. This enables the systematic study of effects of tube diameters and tube wall thickness of carbon nanotubes on endohedral, exohedral and simultaneous endohedral and exohedral adsorption in isolated carbon nanotubes and adsorption in

arrays of carbon nanotubes. Techniques were also developed to modelling adsorption in different arrays of carbon nanotubes and the interaction between neighbouring tubes and adsorbed fluid molecules were included. For the first time, the contribution of endohedral and exohedral adsorption in open tubes were studied and compared.

As possible applications of carbon nanotubes, methane and hydrogen storage in arrays of carbon nanotubes were systematically studied for the first time. Array configurations were optimised to facilitate the calculation of the maximum methane and hydrogen capacities. Also, attempts were made to predict methane and hydrogen capacities from array parameters and nanotube structural parameters.

The GCEMC route described above was adopted in this study. In most cases, the simulation cell is 10 times the adsorbate molecular size and the cross-section of the cell varies according to the model (Chapter 3). The Peng-Robinson equation of state [Peng and Robinson, 1976] was used to calculate the chemical potential. For a given pressure and temperature, the simulation begins with an empty simulation cell or the last configuration at the previous pressure. Then molecules will be created in, removed from and randomly moved within the cell. The ratio of the number of creation, destruction and random move is 10:10:1. After more than 10^5 such movements, equilibrium is assumed to be reached and then the physical properties are calculated from the subsequent 10^6 such movements. Normally, the standard deviations for these quantities are within a few percent. The potentials employed here are mainly based on the Lennard-Jones 12-6 potential and will be introduced in detail in Chapter 3.

Section 2

Fundamentals of Adsorption

Chapter 3
Adsorption Potentials in Carbon Slits and Nanotubes

3.1 Basics of adsorption potentials

The physical adsorption of a fluid in a porous material is determined by the properties of the fluid and the characteristics of the pore system in the solid material. These can be described by the adsorption potential, which includes interactions both between adsorbate-adsorbate molecules and between adsorbate and adsorbent. Most aspects of a system's adsorption behaviour can be explained in terms of the adsorption potential. Therefore, study of the adsorption potentials can lead to a better understanding of the fundamentals of adsorption.

One of the most commonly used potentials to represent both the fluid-fluid and the fluid-solid intermolecular interactions is the Lennard-Jones 12:6 potential [Steele, 1974]:

$$u_{LJ}(r) = 4\varepsilon\left[\left(\frac{\sigma}{r}\right)^{12} - \left(\frac{\sigma}{r}\right)^{6}\right] \tag{3-1}$$

where r is the inter-molecule distance, ε the potential well depth of the interaction and σ the collision diameter (corresponding to $u_{LJ} = 0$). The repulsive term (the r^{-12} term) in Equation (3-1) represents the short-range interaction and is due to the overlap of electron cloud in different molecules or atoms. The dispersion term (the r^{-6} term) represents attractive interaction and is the long-range London term for dispersion potential or the van der Waals interaction. Despite its widespread applications, this equation has some defects [Gubbin and Quirke, 1996; Cracknell *et al.* 1995]: (1) The repulsive term is not sufficiently steep at short distances. (2) Neglect of higher order dispersion terms (that vary as r^{-8}, r^{-10}, etc) leads to some inaccuracy in the well and tail of the potential. (3) Neglect of many-body interactions. (4) Neglect of electrostatic terms

and (5) Neglect of anisotropic polarizability. However, these effects are of the second order and some of them may be partly corrected by using the effective LJ parameters rather than LJ parameters for isolated pair of molecules. Therefore, due to its simplicity and common use in molecular simulations, it is employed in this study as the basis of the calculation of both fluid-fluid and fluid-solid interactions, though there are a number of potentials available [Maitland *et al.*, 1981].

In the case of interaction between fluid-fluid molecules, ε and σ are denoted as ε_{ff} and σ_{ff} respectively, while in the case of fluid-solid interaction they are written as ε_{sf} and σ_{sf}. The Lennard-Jones potential parameters ε and σ are functions of the species of the atoms or molecules and can be determined in a number of ways, such as from gas viscosities, second virial coefficients [Maitland *et al.*, 1981] or by fitting simulations results to experimental data. The LJ parameters for the interaction between fluid molecules and carbon atoms can also be determined from the Lorentz-Berthelot combination rules [Steele, 1974]:

$$\varepsilon_{sf} = \sqrt{\varepsilon_{ff}\varepsilon_{ss}} \tag{3-2}$$

$$\sigma_{sf} = \frac{\sigma_{ss} + \sigma_{ff}}{2} \tag{3-3}$$

Table 3-1 presents the LJ parameters used in this study for some fluids and with carbon atoms. The carbon-carbon interaction parameters are $\sigma_{CC} = 3.400$ Å and $\varepsilon_{CC} / k_B = 28.0$ K.

Table 3-1 L-J parameters for fluid-fluid and solid-fluid interactions

Fluid	σ_{ff} (Å)	ε_{ff} / k_B (K)	σ_{sf} (Å)	ε_{sf} / k_B (K)	references
Hydrogen	2.960	41.5	3.180	34.1	Kihara, 1978
Methane	3.810	148.1	3.605	64.4	Aukett *et al.*, 1992
Nitrogen	3.572	93.98	3.494	53.2	Lastoskie *et al.*, 1993

The total interaction energy in the adsorbate is the sum of LJ potentials, Equation (3-1), over all pairs of molecules. To calculate the interaction potentials between a fluid molecule and the pore wall, we need to sum Equation (3-1) over all atoms or molecules in the pore wall:

$$u = 4\varepsilon_{sf} \sum_{i=1}^{N} \left[\left(\frac{\sigma_{sf}}{r_i} \right)^{12} - \left(\frac{\sigma_{sf}}{r_i} \right)^{6} \right] \tag{3-4}$$

where N stands for the total number of atoms in the pore wall and r_i the distance between the fluid molecule and the ith atom in the wall. In practical applications, summation of Equation (3-1) is time consuming. Therefore, to save computation time, the assumption that atoms in the pore wall are uniformly and continuously distributed is made so that the summation can be replaced by integration over the whole volume of the pore wall.

$$\begin{aligned} u &= 4\varepsilon_{sf} \int_N \mathrm{d}N \left[\left(\frac{\sigma_{sf}}{r} \right)^{12} - \left(\frac{\sigma_{sf}}{r} \right)^{6} \right] \\ &= 4\varepsilon_{sf} \rho_V \int_V \mathrm{d}V \left[\left(\frac{\sigma_{sf}}{r} \right)^{12} - \left(\frac{\sigma_{sf}}{r} \right)^{6} \right] \\ &= 4\varepsilon_{sf} \rho_a \int_A \mathrm{d}A \left[\left(\frac{\sigma_{sf}}{r} \right)^{12} - \left(\frac{\sigma_{sf}}{r} \right)^{6} \right] \end{aligned} \tag{3-5}$$

where ρ_V stands for the number of solid atoms per unit volume and ρ_a for the number of solid atoms per unit area for a single layer of adsorbent atoms in the wall. For a certain pore model, evaluation of Equation (3-5) yields the interaction between one fluid molecule and the wall and the total fluid-solid interaction energy is simply the sum of these potentials over all fluid atoms or molecules. Two systems will be discussed in the following paragraphs: one is the slit pore model and the other is the cylindrical pore model. The former is a good model of micropores in activated carbons, while the latter is a good model of the hollow cavities of carbon nanotubes.

3.2 Models and Potentials

3.2.1 Pore models and the potential formula of slit pores

A schematic representation of a slit carbon pore is shown in Figure 3-1. Each pore consists of two pore walls, which in turn consist of n layers of carbon atoms. The inter-layer distance Δ may be considered as a variable for different systems; for perfect graphite Δ = 3.354 Å [Kelly, 1981]. n also can be regarded as a variable for different systems. In each layer, the number of solid atoms per unit area is ρ_a, which may also vary and equals 0.3818 $Å^{-2}$ for perfect graphite. The pore width is measured as the inter-nuclear distance, H, as shown in Figure 3-1. The position of the fluid molecule relative to the pore is denoted by the perpendicular distance from the molecule to one of the pore walls, z.

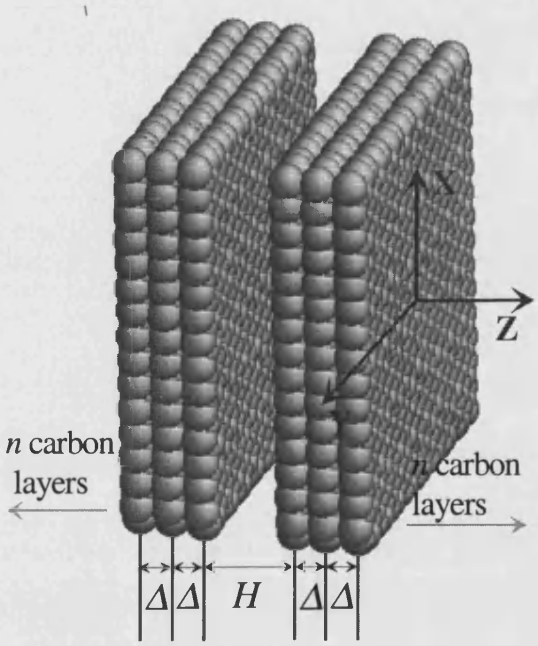

Figure 3-1. Carbon slit pore models. The pore consists of two parallel walls each contains n layers of carbon sheets separated by the interlayer spacing.

A commonly used fluid-wall potential model for a fluid molecule and one carbon wall is the Steele 10-4-3 potential [Steele, 1974]:

$$u(z) = 4\pi \rho_a \varepsilon_{sf} \sigma_{sf}^2 \left[\frac{1}{5}\left(\frac{\sigma_{sf}}{z}\right)^{10} - \frac{1}{2}\left(\frac{\sigma_{sf}}{z}\right)^{4} - \frac{\sigma_{sf}^4}{6\Delta\left(z+0.61\Delta\right)^3} \right] \qquad (3\text{-}6)$$

The first and second terms in Equation (3-6) represent the contribution of the first carbon layer in the pore wall to the potential, while the third represents the contributions of the third and all subsequent carbon layers. In this potential, the pore walls are assumed to be semi-infinite graphite slabs. This excludes some possible studies of real adsorbent systems as pore walls in practical activated carbons are often found to contain only two or three graphite layers. Thus, another approach is introduced below.

By integration of Equation (3-5) over a single infinite graphite sheet, the interaction potentials between a fluid molecule and the single sheet graphite plane can be obtained [Everett and Powl, 1976]:

$$u(z) = 4\pi\rho_a \varepsilon_{sf} \sigma_{sf}^2 \left[\frac{1}{5}\left(\frac{\sigma_{sf}}{z} \right)^{10} - \frac{1}{2}\left(\frac{\sigma_{sf}}{z} \right)^{4} \right] \tag{3-7}$$

The total interaction potential between a fluid molecule and one pore wall comprising n layers of graphite sheets is then given by:

$$u(z) = 4\pi\rho_a \varepsilon_{sf} \sigma_{sf}^2 \sum_{i=0}^{n-1} \left[\frac{1}{5}\left(\frac{\sigma_{sf}}{z+i\Delta} \right)^{10} - \frac{1}{2}\left(\frac{\sigma_{sf}}{z+i\Delta} \right)^{4} \right] \tag{3-8}$$

For slit pores comprising two walls that are H apart, the total potential of a single fluid molecule and the pore is given by:

$$U(z) = u(z) + u(H - z) \tag{3-9}$$

This potential can be used to study the effects of not only pore sizes but also pore wall structures and was first introduced to molecular simulations by Mays [1996].

3.2.2 Pore models and Potentials of cylindrical pores

A representation of a carbon cylindrical pore is shown in Figure 3-2. The pore wall consists of n layers of solid atoms and all the layers are coaxial. The inter-layer distance is also denoted by Δ. The pore size is given by the tube diameter D or radius $R = D/2$, which is measured as internuclear distances. The position of the fluid molecule relative to the pore is

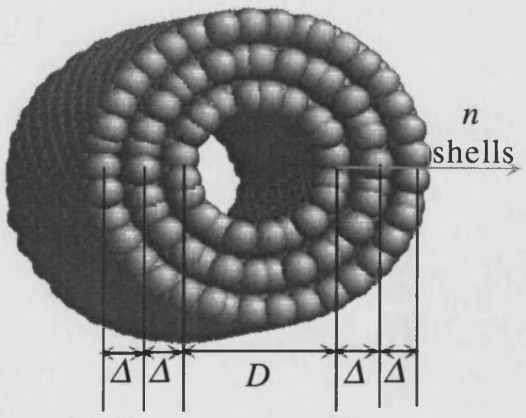

Figure 3-2. Cylindrical carbon pore model consists of n concentric shells of carbon separated by interlayer spacing Δ. D is the inner diameter of the tube.

denoted by the distance of the molecule from the tube axis, r. For a single-sheet tube of inner radius R, the interaction between one fluid molecule and the tube is given by [Everett and Powl, 1976]:

$$U(r) = 3\pi^2 \rho_a \varepsilon_{sf} \sigma_{sf}^2 \left[\frac{21}{32} \left(\frac{\sigma_{sf}}{R} \right)^{10} \sum_{k=0}^{\infty} \alpha_k \left(\frac{r}{R} \right)^{2k} - \left(\frac{\sigma_{sf}}{R} \right)^{4} \sum_{k=0}^{\infty} \beta_k \left(\frac{r}{R} \right)^{2k} \right] \tag{3-10}$$

The two coefficients are as follows:

$$\begin{aligned} \alpha_k^{1/2} &= \frac{\Gamma(-4.5)}{\Gamma(-4.5-k)\Gamma(k+1)} \\ \beta_k^{1/2} &= \frac{\Gamma(-1.5)}{\Gamma(-1.5-k)\Gamma(k+1)} \end{aligned} \tag{3-11}$$

where $\Gamma(\,)$ is the gamma function.

For a tube comprising n sheets in the wall, summation of Equation (3-10) over the n layers gives the following:

$$U(r) = 3\pi^2 \rho_a \varepsilon_{sf} \sigma_{sf}^2 \sum_{i=0}^{n-1} \left[\frac{21}{32} \left(\frac{\sigma_{sf}}{R+i\Delta} \right)^{10} \sum_{k=0}^{\infty} \alpha_k \left(\frac{r}{R+i\Delta} \right)^{2k} - \left(\frac{\sigma_{sf}}{R+i\Delta} \right)^{4} \sum_{k=0}^{\infty} \beta_k \left(\frac{r}{R+i\Delta} \right)^{2k} \right] \tag{3-12}$$

This equation has two main shortcomings: (1) The calculation of the interaction involves the evaluation of infinite series. Thus in practical applications, the series must be cut off at some index values which may cause considerable errors depending on the ratio of $\left(\frac{r}{R+i\Delta} \right)$; (2) Outside a cylindrical pore, the term $\left(\frac{r}{R+i\Delta} \right)$ becomes larger than unity, thus the infinite series is divergent and the equation is no longer valid. Thus a general equation which is applicable both inside and outside carbon tubes is needed.

Consider the area element in Figure 3-3, Equation (3-5) can be rewritten as:

$$U = 4\varepsilon\,\rho_a \int_A \left[\left(\frac{\sigma}{r'}\right)^{12} - \left(\frac{\sigma}{r'}\right)^{6}\right] dA$$

where $r'^2 = R^2 + r^2 - 2Rr\cos\theta + y^2$ is the square of the distance from the fluid molecule to the area element. The area element is $dA = R\,d\theta\,dy$. Therefore, the above integration over the whole surface of the infinitely long tube becomes:

$$U = 4\varepsilon\rho_a R \int_0^{2\pi}\int_{-\infty}^{\infty}\left[\left(\frac{\sigma}{r'}\right)^{12} - \left(\frac{\sigma}{r'}\right)^{6}\right] dy\,d\theta \qquad (1)$$

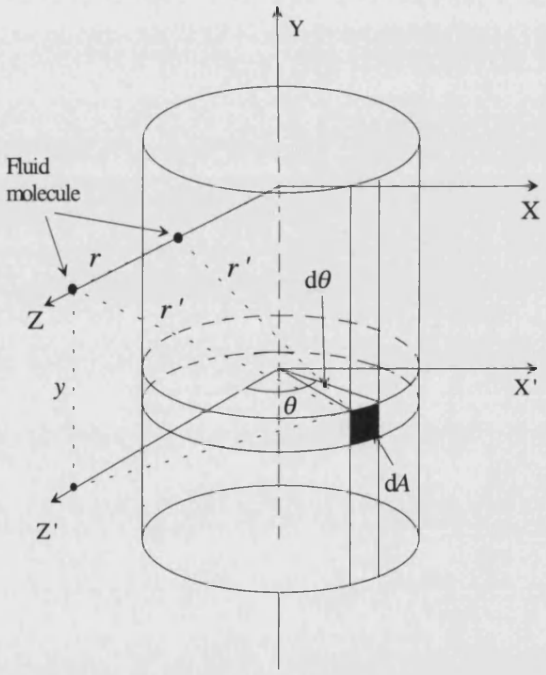

Figure 3-3. Derivation of interaction potentials inside and outside carbon nanotubes.

The evaluation of this double integral is complicated and is only briefly introduced below. After integration over y from $-\infty$ to $+\infty$, (1) becomes:

$$U = 4\varepsilon\rho_a R\left(\frac{945\pi\sigma^{12}}{3840}\int_0^{2\pi}\frac{d\theta}{\left(R^2+r^2-2Rr\cos\theta\right)^{11/2}} - \frac{3\pi\sigma^6}{8}\int_0^{2\pi}\frac{d\theta}{\left(R^2+r^2-2Rr\cos\theta\right)^{5/2}}\right) \qquad (2)$$

To evaluate the two integrals in the above equation, it is convenient to introduce two new parameters:

$$s = \frac{r}{R},$$

$$q = \frac{2\sqrt{s}}{(1+s)}. \tag{3}$$

Then the two integrals over θ in (2) can be reduced to combinations of the following two integrals:

$$E(q) = \int_0^{\pi/2} \sqrt{1-q^2\sin^2\theta}\, d\theta,$$

$$K(q) = \int_0^{\pi/2} \frac{d\theta}{\sqrt{1-q^2\sin^2\theta}}.$$

They are called the complete elliptical integrals of the first and the second kind respectively and can be evaluated numerically when $q \leq 1$ [Gradshteyn and Ryzhik, 1965]. Because the q value defined in Equation (3) always satisfies this condition whether the fluid molecules are inside or outside the tubes, the resultant potential function will be applicable to both endohedral and exohedral adsorption. The final form of the integrated potential can be written as:

$$U(r) = 2\pi\, \rho_a \varepsilon_{sf}\, \sigma_{sf}^2 \left[\frac{G_{12}(s)}{R_*^{10}} - \frac{G_6(s)}{R_*^4} \right] \tag{3-13}$$

where

$$R_* = \frac{R}{\sigma_{sf}},$$

$$G_{12}(s) = \frac{1}{160(1-s)^2(1+s)} \left[E(q)P_1(s) - \frac{4K(q)}{(1+s)^2} P_2(s) \right]$$

$$G_6(s)=\frac{1}{(1-s)^2(1+s)^3}\left[4E(q)\frac{(1+s^2)}{(1-s)^2}-K(q)\right]$$

$$P_1(s)=\frac{128}{(1+s)^8}+\frac{104}{(1-s)^2(1+s)^6}+\frac{99}{(1-s)^4(1+s)^4}+\frac{104}{(1-s)^6(1+s)^2}+\frac{128}{(1-s)^8}$$

$$P_2(s)=\frac{16}{(1+s)^6}+\frac{15}{(1-s)^2(1+s)^4}+\frac{15}{(1-s)^4(1+s)^2}+\frac{16}{(1-s)^6}$$

Obviously, $s > 1$ represents the situation outside the tube, while $s < 1$ inside. Equation (3-13) is similar to the one reported by Breton *et al.* [1994]. However, the equation reported by Breton *et al.* has two errors and cannot lead to correct evaluations of the potential. When inside carbon nanotubes, Equation (3-3) gives the same potential values as the Everett and Powl potential (Equation (3-10)). When $R \rightarrow \infty$, Equation (3-13) will lead to the Everett and Powl potential for single-walled carbon slits, Equation (3-7), as expected. Thus, Equation (3-13) can be thought of as a general potential for both slit and cylindrical pores.

For a cylindrical pore with n sheets in the pore wall, the total potential between one fluid molecule and the tube can be obtained by summing Equation (3-13) over the n layers, that is,

$$U(r)=\sum_{i=1}^{n}\left\{2\pi\rho_a\varepsilon_{sf}\sigma_{sf}^2\left[\left(\frac{G_{12}(s_i)}{R_{*i}^{10}}\right)-\left(\frac{G_6(s_i)}{R_{*i}^4}\right)\right]\right\} \qquad (3\text{-}14)$$

where $R_{*_i}=\dfrac{R+(i-1)\Delta}{\sigma_{sf}}, s_i=\dfrac{r}{R+(i-1)\Delta}$.

3.2.3 Pore models and Potentials of SWCNT arrays

Practically, carbon nanotubes are formed in arrays or bundles rather than in isolation. A model of SWCNT arrays is shown in Figure 3-4. All the nanotubes in the array are supposed to be perfectly aligned with their axis parallel to each other. The arrays are

characterised by tube diameters, D and tube separations, G, which are all measured as internuclear distances as shown in Figure 3-4. Two kinds of arrays are studied, *i. e.* the trigonal ($\theta = 60°$) and square ($\theta = 90°$) arrays. In both arrays, the tubes may be open or closed. Thus both endohedral and interstitial adsorption will take place in open tube arrays, while in closed tube arrays only endohedral adsorption will occur.

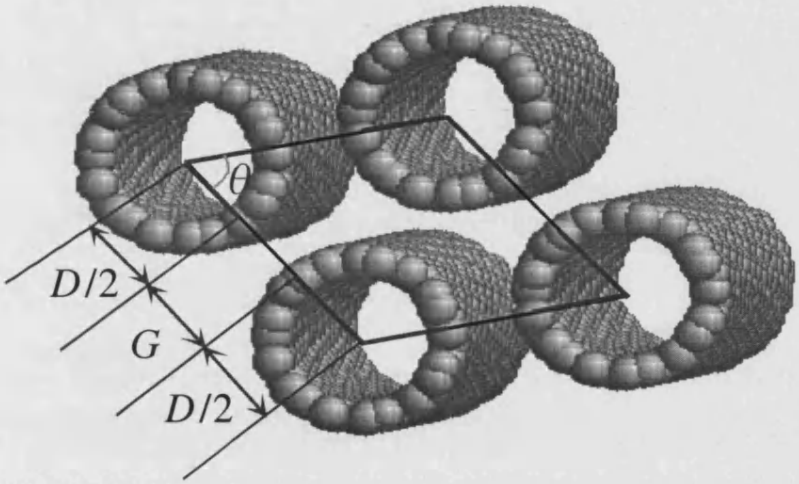

Figure 3-4. Models of perfectly aligned single-walled carbon nanotube arrays characterised by tube diameter, D and tube separation G. $\theta = 60°$, trigonal arrays; $\theta = 90°$, square arrays.

Since Equation (3-13) is applicable to both endohedral and exohedral adsorption, it is easy to adapt this equation to the array situations. The interaction between one fluid molecule and the array will be the sum of Equation (3-13) over all the tubes forming the array. However, as the interaction decreases steeply with increasing distance, only a limited number of tubes close to the fluid molecules will be necessary to be added to the summation.

3.3 Results and discussions on interaction potentials

3.3.1 Potentials in slit shaped carbon pores

For the study of adsorption potentials in both slit and cylindrical pores, the interaction between a single nitrogen molecule and the pore walls is calculated. Figure 3-5 shows the adsorption potentials of a nitrogen molecule in slit carbon pores with varying pore width. As can be seen from the figure, there is little potential enhancement for pores with widths greater than 30 Å. The potential curves can be regarded as two separate interaction curves of the two walls of the slits. For smaller pores, the potential curves of the two walls overlap and the smaller the pore, the stronger the enhancement of the

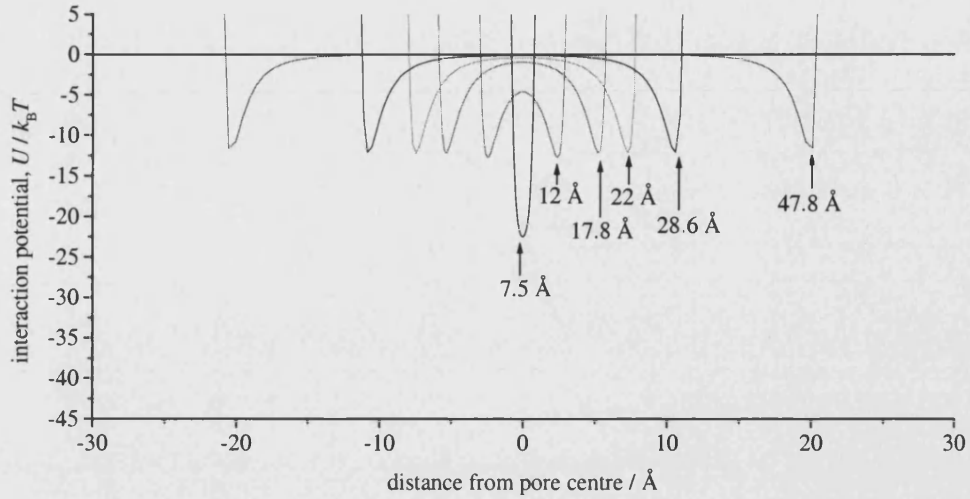

Figure 3-5. Interaction potentials of a nitrogen molecule in slit carbon pores with different pore width. The potential is expressed in the reduced units and the figures labelled in the graph are corresponding slit widths.

potential. However, the enhancement is still not very remarkable when pore widths are greater than about 12 Å. Upon further decrease of pore width, the potential well depth increases sharply. At a pore width of 7.5 Å, the potential minimum is nearly double that of the largest pore in Figure 3-5, which can be regarded as identical to the potential minimum of a single layer graphite sheet. The implication of this potential variation as a function of pore width is that strong adsorption enhancement is found for micropores and small mesopores, as expected.

The effects of pore wall thickness on the adsorption potentials are shown in Figure 3-6 for a pore width of 13.7 Å. For thin wall pores, that is, for small values of n, the effects are considerable, especially the potential minimum decreases sharply when n increases from 1 to 2. However, on further increase of pore wall thickness, the decrease of potential minimum slows down. When n is greater than 5, the curve in Figure 3-6 is nearly a horizontal line,

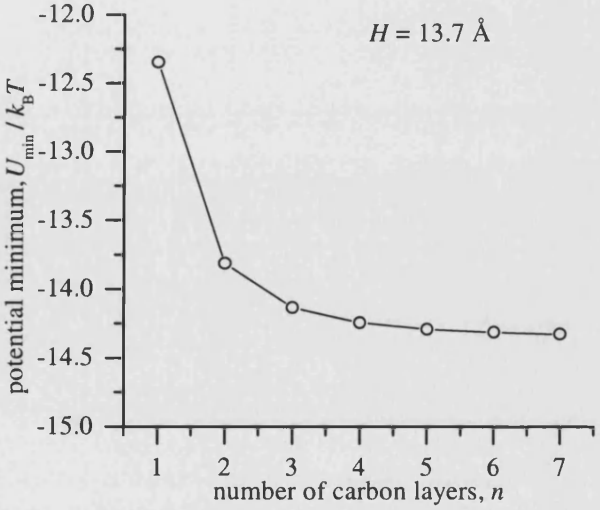

Figure 3-6. Potential minimum of nitrogen in slit carbon pores as a function of pore wall thickness, *i.e.* the number of carbon layers in the wall, n.

indicating that $n \geq 5$ can be effectively regarded as infinitely thick pore walls.

3.3.2 Potentials in cylindrical carbon pores

3.3.2.1 Exohedral cylinder potentials

Some examples of adsorption potentials outside single walled cylindrical pores are shown in Figure 3-7. The potential curves generally have the same shape. The collision diameters corresponding to different tube diameters do not change considerably with tube diameters. However, the depth of the potential well increases with increasing tube diameter. This is due to the curvature of the pore wall and the larger the tube diameter, the nearer the potentials to that of a single graphite sheet. The increase in potential well depth is not marked. From the smallest to the largest tube, the depth increases by only about 30%, while in the case of slits, it increases by about 100%. All the potentials approach zero at a distance around 11-12 Å from the tube wall, that is, about three times of the fluid molecule size. When tube diameter increases to a relatively large value, the exohedral potential approaches the potential of a single flat infinite graphite sheet, as expected.

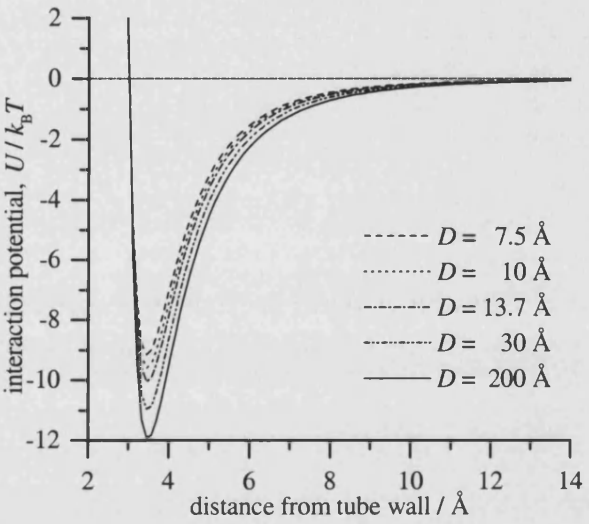

Figure 3-7. Exohedral interaction potentials between a nitrogen molecule and single walled carbon tubes with different tube diameters.

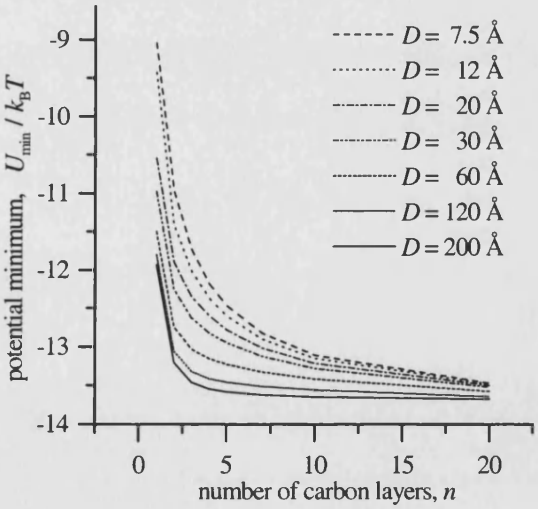

Figure 3-8. Exohedral potential minima as functions of tube wall thickness for nitrogen outside tubes with different inner diameters.

The exohedral potential minimum is also strongly dependent on tube wall thickness, as shown in Figure 3-8, especially when n varies from 1 to 2. This is similar to the variation of potential minimum as a function

of pore wall thickness in slits (Figure 3-6). The variation in potential minimum here is more marked because the outer diameter of the tube increases when n increases. Thus Figure 3-8 shows the combined effects of increasing tube wall thickness and tube outer diameter. For thicker tube walls, the increase of potential well depth slows down and finally levels off.

3.3.2.2 Endohedral cylinder potentials

Inside cylindrical pores, the potentials vary in a similar way to those in slit pores, as shown in Figure 3-9. In large pores, the enhancement of potential can be neglected, while in smaller pores, the enhancement becomes very marked.

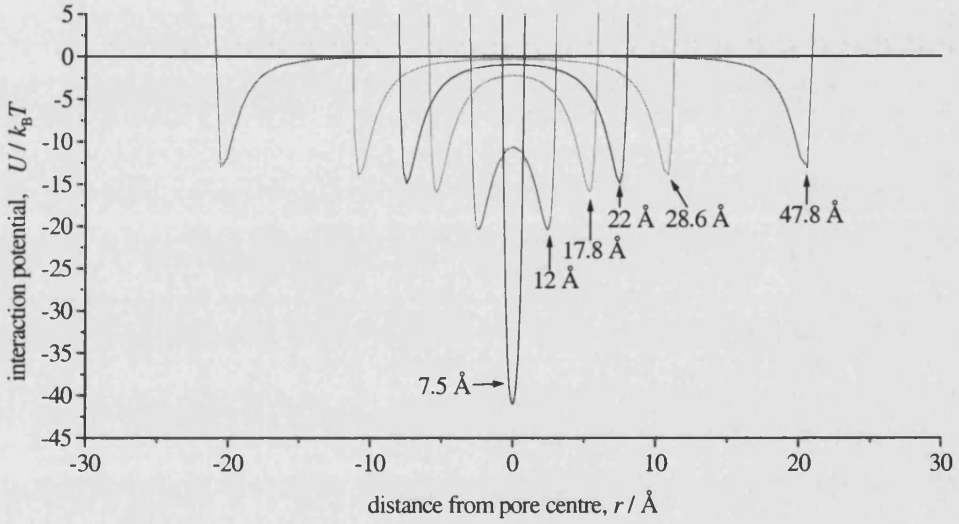

Figure 3-9. Interaction potentials of a nitrogen molecule inside single-walled carbon tubes as functions of tube diameters. The figures shown in the graph are corresponding tube diameters.

The following differences between the potentials inside a cylindrical and a slit pore can be readily seen by comparing Figure 3-9 to Figure3-5: (1) The enhancement of adsorption potentials occurs at larger pore sizes in the case of cylindrical pores. There is some enhancement of the potential at pore diameter of 30 Å in tubes, but little enhancement is found for slit of width greater than 30 Å. (2) The enhancement of adsorption potentials is greater in cylindrical pores than in slit pores. The increase of potential well depth is sharper in tubes than in slits. (3) The maximum enhancement at the smallest pore size studied is around three times in tubes, while it is twice in slits.

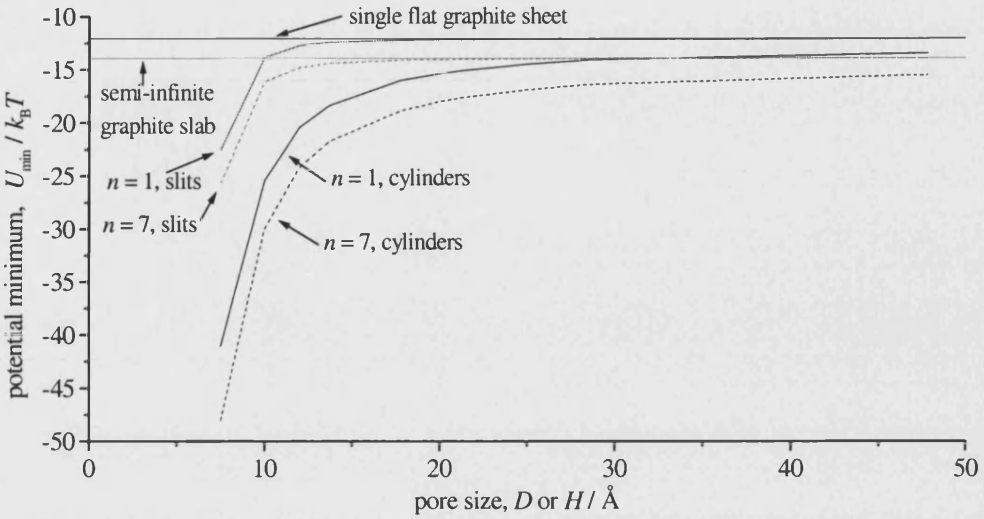

Figure 3-10. Potential minimum of a nitrogen molecule inside carbon tubes and slits as functions of pore size for two different pore wall thickness, together with the potential minima of a semi-infinite graphite slab and a single graphite sheet.

Figure 3-10 shows the adsorption potential minimum as a function of pore size of slit and cylindrical pores with two different pore wall thickness. The potential minima for a single infinite graphite sheet and for a semi-infinite graphite slab are also shown for reference. For slits, the potential minimum for both n = 1 and n = 7 increases sharply with pore width at small pore widths and then approaches the reference values. At a pore width of about 12 Å and with n =1, the potential minimum is in effect the same as the reference and the minimum is identical to the reference when pore widths greater than about 18 Å. For n = 7, the potential minima approach the reference values slower, but only for a few angstroms and is still within the micropore region. On the other hand, the potential minima in tubes show more pronounced increases as tube diameter increases. Even for tube diameters up to 50 Å, the potential minimum is still markedly different from the reference values. This again shows a much stronger enhancement of adsorption potentials in tubes than in slits. This suggests that (1) tubes with diameters up to about 50 Å will show microporous behaviour, (2) if adsorption potential enhancement is set as the criteria of the boundary between micropores and mesopores, the upper limit of micropores should be larger than 50 Å in case of tubular pores.

Similar effects of pore wall thickness on the adsorption potentials are found for tubes, as shown in Figure 3-11. Except the values of the potential minima, all the four lines in the figure have similar shapes. They all decrease sharply at the beginning and level off at about n = 5. Therefore, as far as the adsorption potentials are concerned, strong effects

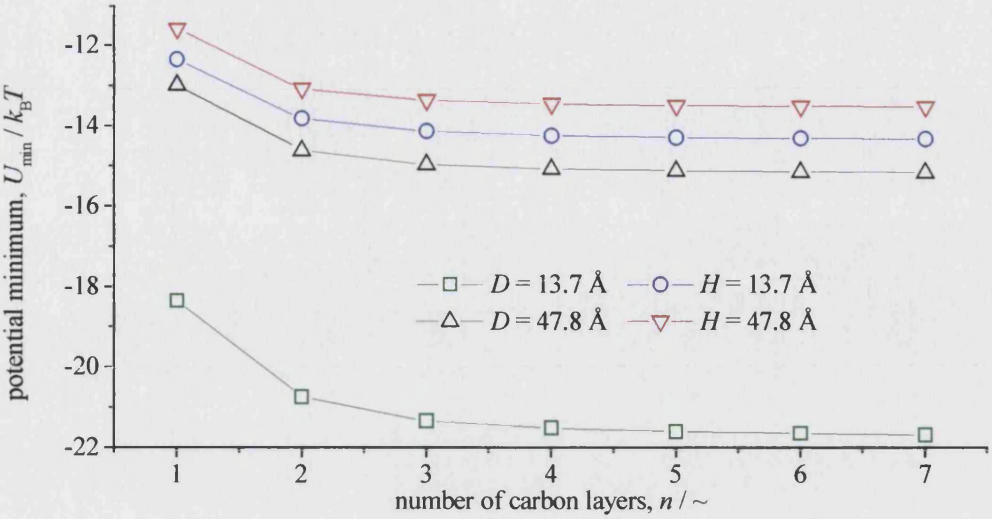

Figure 3-11. Effects of pore wall thickness on the potential minimum of a nitrogen molecule inside both tubes and slits with two different pore widths.

of pore wall thickness only can be found for thin pore walls and pore walls with five or more graphene sheets can be effectively regarded as infinitely thick. These are true both for tubes and slits.

3.3.3 *Potentials in SWCNT arrays*

Potential maps of some typical square arrays are shown in Figures 3-12 to 3-15, together with some plots of the potentials along three directions, ab, AB and AB'. The potentials

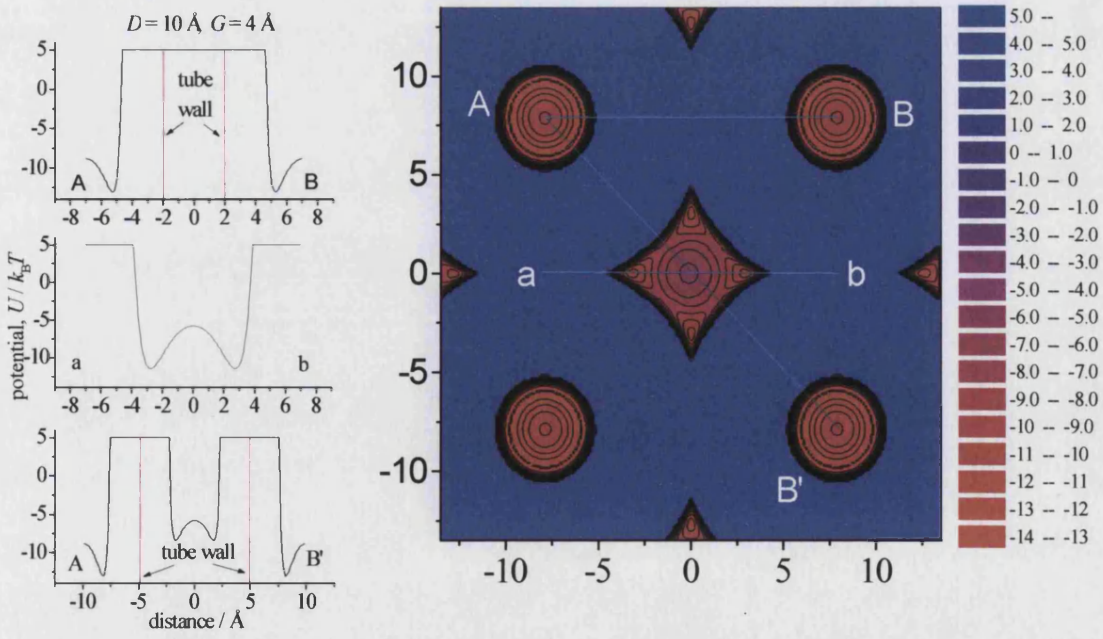

Figure 3-12. Potentials of a nitrogen molecule in single walled carbon nanotube arrays with tube diameter of 10 Å and separation 4 Å. The potentials along three directions AB, ab and AB' are plotted at the left of the potential map. The dark blue areas are carbon nanotube walls.

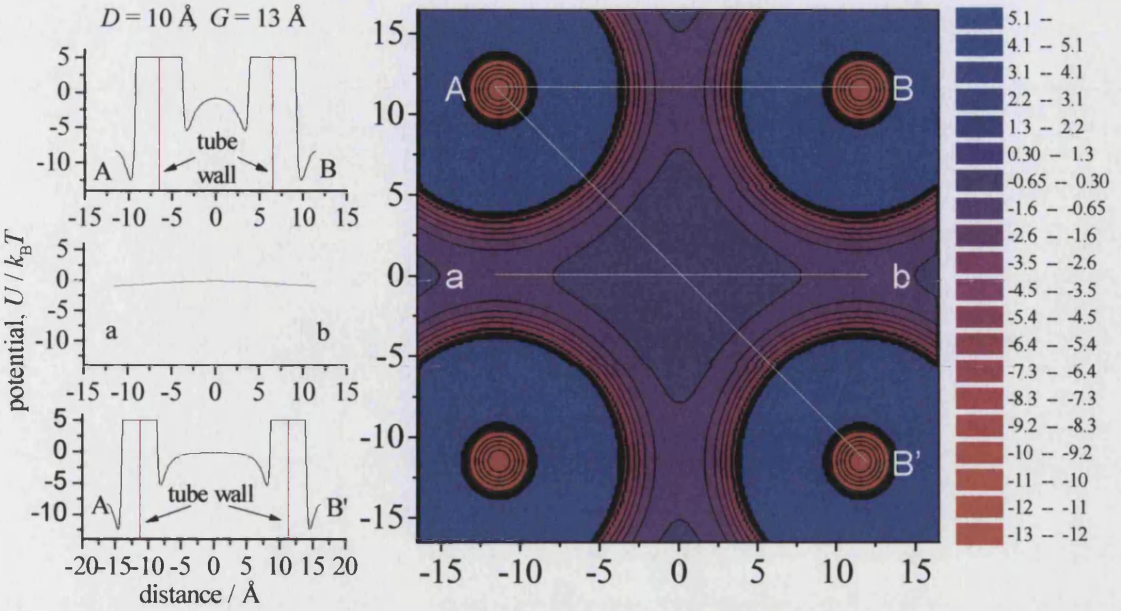

Figure 3-13. Potentials of a nitrogen molecule in single walled carbon nanotube arrays with tube diameter of 10 Å and separation 13 Å. The potentials along three directions AB, ab and AB' are plotted at the left of the potential map. The dark blue areas are carbon nanotube walls.

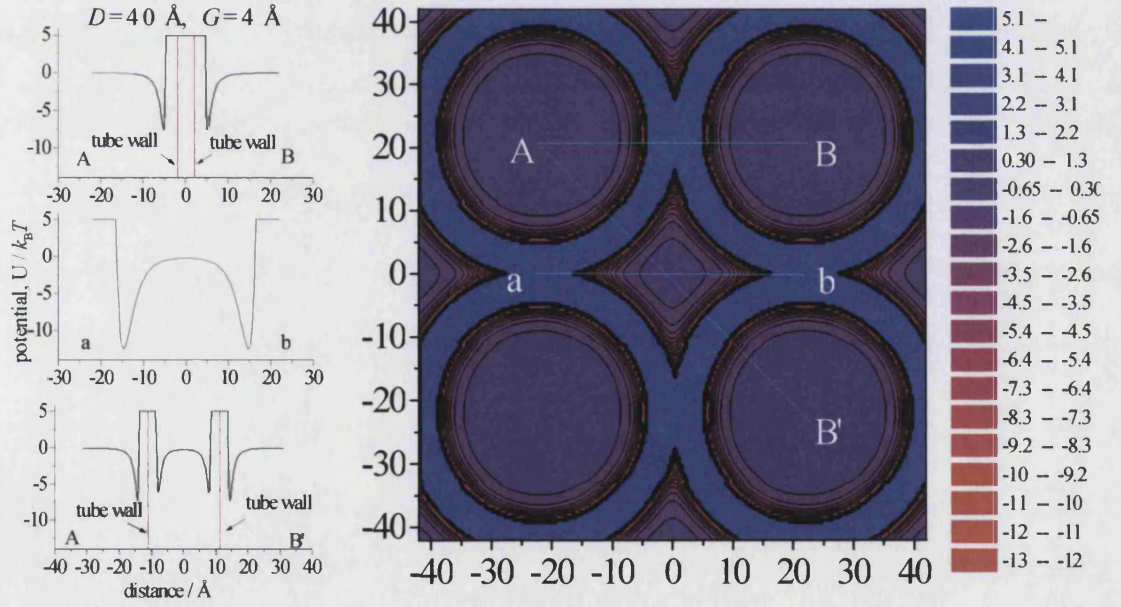

Figure 3-14. Potentials of a nitrogen molecule in single walled carbon nanotube arrays with tube diameter of 40 Å and separation 4 Å. The potentials along three directions AB, ab and AB' are plotted at the left of the potential map. The dark blue areas are carbon nanotube walls.

are calculated from Equation (3-13) by taking the contribution of neighbouring 36 nanotubes into consideration. In these graphs, the blue circles are the nanotubes and the red areas are of the strongest interactions. Generally, the potentials are stronger inside the tubes. However there are also significant potentials between tubes. For example, comparison of the plots of potentials shown in Figure 3-14 along the AB and ab directions shows that the strongest potential is along the ab direction. Therefore, these corners may be occupied by adsorbate at very low pressures.

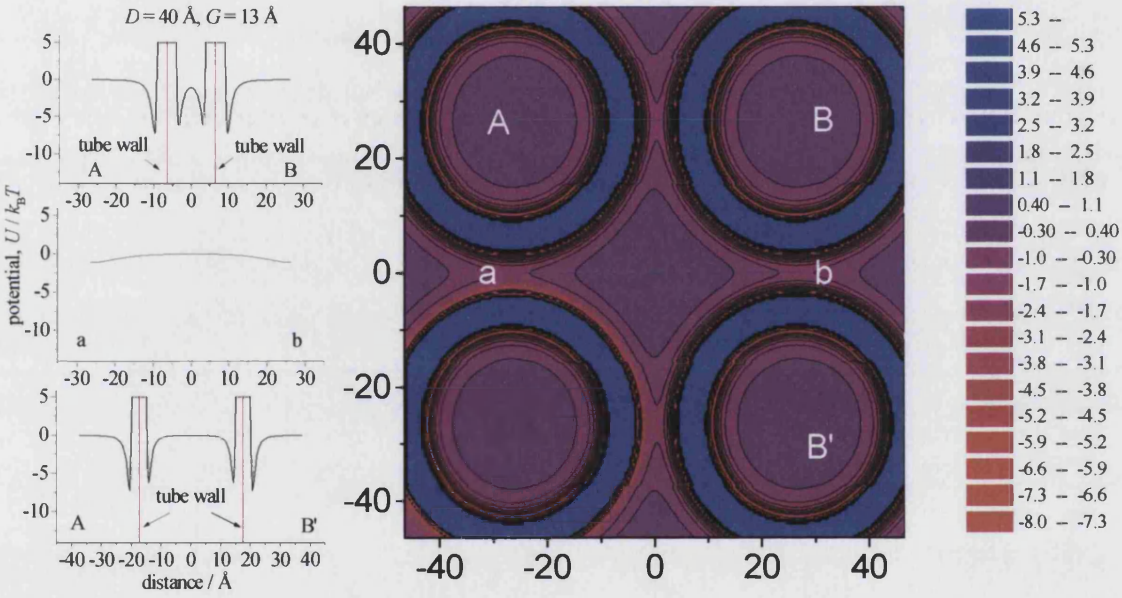

Figure 3-15. Potentials of a nitrogen molecule in single walled carbon nanotube arrays with tube diameter of 40 Å and separation 13 Å. The potentials along three directions AB, ab and AB' are plotted at the left of the potential map. The dark blue areas are carbon nanotube walls.

At larger tube separations, the strongest potential is inside the tube and about σ_{sf} from the tube wall. Thus a monolayer will be formed inside the tube at low pressures. The next strongest potential zone is outside the tube and also about σ_{sf} from the tube wall. A monolayer should be formed in this area.

At the centres of the tubes and the interstitial space, the interaction potentials can be very weak, especially at large tube diameters and separations. This indicates that the density of adsorbed fluids in these parts of the array can be much lower than the density of the monolayers.

3.4 Summary and conclusions

New potentials have been adopted to describe the interaction between fluid molecules and slit carbon pores. Potentials which are applicable to both endohedral and exohedral cylindrical carbon pores have been derived. These potentials can be used to study the effects of not only pore sizes but also pore wall structures on adsorption behaviour. Marked enhancement of potentials only can be found in small slit micropores, but can be found in tubes as wide as 50 Å. The enhancement of potentials in cylindrical pores is much stronger than in slit pores, indicating that carbon nanotubes might be a good adsorbent. Pore walls thickness has marked influence on the adsorption potentials in thin wall pores and pore walls with five or more carbon layers can be effectively regarded as infinitely thick. Interstitial potentials in nanotube arrays can be very strong due to the overlap of potentials of different tube walls, indicating that interstitial adsorption can make marked contributions to the adsorption of carbon nanotube arrays.

Chapter 4
Adsorption in Activated Carbons

Chapter 2 and Chapter 3 form the basis of simulation study of adsorption in porous carbons. This chapter presents results of simulation study of adsorption in activated carbons while the subsequent chapters present results of adsorption in carbon nanotubes.

4.1 General features of adsorption in carbon slits

Figure 4-1 shows a series of isotherms of nitrogen adsorbed at 77 K in single-walled carbon slits with varying pore widths. These isotherms were simulated using the Monte Carlo method described in Chapter 2 and based on the adsorption potentials given in Chapter 3 with the surface density of carbon atoms of ρ_a = 0.3818 Å^{-2}. The adsorbed amount is presented in reduced density, which is equal to the simulated nitrogen density divided by the density of bulk liquid nitrogen at 77 K (28.87 mmol cm^{-3}). From Figure 4-1, we can see that:

(1) As pore width decreases, the pore is filled at lower and lower pressures, due to stronger enhancement of potentials in smaller pores. For slit of width 7.5 Å, the pore is filled at a relative pressure of about 10^{-7}.

(2) The reduced density at saturation increases with pore width. This is mainly

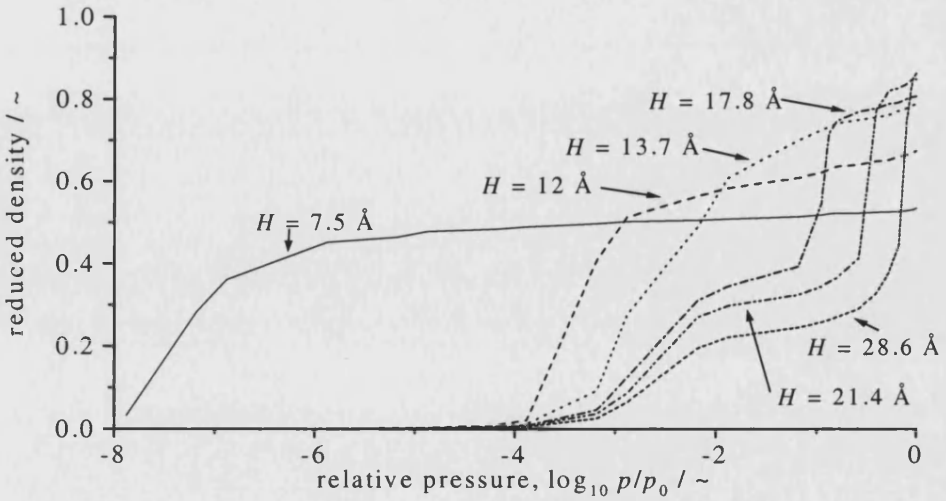

Figure 4-1. Simulated adsorption isotherms of nitrogen at 77 K in single-walled carbon slits with varying pore widths, H with ρ_a = 0.3818 Å^{-2}.

due to the calculation method of the simulated density. In the calculation of the pore volume, pore width is measured as internuclear distance rather than the volume actually occupied by nitrogen molecules. The density may be better represented using the effective pore width H_{eff}. There are a number of expressions for the effective pore width [Quirke and Tennison, 1996; Chen *et al.*, 1997]. But according to our study [McEnaney *et al.*, 1998], the effective pore width can be represented as $H_{eff} = H - \sigma_{cc}$, where σ_{cc} is

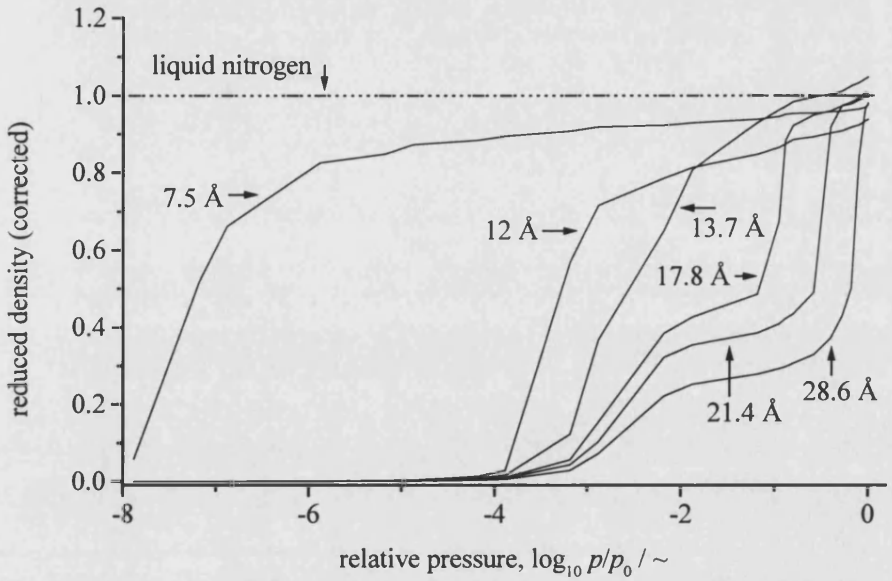

Figure 4-2. Adsorption isotherms of nitrogen at 77 K adsorbed in single-walled carbon slits with reduced density corrected.

3.400 Å. Thus, the modified density will be $\rho' = \rho \frac{H}{H - \sigma_{cc}}$, where ρ is the reduced density. This modification is most significant for smaller pores. The corrected isotherms are shown in Figure 4-2. As can be seen from Figure 4-2, the saturation density of the adsorbed phase is around liquid nitrogen density.

(3) For larger micropores, the isotherms are of type IV showing not only the monolayer completion, but also condensation at higher pressures. However, the simulated capillary condensation is not an equilibrium transition, but rather is a consequence of the GCEMC simulation algorithm.

(4) The monolayer density decreases with increasing pore width. This is reasonable, because the volume of the simulation cells is proportional to pore width H while in ideally close packed situations, the amount adsorbed in the monolayer is fixed for different pore width, provided the areas are the same. Also, the potential is stronger in smaller pores due to the overlap of the interaction between the molecules adsorbed in

the monolayer and two pore walls. Thus the monolayer may be more densely packed in smaller pores.

(5) It is interesting that for pores of widths greater than 12 Å, the uptake of nitrogen molecules starts at similar pressures around 10^{-4}. A possible reason is that for pores of such widths, the molecule-wall potential minimum only changes little and are all very close to the value for a single infinite graphite sheet (Figures 3-5 and 3-10).

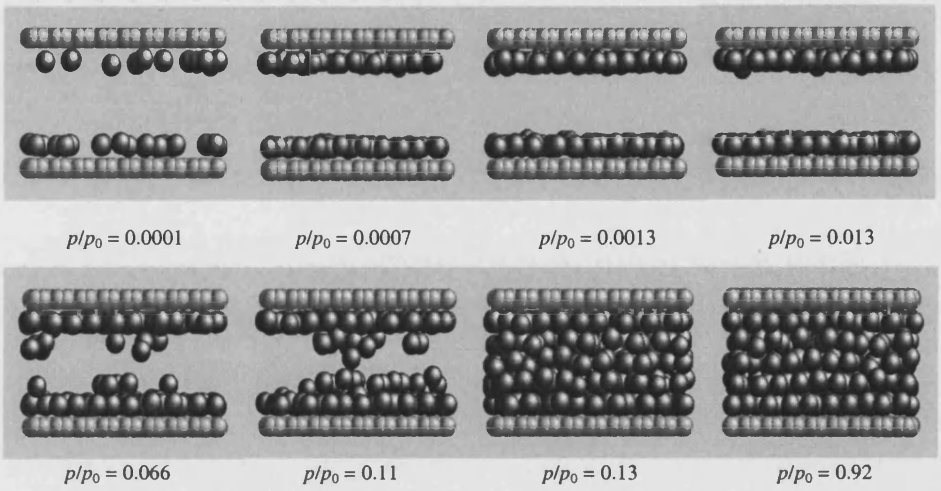

Figure 4-3. Snapshots of nitrogen adsorbed in single-walled carbon slits of width H = 20 Å at 77 K at different relative pressures p/p_0. The dark spheres are nitrogen molecules and the grey ones are carbon atoms in the pore wall.

The adsorption process is illustrated in Figure 4-3 by snapshots at different relative pressures. In each picture in Figure 4-3, the grey spheres represent carbon atoms in the pore walls while the dark spheres represent nitrogen molecules adsorbed in the carbon slit at corresponding relative pressure. At very low relative pressures (< 0.0001), there are some molecules adsorbed in the pore and the adsorption is due to the build up of the monolayer. The monolayer is completed in relative pressure range from 0.013 to 0.066 for the 20 Å slit and few molecules can be found between the monolayers. From p/p_0 = 0.066 to p/p_0 = 0.11, there is not much change in the number of molecules adsorbed in the slit and the adsorption is the build up of the second layers. However, when p/p_0 increases from 0.11 (where the second layers are not complete) to 0.13, the pore will be filled with molecules, resulting in a sharp increase in the amount adsorbed, a clear indication of condensation. Although the pressure may vary, condensation generally occurs for large micropores and small mesopores as shown in Figure 4-1 by the sharp increase in reduced density after monolayer completion.

It should be noted that the isotherms presented here are in most cases different from experimental ones. This is because that in practice, activated carbons often have pores distributed over a wide rage of sizes. Basically, from the isotherms simulated and given pore size distributions, one can generate various types of isotherms. In principle, the reverse procedure will enable the determination of pore size distribution from experimental isotherms and some efforts have been put on this subject by several authors [Lastoskie *et al.*, 1993; Samios *et al.*, 1997].

4.2 Influence of pore wall structure

In practical activated carbons, the carbon material comprising the pore walls contains defects and is different from ideal graphite structure as transmission electron microscopy and X-ray diffraction study show [Bansal *et al.*, 1988]. Firstly, the thickness of the pore wall is finite and often found to be only a few layers thick rather than infinite as assumed in common simulations. Secondly, the interlayer spacing is commonly larger than 3.354 Å for perfect graphite and extremely large layer separations as large as 7 Å have been reported [Fryer, 1981]. Finally, defects inevitably exist in the carbon layers. The degree of the deviation from perfect graphite structure of the pore wall will definitely have effects on the adsorption properties. The effects of pore wall structure are studied in three ways. (1) Pore wall thickness by varying the number of carbon layers contained in pore wall, n. (2) by increasing the perfect graphite interlayer spacing of 3.354 Å by 5%, 10%, 15% and 20% (Δ increases from 3.354 to 4.025 Å). (3) by decreasing the carbon atom density in the perfect graphite of 0.3818 $Å^{-2}$ by 5%, 10%, 15% and 20% of the value for perfect graphite. These are presented below with pores of width 16 Å. It should be noted that when one parameter varies, the others are of the values for perfect graphite. Similar results were found for other pore widths.

4.2.1 Effects of pore wall thickness

As shown in Figure 4-4, the influence of pore wall thickness is marked and the isotherms are shifted to lower pressures as pore wall thickness is increased. It is also interesting that there is a dramatic change from $n = 1$ to $n = 2$, while for $n > 2$ the changes are relatively small. Also, more marked variations in isotherms are found at low pressures than at higher pressures, and the monolayer formation steps become more clearly separated as the number of layers in the pore wall increases (Figure 4-4). These

effects of pore wall thickness on the isotherms are summarised in Figure 4-5. Five parameters were introduced in Figure 4-5 to describe and compare adsorption isotherms: (1) p_m, the mid-point pressure of monolayer forming process; (2) p_{mc}, the mid-point pressure of monolayer completion; (3) p_c, the mid-point pressure of condensation branch of the isotherm; (4) RD_M, reduced density at monolayer completion; (5) RD_S, reduced density at saturation.

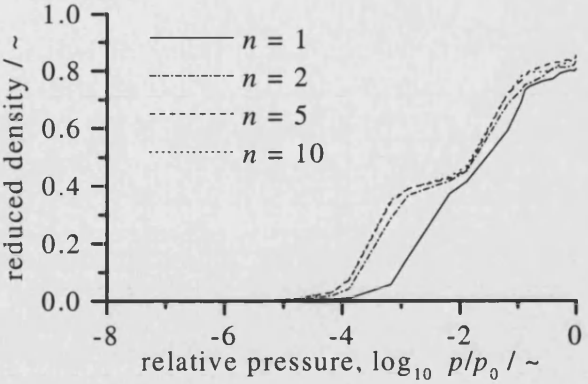

Figure 4-4. Adsorption isotherms of nitrogen adsorbed at 77 K in carbon slit pores of width 16 Å with different pore wall thickness, n.

It can be seen that there are sharp drops at the beginnings of all the three pressure curves. Then the decreases slow down upon increasing n. At around n = 5, all these curves level off, indicating no decreases upon further increases in pore wall thickness. When n < 3, there is an increase in saturation density upon increasing pore wall thickness. However, when n exceeds 3, there is no systematic variations of saturation density, indicating that $n \geq 3$ may be regarded as $n = \infty$ in this situation. Figure 4-5 also shows that there is nearly no change in monolayer density for different pore wall

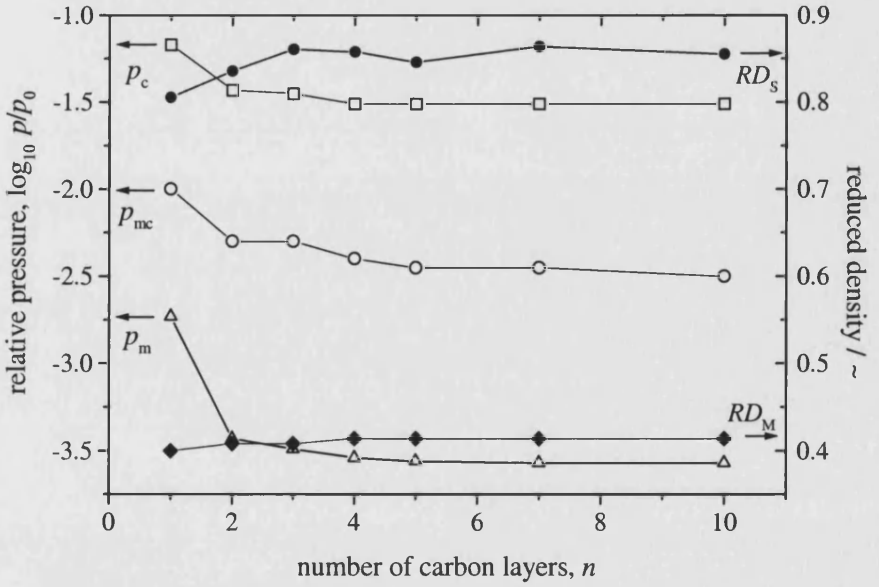

Figure 4-5. Effects of pore wall thickness, n, on the adsorption isotherm parameters, p_m, p_{mc}, p_c, RD_M and RD_S.

thickness. Thus, it may be concluded that wall thickness has significant influence on the characteristics of adsorption isotherms for thin walls and $n \geq 5$ can be effectively considered as $n = \infty$. The influence of pore wall thickness is significant not only on monolayer filling, but also on condensation. These influences of pore wall thickness may be well understood by considering the variation of nitrogen-wall potential minimum due to the change of wall thickness (Figures 3-6). When n changes from 1 to 2, there is a jump in the potential minimum. Upon further increase of n, the variation of the potential minimum slows down quickly and nearly levels off at around $n = 5$.

4.2.2 Effects of atom density in pore wall

Figure 4-6 shows a series of nitrogen adsorption isotherms at 77 K with varying atom densities in the pore wall. The left-most isotherm is for an atom density of perfect graphite, $\rho_a = 0.3818$ atoms Å^{-2}. The remaining isotherms are for atom densities that are 5, 10, 15 and 20% less than that for perfect graphite. Consequently, the range of atom density is from 0.3054 to 0.3818 atoms Å^{-2}. These are equivalent to the carbon skeleton density of from 1.81 to 2.27 g cm^{-3} when the interlayer spacing is 3.354 Å.

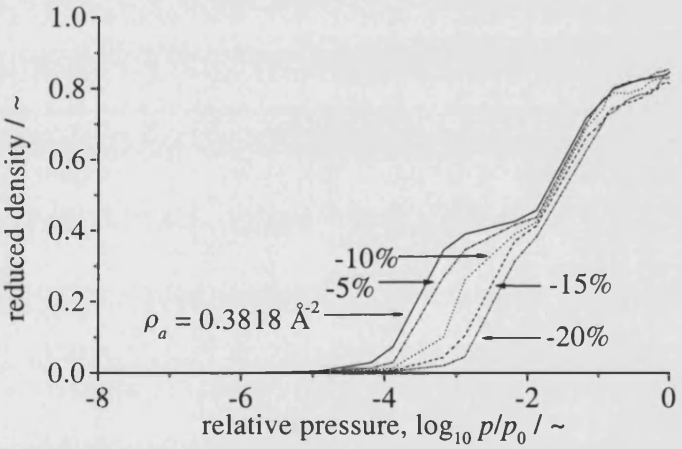

Figure 4-6. Adsorption isotherms of nitrogen adsorbed at 77 K in carbon slits of width 16 Å with different variations in carbon atom densities, ρ_a, in the pore wall from perfect graphite ($\rho_a = 0.3818$ Å).

As can be seen from Figure 4-6, the variation in atom density has a significant influence on the adsorption isotherms of N_2, especially at low pressures. For the model pore with perfect graphite walls the isotherm has two stages corresponding to monolayer formation at low pressures and condensation, or pore filling, at high pressures. With decreasing pore wall density there is a shift of the isotherm to higher pressures and a transition in the shape of the isotherm, so that, for model pores with the lowest pore wall atom density studied, a single step isotherm is found. The variation of the characteristics of the isotherms as a function of pore wall atom density is shown in Figure 4-7. As Figure 4-7 shows, all the pressures, namely p_m, p_{mc} and p_c decrease with

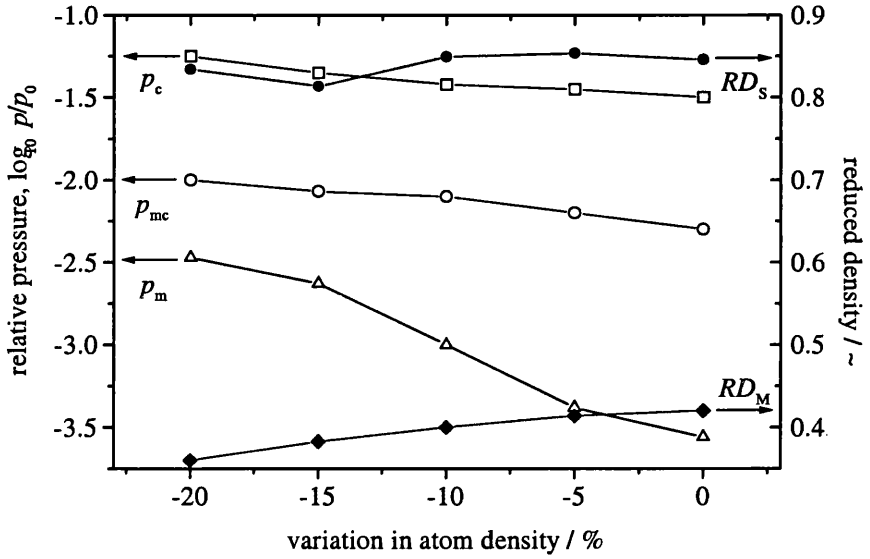

Figure 4-7. Effects of carbon atom density in pore wall, ρ_a, on the adsorption isotherm parameters, p_m, p_{mc}, p_c, RD_M and RD_S.

increasing atom density. This is reasonable, for larger atom density in the pore wall means a larger number of atoms that attract the N_2 molecules, thus a deeper nitrogen-wall potential well. However, the variations in p_c and p_{mc} are not very marked, comparing with p_m. For the whole range of atom density variation, p_m changes by more than one order, while p_{mc} and p_c change by around $10^{0.25}$, that is roughly two times.

In contrast to the pressures, the monolayer density of adsorbed nitrogen, RD_M, increases slightly with increasing atom density in the wall. This is due to the stronger fluid-wall interaction between N_2 molecules and pore walls with higher atom density. No significant and systematic variations of saturation density, RD_S, were found (Figure 4-7). Therefore, the atom density in the pore wall has some effects on the monolayer density, but little on saturation density.

From Equation (3-6), it is clear that the only effect of decreasing atom density in the pore wall is decreasing the depth of the nitrogen-wall potential well. According to the above discussion, this will have more marked effect on monolayer formation than on the condensation process.

4.2.3 Effects of graphite interlayer spacing

Figure 4-8 shows the adsorption isotherms of N_2 for a 16 Å carbon slit in which the graphite interlayer spacing, Δ, is varied over the range 3.354 to 4.025 Å. The isotherms

are shifted to higher pressures as the interlayer spacing is increased, and the shifts are similar to those found by Suzuki *et al.* [1996]. However, they are much smaller than those found when ρ_a and n are varied. Figure 4-9 shows the characteristics of these isotherms as a function of interlayer spacing. Although

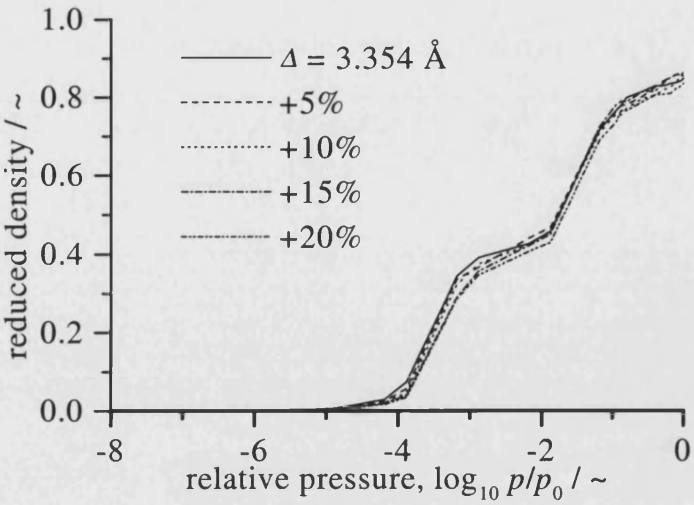

Figure 4-8. Adsorption isotherms of nitrogen at 77 K adsorbed in carbon slits of width 16 Å with different interlayer spacing between graphite sheets in pore wall.

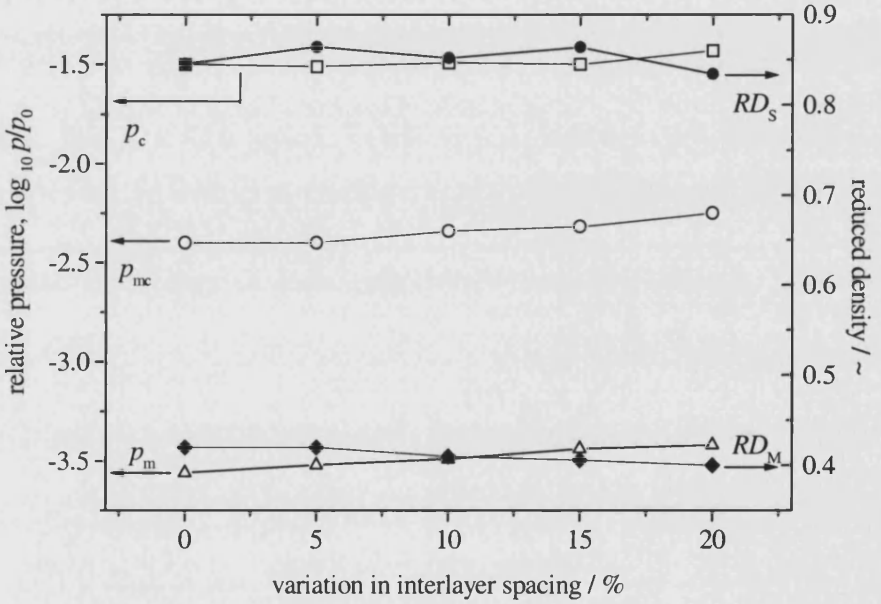

Figure 4-9. Effects of interlayer spacing in pore wall, Δ, on the adsorption isotherm parameters, p_m, p_{mc}, p_c, RD_M and RD_S.

there are increases in the pressures, the increases are very small. Little changes of both saturation density and monolayer density have been found. Figures 4-8 and 4-9 provide sound evidence that graphite interlayer spacing has little influence on the adsorption isotherms.

These conclusions can be understood by considering the effect of varying the interlayer spacing on the potential minimum. For example, for a pore of width H = 16 Å and with n = 5, potential minimum decreases by only 2% when interlayer spacing is increased by

20% from the value for perfect graphite. This is because that the first carbon layer makes the predominant contribution to adsorption potential. Subsequent carbon layers in pore walls only make very little contributions to the potential.

4.3 Effects of interacting slits

In common molecular simulations of adsorption in activated carbons, the model is isolated carbon slits, *i.e.* neighbouring pore walls and fluid molecules adsorbed in neighbouring pores make no contribution to the adsorption potential in the slit in the simulation cell. For effectively infinitely thick pores, this is reasonable. However, in reality, pores in activated carbons are next to each other and pore walls are not infinitely thick. The interaction between the adsorbed molecules and the neighbouring pores enhances the adsorption potential, especially when the pore walls contain very few carbon layers. The effects of the interaction were studied by the following method. First, the pores are treated as arrays of carbon slits rather than isolated slits. Normally, five slits were taken into consideration, *i.e.* not only the two pore walls but also their two nearest images were included when calculating the fluid-solid interaction. Secondly, the molecules in the pore were imaged to the neighbouring pores and the interaction between the molecules and their images was included in the calculation of the fluid-fluid interaction. Here the results on nitrogen adsorption in carbon slits at 77 K are discussed.

Figures 4-10 to 4-12 show nitrogen adsorption isotherms of a number of carbon slits with three different pore widths, 8, 15 and 20 Å and three different pore wall thickness, n = 1, 2 and 5. It is clear that the influence of the interaction is marked for the smallest pores studied when n = 1. As expected, the isotherm is shifted to lower pressures when the interaction is taken into account (Figure 4-10). Also, the monolayer capacity seems to increase slightly. When n = 2, the effect is less

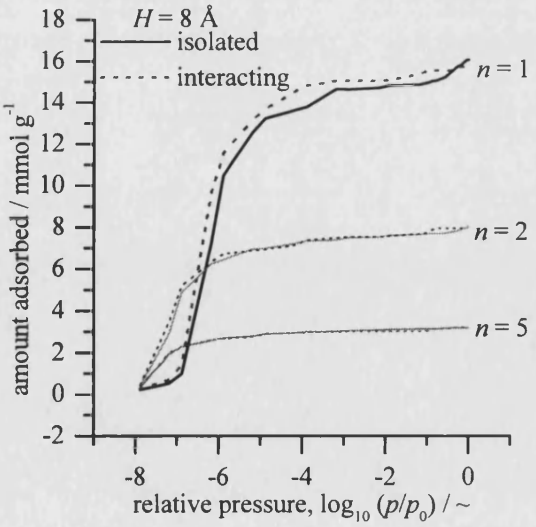

Figure 4-10. Comparison of nitrogen adsorption at 77 K in carbon slits with and without the interaction between neighbouring slits and fluid molecules for different pore wall thickness. The pore width is 8 Å.

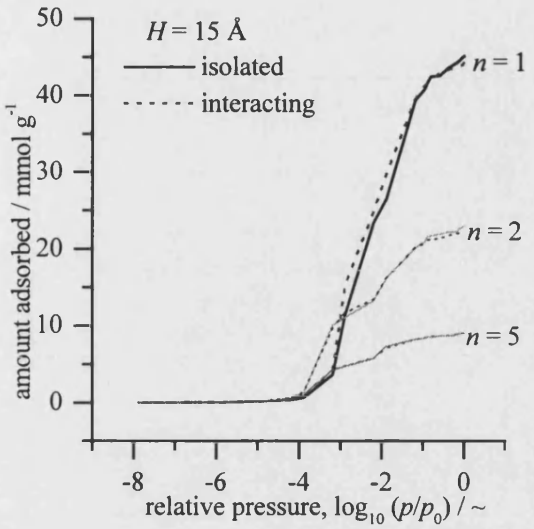

Figure 4-11. Comparison of nitrogen adsorption in carbon slits at 77 K with and without the interaction between neighbouring slits and fluid molecules for different pore wall thickness. The pore width is 15 Å.

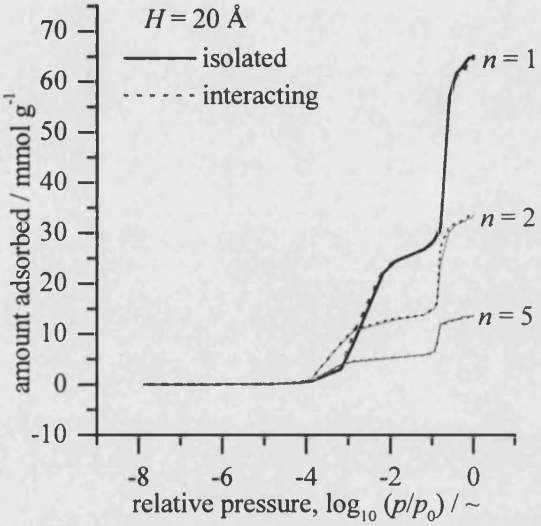

Figure 4-12. Comparison of nitrogen adsorption in carbon slits at 77 K with and without the interaction between neighbouring slits and fluid molecules for different pore wall thickness. The pore width is 20 Å.

marked and when n = 5, there is no appreciable difference between the isotherms of isolated and interacting slits. This is because that the thicker the pore wall, the further the neighbouring pore walls and the molecules adsorbed in the neighbouring pores. In addition, the thicker the pore wall, the stronger the potential in the pore due to its own walls, and thus the smaller the proportion of the interaction in the total adsorption potential.

When H = 15 Å, appreciable effects are found only when n = 1. For thicker walled pores, the isotherms are identical within statistical errors and thus the effects of interacting slits are negligible. For the slit with H = 20 Å, the formation of the monolayer in the single-walled slit is shifted to lower pressures, but this shift is very small and other parts of the isotherms are identical. For thicker walled pores, the same results as H = 15 Å are found. Thus, the effects are only important in small and thin-walled carbon slits.

4.4 Effects of Lennard-Jones parameters

In recent molecular simulations of nitrogen adsorption in carbon materials, different values of the Lennard-Jones length and energy parameters have been used. This is reasonable because the LJ parameters can be determined in different ways as mentioned in Chapter 3. Also, different researchers may adopt values from different literature.

the effects of the variations in both LJ parameters upon the adsorption isotherms are briefly presented. More detail of this can be found elsewhere [Yin *et al.*, 1998].

4.4.1 Influence of potential well depth parameter, ε

A typical example of the influence of the potential well depth, ε_{ff}, on the adsorption isotherms of nitrogen adsorbed in carbon slits of width 16 Å at 77 K is shown in Figure 4-13. The values of ε_{ff} are varied in the range ±20% of the reference value of 93.98 $k_B T$. From the application of the Lorentz-Berthelot combination rules these variations produce corresponding variations in ε_{sf}. In the figure, the relative variation in ε_{ff} is labelled near the corresponding isotherm and the significant influence of variations in ε_{ff} on the adsorption isotherms is readily seen. Firstly, as expected from adsorption potential considerations, the pore filling pressures decrease with increasing values of ε_{ff}. These trends are reflected in the near-exponential reduction in the pressure parameters p_m, p_{mc} and p_c with increasing ε_{ff}, as shown in Figure 4-14. All the three pressures

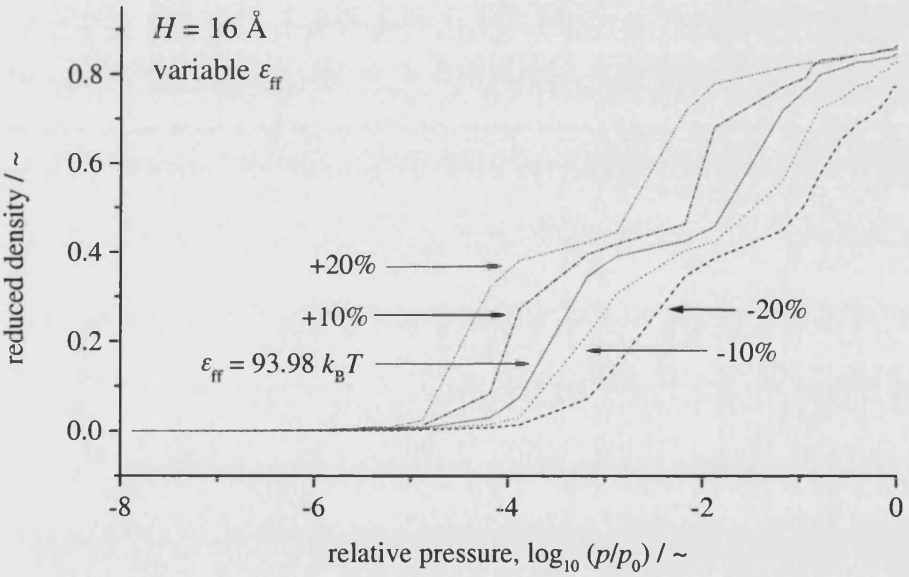

Figure 4-13. Nitrogen adsorption isotherms at 77 K in carbon slits. The LJ energy parameter ε_{ff} varies by ±10% and ±20% about the reference value.

decrease by nearly 2 orders of magnitude. Secondly, the saturation density increases with increasing ε_{ff}, though the increase is only about 10% in the whole range of ε_{ff} studied. Finally, different from saturation densities, the monolayer densities are somewhat independent of ε_{ff}. This suggests that monolayer density is strongly influenced by geometric factors associated with the packing of adsorbate molecules in the monolayer and the variations of ε_{ff} by ±20% about the reference value have little or

no effect. The different effects of changing ε_{ff} on monolayer and saturation densities can be understood by considering the variations in ε_{ff} and ε_{sf}. According to the Lorentz-

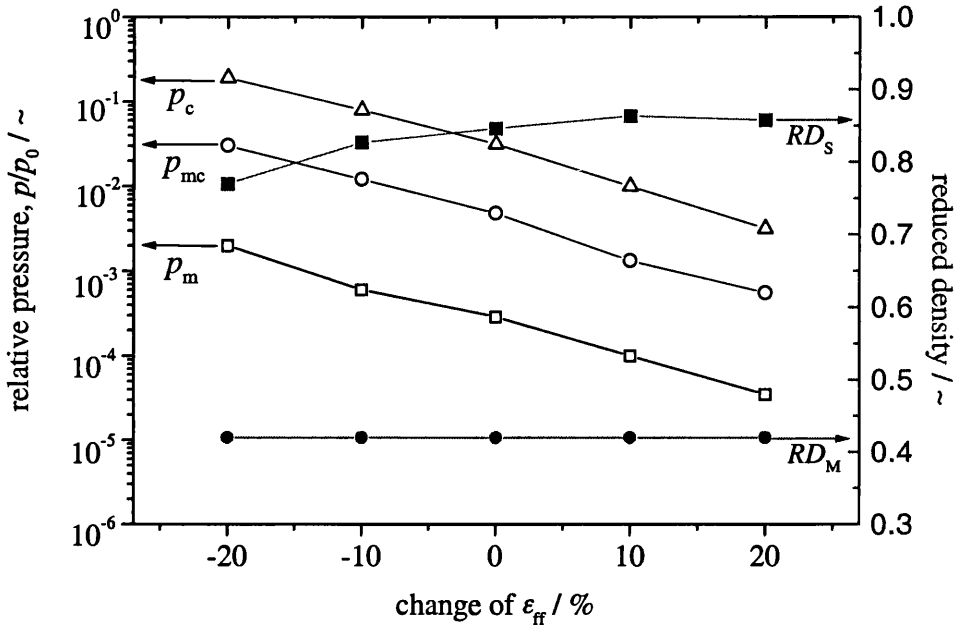

Figure 4-14. Effects of variations in ε_{ff} on the adsorption isotherm parameters, p_m, p_{mc}, p_c, RD_M and RD_S.

Berthelot combination rules, Equation (3-2), a variation of 20% in ε_{ff} only produces 10% variation in ε_{sf} when ε_{ss} is fixed. The monolayer density is mainly determined by ε_{sf}, while saturation density is mainly determined by ε_{ff}. Thus, more marked influence of ε_{ff} is found for saturation density.

A similar study has been conducted on other pore sizes and similar results have been found [Yin *et al.*, 1998].

4.4.2 Influence of molecular size, σ

Figures 4-15 shows isotherms of adsorption of nitrogen at 77 K on pores of width 16 Å, obtained using simulations with varying molecular sizes σ_{ff} by ±20% about the reference value of 3.572 Å. Each isotherm shows a monolayer formation step at low pressures, followed by a condensation step at high pressures. It is clear that one of the effects of increasing molecular size is to displace both the monolayer step and the condensation step to lower pressures, although the displacement is more marked for the monolayer formation step. These trends are clearly seen in Figure 4-16 which show that increasing σ_{ff} from -20% to +20% of the reference value reduces the pressure

parameters p_m, p_{mc} and p_c by two to more than three orders of magnitude. The effects of varying molecular size on the pressure parameters are much more marked than those found when the potential parameter ε_{ff} is varied. This is because the interaction between an adsorbate molecule and the pore wall varies as σ_{ff}^2, but only as $\sqrt{\varepsilon_{ff}}$ (Equation (3-6)) when the Lorentz-Berthelot combination rules are used to calculate ε_{sf}. The molecular size parameter also appears in the summation terms in Equation (3-6).

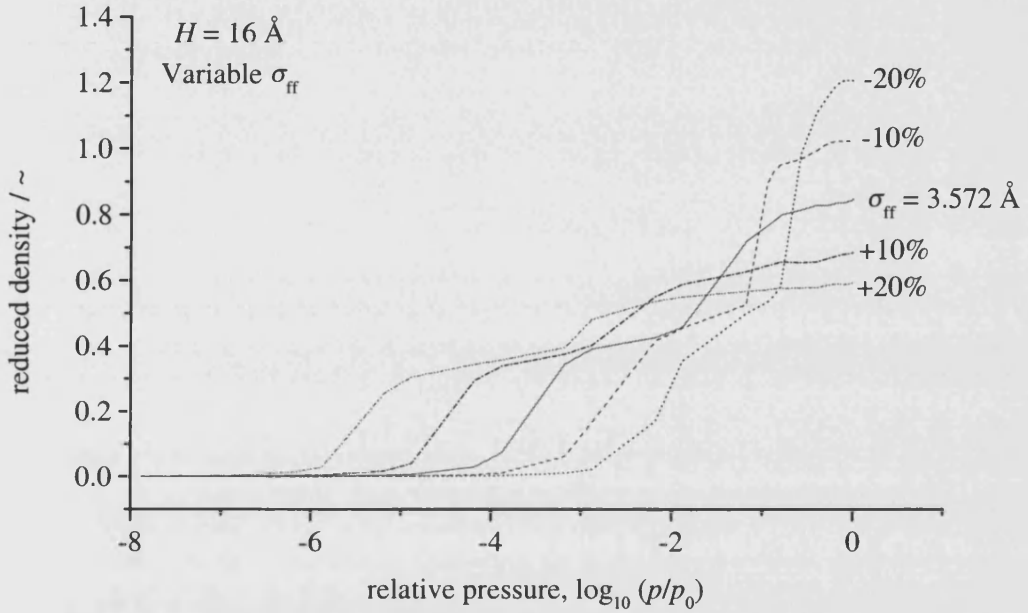

Figure 4-15. Nitrogen adsorption isotherms at 77 K in carbon slits. The LJ molecular size parameter σ_{ff} varies by ±10% and ±20% about the reference value.

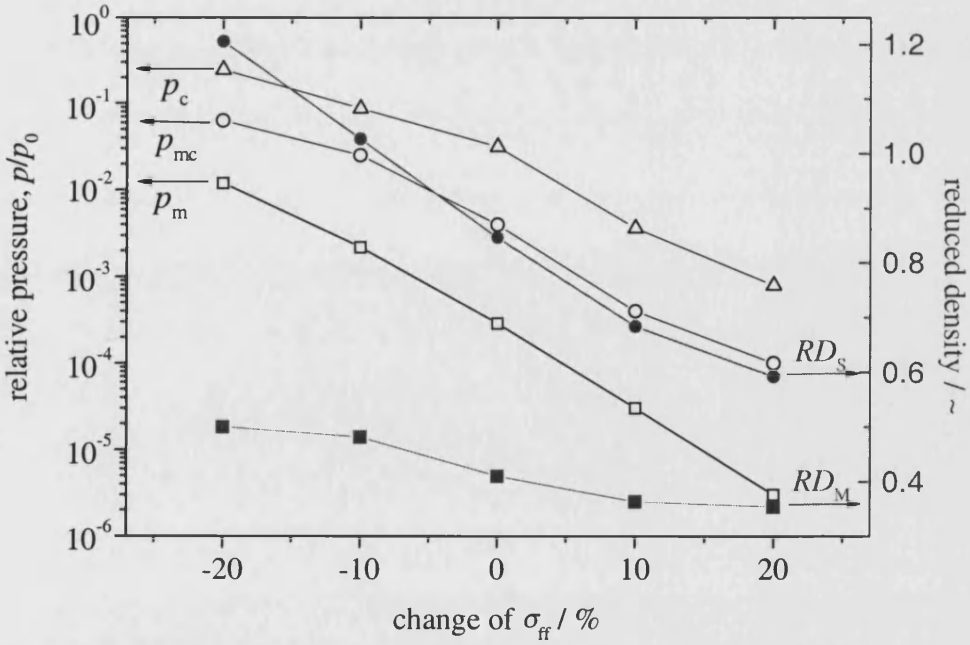

Figure 4-16. Effects of variations in σ_{ff} on the adsorption isotherm parameters, p_m, p_{mc}, p_c, RD_M and RD_S

The effects of varying molecular size on both the monolayer density and the saturation density are marked. The monolayer density decreases by about 30%, while the saturation density reduces by more than 50% when molecular sizes increase from -20% to +20% about the reference value. From pure geometric analysis, it can be shown that the reduced density at saturation of the adsorbed phase is proportional to $\frac{1}{\sigma_{ff}^3}$ when the pore width is fixed and the length and breath of the simulation cell are multiples of σ_{ff}. This is in a very good agreement with the results shown in Figure 4-16. Similar analysis shows that the monolayer density is independent of molecular size, if the molecular packing remains unchanged. Thus the decrease in monolayer density with increasing molecular size in Figure 4-16 suggests that the molecular packing factor changes with changing molecular size.

4.5 Summary and conclusions

Nitrogen adsorption in activated carbons at 77 K is strongly dependent on the sizes of the pores in the material. Activated carbons with small micropores show type I adsorption behaviour, while those with larger micropores and small mesopores show type IV adsorption isotherms with clear monolayer formation and condensation steps. The density of the adsorbed phase at saturation is around liquid nitrogen density.

Pore wall structures have marked effects on the adsorption behaviour of model activated carbons. The thicker the pore wall, the lower the pore filling pressure. However this effect is significant only in thin wall pores and walls with five or more graphene sheets can be effectively regarded as infinitely thick. Defects in pore walls mainly affect the monolayer formation pressure. The lower the carbon atom density in the wall, the higher the monolayer formation pressure. Thus, the atom density also has effects on the shapes of adsorption isotherms. The monolayer plateau will completely disappear when the atom density falling below 80% of the value for perfect graphite. The effects of the interlayer spacing are small and can be neglected in most cases. In thin walled small pores, the interaction between fluid molecules adsorbed in neighbouring slits and the contribution of neighbouring pore walls to the adsorption potential have marked effects on the low pressure part of adsorption isotherms. In large and thick-walled pores, this influence is small and can be neglected. The value of the LJ energy and length

parameters used in the simulation have very marked influence on the simulation results, especially on the pore filling pressures. The pressures can be changed by a few orders of magnitude when varying the energy and length parameter from -20% to +20% about the reference value. Also the monolayer and saturation densities can change markedly. The effects of changing molecular sizes are much more marked than that of changing the energy parameter. Therefore, the selection of LJ parameters for molecular simulations should be made with care and possible errors in these parameters and their effects on the simulation results should be considered.

Chapter 5
Adsorption in Isolated Carbon Nanotubes

For simplicity and as a necessary stage in the development of simulations of adsorption in carbon nanotube arrays, the adsorption of nitrogen in isolated carbon nanotubes is studied initially. The simulations were carried out for endohedral, exohedral and simultaneous endohedral and exohedral adsorption. The results are presented in this chapter.

5.1 Endohedral adsorption in isolated carbon nanotubes

From the practical point of view, it is meaningless to study only endohedral adsorption in isolated carbon nanotubes as there will always be adsorption on the outside of tubes. However, as most simulations of adsorption in activated carbons consider fluids inside isolated slits, it is useful for comparison to simulate only endohedral adsorption in nanotubes.

5.1.1 General features of endohedral adsorption in carbon tubes

A series of simulated endohedral isotherms of nitrogen at 77 K adsorbed in isolated SWCNTs with varying tube diameters are shown in Figure 5-1. The amount adsorbed is expressed in reduced units, *i. e.* the ratio of the simulated nitrogen density in the simulation cell to the density of bulk liquid nitrogen at 77 K (28.87 mmol cm^{-3}). The calculated reduced density is corrected using the following equation (section 4.1):

$$\rho' = \rho \frac{D^2}{(D - \sigma_{cc})^2} \tag{5-1}$$

where D is the inner diameter of the tube, ρ is the reduced density directly calculated from the volume of the simulation cell and ρ' the corrected reduced density. The advantage of expressing the amount adsorbed in this way is to facilitate direct comparison between the adsorbed phase and the liquid phase.

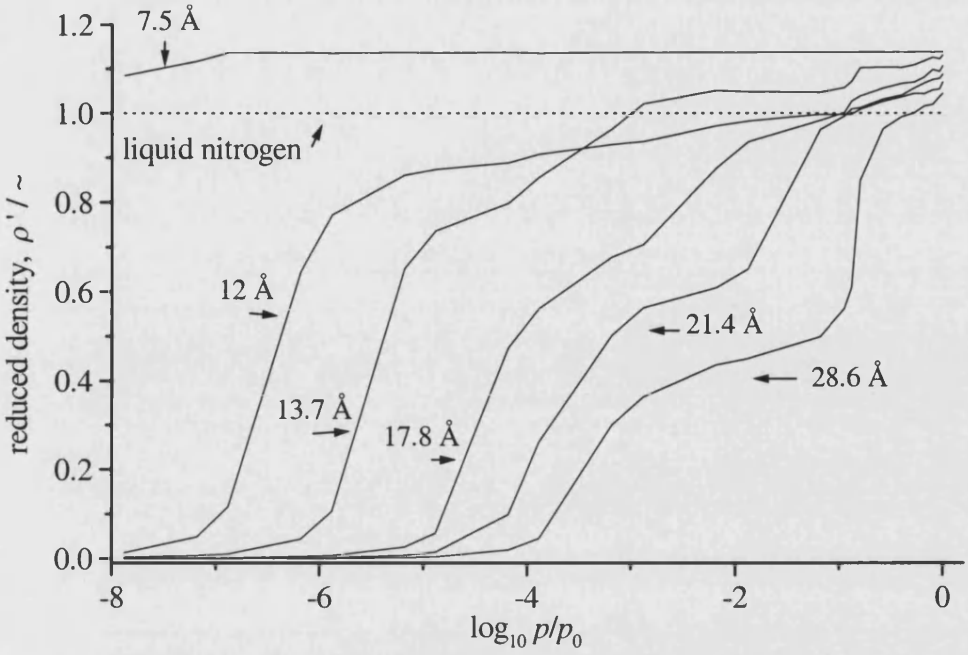

Figure 5-1. Simulated isotherms for nitrogen adsorbed at 77 K endohedrally in isolated single wall carbon nanotubes with different tube diameters as labelled in the graph.

For very small tubes, which can accommodate only a single column of fluid molecules, the tubes are filled at very low pressures and the isotherms show only one step. For larger tubes, the simulation yields type IV isotherms which have two stages, the first corresponds to the formation of the monolayer and the next to condensation and pore filling. The larger the tube diameter, the clearer the condensation process. All the densities for different tube diameters at saturation are larger than that of liquid nitrogen, showing that carbon tubes might be a good adsorbent. This is in a good agreement with potential studies (section 3.3.2) which show that strong potential enhancement inside carbon tubes. The maximum density enhancement over liquid nitrogen is about 15% which is in the smallest tube where a single column of nitrogen molecules is adsorbed in the centre of the tube.

As shown in Figure 5-1, isotherms of smaller tubes shift to lower relative pressures, an indication of stronger potential enhancement. The shift to lower pressure is about three orders of magnitude from the largest to the smallest tubes studied. In addition, both saturation and monolayer densities decrease with increasing tube diameters. This is because the larger the diameter, the weaker the enhancement of adsorption potentials as discussed in Chapter 3.

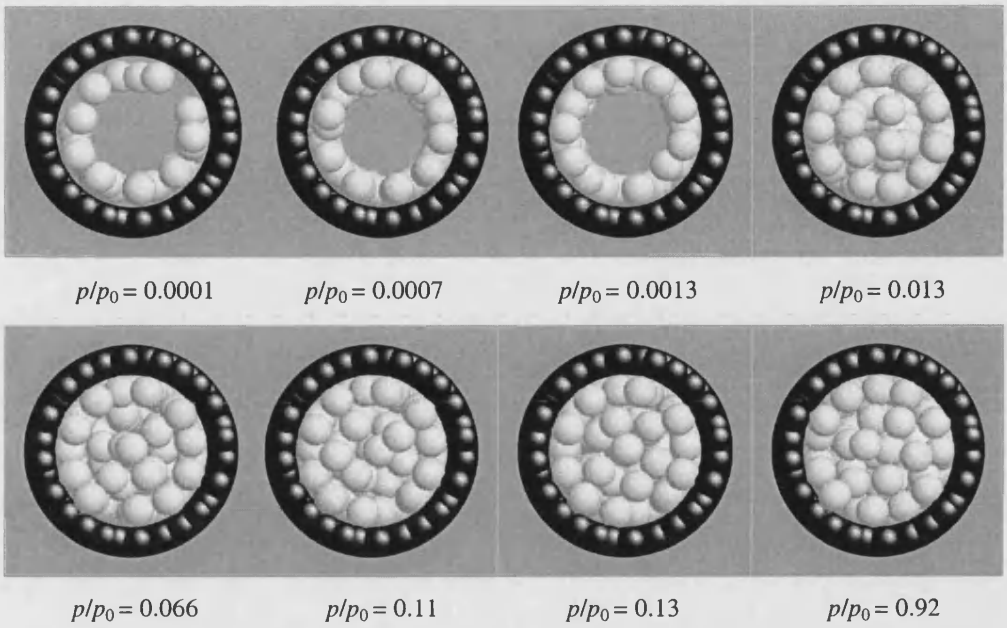

Figure 5-2. Snapshots of nitrogen adsorbed at 77 K endohedrally in a single wall carbon nanotube with inner diameter 20 Å at different relative pressures. The black spheres are carbon atoms and the white ones are nitrogen molecules adsorbed.

The adsorption process may be made clearer by viewing the snapshots at different relative pressures as shown in Figure 5-2 for a tube with 20Å diameter. The black spheres represent the carbon atoms forming the nanotube, while the white ones represent the nitrogen molecules adsorbed. At very low pressures (p/p_0 <0.0007), the adsorption involves the formation of a monolayer. This monolayer is completed at also very low pressures (p/p_0 ~ 0.001). Then, cooperative effects take place and the pore is essentially filled with adsorbate molecules at relative pressures less than 0.1.

5.1.2 Effects of tube wall thickness on endohedral adsorption.

Tube wall structures have effects on endohedral adsorption. The effects of the number of carbon layers in tube wall, that is wall thickness, on endohedral adsorption isotherms are shown in Figures 5-3 and 5-4 for two different inner tube diameters, 12 and 25 Å respectively. As can be seen from these figures, the effects of tube wall thickness are significant, especially for thin wall tubes. Generally, the isotherms shift to lower pressures when increasing tube wall thickness, an indication of stronger interaction potential. However, in accordance with potential studies, this is only considerable when n is small. When n exceeds five, the isotherms are nearly identical in shape, indicating that walls with more than five carbon layers can be effectively regarded as infinitely thick. Both monolayer and saturation densities do not change significantly. The effects

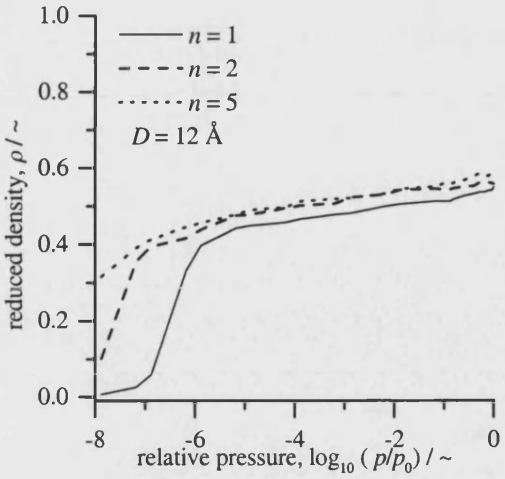

Figure 5-3. Simulated isotherms of nitrogen adsorbed endohedrally in a 12 Å inner diameter single-walled carbon nanotube at 77 K with different wall thickness, *n*.

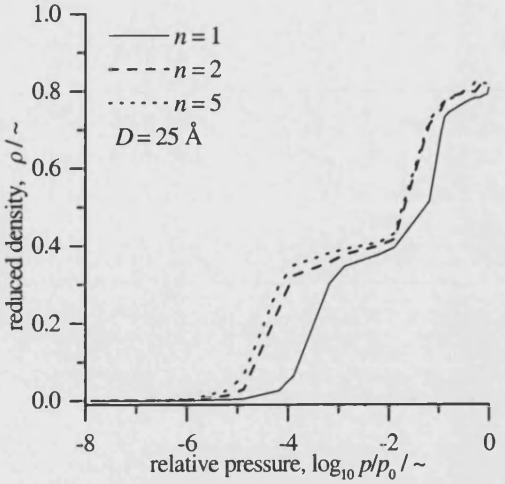

Figure 5-4. Simulated isotherms of nitrogen adsorbed endohedrally in a 25 Å inner diameter single-walled carbon nanotube at 77 K with different wall thickness, *n*.

of wall thickness on adsorption in nanotubes are similar to that in carbon slits [Yin *et al.*, 1998].

5.1.3 Comparison between endohedral adsorption and adsorption in carbon slits.

Comparison of Figures 5-1 and 4-2 shows that the isotherms for adsorption in carbon slits and carbon tubes have common features. Firstly, small micropores are filled with adsorbate at very low pressures and larger micropores yield type IV isotherms showing both monolayer completion and saturation. Secondly, the adsorption properties are strongly dependent on the pore size, namely pore width or diameter. Finally, in both cases, the effects of pore wall thickness are important only when the number of carbon layers in the wall is less than five. When *n* exceeds five, the pore wall can be effectively regarded as infinitely thick.

However, there are also some differences between the adsorption in tubes and slits. (1) In the case of carbon slits, the density of adsorbed nitrogen at saturation are around the value of liquid nitrogen. On the other hand, the density of adsorbed nitrogen at saturation in carbon tubes is higher than that of liquid nitrogen. Therefore, adsorption in carbon tubes is more enhanced than in carbon slits. This may be due to the stronger fluid-pore interactions in carbon nanotubes. From this point of view, carbon nanotubes could be better adsorbents than activated carbons. (2) Except for very small pores, all

the isotherms of carbon slits start their first steep increase in the amount adsorbed at nearly the same pressure ($\sim p/p_0 \approx 10^{-4}$). However, in the case of carbon tubes, the isotherms start at considerably different pressures. This can be explained by considering the interaction potentials as a function of pore width. In the case of carbon slits, there is little difference between the potential minimum of a slit and a single graphite sheet when pore width is larger than 12 Å, that is the enhancement of adsorption potentials can be neglected. For carbon tubes, there is still significant enhancement in adsorption potentials even in tubes of inner diameters exceeding 30 Å (Figure 3-10). (3) The monolayer formation and condensation pressures in tubes are much lower than in slits with the same sizes due to higher interaction potential in tubes.

5.1 Exohedral adsorption in isolated carbon nanotubes

Closed carbon nanotubes, which are the products of most nanotube manufacturing processes, can be regarded as cylindrical pores with only their external surfaces accessible to adsorptive. In such nanotubes, adsorption is only exohedral.

Figure 5-5 shows a series of simulated isotherms for nitrogen at 77 K adsorbed onto the outer surface of single walled carbon tubes with different inner diameters. The amount adsorbed here is expressed in numbers of nitrogen molecules per unit surface area.

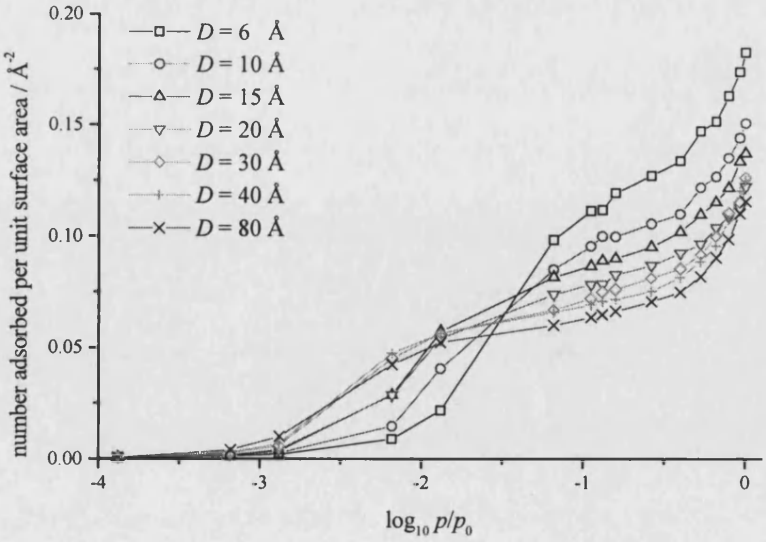

Figure 5-5. Simulated isotherms of nitrogen adsorbed at 77 K on the outside of isolated single-walled carbon nanotubes with different inner diameters, *D*.

Clearly, the isotherms shift to lower pressures as tube diameter increase, a clear demonstration of stronger fluid-wall interaction for larger tubes. The amount adsorbed per unit surface area decreases with increasing tube diameter, as a result of the decreasing curvature of the tube surface. The isotherms show clear stages corresponding to monolayer completion. Then there are sharp increases in the adsorbed amount due to multilayer adsorption. The monolayer coverage is similar for all tubes irrespective of diameter, except the very small tubes.

The effects of tube wall thickness on the isotherms are shown in Figure 5-6 for a 40 Å tube. It is clear that the effects of wall thickness here are similar to those discussed previously. Note the inner diameter is fixed, but the outer diameter increases with increasing wall thickness. Therefore the effects of increasing wall thickness are two fold. One is the contribution to the fluid-wall interaction by the extra carbon layers and the other is the increase of tube outer diameter. The latter not only increases the fluid-wall interaction, but also increases the surface area accessible to fluid molecules. Thus, the second effect itself has two opposite influence on the amount adsorbed. One is the increase of amount adsorbed due to the increase of interaction energies and accessible surface areas. The other is the decrease in the amount adsorbed per unit surface area due to the increase of the value of surface area. At higher pressures, the last effect can play an even more important role than the increase of the number of molecules adsorbed due to the enhancement of interaction and increase of surface area. Therefore, the total amount adsorbed per unit surface area remains nearly the same, as shown in Figure 5-6. At lower pressures, the isotherms for thick tube walls shit to the left, indicating stronger adsorbent-adsorbate interaction.

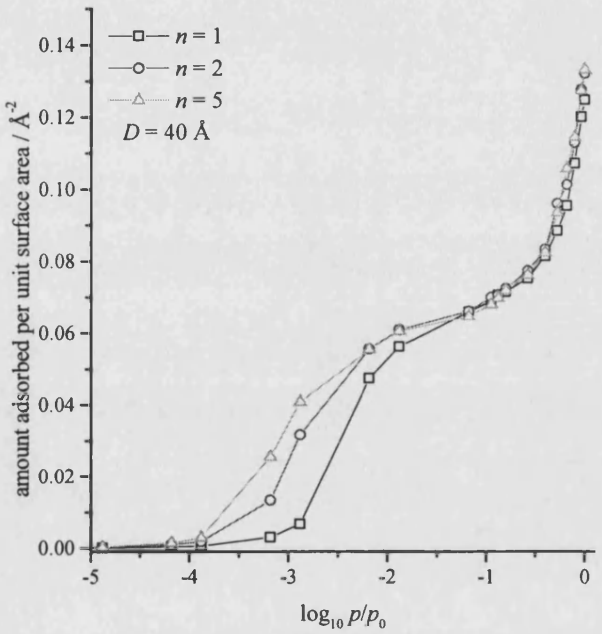

Figure 5-6. Effects of tube wall thickness on the adsorption of nitrogen at 77 K on the outside of carbon nanotubes with the same inner diameter.

5.3 Simultaneous endohedral and exohedral adsorption of isolated carbon nanotubes

5.3.1 General features of adsorption isotherms

If the nanotubes are open, then both endohedral and exohedral adsorption can take place at the same time. In this case, the fluid molecules adsorbed inside and outside the tubes interact with each other and may result in enhancement in the amount adsorbed.

The adsorption isotherms of nitrogen at 77 K adsorbed in isolated open single-walled nanotubes are shown in Figure 5-7 for five different tube diameters. The main features of these isotherms are similar and all of them mainly consist of two steps and a sharp increase in the amount adsorbed when relative pressures approach unity. The first step has a very low capacity, while that of the second is considerably higher. The pressure difference between the two stages is large for small tubes. This difference decreases with increasing tube diameter and merges to one stage for tubes with D = 60 Å. This suggests that the two stages correspond to the monolayer formation inside and outside the tubes. For small tubes, the difference between endohedral and exohedral adsorption potential is large, resulting in a large difference in pressures for monolayer formation inside and outside. When tube diameter increases the difference in potential decreases and so does the difference in the pressures of monolayer formation.

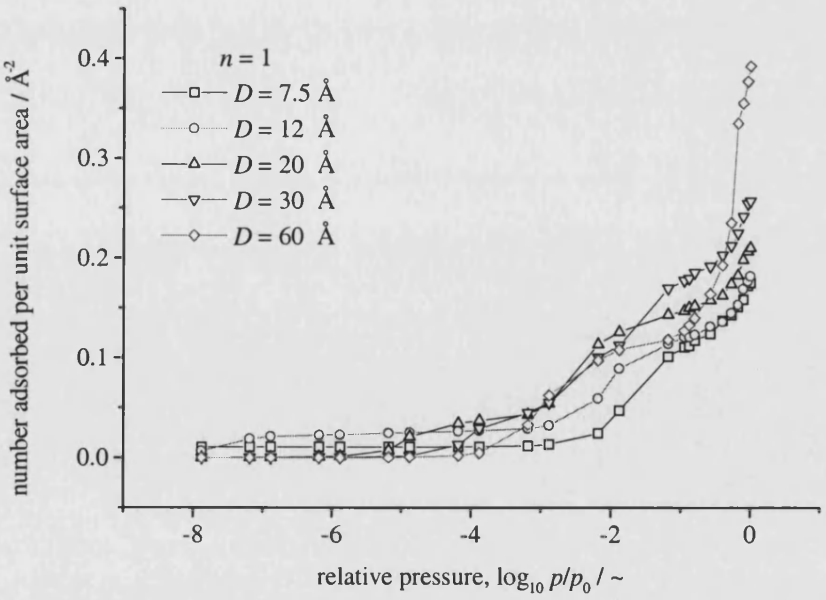

Figure 5-7. Simulated isotherms of nitrogen at 77 K adsorbed in isolated open single-walled carbon nanotubes with different tube diameter, D. Both endohedral and exohedral adsorption can take place.

To verify the above argument, the isotherm of a tube with 20 Å diameter is divided into endohedral and exohedral isotherms, as shown in Figure 5-8. It is clear that the first step in the total isotherm corresponds to the monolayer completion of endohedral adsorption. At such low pressures, there is nearly nothing adsorbed outside the tubes. Therefore, the overall adsorbed amount is very low. Only when relative pressures are higher than 10^{-4} ~ 10^{-3} does exohedral adsorption make appreciable contribution to the total amount adsorbed. The second step corresponds to the saturation of endohedral adsorption and monolayer completion of exohedral adsorption. Thus, the second step has much higher capacity than the first, about three times in Figure 5-8. Also, exohedral adsorption makes greater contribution to the total amount at the second step than endohedral adsorption. The sharp increase of the amount adsorbed at higher pressures is predominantly due to the contribution of exohedral adsorption.

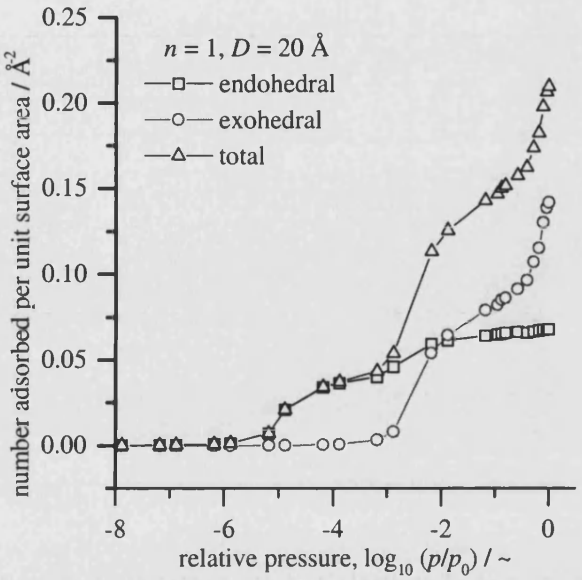

Figure 5-8. Example of the exohedral, endohedral and total adsorption isotherms of nitrogen adsorbed at 77 K in isolated open single-walled carbon nanotubes with 20 Å diameter.

One interesting point from Figure 5-8 is that at lower pressures ($p/p_0 < 10^{-3}$), the amounts adsorbed outside tubes are much lower than those adsorbed inside tubes, while at high pressures (p/p_0 ~ 1), the amounts adsorbed outside tubes are much higher than those adsorbed inside tubes. This suggests that exohedral adsorption might be more important than endohedral adsorption in applications such as gas storage, where fluid is adsorbed at a higher pressure and then is released at a lower pressure. In such cases, bringing exohedral adsorption into play may markedly improve the delivered capacities of carbon nanotubes.

The adsorption process in isolated open nanotubes discussed above is visualised as snapshots in Figure 5-9. The black spheres are carbon atoms forming the tubes and the

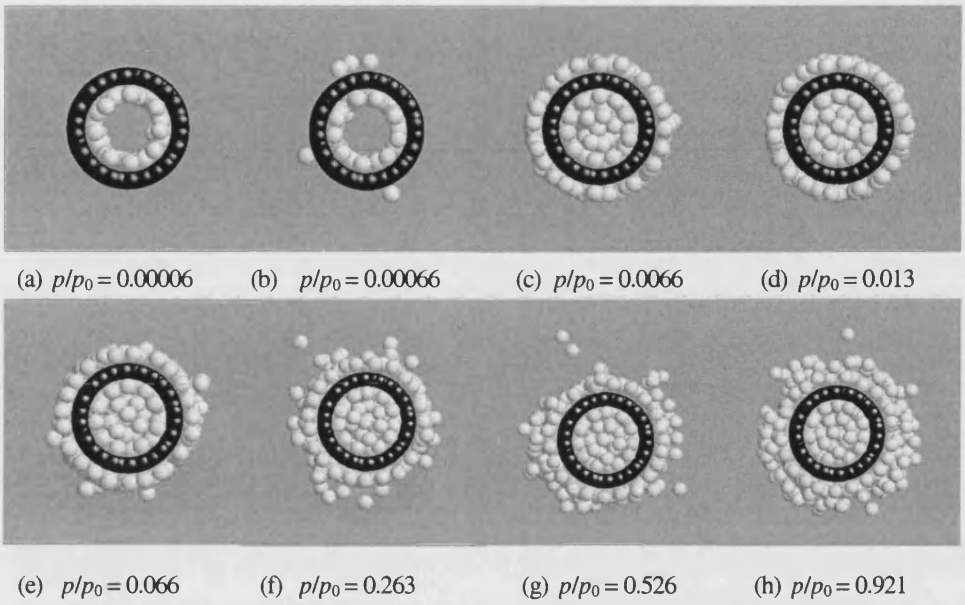

Figure 5-9. Snapshots of nitrogen adsorbed at 77 K in isolated open single-walled carbon nanotubes with diameter of 20 Å at different relative pressures. The black spheres are carbon atoms and the white ones are nitrogen molecules adsorbed.

white ones are the nitrogen molecules adsorbed. At very low relative pressures, such as shown in (a), adsorption only takes place inside tubes because the endohedral potential is stronger than the exohedral potential. After the endohedral monolayer is nearly completely formed, the formation of the exohedral monolayer is the main adsorption mechanism (Figure 5-9b). This is followed by completion of the exohedral monolayer and saturation inside the tube ((c)-(e) in Figure 5-9). The sharp increase in the amount adsorbed at high relative pressures are due to exohedral adsorption outside the monolayer, as shown in (f)-(h) in Figure 5-9. It can also be seen from the snapshots that only the monolayer is well defined for exohedral adsorption. Subsequent layering is not clear due to the weaker interactions involved.

5.3.2 Effects of the interaction of adsorbed fluid molecules inside and outside tubes

In open tubes, the exohedrally and endohedrally adsorbed molecules interact with each other, especially those in the monolayers where the distance between molecules inside and outside is smaller and the packing density of molecules is higher. The interaction enhances the adsorption potential both inside and outside the tubes in a way similar to increasing the thickness of tube walls, but not so strong as the packing density of the adsorbed molecules is much lower than that of the solid atoms. Thus both endohedral and exohedral adsorption are expected to be enhanced.

Figure 5-10 shows endohedral adsorption isotherms of single wall carbon nanotubes with three different tube diameters. The solid lines are isotherms for isolated tubes without consideration of the interaction, *i. e.* the outside of the tube is considered as empty. The dotted lines are endohedral isotherms of isolated tubes with consideration of the interaction, *i. e.* exohedral adsorption takes place at the same time and the exohedrally-adsorbed molecules interact with the molecules inside the tubes. It is clear that the effects of the interaction are marked at all tube diameters. All the dotted isotherms shift to lower relative pressures appreciably, indicating higher adsorption potentials. However, both the monolayer coverage and the saturation capacities do not change significantly, though there is some increase in the amount adsorbed.

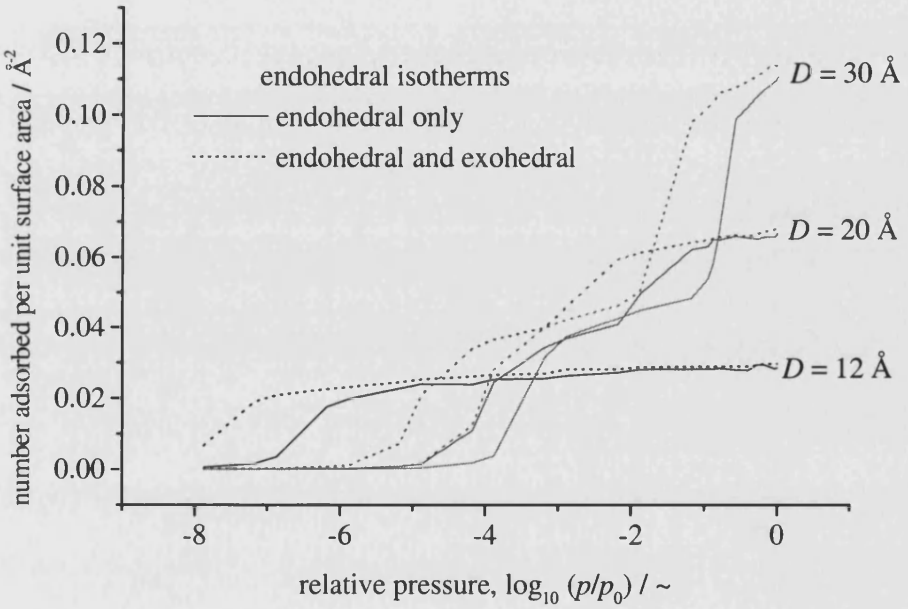

Figure 5-10. Simulated endohedral isotherms of nitrogen adsorbed at 77 K in isolated single-walled carbon nanotubes showing the effects of the interaction between the adsorbed molecules inside and outside the tubes for three different tube diameters, *D*.

The effects of the interaction between the adsorbed molecules inside and outside the tubes upon exohedral adsorption are shown in Figure 5-11 for a 20 Å tube as an example. The solid line is the exohedral isotherm with no interaction, *i. e.* adsorbed on the outer surface of a closed tube. The dotted line is the exohedral isotherm with the interactions taken into account, *i. e.* adsorbed on the outer surface of an open tube. Once again, the isotherm shifts to lower pressures. Here the monolayer coverage and the amount adsorbed at relative pressures close to unity increase. However, these changes are functions of tube diameter and sometimes the change is insignificant. Note that the

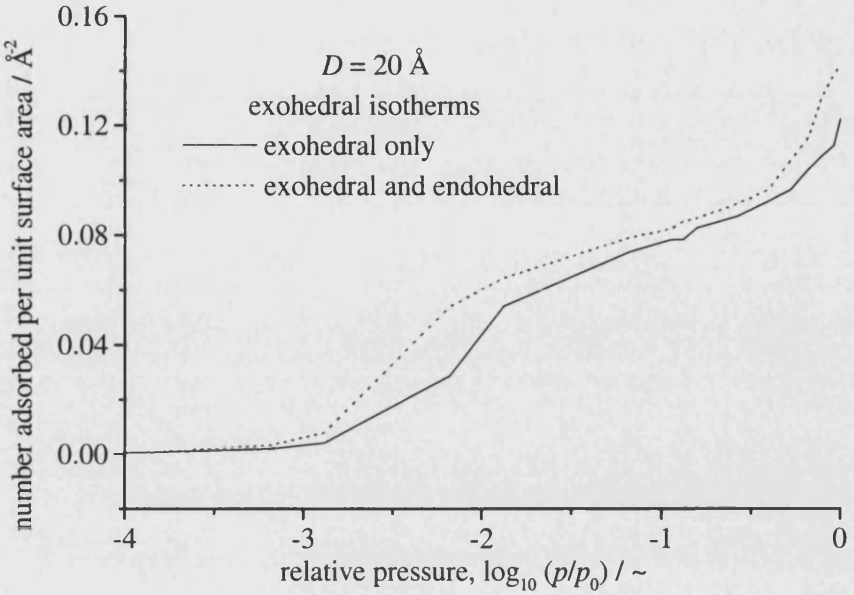

Figure 5-11. Simulated exohedral isotherms of nitrogen adsorbed at 77 K in isolated single-walled carbon nanotubes showing the effects of the interaction between the adsorbed molecules inside and outside the tubes with 20 Å diameter.

pressure scale in Figure 5-11 is different from that in Figure 5-10. The effects on exohedral adsorption are not so significant as in the case of endohedral isotherms.

5.3.3 Effects of wall thickness

The effects of tube wall thickness on the total isotherms are shown in Figure 5-12, for tubes with inner diameter of 20 Å and 1, 2 and 5 shells in the wall respectively. The amount adsorbed here is also expressed as number of molecules per unit surface area, but the surface area is taken as the mean of the inner and outer surfaces of the tubes. As for the results discussed before, isotherms shift to lower pressures for thicker wall tubes, an indication of stronger adsorption potential. The effects of wall thickness on the endohedral monolayer capacity are very limited, as shown in Figure 5-12 by the nearly identical first steps. The capacities at the second step and at relative pressures close to unity increase markedly with increasing wall thickness. Here increasing tube wall thickness has dual effects, one is increasing the number of layers of carbon atoms to contribute to the adsorption potential, and the other is increasing the outer diameter of the tube. Both effects will increase the exohedral adsorption potential. It is believed that this is why the capacities increase with increasing wall thickness and even for thicker wall tubes wall thickness may still have appreciable effects.

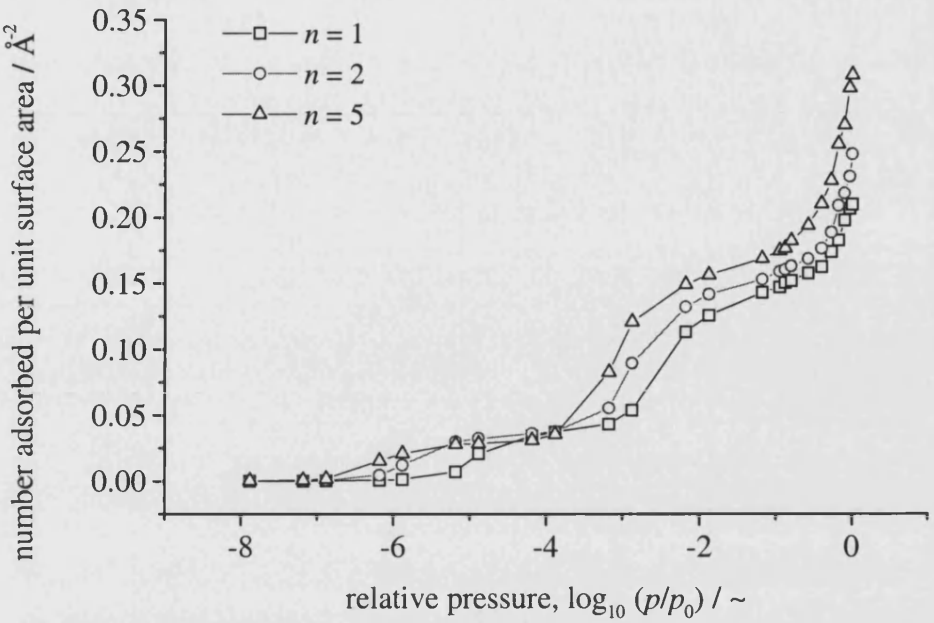

Figure 5-12. Simulated total isotherms of nitrogen adsorbed at 77 K in isolated open carbon nanotubes with different tube wall thickness, *n* and inner tube diameter of 20 Å.

5.4 Summary and conclusions

The observations made in this chapter can be summarised as follows:

(1) The insides of small nanotubes are filled with nitrogen molecules at 77 K at very low pressures. Isotherms of nitrogen adsorbed in nanotubes with diameters close to the upper limit of micropores are of Type IV shape.

(2) The endohedrally adsorbed nitrogen density is higher than that of bulk liquid nitrogen and is also higher than the nitrogen density adsorbed in carbon slits due to the stronger enhancement of adsorption potential.

(3) Tube wall thickness has significant effects on the adsorption of thin wall tubes. When the number of graphene sheets in the walls exceeds five, the wall can be effectively regarded as infinitely thick

(4) The exohedrally adsorbed amount increases with increasing tube diameters and wall thickness has similar effects on the exohedral adsorption as on endohedral.

(5) In open tubes, the molecules adsorbed inside and outside the tubes interact with each other and thus both endohedral and exohedral adsorption are enhanced. The effects of wall thickness are similar to endohedral adsorption.

Chapter 6
Nitrogen Adsorption in Trigonal SWCNT Arrays

Chapter 5 has dealt with isolated carbon nanotubes to give an initial picture of adsorption in these new materials. However, as carbon nanotubes are often found in bundles [Dillon *et al.*, 1997], it is difficult to directly compare results for isolated tubes with experimental observations or to predict adsorption behaviour in model carbon nanotube arrays. Hence, nitrogen adsorption at 77 K in arrays of SWCNTs needs to be studied. This chapter presents simulation results for adsorption in trigonal arrays and the next chapter will present results for adsorption in square arrays. As a reminder, trigonal arrays are close packed, when the tubes touch each other, while in square arrays tubes are located at the corners of squares (Figure 3-4).

6.1 Adsorption in trigonal arrays of closed SWCNTs

In closed SWCNT arrays, adsorption only takes place in the interstitial spaces between the tubes. The space available to adsorptive and the adsorption potential are dependent both on tube diameters and the separations or gaps between tubes.

6.1.1 Adsorption isotherms

Figures 6-1 to 6-3 show simulated adsorption isotherms for nitrogen adsorbed at 77 K in trigonal arrays of closed SWCNTs as a function of tube diameters with three different tube separations (4, 15 and 25 Å) respectively. For a separation of 4 Å, that is the tubes are nearly as closely packed as possible, all isotherms of tubes with diameters up to 120 Å are of type I shape with filling at very low relative pressures, indicating microporous behaviour. Simple calculations show that the size of the interstitial spaces in this kind of array with D = 120 Å is about 19 Å, that is within the region of the classical definitions of micropores. Therefore the interaction potentials within the interstitial space are strongly enhanced. The amount adsorbed at saturation varies with tube diameter considerably. At large tube diameters, the saturation amount increases with increasing tube diameter as a result of the increase of the interstitial space available to the adsorptive. However, when tube diameters are smaller than 30 Å, the variation of the saturation amount as a function of tube diameter is not simple. As shown in Figure 6-1,

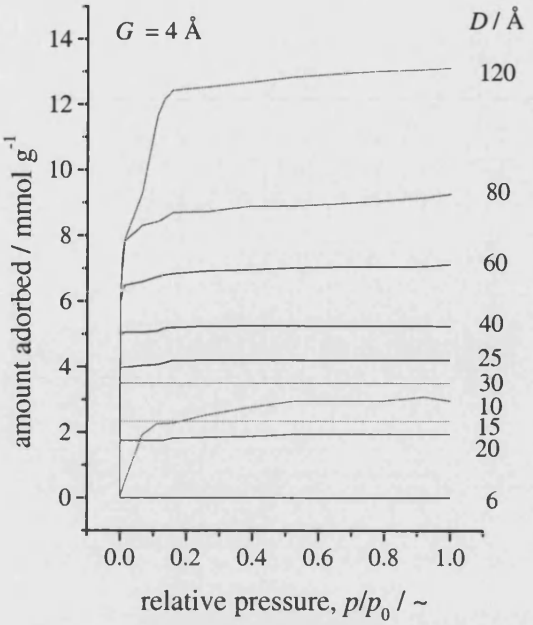

Figure 6-1. Simulated isotherms for nitrogen adsorbed at 77 K in trigonal arrays of closed SWCNTs with different tube diameters, *D*, but with the same tube separation, *G*, of 4 Å.

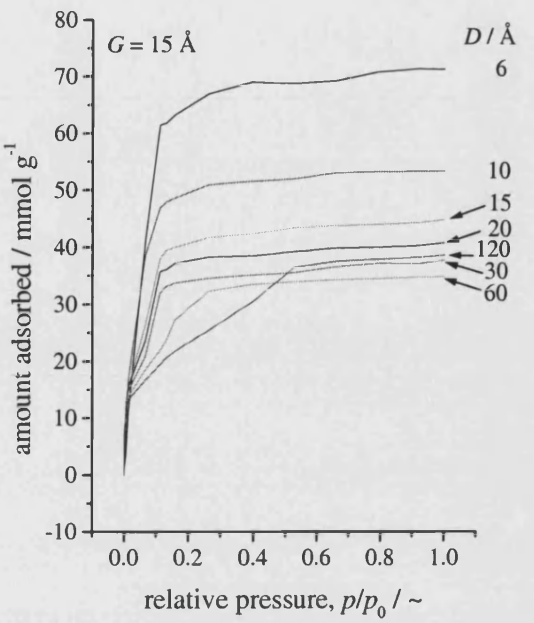

Figure 6-2. Simulated isotherms of nitrogen adsorbed at 77 K in trigonal arrays of closed SWCNTs with different tube diameters, *D*, but with the same tube separation, *G*, of 15 Å.

there are two local maximums in saturation capacity at D =10 Å and D = 25 Å. The reason is that the mass of the carbon nanotubes in the simulation cell increases linearly with increasing tube diameter. On the other hand, the amount adsorbed reaches maximums when the interstitial space can accommodate integer number columns of nitrogen molecules. From Figure 6-4(a), when tube diameter is around 10 Å, the interstitial space is wide enough to hold one column of nitrogen molecules. Thus, when tube diameters are smaller than this, no nitrogen may get into the interstitial space. When tube diameters are larger than 10 Å, but are smaller than 25 Å, essentially there is still one column of nitrogen molecules adsorbed in the interstitial space, as shown in Figure 6-4(b). Thus, when tube diameters are within this range, the specific amount adsorbed decreases with increasing tube diameter due to the

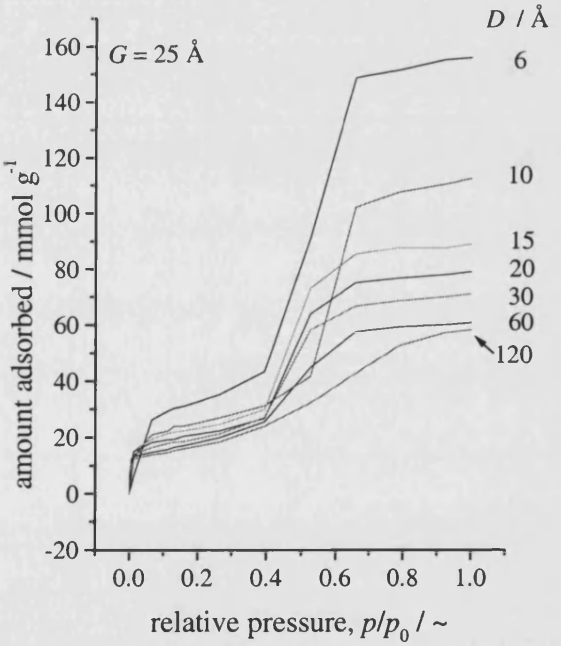

Figure 6-3. Simulated isotherms of nitrogen adsorbed at 77 K in trigonal arrays of closed SWCNTs with different tube diameters, *D*, but with the same tube separation, *G*, of 25 Å.

increase of the mass of the tubes. When tube diameters are around 25 Å, the interstitial space is wide enough to hold three columns of nitrogen molecules, as shown in Figure 6-4(c), and thus the amount adsorbed reaches another local maximum. In principle, this kind of effect exists at all tube diameters. However, at large tube diameters, this effect will be smoothed out due to the large number of molecules adsorbed in the interstitial space.

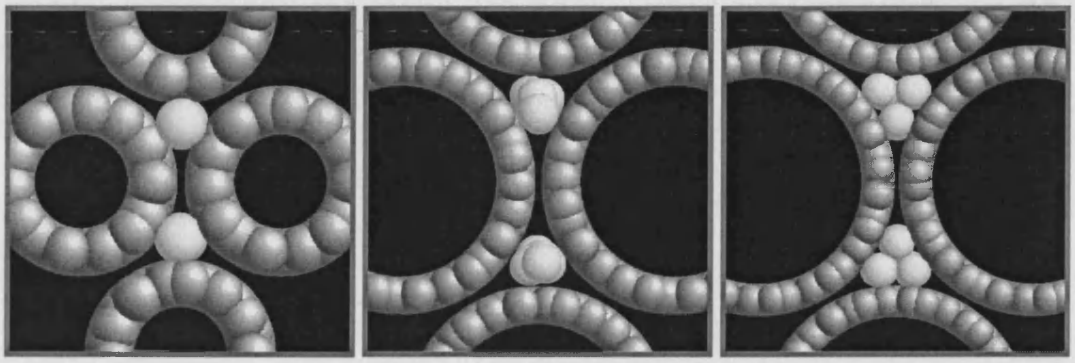

(a) (b) (c)

Figure 6-4. Simulation snapshots of nitrogen adsorbed in trigonal arrays of closed SWCNTs with tube diameters (a) 10 Å, (b) 20 Å and (c) 25 Å and tube separations 4 Å at 77 K and $p/p_0 \sim 1$. The grey spheres are carbon atoms forming the tubes and the white spheres are nitrogen molecules adsorbed.

When tube separations increase to 15 Å, the basic features of adsorption are not changed, *i. e.* the interstitial space is filled at very low pressures and the isotherms are close to type I (see Figure 6-2). However, there are some significant differences. First, the amount adsorbed increased dramatically, especially in arrays of small tubes. For example, the amount adsorbed in the arrays with the 10 Å tubes increases from about 3 mmol g^{-1} to more than 50 mmol g^{-1}, an increase of about 16 times. Even in the largest tube arrays, the amount increases by nearly three times. This indicates that the adsorption properties of SWCNT arrays are very sensitive to tube separation. Also, in contrast to the situations in Figure 6-1, the amount adsorbed at relative pressures close to unity decreases with increasing tube diameter, except for the largest tube diameter. This is because with large tube separations, the increase in the mass of the nanotube in the simulation cell is greater than the increase in the number of molecules adsorbed due to the increase of tube diameter. Finally, in most of the isotherms, *e. g.* the one for the array with D = 60 Å in Figure 6-2, there is a turning point and it is clearer for larger

tube arrays. These turning points are believed corresponding to the monolayer formation.

Increasing tube separations further to 25 Å, all the isotherms are of type IV, *i.e.* with two clear steps, one corresponding to the formation of monolayers and the second corresponding to condensation or saturation (see Figure 6-3). The saturation amount here is roughly doubled compared to that in Figure 6-2, and decreases with increasing tube diameter due to the reasons discussed above. It is also clear that monolayer capacities decrease with increasing tube diameter.

6.1.2 Saturation capacities as functions of array configuration

As discussed above, the saturation capacities vary markedly with tube diameter and separation. These variations are shown in Figure 6-5 in more detail. The amount adsorbed increases progressively with increasing G for different tube diameters. This is because the only effect of increasing tube separation is to increase the volume of the interstitial space. At the smallest separation, the amount adsorbed increases with increasing tube diameter. This is because more interstitial space is available and most of the space can be filled with fluid molecules due to the strong enhancement of adsorption

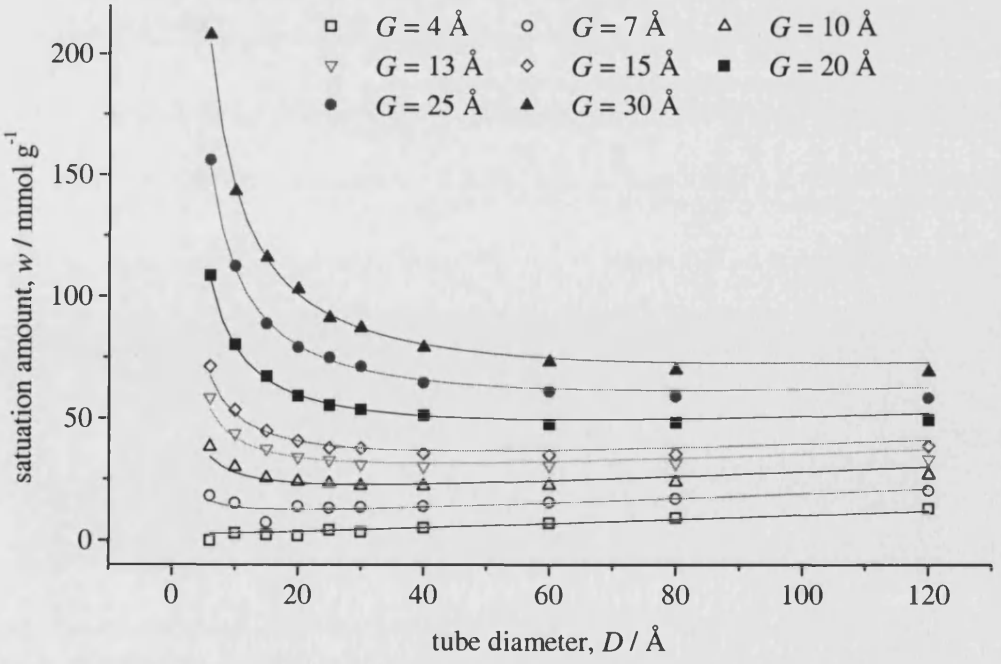

Figure 6-5. Saturation capacities of trigonal arrays of closed SWCNTs as functions of tube diameter, D, and tube separation, G. Curves are fits of Equation (6-3) to the simulation data.

potential. However, at larger tube separations, saturation capacity first decreases with increasing tube diameters, then increases. The larger the tube separation, the steeper the decrease of saturation capacity. When tube diameters are greater than 40 Å, the change of saturation capacity with changing tube diameter is small.

Thus, as expected, the saturation capacities of trigonal arrays of closed SWCNTs are closely related to array geometry. According to simple mathematical arguments, the volume of space available to adsorbate per unit mass, V_a, in trigonal arrays of closed SWCNTs is

$$V_a = \frac{N_A}{12\rho_a}\left[\frac{\sqrt{3}D}{2\pi}\left(1+\frac{G}{D}\right)^2 - \frac{D}{4}\left(1+\frac{\sigma_{cc}}{D}\right)^2\right] \tag{6-1}$$

where N_A is the Avogadro's number, ρ_a is the number of carbon atoms per unit area in tube wall, σ_{cc} the collision diameter of carbon atoms and D and G are tube diameter and separation respectively. Now, we may define a packing factor, f, as the ratio of the volume occupied by the adsorbed molecules to the total volume available, that is

$$f = \frac{N_1 \pi \sigma_{ff}^3 / 6}{V_a} \tag{6-2}$$

where N_1 is the number of molecules adsorbed per unit mass of the carbon material in the array, and $\pi\sigma_{ff}^3 / 6$ is the volume of each molecule assuming them to be solid spheres with diameter σ_{ff}. Replacing N_1 in Equation (6-2) with the capacity, w, expressed in mmol g^{-1}, the following equation can be derived:

$$w = Af\left[\frac{\sqrt{3}D}{2\pi}\left(1+\frac{G}{D}\right)^2 - \frac{D}{4}\left(1+\frac{\sigma_{cc}}{D}\right)^2\right] \tag{6-3}$$

where

$$A = \frac{500}{\pi \sigma_{ff}^3 \rho_a} \tag{6-4}$$

is a constant. For nitrogen adsorbed in carbons, A = 9.146 mmol g^{-1} $Å^{-1}$. The fits of Equation (6-3) to the simulated data are shown in Figure 6-5. As there is only one fitting parameter, f, in Equation (6-3), the fits are extremely good though the equation leads to overestimate the capacity of large tube arrays. The goodness of the fit of Equation (6-3) to the simulated data confirms that adsorption in trigonal arrays of closed SWCNTs is dominated by geometrical factors.

6.1.3 Packing of the adsorbed phase

The packing factor defined in Equation (6-2) describes how close adsorbed molecules are packed together and is a function of tube separations. Packing factors determined by fitting Equation (6-3) to the simulated adsorption data are shown as a function of tube separation in Figure 6-6. The error bars indicate ±1 standard deviation of the mean value of f. The packing factors for the interstitial adsorbate in the nanotube arrays are quite close to the molecular packing factor (f = 0.415) calculated from the density of liquid nitrogen at 77 K, which is 28.87 mmol cm^{-3} (Figure 6-6). The packing factor increases with increasing G at small G values and reaches a maximum at around G = 10 Å, then decreases. When G is in the range from 7 to 25 Å, f is greater than that of liquid nitrogen, indicating that in these cases the adsorbed phase is denser than liquid nitrogen.

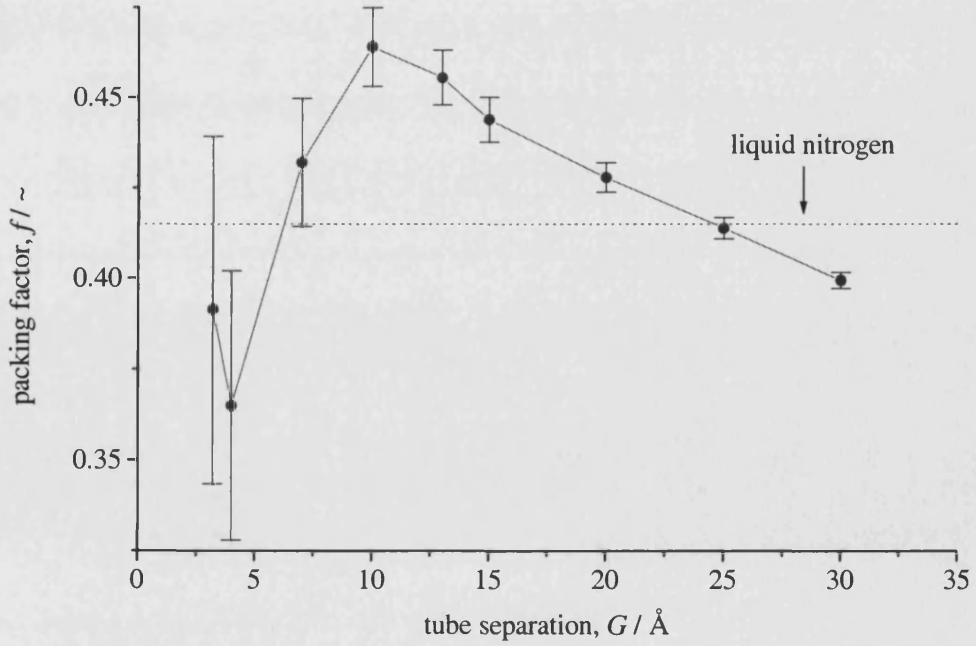

Figure 6-6. Packing factor of nitrogen adsorbed at 77 K in trigonal arrays of closed SWCNTs as a function of tube separation. The horizontal line shows the molecular packing factor calculated for bulk liquid nitrogen density at 77 K. Error bars indicate ±1 standard deviation of the mean.

(a) (b) (c)

Figure 6-7. Molecular snapshots for adsorption of nitrogen at 77 K and 760 Torr in trigonal arrays of closed SWCNTs of diameter 10 Å and varying tube separations, G. (a) G = 4 Å, showing the low dimensionality of the adsorption space; (b) G = 10 Å, sowing the formation of a monolayer on each nanotube surface; (c) G = 30 Å, showing the extent of the condensed phase adsorbate in the centre of the array.

The low packing factor when G = 4 Å is because the interstitial space is only slightly larger than the molecular diameter of nitrogen, so the adsorption space is nearly one-dimensional and a large portion of the space is not occupied. An adsorption snapshot of an array with G = 4 Å, D = 10 Å, and bulk gas-phase pressure p = 760 Torr (Figure 6-7a) illustrates this point. The maximum packing factor is found for tube spacings that are just wide enough to accommodate two monolayers in the exohedral adsorption space, a monolayer on the surface of each tube. Consequently, the adsorbate is essentially two-dimensional and more ordered and denser than a liquid-like phase. The formation of two monolayers between the nanotubes is illustrated in the molecular snapshot (Figure 6-7b) for an array with G = 10 Å and D = 10 Å and p = 760 Torr.

As tube spacing increases beyond G ~ 10 Å, the adsorbate consists of monolayers overlaid by a condensed phase, which will be more liquid-like and less ordered than the monolayers. This two-stage process of space filling is illustrated by the shape of isotherms for G = 25 Å (Figure 6-3). The decrease in packing factor with increasing tube separations results from the increasing proportion of the condensed phase that is formed as tube spacing increases. The nature of the condensed adsorbate in arrays with large values of G is illustrated in the snapshot for G = 30 Å, D = 10 Å, and p = 760 Torr (Figure 6-7c).

6.1.4 BET surface areas of trigonal arrays of closed SWCNTs

The BET (Brunauer-Emmett-Teller) surface area is commonly used as a characteristic parameter for adsorbents and the larger the BET surface area, the higher the capacity. For example, Parkyns and Quinn [1995] found that the methane uptake of activated carbons increases linearly with increasing BET surface areas. The BET surface area can be determined using the BET Equation:

$$\frac{p/p_0}{n(1-p/p_0)} = \frac{1}{n_m C} + \frac{C-1}{n_m C}\cdot\frac{p}{p_0} \tag{6-5}$$

where n is the uptake at pressure p, n_m is the monolayer capacity and C is a constant related to the adsorbate-adsorbate interaction energy. In practical applications, Equation (6-5) is fitted to the linear part of the isotherm at low p/p_0 and n_m and C are determined from the slope and intercept. The BET surface area is then calculated from $A_{BET} = n_m N_A a_m$, where $a_m = 16.2$ Å^2 is the average area occupied by a nitrogen molecule in the completed monolayer.

An example of a BET plot for simulated nitrogen adsorption at 77 K in trigonal arrays of closed SWCNTs is shown in Figure 6-8 for an array with D = 120 Å and G = 30 Å. As can be seen, the BET equation is a good fit to the simulated adsorption data in the relative pressure range from 0.05 to 0.4. Similar results were found for all isotherms simulated. Therefore, BET surface areas were determined for arrays with different tube diameters and separations.

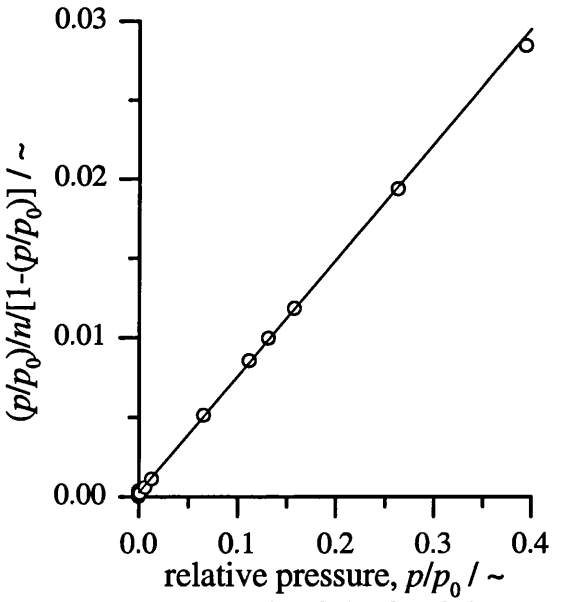

Figure 6-8. An example of the fit of the BET equation to simulated nitrogen adsorption at 77 K in trigonal arrays of closed SWCNTs with D = 120 Å and G = 30 Å. n is specific amount adsorbed and p/p_0 is relative pressure.

The variation of BET surface area as a function of array configuration is shown in Figure 6-9. For arrays with small tube separations, the surface area that is accessible to adsorbate molecules increases with increasing tube diameter. Therefore, as tube diameter increases, the BET surface area increases. At larger tube separations, all

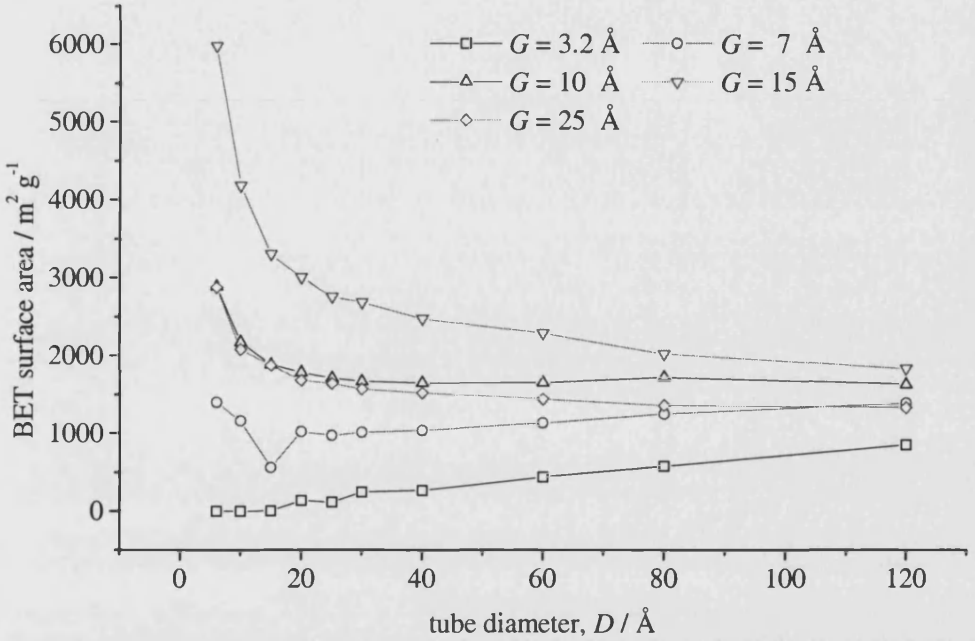

Figure 6-9. BET surface areas for simulated adsorption of nitrogen at 77 K in trigonal arrays of closed SWCNTs as a function of tube diameter, *D*, and separation, *G*.

geometrical surfaces of the tubes are accessible to adsorbate molecules and the mass of the carbon increases with increasing tube diameter. Therefore, the BET surface area decreases as tube diameter increases. Similarly, at small tube separations, increasing tube separation increases the accessible geometrical tube surface area and results in increases in BET surface areas. The maximum BET surface area is for arrays with the smallest tubes and about 15 Å separation. Upon further increase of *G*, the accessible geometrical surface does not increase. However, the potential in the monolayer zone weakens. Thus, the BET surface area decreases with increasing *G*.

It is worth noting that the maximum BET area in Figure 6-9 is about 6000 $m^2 g^{-1}$, much higher than the experimentally measured values for activated carbons and also higher than the geometrical surface areas of the arrays. The reasons for this are: (1) Due to the negative curvature of the surface, the occupied surface area here by each adsorbate molecule is considerably less than that when the surface is flat. This effect is more marked for smaller tubes. (2) As shown in Figure 6-6, the average molecular packing factor of the adsorbate in most arrays is higher than that of liquid nitrogen and the packing in the monolayer is believed to be denser than the more liquid-like phase; in this case, the molecules in the monolayer are nearly close-packed. Here, the area occupied by the adsorbate molecules will be much smaller than 16.2 $Å^2$ even on a flat

surface when the molecules are considered as soft Lennard-Jones spheres with diameter of 3.572 Å. (3) In ultramicropores, the potentials are extremely enhanced. Thus, there actually is no clear plateau corresponding to the completion of the monolayer, such as the isotherms in Figure 6-2. In such a situation, the BET monolayer capacity is greater than the true value. However, This BET analysis is useful as it is similar to how experimental isotherms are often analysed, though the model is rather idealised, assuming a regular array of tube which might not occur very often in reality.

6.2 Adsorption in trigonal arrays of open SWCNTs

If the tubes are open, endohedral adsorption, that is adsorption inside tubes, will contribute to the amount adsorbed. Thus, more will be adsorbed at a given pressure in arrays of open tubes compared to closed tubes. This section explores combined exohedral and endohedral adsorption in trigonal arrays of open SWCNTs.

6.2.1 Adsorption isotherms

Simulated nitrogen adsorption isotherms for trigonal arrays of open SWCNTs with different tube diameters and three tube separations (4 Å, 15 Å and 25 Å) are shown in Figures 6-10 to 6-12 repectively. Generally, most of the isotherms are similar to those

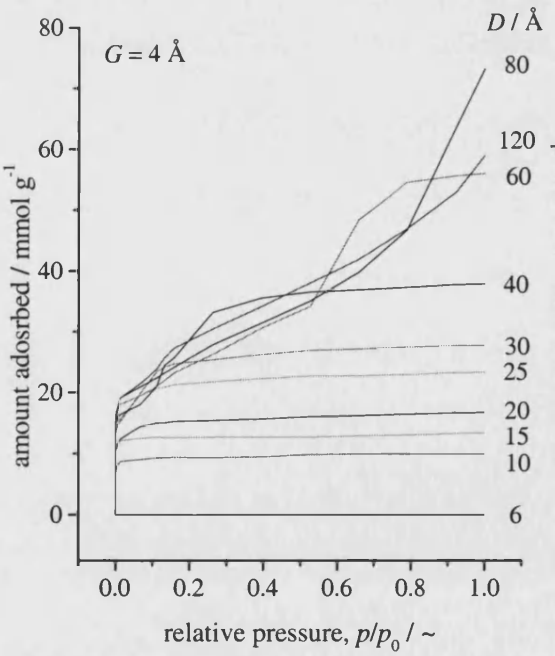

Figure 6-10. Simulated isotherms for nitrogen adsorbed at 77 K in trigonal arrays of open SWCNTs with different tube diameter, *D*, but with the same tube separation, *G*, of 4 Å.

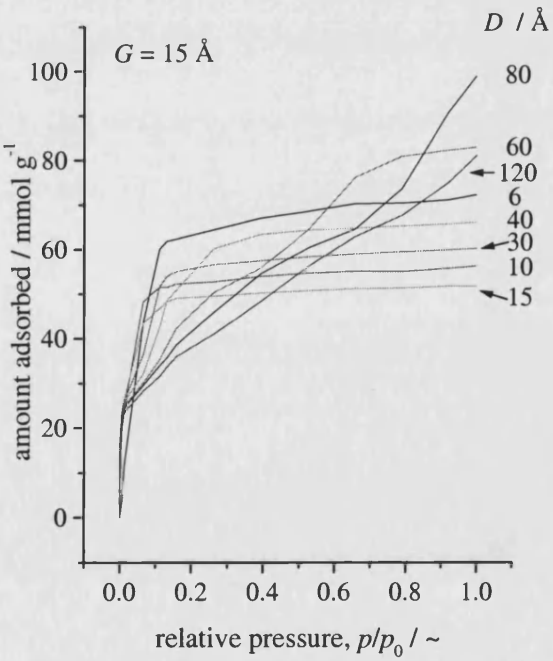

Figure 6-11. Simulated isotherms for nitrogen adsorbed at 77 K in trigonal arrays of open SWCNTs with different tube diameter, *D*, but with the same tube separation, *G*, of 15 Å.

of closed SWCNT arrays (see Figures 6-1 to 6-3). For small tube arrays with not very large separations, the isotherms are of type I. For larger tubes and larger separations, the isotherms are of type IV.

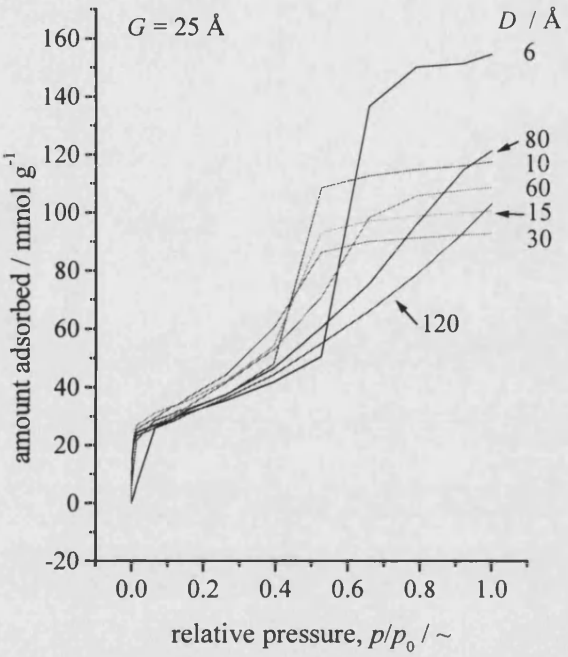

Figure 6-12. Adsorption isotherms of nitrogen at 77 K adsorbed in trigonal arrays of open SWCNTs with different tube diameters, but with the same tube separations of 25 Å.

However, there are some differences between the isotherms for closed and open tubes. (1) The amount adosrbed in open tube arrays is much higher than in closed tube arrays due to endohedral contributions. This effect is more marked in arrays with large tube diameters and small separations. For example, the amount adsorbed in the array of open tubes with D = 60 Å and G = 4 Å is about seven times that in closed tube arrays with the same array parameters. However, this improvement is insignificant in arrays with small D and large G. For example, there is little difference in the amount adsorbed in open and closed tube arrays with D = 6 Å and G = 25 Å. Therefore, it is concluded that opening tubes only improves adsorption capacities of arrays with large tube diameters and small tube separations. (2) In closed tube arrays, all the isotherms for arrays with G = 4 Å and G = 15 Å are essentially of type I. In the case of open tube arrays, larger tube arrays with those two G values give type IV isotherms. For example, the isotherms of open tube arrays with D = 60 Å in Figures 6-10 and 6-11 show clearly two stages corresponding to monolayer formation and saturation. This is because the endohedral porosity in this kind of arrays is outside the range of micropores and the interaction potential here is less enhanced. (3) Arrays with $D \geq 60$ Å give isotherms of type II in shape which is characteristic of meso- and macroporous materials. However, this is a consequence of the GCEMC simulation algorithm and does not necessarily indicate that condensation does not occur at equilibrium. In GCEMC simulations, a move is accepted according to the probability described in section 2.3.2. When an adsorbate molecule is created at a place far from the pore wall with no significant potential enhancement, the

interaction potetnial is close to zero. Therefore, acceptance of such a move is highly unlikely. The system may be trapped in a metastable state and the final state in the simulations is not truly at equilibrium. Thus, GCEMC is most suitable to confined systems where the interaction is significantly enhanced.

The adsorption process of nitrogen in trigonal arrays of open SWCNTs is shown schematically in Figure 6-13 using simulation snapshots at different relative pressures for arrays with tube diameter D = 20 Å and tube separation G = 7 Å. In such arrays, the adsorption potentials in the interstitial spaces are so strong that there are some molecules adsorbed in the interstitial space at relative pressures even lower than 10^{-7}. The strongest adsorption sites are exactly half way between two adjancent tubes. However, the exohedral monolayer is not formed until relative pressures reach 10^{-4}, at which the endohedral monolayer is also completed. Therefore, endohdral and exohedral monolayers are formed at similar relative pressures. Adsorption effectively reaches a saturation state at relative pressures about 0.013.

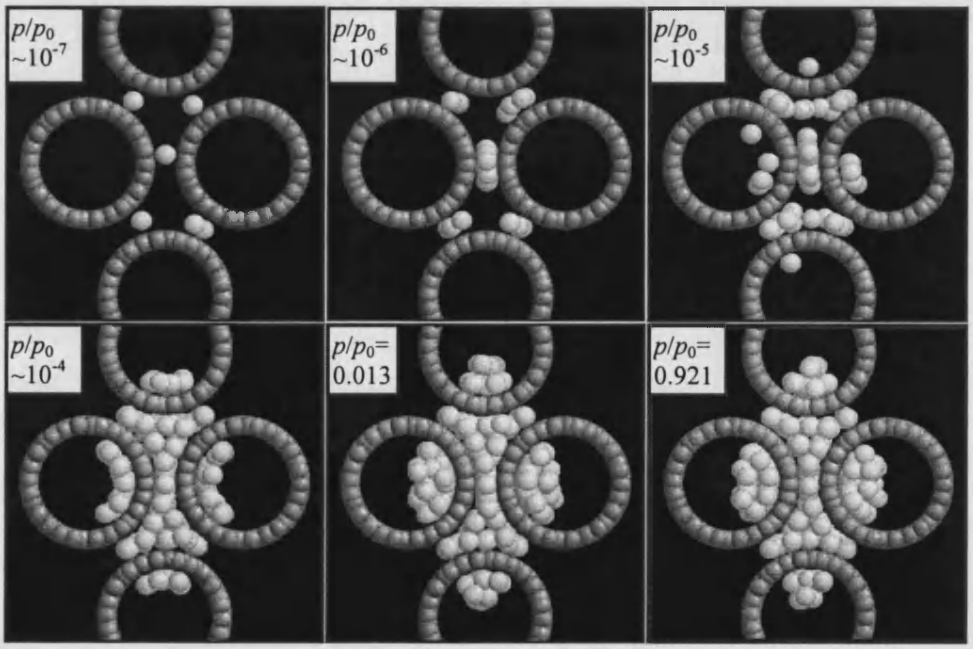

Figure 6-13. Simulation snapshots of nitrogen adsorbed at 77 K in trigonal arrays of open SWCNTs with diameter D = 20 Å and separation G = 7 Å at different relative pressures, p/p_0, showing the interstitial (exohedral) space is occupied at lower pressures than the inside (endohedral) space of the tubes. Grey spheres are carbon atoms forming the tubes and white ones are nitrogen molecules adsorbed.

For arrays with larger tube separations, the process is different from the process described above. An example is shown in Figure 6-14 for arrays with D = 20 Å and

G = 15 Å. In this case, the endohedral space is filled with fluid molecules first and there is no exohedral adsorption until the endohedral monolayer is formed at relative pressures of about 10^{-5}. Similarly, the relative pressure range for formation of the exohedral monolayer is higher. At relative pressures about 0.013, both the exohedral and endohedral monolayer are completed and cooperative effects take place. Soon after that, the open space is filled with molecules and adsorption essentially reaches saturation at $p/p_0 \sim 0.066$.

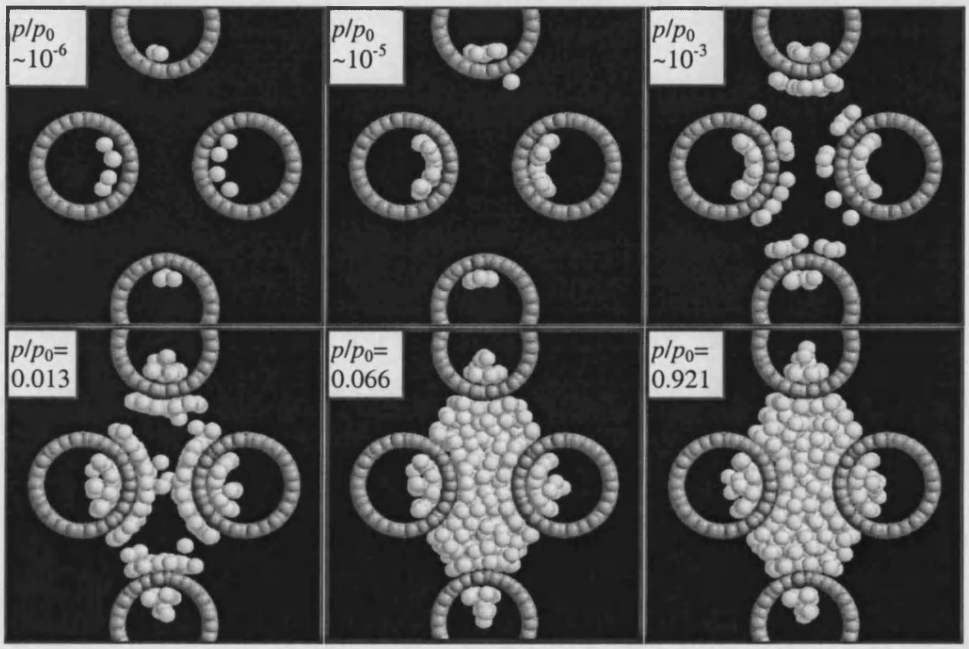

Figure 6-14. Simulation snapshots of nitrogen adsorbed at 77 K in trigonal arrays of open SWCNTs with diameter D = 20 Å and separation G = 15 Å at different relative pressures, p/p_0, showing the interstitial (exohedral) space is occupied at lower pressures than the inside (endohedral) space of the tubes. Grey spheres are carbon atoms forming the tubes and white ones are nitrogen molecules adsorbed.

6.2.2 *Saturation capacities as functions of array configuration*

Simulated saturation capacities of nitrogen adsorbed in trigonal arrays of open SWCNTs as functions of array configuration are shown in Figure 6-15. Similar to the situations in closed tube arrays, saturation capacities increase with increasing tube separations at all D; capacities of arrays with small G increase with increasing D and capacities of arrays with small D and large G decrease with increasing D. The difference is that saturation capacities of arrays with large D here increase sharply with increasing D, because the amount adsorbed endohedrally increases with D. The decrease of capacities at D larger than 80 Å is not real, as can be seen from Figures 6-10

to 6-12, they are actually not saturation capacities and may be due to the shortcomings of the simulation method used here as explained in the above section.

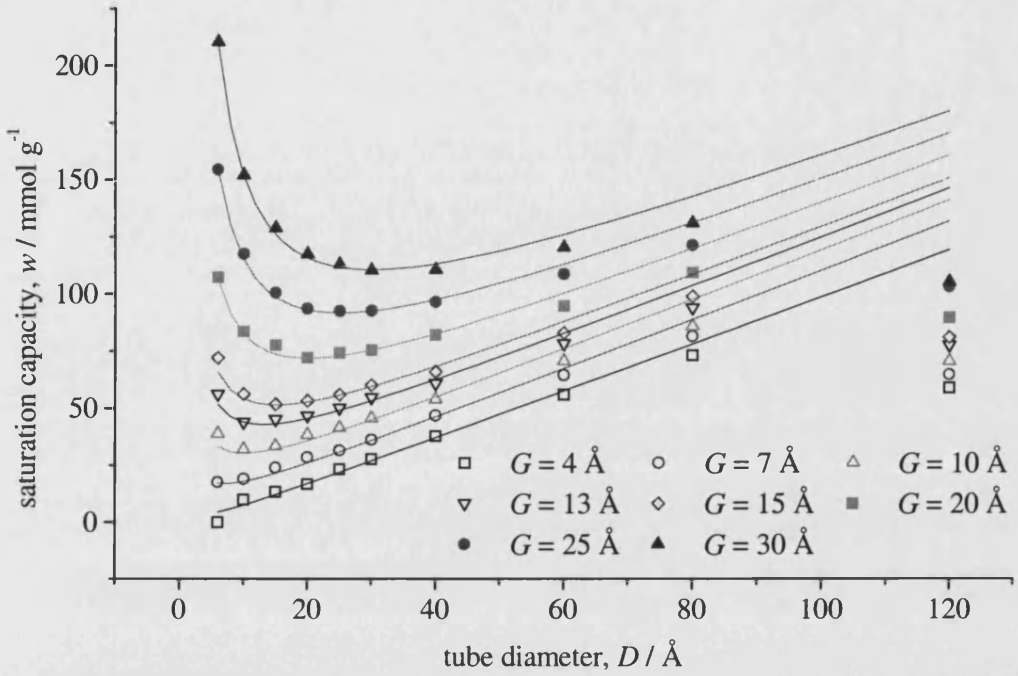

Figure 6-15. Simulated saturation capacities for adsorption of nitrogen at 77 K in trigonal arrays of open SWCNTs as functions of tube diameters, D, and tube separations, G. Curves are fits of Equation (6-6) to the simulation data up to D = 60 Å.

Similar analysis to that in section 6.1.2 for closed tubes leads to a counterpart of Equation (6-3) for trigonal arrays of open SWCNTs:

$$w = Af\left[\frac{\sqrt{3}D}{2\pi}\left(1+\frac{G}{D}\right)^2 - \sigma_{cc}\right] \tag{6-6}$$

where A = 9.146 mmol g^{-1} Å^{-1}. The curves in Figure 6-15 are fits of Equation (6-6) to the simulated data in the range of D from 6 Å to 60 Å. This range is chosen because the capacities of arrays with D larger than 60 Å shown in Figure 6-15 are not saturation capacities. It is clear that the equation fits the data quite well with only one fitting parameter, although the equation overestimates the capacities of larger tube arrays. This again shows that adsorption in trigonal arrays of SWCNTs is dominated by geometric effects.

6.2.3 *Molecular packing factors*

The packing factor, f, determined according to Equation (6-6) as a function of G is shown in Figure 6-16, together with the packing factors for closed tube arrays and the molecular packing factor calculated for bulk liquid nitrogen. Packing factors are all around that of liquid nitrogen, indicating a densely packed adsorbate phase. Packing factors for arrays with intermediate tube separations are higher than that for liquid nitrogen. The maximum packing factor at $G \sim 10$ Å is lower for open tube arrays. This suggests that the endohedrally adsorbed phase is more liquid-like than the ordered, exohedral monolayers that are formed at this tube spacing. For $G \leq 4$ Å, the situation is reversed. This is because that the adsorption is nearly one-dimensional and a large portion of the interstitial space is not accessible to adsorbate molecules.

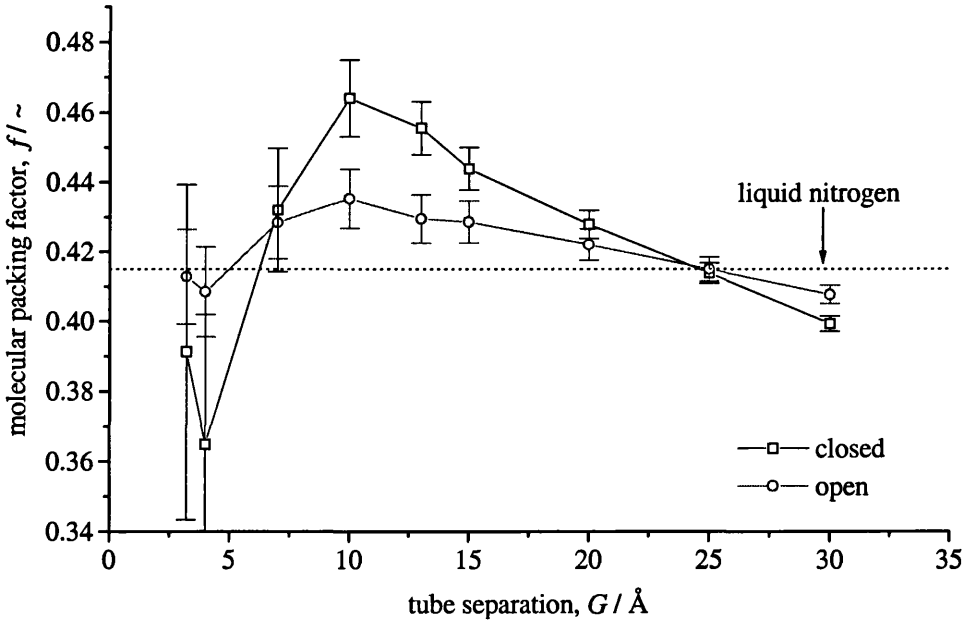

Figure 6-16. Molecular packing factor of nitrogen adsorbed at 77 K in trigonal arrays of open and closed SWCNTs as functions of tube separation. The horizontal line shows the molecular packing factor calculated for bulk liquid nitrogen at 77 K. Error bars indicate ±1 standard deviation of the mean.

6.2.4 *Endohedral and exohedral contributions to adsorption capacities*

The contribution of exohedral adsorption to the total saturation capacity can also be described by Equation (6-3), thus packing factors can also be determined and the values are similar to those of closed tube arrays. Similar geometrical analysis show that the contribution of endohedral adsorption to the total saturation capacity may be described by the following equation:

$$w = Af\left[\frac{1}{4}\left(1-\frac{\sigma_{cc}}{D}\right)^2\right] \tag{6-7}$$

where A = 9.146 mmol g^{-1} $Å^{-1}$ and f is the packing factor defined in Equation (6-2). The simulated packing factors as functions of tube separations are shown in Figure 6-17, together with the exohedral and liquid nitrogen packing factors. Unlike exohedral packing factors, endohedral packing factors do not change very much with tube separation and are all very close to the molecular packing factor calculated for bulk liquid nitrogen. However, at small tube separations, the packing factors seem to decrease with increasing tube separation. This is due to the decreases in the contribution to the adsorption potential from neighbouring tubes and adsorbed molecules. This contribution decreases with increasing tube separation. At large tube separations, this effect is very small. Thus endohedral packing factors nearly remain constant. Another interesting point is that only at small tube separations is endohedral packing factor greater than that of liquid nitrogen. When tube separation exceeds 10 Å, packing factors

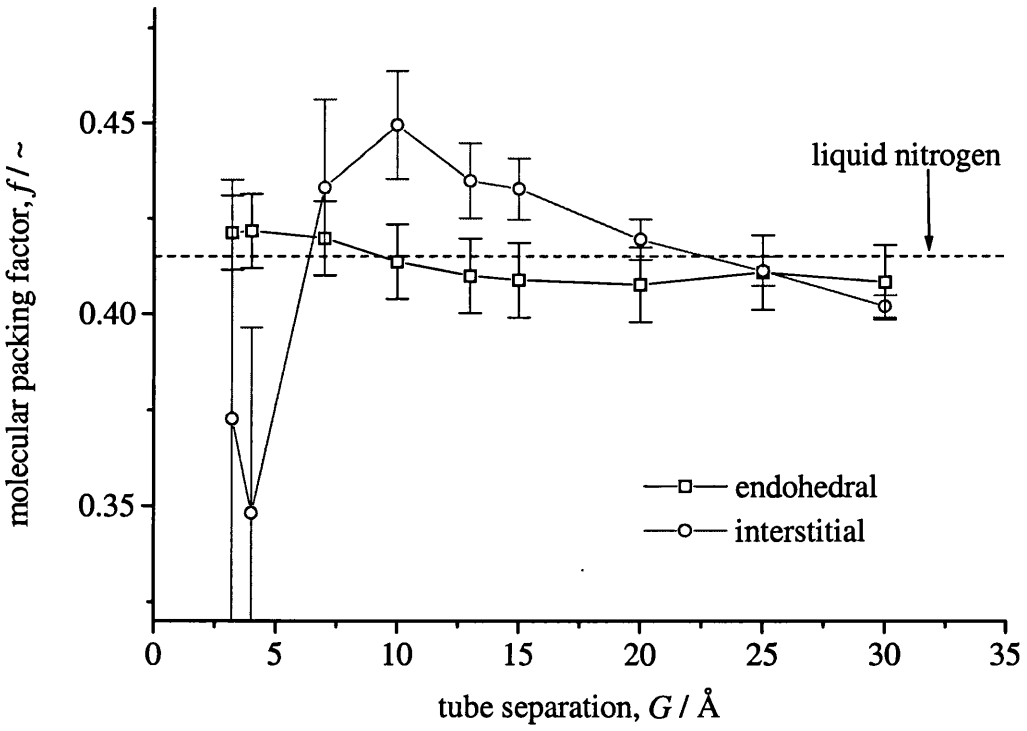

Figure 6-17. Simulated molecular packing factors of endohedral and interstitial adsorbed phases of nitrogen at 77 K as functions of tube separations in trigonal arrays of open SWCNTs. Error bars indicate ±1 standard deviations of the mean packing factors. The horizontal line shows the molecular packing factor calculated for bulk liquid nitrogen at 77 K.

are lower than that of liquid nitrogen. The exohedral packing factors vary with varying tube separations in the same way as in the case of closed tubes, as expected.

Examples of simulated endohedral and exohedral adsorption isotherms for nitrogen at 77 K are shown in Figure 6-18 for trigonal arrays with D = 15 Å and G = 3.2 and 15 Å. It is interesting to note that: (1) The exohedral amount adsorbed increases dramatically with increasing tube separation, though in arrays of larger tubes this effect is not so marked. (2) The amount adsorbed endohedrally is higher in arrays with G = 15 Å, a clear demonstration of the effect of the interaction between the adsorbed molecules, as discussed in the previous chapter. (3) In the arrays with D = 15 Å and G = 15 Å, the amount adsorbed exohedrally is more than 3 times greater than that adsorbed endohedrally. This suggests that in some arrays, exohedral adsorption will play a predominant role.

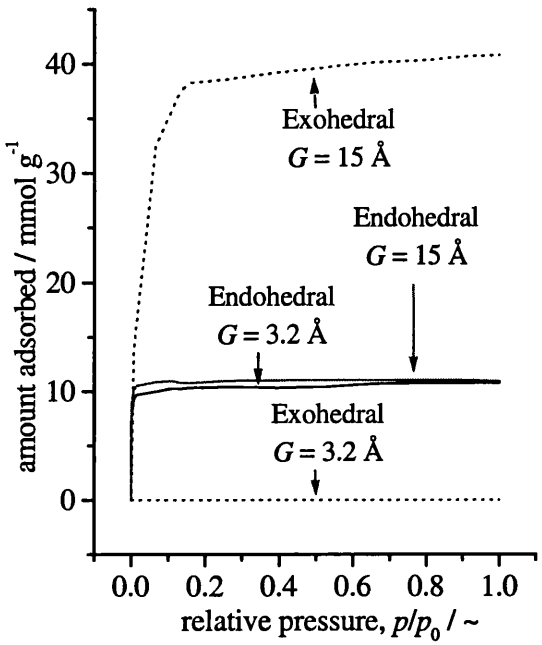

Figure 6-18. Examples of simulated endohedral and exohedral isotherms for nitrogen adsorbed at 77 K in trigonal arrays of open SWCNTs with D = 15 Å and G = 3.2 Å or 15 Å.

Details of exohedral contributions to the total saturation capacities in trigonal arrays of open SWCNTs as functions of tube diameter and separation are shown in Figure 6-19. It is clear that exohedral contribution decreases steeply with increasing tube diameter due to the increasing endohedral contribution to adsorption capacity. However, exohedral adsorption is important in most cases. For the most densely packed array (G = 4 Å), the exohedral contribution is about 10% of the total. The smaller the tube and the larger the tube separation, the larger the exohedral contribution. For arrays with D ≤20 Å, if there are gaps even as narrow as a single molecular diameter width between the tubes, the exohedral contribution to the total saturation capacities will be greater than that of endohedral adsorption. Refering to Figure 6-15, the capacities of arrays with open tubes with D ≤20 Å are very low and can only be increased by increasing tube separations. The highest capacity is from the arrays with smallest tube diameter and

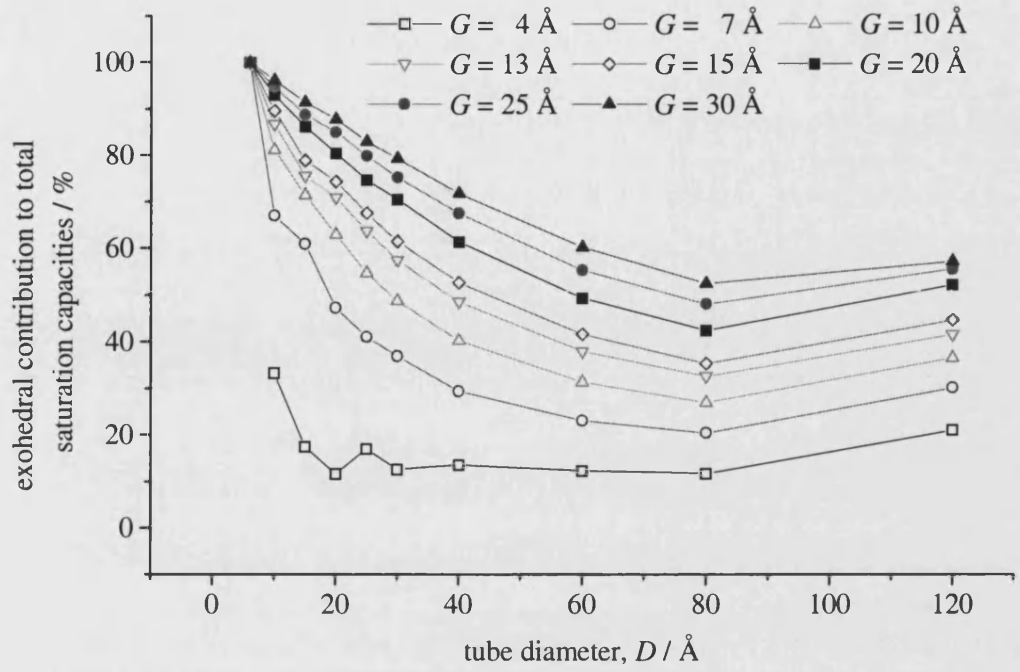

Figure 6-19. Simulated exohedral contributions to the total saturation capacities of nitrogen adsorbed at 77 K in trigonal arrays of open SWCNTs as functions of tube diameters, D, and separations, G.

large tube separations. In such arrays, the adsorption is completely by exohedral adsorption. Therefore, it can be concluded that (1) To achieve high adsorption capacities, sufficiently large gaps must be introduced into the tube arrays to admit exohedral adsorption. (2) It is not necessary to open tubes to achieve high adsorption capacities.

6.2.5 BET surface areas of trigonal arrays of open SWCNTs

BET surface areas of trigonal arrays of open SWCNTs were determined in the same way as discussed in section 6.1.4. BET surface areas as functions of tube diameter and separation are shown in Figure 6-20. At small D and G, surface areas increase with increasing D and G. At small D but large G, suface areas decrease with increasing D and G. The optimal tube separation corresponding to the maximum BET surface areas is G = 15 Å. In such a spacing, three layers of adsorbate molecules can be formed between the tubes (Figure 6-14). Increasing G from this point leads to a decrease in the interaction between neighbouring tubes and adsorbed molecules, and therefore a decrease in monolayer packing density. In turn, the BET surface area decreases. It is interesting that there are local maximums at about D = 40 Å for arrays with G < 15 Å. In arrays with small G, increasing D will increase the proportion of the surface area

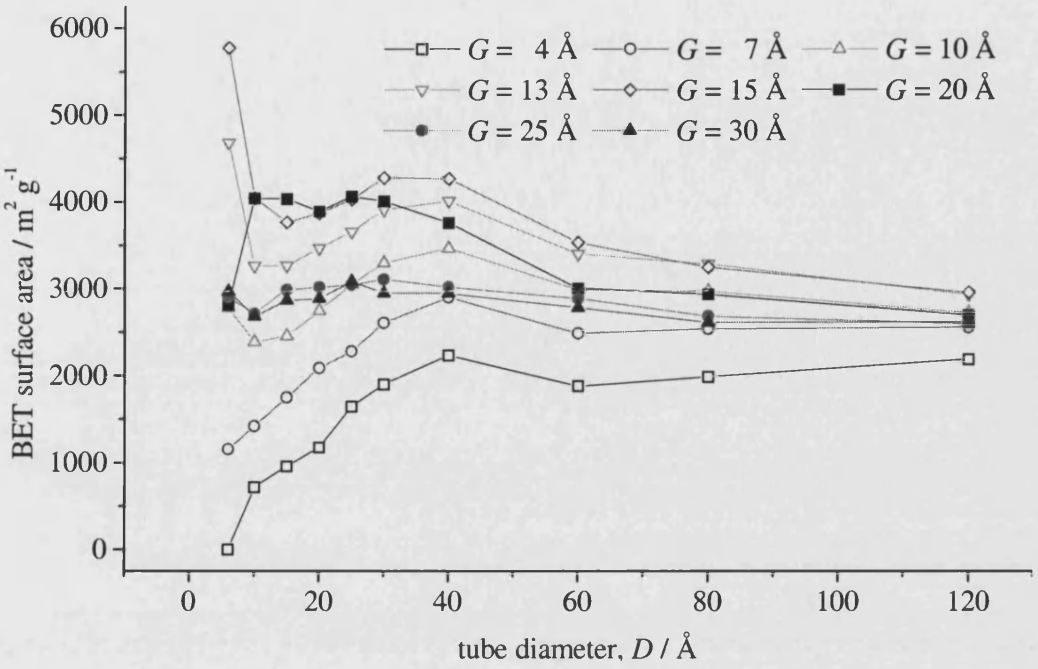

Figure 6-20. BET surface areas for simulated adsorption of nitrogen at 77 K in trigonal arrays of open SWCNTs as a function of tube diameter, D, and separation, G.

accessible to guest molecules and this effect can be more marked than the increase in the mass of the carbon atoms in the simulation cell. Thus, the BET surface areas increase with increasing D. However, when D is large enough, the increase in the proportion of the accessible surface area will not be so rapid while the increase in the mass of carbon atoms is still proportional to the increase of D. Therefore, there is a decrease in BET surface area. At sufficiently large D or G, this effect will be very small. In such cases, BET suface areas of all arrays have values that are close to the maximum geometrical specific surface areas of graphitic carbons, *i.e.* ~ 2600 $m^2 g^{-1}$.

6.2.6 *Comparison with experimental measurements*

Experimental adsorption isotherms of nitrogen at 77 K adsorbed in carbon nanotubes have been reported by a few research groups. However, the information is still not enough to make a full comparison with the simulation results discussed here. One reason is due to the lack of proper samples of carbon nanotubes, and the other is that different groups may obtain different adsorption isotherms even for carbon nanotubes from the same source. Here we present adsorption measurements carried out at Bath on single wall carbon nanotubes supplied by Dr. W. Maser of CSIC, Zaragosa, Spain.

The nanotubes were made by the arc discharge technique and, as observed using transmission electron microscopy, are in the form of aligned bundles of single wall carbon nanotubes. The nanotubes are closely packed in a trigonal way with lattice constant of 17 Å, *i.e.* D = 13.8 Å and G = 3.2 Å. According to the supplier, most of the nanotubes are closed and each bundle contains a few tens of carbon nanotubes. A nitrogen adsorption isotherm at 77 K for these nanotubes was measured volumetrically using Micromeritics ASAP 2010 and is shown in Figure 6-21, together with simulated adsorption isotherms of trigonal arrays of closed and open SWCNTs with the same array parameters and under the same environmental conditions. The central part of these isotherms are qualitatively in good agreement, although the absolute amounts adsorbed are different.

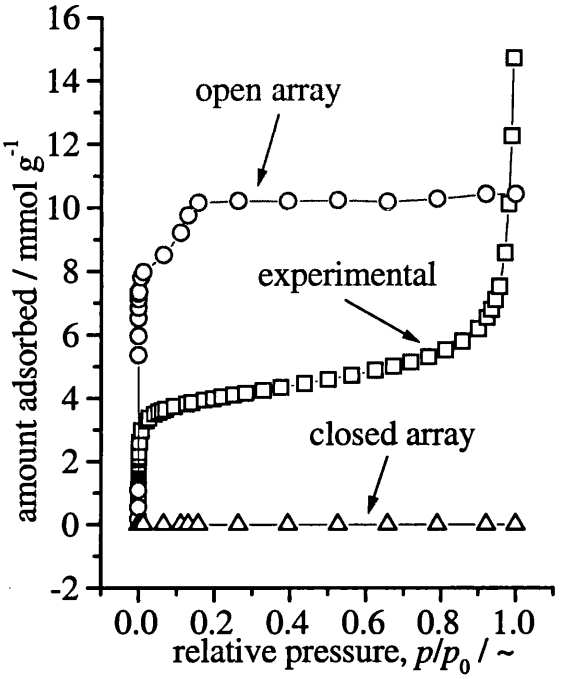

Figure 6-21. Simulated and experimental isotherms for nitrogen adsorbed at 77 K in trigonal arrays of SWCNTs with D = 13.8 Å and G = 3.2 Å.

Geometrical analysis of trigonal arrays of close packed nanotubes show that the diameter of the interstitial space is

$$d \approx \left(\frac{2}{\sqrt{3}} - 1 \right) D \approx 0.155 D \qquad (6\text{-}8)$$

where D is the diameter of the tubes forming the array. For the particular arrays with D = 13.8 Å, d ~ 2.2 Å, only two thirds of the diameter of nitrogen molecules (3.572 Å). Thus, the interstitial space is not accessible to nitrogen molecules and the amount adsorbed in the closed tube arrays is essentially zero (Fgiure 6-21). The experimental measurements of the amount adsorbed at low relative pressures are between the

simulated amounts of open and closed tube arrays. The discrepancy between the experimental and simulated adsorption amount at low pressure may be due to a small portion of the nanotubes in the sample being open and / or the adsorption in the inter-bundle space. Also impurities in the nanotube sample make their contributions to the amount adsorbed. Rough estimation of the surface areas of the nanotube bundles give a value that is of the same order of magnitude as the experimentally measured value, 302 m^2 g^{-1} [Alain *et al.*, 2000]. The sharp increase in the amount adsorbed at relative pressures close to unity shows macroporous behaviour and is a clear demonstration of adsorption in the interbundle or interparticle space. On the other hand, the experimentally measured amount may be less than the equilibrium amount because the possibility that experimental isotherms are not at equilibrium due to diffusion effects. Therefore, taking all these into consideration, the simulated isotherms are in reasonable agreement with experimental measurements, which is encouraging.

6.3 Summary and conclusions

(1) Adosrption isotherms of nitrogen adsorbed at 77 K in trigonal arrays of SWCNTs with small tube diameters and separations are of type I, showing microporous behaviour. Isotherms for arrays with large tube separations or large tube diameters are of type IV, showing both monolayer formation and saturation.

(2) The amount adsorbed in nanotube arrays is dominated by geometrical factors, *i.e.* tube diameters and separations.

(3) At saturation, the packing density of the adsorbed phase is close to that of liquid nitrogen. In arrays with intermediate tube separations, the packing density is higher than that of liquid nitrogen. Endohedral packing density does not change much with chaging tube separations, while exohedral packing density does and shows a maximum at $G \sim 10$ Å.

(4) Close packed nanotube arrays with tube diameters similar to experimental tubes have very low simulated adsorption capacities. Introducing gaps between the tubes forming the arrays can markedly improve the capacities and the highest capacities are in arrays with the smallest tubes but with large tube separations. In such arrays, interstitial adsorption is predominant and opening up the tubes is not necessary to improve capacities. This also indicates that dispersed nanotube materials may have capacities higher than close packed aligned nanotube materials.

(5) Very high BET surface areas might be reached with certain nanotube arrays, even higher than most experimentally-determined values for activated carbons. This suggests that carbon nanotubes might be excellent adsorbents.

(6) Simulated adsorption isotherms are in reasonable agreement with experimental observations and can be studied and used to obtain some insight into adsorption in carbon nanotubes, though more experimental measurements on well purified and characterised nanotube samples are required to facilitate further comparison.

Chapter 7
Nitrogen Adsorption in Square SWCNT Arrays

The densest and hence most stable packing of carbon nanotubes in arrays is the trigonal or hexagonal pattern. However, experimentally nanotubes may not always be packed in perfect trigonal arrays. In addition, it may be possible to arrange nanotubes in square arrays rather than in trigonal arrays. Also, from a purely scientific point of view, the influence of different array patterns on adsorption capacity is of interest. Therefore, the adsorption of nitrogen in square arrays of carbon nanotubes was studied and the results are presented in this chapter.

In microporous materials, the amount adsorbed is proportional to the micropore volume. If nanotubes are packed as square arrays, there will be more interstitial space available to the adsorptive. As discussed in the previous chapter, interstitial space plays an important role in the adsorption of nanotube arrays. Thus it is expected that square arrays of carbon nanotubes might have higher capacities than trigonal arrays.

7.1 Adsorption in square arrays of closed SWCNTs

7.1.1 Adsorption isotherms

Figures 7-1 to 7-3 show simulated adsorption isotherms of nitrogen adsorbed at 77 K in square arrays of closed SWCNTs as functions of tube diameters, D, with three different tube separations G = 4, 15 and 25 Å, respectively. For a separation of 4 Å, isotherms of tubes with diameters up to 50 Å are close to type I and the interstitial space is filled up at very low relative pressures, indicating microporous behaviour. For larger tube arrays, the isotherms are neither type I nor type IV. Instead a horizontal plateau corresponding to the monolayer completion and a rapid increase in the amount adsorbed corresponding to condensation, there is a gradual and nearly linear increase in the amount adsorbed after the turning point. Let d standard for the diameter of the largest sphere that will fit in the interstitial space, geometrical analysis shows that d can be described by

$$d = \left(\sqrt{2}-1\right)D + \sqrt{2}G - \sigma_{CC} \approx 0.414D + \sqrt{2}G - \sigma_{CC} \quad (7\text{-}1)$$

where σ_{cc} is the collision diameter of carbon atoms. Thus, when $D \geq 50$ Å, d is larger

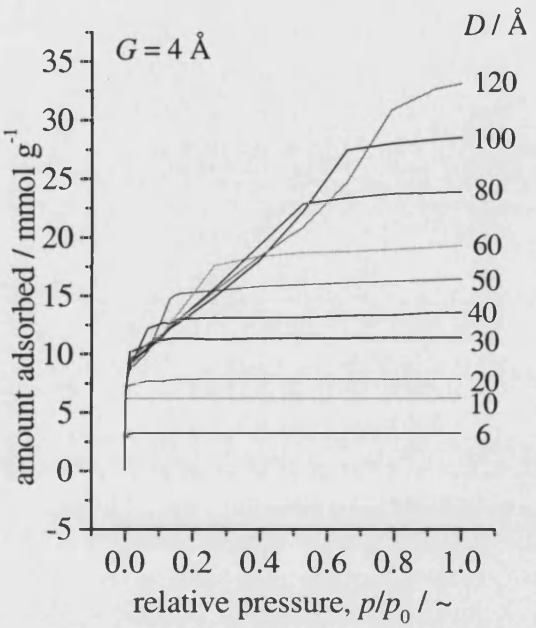

Figure 7-1. Simulated isotherms of nitrogen adsorbed at 77 K in square arrays of closed SWCNTs with different tube diameters, D, but with the same tube separations, G, of 4 Å.

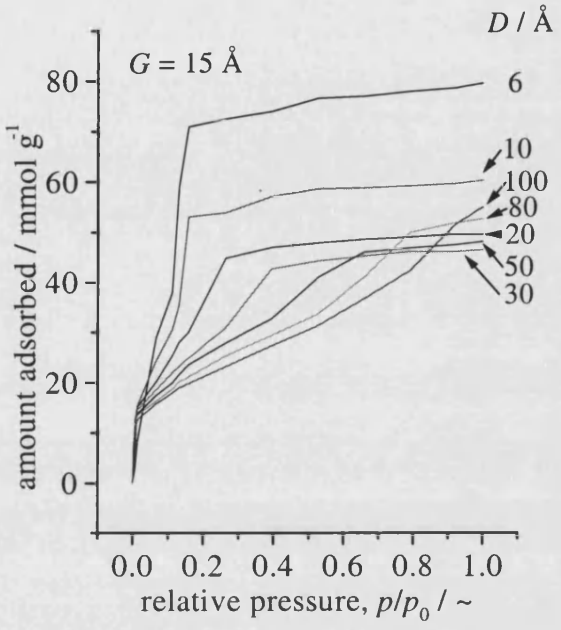

Figure 7-2. Simulated isotherms of nitrogen adsorbed at 77 K in square arrays of closed SWCNTs with different tube diameters, D, but with the same tube separations, G, of 15 Å.

than 20 Å. Therefore, the interstitial space is not within the range of micropores. However, for large micropores and small mesopores, the isotherms should be of type IV. The deviation of the isotherms shown in Figure 7-1 from type IV is explained as follows.

In slit pores, the adsorption potential outside the monolayer region is weak and there is not much difference between the potentials at different sites. Thus, after the formation of the monolayer, the probability of adsorbing molecules at different

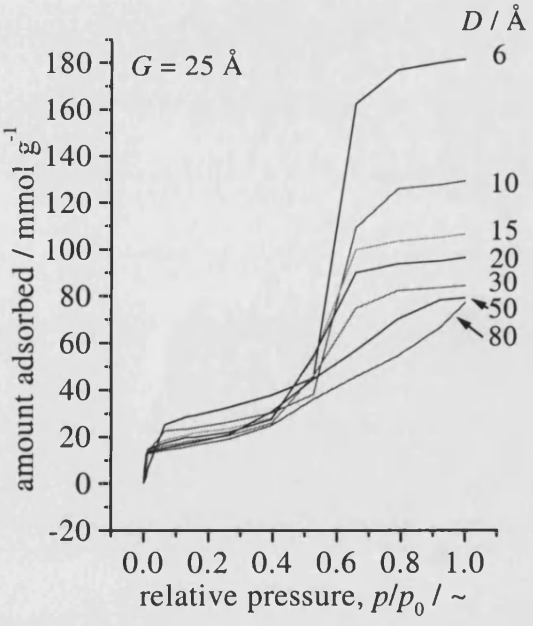

Figure 7-3. Simulated isotherms of nitrogen adsorbed at 77 K in square arrays of closed SWCNTs with different tube diameters, D, but with the same tube separations, G, of 25 Å.

positions in the pore is small and the difference in the probability corresponding to different positions is small. Consequently, when pressures approach saturation, the amount adsorbed in the pore would increase markedly and all the sites will be occupied by adsorbate molecules. In the interstitial space here, however, much larger differences in the adsorption potentials are expected. For example, the corners formed by the monolayer (Figure 7-4) are stronger adsorption sites due to enhancement of interaction, comparing with other positions in the interstitial space. This variation in adsorption potentials within the interstitial space is similar to potential variations in different sized pores. In other words, larger interstitial spaces result in a material that appears to have some kind of pore size distributions. Therefore, the amount adsorbed would increase gradually until there is no significant difference in the potentials in the interstitial space and then the space will be filled with adsorbate molecules. This process is shown in Figure 7-4 which contains snapshots for the array with D = 80 Å and G = 4 Å. The amount adsorbed after monolayer formation gradually increase with increasing pressure until the interstitial space is filled with molecules. Similar situations are found in arrays with larger tube separations as shown in Figure 7-2.

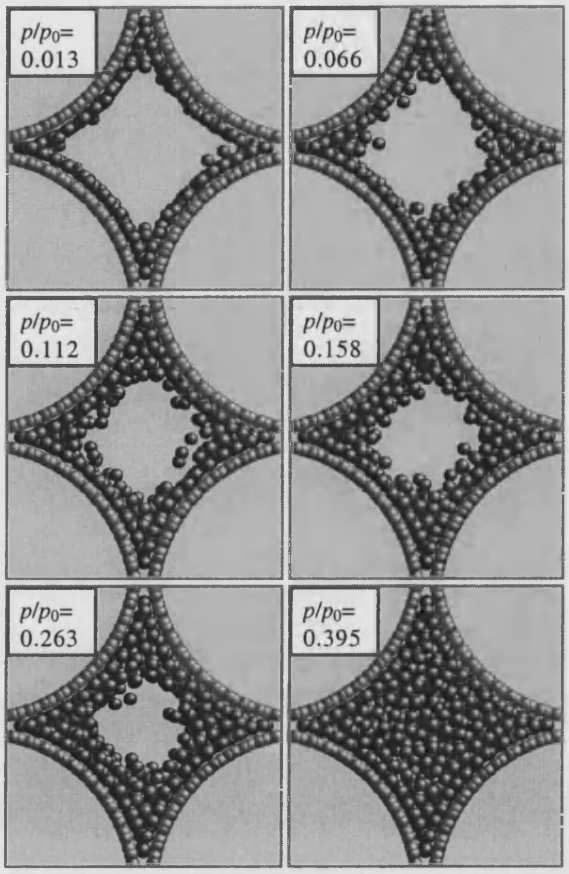

Figure 7-4. Snapshots of nitrogen adsorbed at 77 K in square arrays of closed SWCNTs with diameter D = 80 Å and separation G = 4 Å and different relative pressures p/p_0, showing a gradual increase in the amount adsorbed after the formation of the monolayer. The grey spheres are carbon atoms and the dark spheres are nitrogen molecules adsorbed.

The saturation density increases with increasing tube diameters when G = 4 Å (Figure 7-1). This is different from the case of trigonal arrays, where two local maximums are clearly shown (Figure 6-1). The non-existence of these local maximums is due to larger interstitial spaces in square arrays. The saturation density decreases and then increases

with increasing tube diameter when G = 15 Å (Figure 7-2) and decreases with increasing tube diameter when G = 25 Å (Figure 7-3). These trends are the same as in the case of trigonal arrays. Other features of the isotherms are similar to those for trigonal arrays. Comparison of Figure 7-1 with Figure 6-1 shows that square arrays have much higher capacities than trigonal arrays at small tube separations. This improvement of capacities is small or does not exist at larger tube separations (cf. Figures 7-2, 7-3 and 6-2, 6-3).

7.1.2 Saturation capacities as functions of array configuration

The variation of saturation capacities as a function of array configuration is shown in Figure 7-5. The main features of Figure 7-5 are similar to those of Figure 6-5 and the saturation capacities of square closed SWCNT arrays are also closely related to array geometry. Similar geometrical analysis shows that in the case of square arrays, Equations (6-1) and (6-2) become:

$$V_a = \frac{N_A}{12\rho_a}\left[\frac{D}{\pi}\left(1+\frac{G}{D}\right)^2 - \frac{D}{4}\left(1+\frac{\sigma_{cc}}{D}\right)^2\right] \tag{7-2}$$

$$w = Af\left[\frac{D}{\pi}\left(1+\frac{G}{D}\right)^2 - \frac{D}{4}\left(1+\frac{\sigma_{cc}}{D}\right)^2\right] \tag{7-3}$$

where V_a is the volume available to adsorptive per unit mass of carbon material, N_A the Avogardro's number, ρ_a the number of carbon atoms per unit area of perfect graphite sheet, σ_{cc} the collision diameter of carbon atoms, w the saturation capacity expressed in mmol g^{-1} , f the molecular packing factor defined in Equation (6-2) and A = 9.146 mmol g^{-1} $Å^{-1}$ is a constant for nitrogen adsorbed in carbons. The fits of Equation (7-3) to the simulated data up to D = 60 Å are shown in Figure 7-5. As there is only one fitting parameter, f, in Equation (7-3), the fits are extremely good at small D or G. The large deviations of the simulated data at larger D and G from Equation (7-3) are reasonable, because in such cases the final density simulated is actually not the saturation density (Figure 7-3 isotherm for D = 80 Å). Thus, the adsorption in square arrays of closed SWCNTs is dominated by geometrical factors as in trigonal arrays.

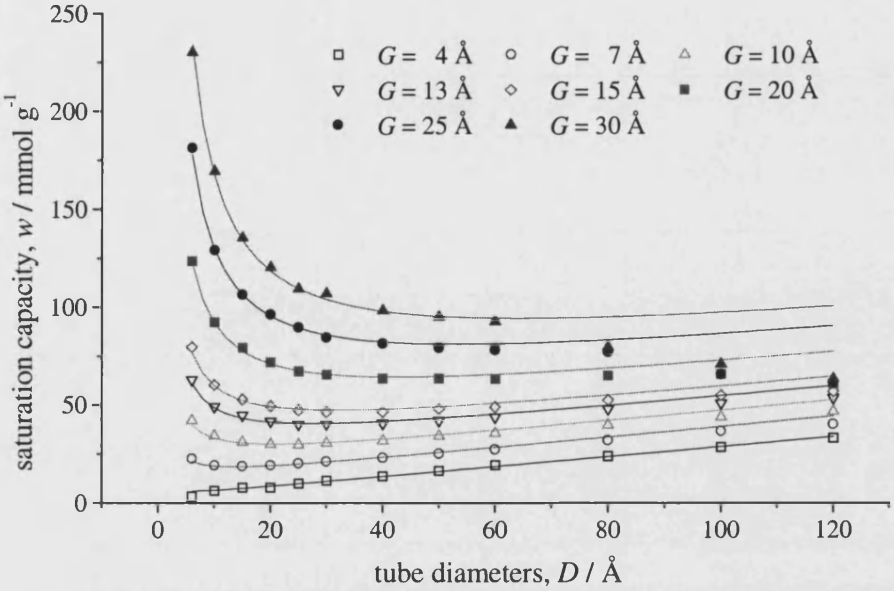

Figure 7-5. Saturation capacities for nitrogen adsorbed at 77 Kin square arrays of closed SWCNTs as functions of tube diameter, D, and tube separation, G. Curves are fits of Equation (7-3) to the simulation data up to D = 60 Å.

7.1.3 Packing of the adsorbed phase

The packing factors obtained by fitting Equation (7-3) to the simulated data are shown in Figure 7-6 as a function of tube separation. The packing factors for closed trigonal arrays are also shown in the figure for comparison. It is clear that the variations of packing factors as functions of tube separations are similar in both cases. However, the packing factors for square arrays are closer to the molecular packing factor calculated from the density of liquid nitrogen at 77 K (Figure 7-6). At small tube separations, packing factors of square arrays are larger than that of trigonal arrays and the situation is reversed at larger

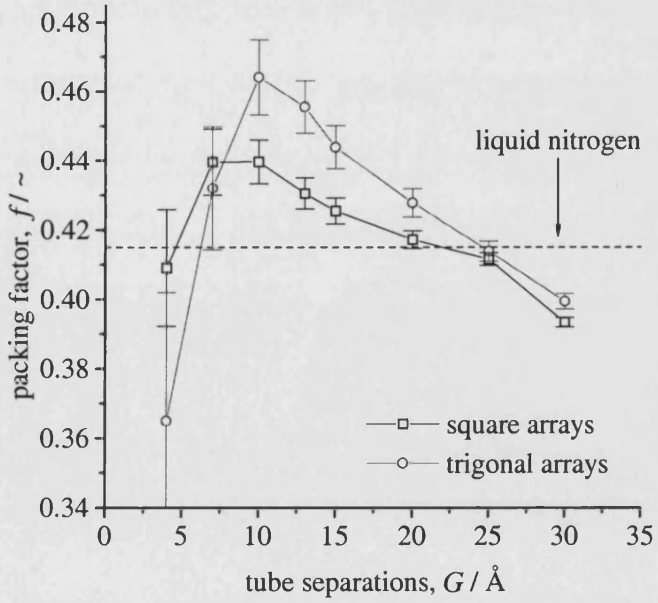

Figure 7-6. Packing factor of nitrogen adsorbed in square arrays of closed SWCNTs at 77 K as a function of tube separation, G. The horizontal line shows the molecular packing factor calculated for bulk liquid nitrogen at 77 K. Error bars indicate ±1 standard deviation from the mean.

tube separations. This is because the interstitial space in square arrays is much larger than in trigonal arrays [cf. Equations (7-1) and (6-8)] and the shape of the interstitial space. At small G, less volume fraction is not occupied by the adsorbate because the shape of the interstitial space is more favourable to packing of spheres, thus resulting in a higher packing factor comparing with trigonal arrays. At larger G, however, the adsorbed phase is more liquid-like in square arrays because the adsorption potential is not so strongly enhanced as in trigonal arrays, thus the packing factor is lower. Due to the same cause, the maximum packing factor is shifted to smaller G values.

7.1.4 BET surface areas of square arrays of closed SWCNTs

The variation of BET surface area as a function of configuration for square arrays is shown in Figure 7-7. The variation of BET surface area with tube diameter is similar to that in the case of trigonal arrays (cf. Figure 6-9). The main difference is that the BET surface areas for arrays of small tubes are higher than those for trigonal arrays. For example, trigonal arrays with D = 6 Å and G = 10 Å have BET surface areas ~ 2850 $m^2 g^{-1}$, while surface areas of square arrays with the same D and G are ~ 3050 $m^2 g^{-1}$, an increase of ~ 7%. This is in a good agreement with the higher capacities found for square arrays.

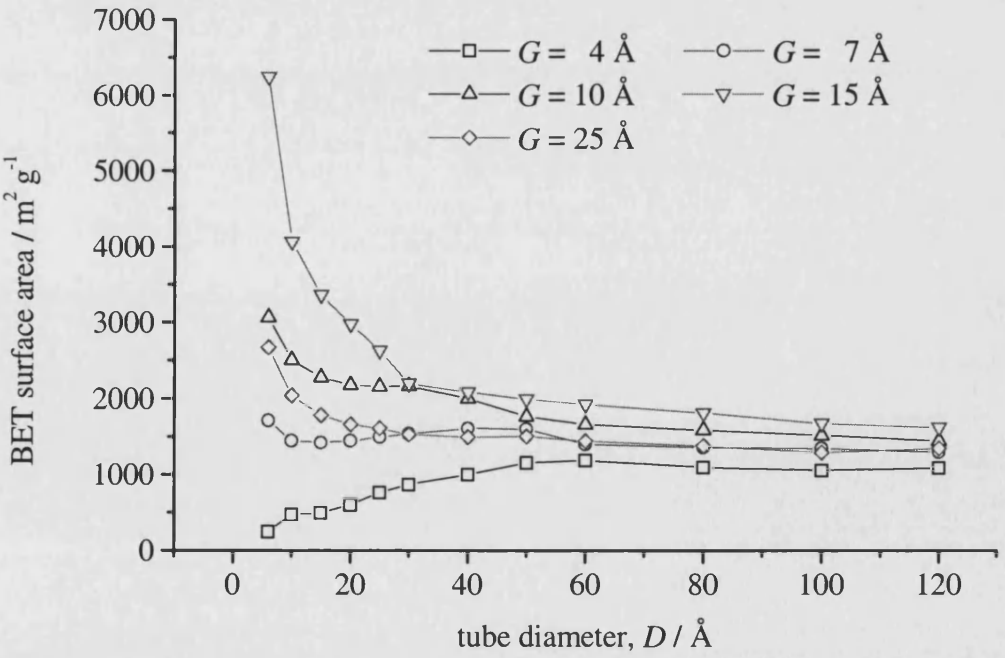

Figure 7-7. BET surface areas for simulated adsorption of nitrogen at 77 K in square arrays of closed SWCNTs as functions of tube diameter, D, and separation, G.

7.2 Adsorption in square arrays of open SWCNTs

7.2.1 Adsorption isotherms

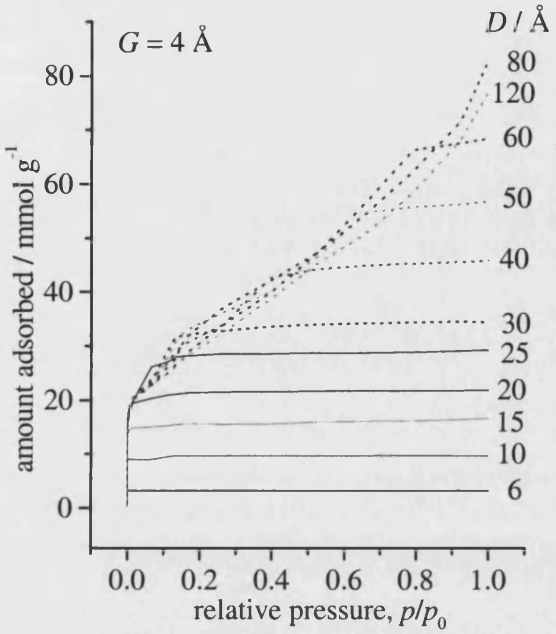

Figure 7-8. Simulated isotherms of nitrogen adsorbed at 77 K in square arrays of open SWCNTs with different tube diameter, *D*, but with the same tube separation, *G*, of 4 Å.

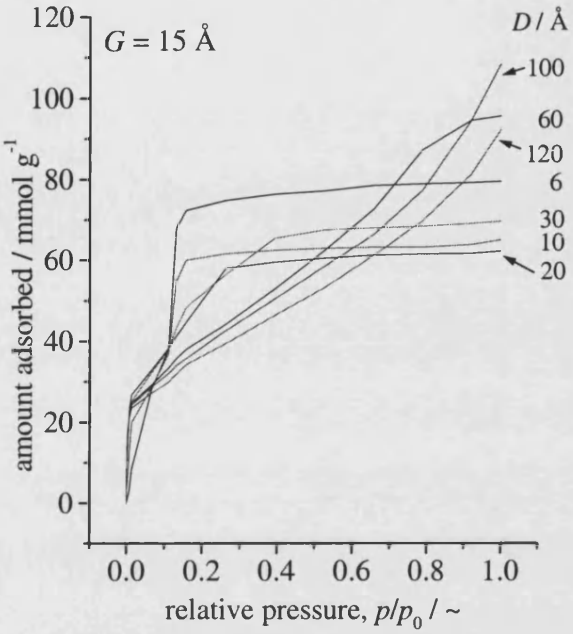

Figure 7-9. Simulated isotherms of nitrogen adsorbed at 77 K in square arrays of open SWCNTs with different tube diameter, *D*, but with the same tube separation, *G*, of 15 Å.

Nitrogen adsorption isotherms of square arrays of open SWCNTs with different tube diameters and three tube separations 4 Å, 15 Å and 25 Å are shown in Figures 7-8 to 7-10 respectively. Comparison with Figures 7-1 to 7-3 shows that most of the isotherms are similar to those of closed SWCNT arrays. Arrays with small *D* and *G* show type I behaviour, while larger tubes show gradual increases in the amount adsorbed with increasing relative pressure (Figure 7-8) as discussed in section 7.1. Type IV isotherms were only found for arrays

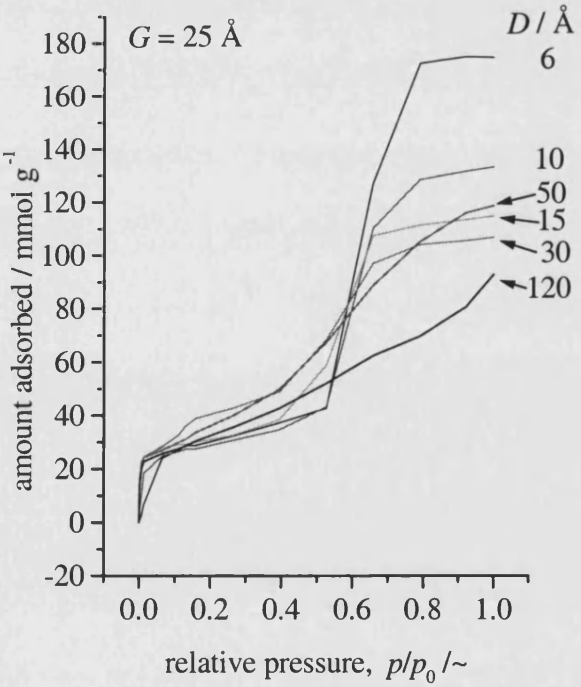

Figure 7-10. Simulated isotherms of nitrogen adsorbed at 77 K in square arrays of open SWCNTs with different tube diameter, *D*, but with the same tube separations, *G*, of 25 Å.

with small D and large G (Figure 7-10). Due to the statistical limitations of the simulation technique employed here (see section 6.2.1), nitrogen does not always condense in very large tubes even at relative pressures ~1. The amount adsorbed increased markedly for arrays with small G when compared with closed tube arrays due to the contribution of endohedral adsorption. The amount adsorbed here is also higher than trigonal arrays of open SWCNTs with small D and G due to more space is available.

7.2.2 Saturation capacities as functions of array configuration

Saturation capacities of nitrogen adsorbed at 77 K in square arrays of open SWCNTs as functions of array configuration are shown in Figure 7-11. Variations of saturation capacities as functions of array configuration are similar to those for closed square arrays and those of trigonal arrays. If adsorption is dominated by geometrical factors, the saturation capacities can be described by the following equation as discussed before:

$$w = Af\left[\frac{D}{\pi}\left(1+\frac{G}{D}\right)^2 - \sigma_{cc}\right] \tag{7-4}$$

where w is the capacity expressed in mmol g^{-1}, f the molecular packing factor defined in Equation (6-2), σ_{cc} the collision diameter of carbon atoms and A = 9.146 mmol g^{-1} $Å^{-1}$ is a constant for nitrogen adsorbed in carbons. The curves in Figure 7-11 are fits of Equation (7-4) to the simulated data in the range of D from 6 Å to 60 Å. This range is chosen because that the capacities of arrays with D larger than 60 Å shown in Figures 7-8 to 7-10 are not saturation capacities due to the reasons mentioned in section 7.2.1. It is clear that the equation fits the data quite well when D < 50 Å with only one fitting parameter. The equation overestimates the capacities of larger tube arrays considerably and the overestimation is more marked in square arrays than in trigonal arrays. This is because the force field in square arrays is weaker than that in trigonal arrays. Therefore, the applicable upper-limit of tube diameter ranges of Equations (7-3) and (7-4) is lower than that of Equations (6-3) and (6-6) (cf. Figures 7-5, 7-11, 6-5 and 6-15).

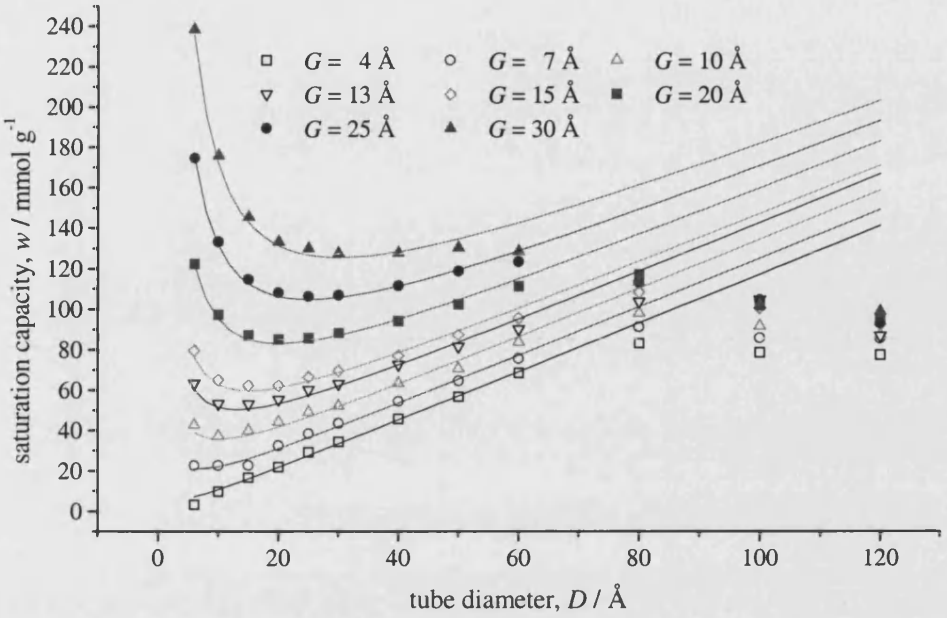

Figure 7-11. Saturation capacities for nitrogen adsorbed at 77 K in square arrays of open SWCNTs as functions of tube diameters, D, and tube separations, G. Lines are fits of Equation (7-4) to the simulation data up to $D = 60$ Å.

7.2.3 Molecular packing factors

The packing factor, f, of nitrogen adsorbed at 77 K in square arrays of open SWCNTs is shown in Figure 7-12, together with the packing factors for square arrays of closed tubes and for trigonal arrays, and for bulk liquid nitrogen. The packing factors for square arrays of open SWCNTs with $G \leq 20$ Å are very close to the packing factor of liquid nitrogen, while the packing factor for arrays with larger G is markedly lower than that of liquid nitrogen.

Comparison of the curves in Figure 7-12 shows: (1) At the smallest tube separations where tubes are closely packed, the packing factors of square arrays are higher than those of trigonal arrays and all packing factors are lower that that of liquid nitrogen. This is because the adsorbed phase is nearly one-dimensional. Thus, the packing factor is mainly determined by the wasted volume fraction and this volume fraction is smaller in square arrays than in trigonal arrays. (2) At large tube separations ($G \geq 15$ Å), packing factors of square arrays are lower than that of trigonal arrays. This is because in square arrays both endohedral and exohedral adsorption potentials are weaker than that

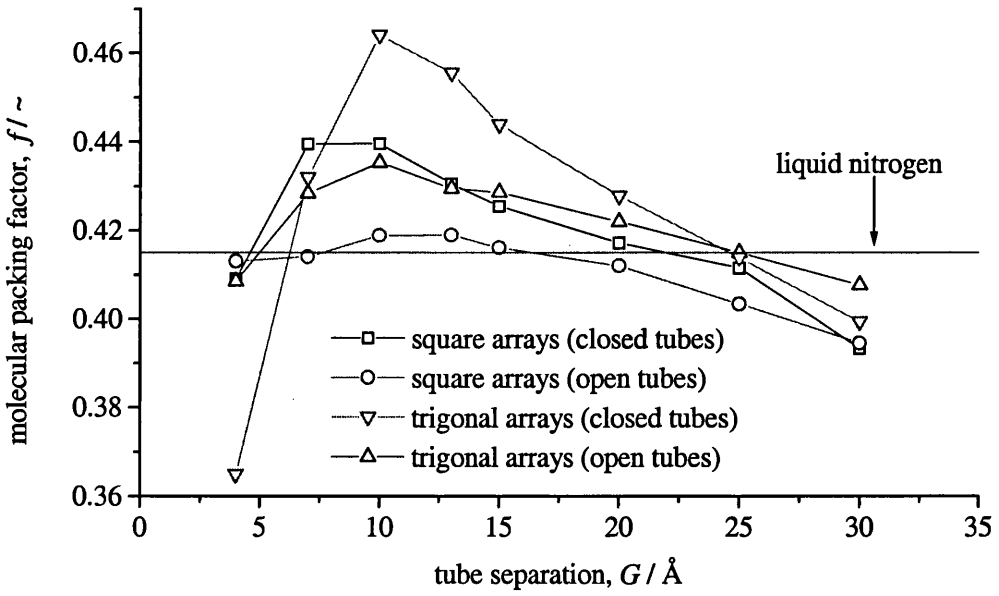

Figure 7-12. Molecular packing factor of nitrogen adsorbed at 77 K in square and trigonal arrays of open and closed SWCNTs as functions of tube separation, *G*. The horizontal line shows the molecular packing factor calculated for bulk liquid nitrogen at 77 K.

in trigonal arrays. Therefore, the adsorbed phase is more liquid-like or less ordered. (3) At intermediate tube separations, the packing factors of different tube arrays are all higher than that of liquid nitrogen and arrays of closed tubes with $G \sim 10$ Å have the highest packing factors. This indicates that exohedrally adsorbed nitrogen is more densely packed than those endohedrally adsorbed and nanotube arrays with intermediate tube separations might have the highest volumetric adsorptive capacities.

7.2.4 BET surface areas

BET surface areas of square arrays of open SWCNTs as functions of array configurations are shown in Figure 7-13. The surface areas are higher than those of closed tube arrays, especially at large tube diameters where endohedral adsorption is more important. As far as the surface areas are concerned, the optimal tube separation is $G = 15$ Å, which is also true for all the arrays studied. The maximum surface area here is about 6540 $m^2 g^{-1}$, which is about 5% higher than that of closed tube arrays and is about 13% higher than that of trigonal open tube arrays. For sufficiently large tube arrays, BET surface areas are nearly independent of D and G and are in the range from 2400 to 3000 $m^2 g^{-1}$, which is in a good agreement with simple geometrical calculations. Local maximums appear at $D \sim 30$ Å, which is a ~10 Å shift to smaller tube diameters when compared with trigonal arrays of open SWCNTs. This is a clear indication of the

weaker interaction within square arrays compared with trigonal arrays with the same configuration parameters.

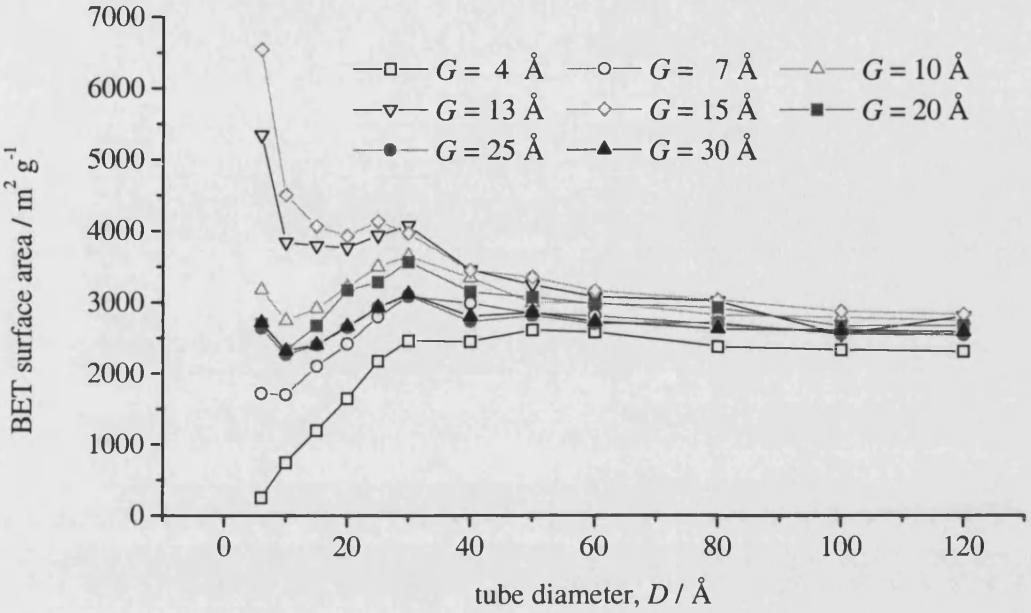

Figure 7-13. BET surface areas for simulated nitrogen adsorption at 77 K in square arrays of open SWCNTs as functions of tube diameter, *D*, and separation, *G*.

7.3 Summary and conclusions

(1) Isotherms of nitrogen adsorbed at 77 K in square arrays of SWCNTs with small tube diameters and separations are of type I, showing microporous behaviour. Isotherms of arrays with large tube diameters show gradual increases in the amount adsorbed after the formation of monolayers with increasing pressure due to large differences in the potentials at different adsorption sites. Adsorption isotherms of arrays with large tube separations are of type IV, showing both monolayer formation and condensation.

(2) Saturation capacities of all types of nanotube arrays can be described accurately by one-parameter equations based on consideration of the volume available to the adsorptive in nanotube arrays when tube diameters is less than 60 Å. This suggests strongly that adsorption in carbon nanotube arrays is dominated by geometrical factors, *i. e.* tube diameters and separations.

(3) At saturation, the packing density of the adsorbed phase is close to that of liquid nitrogen. In arrays with intermediate tube separations, the packing density is higher

than that of liquid nitrogen, while in arrays with either small or large tube separations packing factors are lower than that of liquid nitrogen. This suggests that the introduction of gaps between nanotubes in arrays might increase volumetric capacities; this might be a practical solution to increased capacities. The volume in square arrays with small tube separations is more efficiently filled up than that in trigonal arrays, while for arrays with large tubes the situation is reversed. The maximum packing factor appears at $G \sim 10$ Å, in such cases two layers can be formed between two adjacent nanotubes.

(4) Close packed nanotube arrays with the most commonly observed tube diameters have very low adsorption capacities. Introducing gaps between the tubes forming the arrays can markedly improve the capacities and the highest capacities come from the arrays with the smallest tube but with sufficiently large tube separations. In such arrays, interstitial adsorption is predominant. Capacities of square arrays are higher than that of trigonal arrays, especially in the case of small tube arrays where exohedral adsorption is predominant and square arrays have more interstitial space available.

(5) Very high BET surface areas can be reached with certain nanotube arrays, even higher than most experimentally found values for activated carbons. This suggests that carbon nanotubes might be good adsorbents.

Section 3

Fuel Gas Storage

Chapter 8
Introduction to Fuel Gas Storage

Ever-stricter environmental regulations put great pressure on energy companies and automobile manufacturers to develop cleaner burning fuels and running vehicles. Thus, various environmentally friendly fuels and related technologies are being developed to replace fossil fuels, especially coal, oil and petroleum. For example, numerous studies have been carried out on the use of natural gas and hydrogen as clean energy fuels. Compared with petroleum, natural gas is a much cleaner fuel as shown in Table 8-1 [Ingersoll, 1996]. Except carbon dioxide, all other emissions from the burning of compressed natural gas (CNG) are several times lower than those from the burning of petroleum and are also lower than emission standards in the US. Hydrogen is the only energy carrier that can be used as a fuel without any environmental damage [Rodriguez and Baker, 1997]. It is believed that the generation of electrical and thermal energy from hydrogen using fuel cells and the production of hydrogen by photoelectrolysis of water forms a complete process cycle that can be repeated without limits and produces no ecological harmful side products. Lipman and DeLucchi [1996] recently found that hydrogen engines produce an order of magnitude less hydrocarbons, carbon monoxide, greenhouse gases, and toxic air pollutants than do controlled gasoline engines. In this chapter, a review of concepts and technologies associated with the application of hydrogen and methane as energy fuels, especially by adsorption, is given. This gives perspective to the subsequent chapters which deal with the specific cases of hydrogen and methane storage.

Table 8-1. Full fuel cycle emissions in g/mile for the 1995 Chrysler Mini Van operating on gasoline and compressed natural gas [From Ingersoll, 1996]

	Oxides of Nitrogen	Non-methane Hydrocarbon	Carbon Monoxide	Particulate Matter	Oxides of Sulphur	Carbon Dioxide
CNG*	0.093	0.085	0.420	0.002	0.004	371
Gasoline	0.626	0.698	3.462	0.013	0.044	468
Emission STD**	0.400	0.125	3.400	0.080		

*CNG: Compressed Natural Gas

**Emission STD: The emission standards for passenger cars and light trucks in the United States in 1996.

8.1 Present hydrogen and methane storage systems

8.1.1 Hydrogen storage systems

There are a number of hydrogen storage technologies available at present, including liquid hydrogen systems, compressed hydrogen systems, metal hydride systems and activated carbon adsorption systems [Lipman and DeLucchi, 1996; Hynek *et al.*, 1997]. In the liquid hydrogen systems, hydrogen is condensed to liquid hydrogen to enable a larger amount of hydrogen to be stored. However, converting hydrogen gas to liquid hydrogen is costly and requires a large input of energy. Further, liquid hydrogen must be kept cold (~-252 °C) to prevent it from boiling away even if it is not in use. In the compressed hydrogen systems, very high pressures are required to reach a reasonable capacity. For example, the pressure in a typical vehicular compressed hydrogen system is 200 bar. Thus the compressed hydrogen systems are not only very dangerous, but also bulky, excessively heavy and expensive for average all purpose family vehicles.

Hydrogen molecules can be split to two hydrogen atoms by some metals. Then the metals combine with the atoms, froming stable metal hydrides. The hydrides decompose and release hydrogen when heated. This is the metal hydride storage system. The disadvantages of this kind of system are that they are heavy and relatively high temperature (up to ~ 563 K) is required to release the hydrogen. Physisorption of hydrogen on to activated carbons can approach liquid hydrogen densities and has shown commercial potential. At present, low capacity and the requirement of low temperature (such as 77 K) are the main disadvantages of such systems. Recently, claims have been made that carbon nanotubes and nanofibres can reach high capacities even at room temperature. Thus adsorption of hydrogen on carbon materials has attracted the attention of many scientists and technologists.

The ideal hydrogen storage system needs to be light, compact, relatively inexpensive, safe, easy to use and reusable without the need for regeneration. At present, no such hydrogen storage systems are available [Lipman and DeLucchi, 1996].

8.1.2 Natural gas storage systems

Various approaches can be used to store natural gas, including compression, liquefaction, dissolution, clathration and adsorption [Parkyns and Quinn, 1995; Cook *et al.*, 1999]. Compression is the currently used fuel storage technique for natural gas vehicles. To reach a substantial capacity, very high storage pressures are used and are likely to increase to ~250 bar. Therefore, the tanks are heavy, expensive and unsafe. Conventionally large scale natural gas storage is by liquefaction. In this method, natural gas is cooled to ~-164 °C. Thus, the cost of liquefaction, the special insulating vessels required and the potential fire hazard are such as to make it unsuitable for use on a small scale. Another technique for natural gas storage is the dissolution of natural gas in heavier hydrocarbons, such as ethane and propane. Due to the change of physical properties of the fuel mixture when natural gas is depleted, expensive adjustment in the air-fuel mixing mechanism and the ignition mechanism are required. Clathrates are formed by inclusion of guest molecule in a cavity made by several host molecules. Natural gas hydrates are a kind of clathrate where methane molecules are held in cages of water molecules. This kind of system is either of very low capacity or very high pressure (~240 bar at 25 °C). Another storage method is adsorbed natural gas (ANG). Due to the strong enhancement of adsorption potentials in micropores (pores narrower than 2 nm), the density of the adsorbed phase can be higher than that of liquid natural gas. The main advantage of ANG over CNG is to reduce the storage pressure. This reduces the cost and increases safety. Activated carbons are the most promising ANG material though to date have only been used in a small scale.

8.2 Principles of fuel gas storage by adsorption

As mentioned before, gas storage by adsorption uses the micropores in the adsorbent material to enhance the density of the stored gas. The first thing to consider is whether the introduction of the adsorbent is beneficial when compared with compressed gas. Figure 8-1 schematically shows the amount adsorbed increases with increasing storage pressure, and so does the amount stored by compression. If the storage pressure is higher than p_c, then compression is better than adsorption. However, at lower pressures, adsorption is better than compression and the introduction of adsorbent can markedly improve the capacity. It is in this pressure range that adosrbed gas has its advantage.

The second thing to consider is the capacity. If only the storage capacity is concerned, then the capacity is the amount adsorbed at a certain pressure converted to appropriate units. Figure 8-2 shows four storage capacities V_{S1}, V_{S2}, V_{S3} and V_{S4} at two different pressures, p_S and p_D and two temperatures T_L and T_H. However, in most cases such as vehicular applications, where the gas is adsorbed to storage and then desorbed to use, the most relevant is the delivered capacity. Generally, if the storage capacity at the storage condition is V_S and is V_D at the delivery condition, then the delivered capacity is:

$$V_{DEL} = V_S - V_D \qquad (8\text{-}1)$$

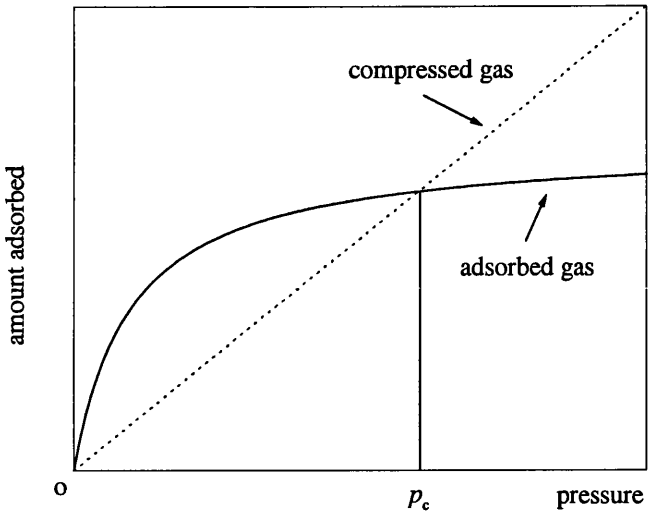

Figure 8-1. Schematic comparison of the amount of compressed and adsorbed gas as functions of the pressure applied.

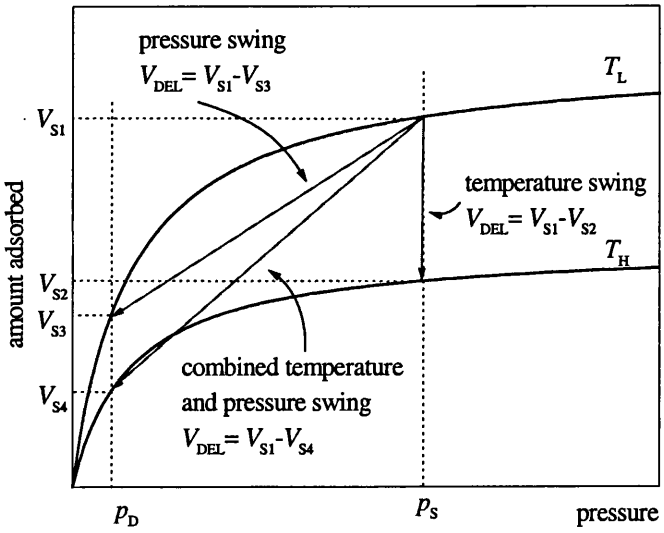

Figure 8-2. Storage and delivered capacities and the concepts of pressure swing desorption, temperature swing desorption and combined temperature and pressure swing desorption.

Suppose that the gas is adsorbed in the adsorbent at temperature T_L and pressure p_S, then there are a few ways to deliver the adsorbed gas. (1) Pressure swing desorption. Here, the system is kept at the temperature T_L, but the pressure is lowered to p_D to allow the delivery of the adsorbed gas. In this case, the delivered capacity will be the storage capacity at p_S minus the storage capacity at p_D, *i. e.* $V_{DEL} = V_{S1} - V_{S3}$. (2) Temperature swing desorption. In this case, the pressure of the system is kept at p_S, but the system is heated to a higher temperature T_H to deliver the adsorbed gas. The delivered capacity now is $V_{DEL} = V_{S1} - V_{S2}$. (3) Combined

temperature and pressure swing desorption. The pressure is lowered to p_D and the system is heated to a higher temperature T_H to deliver the adsorbed gas and the delivered capacity is $V_{DEL} = V_{S1} - V_{S4}$. The combined process gives the highest capacity. However, the pressure swing process is most commonly studied and used, therefore in this section, only this process will be discussed.

8.3 Volumetric and gravimetric capacities

8.3.1 Definition of volumetric and gravimetric capacities

There are two capacities commonly used in dicussions of gas storage. One is the volumetric capacity and the other is the gravimetric capacity. The volumetric capacity is defined as the amount of gas adsorbed either in mass or in volume divided by the total volume occupied by the adsorbent and the adsorbed gas, *i. e.* the volume of the container. Because the gas is adsorbed in the solid, the volume of the adsorbent can be regarded as the total volume, though sometimes the volume occupied by the container may be taken into consideration. For ease of comparison, the volume of the adsorbed gas is commonly converted to the volume at a reference point. Here we take standard temperature and pressure (STP, 1 bar and 0°C) as the reference point, then the volumetric storage capacity is defined as:

$$V = \frac{volume\ of\ adsorbed\ gas\ converted\ to\ STP}{volume\ of\ the\ solid}\ \text{(STP) v/v} \qquad (8\text{-}2)$$

The volumetric capacity is more important in situations where space is limited, such as in a family car. Similarly, the gravimetric capacities are often defined as the weight percentage of the adsorbed gas to the total weight of the system, including the weight of the gas:

$$V = \frac{weight\ of\ adsorbed\ gas}{weight\ of\ the\ solid + weight\ of\ adsorbed\ gas} \times 100\ \text{wt\%} \qquad (8\text{-}3)$$

The gravimetric capacity is more important in cases where weight of the system is the first priority. In some cases both capacities may need to achieve a certain target.

8.3.2 The targets for hydrogen and methane storage

For large scale applications, gas storage needs to reach a reasonable capacity at suitable conditions. The United States Department of Energy (DOE) has set a target for hydrogen storage. The target was based on a family car for a non-refueling distance of 500 km. The targeted volumetric capacity is 62 kg H_2 m^{-3}, that is equivalent to 695 (STP) v/v. The gravimetric target is 6.5 wt% [Dillon *et al.*, 1997].

Compared with the target of hydrogen storage, the natural gas storage target is mainly based on experimental work. The target is 150 v/v in the following conditions: storage pressure 34 bar, delivery pressure 1 bar and at 25 °C [Parkyns and Quinn, 1995; AGLARG, 1994]. This volumetric capacity is equivalent to about 136 (STP) v/v. This target was chosen because that it was thought to be reasonable and reachable from detailed experimental studies of methane storage in activated carbons and theoretical analysis. Although higher capacities have been claimed, this capacity is still difficult to reach by commercially available activated carbons at the stated storage and delivery conditions.

8.3.3 Calculation of capacities from simulation data

In our simulations, the results are presented as the number of molecules adsorbed in the simulation cell, N_{cell}, as functions of storage pressure. Thus it is necessary to convert this to an appropriate, practical unit. However, the conversion is simple. The simulation results can be converted to volumetric capacities according to the following equation:

$$V_p = \frac{N_{cell}}{N_A} \frac{V_{mol,STP}}{V_{cell}} \tag{8-4}$$

where V_p is the storage volumetric capacity at pressure p, N_A = 6.023×10^{23} mol^{-1} is Avogadro's number, and $V_{mol,\,STP}$ = 22.4×10^{-3} m^3 mol^{-1} is the molar volume of a gas at STP. V_{cell} is the volume of the simulation cell, which can be determined from the geometry of the simulation cell and is expressed in m^3. Similarly, gravimetric capacities for arrays of SWCNTs can be obtained from the equation below:

$$V_p = \frac{N_{cell} m_v}{N_{cell} m_v + 12\pi DL\rho_a} \times 100 \quad (8\text{-}5)$$

where V_p is the storage gravimetric capacity, m_v is the molar mass of the gas, D is the diameter of the tube, L the length of the simulation cell and ρ_a = 0.3818 Å^{-2} is the number of carbon atoms per unit area in the graphene sheet.

8.4 Review of hydrogen and methane storage using carbons

8.4.1 Experimental studies

8.4.1.1 Methane storage

The adsorption of methane by activated carbons has been studied for some time [Ray and Box, 1950; Peterson *et al.*, 1966]. In their pioneering work, Peterson *et al.* [1966] reported a storage gravimetric capacity of 0.12 g/g (gram of methane adsorbed per gram of activated carbons) at 3.5 MPa and room temperature. Assuming the packing density of the activated carbon is ~ 0.5 g cm^{-3}, this gravimetric capacity is equivalent to a volumetric capacity of 84 (STP) v/v. This work was followed by a number of other research groups to look for a better activated carbon. Some illustrative examples of capacities of a variety of carbons for storage of methane are shown in Table 8-2. Because about 15%-30% of the stored methane will be retained, the delivered capacities are much lower than the stored capacities. Thus, few of the carbons listed in Table 8-2 meet the targeted value. Parkyns and Quinn [1995] and Cook *et al.* [1999] recently reviewed natural gas storage on various commercially available activated carbons. Parkyns and Quinn [1995] studied several activated carbons, derived from a variety of carbon precursors with BET surface areas from 81 m^2 g^{-1} to 3410 m^2 g^{-1} and Dubinin-Radushkevitch micropore volumes from 0.20 cm^3 g^{-1} to 1.42 cm^3 g^{-1}. They found that methane storage capacities of activated carbons, V_S, expressed in g/g are linearly correlated with both BET surface areas, S_{BET} in m^2 g^{-1} and micropore volumes, V_μ in cm^3 g^{-1}:

$$V_S = 0.000049 S_{BET} + 0.025 \quad (8\text{-}6)$$

$$V_S = 0.12 V_\mu + 0.021 \quad (8\text{-}7)$$

These equations provide tools for evaluating methane capacities of activated carbons from conventional nitrogen adsorption measurements. In addition, Equation (8-7) indicates that one way to improve methane capacity is to increase the microporosity. Parkyns and Quinn [1995] also showed that the methane storage capacity, V_S, expressed in v/v is related to fractional microporosity, P (=volume of micropores over total volume of the material) and packing density, ρ of the carbon:

$$V_S = 237P + 9.2\rho \tag{8-8}$$

Interestingly, this equation shows that one must increase both microporosity and packing density of the carbon to obtain high methane storage capacity. This means that meso- and macroporosity should be minimised. Several attempts to increase packing density and the consequent improvement in volumetric methane capacities have been reported [Bose *et al.*, 1991]. To date, activated carbons have yielded the best performance when comparing with other candidates, such as zeolites and silica, and the target can be achieved by using activated carbons whose micropore volume and pore sizes are carefully controlled.

Adsorption of methane on to carbon nanotubes was first reported by Mackie *et al.* [1997]. They studied two sets of catalytic carbon tubes, one with diameters of ~ 1 μm and the other 10~100 nm. Their adsorption experiments were carried out at temperatures ranging from 77 K to 92.5 K. Therefore it is not particularly helpful to the study of storage of methane in carbon nanotubes. However, from their results of surface areas, which are 17.3 $m^2\ g^{-1}$ and 23 $m^2\ g^{-1}$ for closed and open tubes respectively, the storage methane capacity is very low. No other studies have been published.

8.4.1.2 Hydrogen storage

Several experimental studies have been conducted on hydrogen storage in carbon materials. Some of the recent results are shown in Table 8-3. In 1980, Carpetis and Peschka [1980] studied the storage capacities of a range of adsorbent materials, most of them activated carbons. They found that hydrogen capacities of most activated carbons were higher than other materials studied. The maximum measured gravimetric capacity of an activated carbon called F12/350 was ~ 7.6 wt% at 65 K and 42 bar. Noh *et al.*

[1987] reported the storage capacity of a so-called superactive carbon as 4.7 wt% and ~ 250 (STP) v/v at 77 K and 60 bar. Later the same group reported a storage capacity of 5.13 wt% and 192 (STP) v/v of an AX-31M carbon at 150 K and 54 bar [Amankwah *et al.*, 1989]. These studies show that it is still difficult to achieve the DOE target for activated carbons even at refrigeration temperatures and moderate pressures. At ambient temperature, hydrogen storage capacities of activated carbons are far lower than the DOE target [Chahine and Bose, 1994].

Recently, there has been a resurgence of interest in the potential of carbon materials as hydrogen storage media following claims that single wall carbon nanotubes, SWCNTs [Dillon *et al.*, 1997], and certain types of vapour grown carbon fibres [Chambers *et al.*, 1998] may have high hydrogen storage capacities at room temperature. Dillon *et al.* [1997] postulated that single wall carbon nanotubes with diameters of 20 Å bounded together in a triangle or close-packed manner will give a gravimetric capacity of about 4 wt% and a volumetric capacity of 560 (STP) v/v at 0.4 bar and 133 K by temperature programmed desorption, much better than activated carbons. They also calculated that for an individual nanotube, the gravimetric capacity can be as high as 5~10 wt%. A similar capacity of 4.5 wt% of relatively larger nanotubes at storage pressures ~100 bar and temperature 298 K has been reported recently [Liu *et al.*, 1999]. Chen *et al.* [1999] have reported gravimetric hydrogen capacities of 14 wt% and 20 wt% at 473 ~ 673 K and 1 bar for K-doped and Li-doped multi-walled carbon nanotubes respectively. Ye *et al.* [1999] also studied adsorption of hydrogen in ropes of SWCNTs and found capacities approach 8.25 wt% at 80 K and 120 bar. They also found that hydrogen was first adsorbed on the outer surface of the crystalline ropes. At pressures higher than about 40 bar at 80 K, a phase transition occurred where there was a separation of the individual SWCNTs and hydrogen was physisorbed on their exposed surfaces.

It is worth mentioning that significant hydrogen uptake by carbon nanotubes is eclipsed by the astonishingly high uptakes of hydrogen claimed for vapour grown graphite nanofibres, GNF [Chambers *et al.*, 1998; Park *et al.*, 1999]. The highest claimed

Table 8-2 Methane capacities of some adsorbent carbons

Carbon	Form	Gravimetric capacity (mg/g)	Volumetric capacity (V/V)	Storage Pressure (MPa)	Storage temperature (K)	Reference
AK-AX	pellets	180 stored		3.5	293	Chaudron, 1989
Wood based AC+KOH	granular		150 delivered	3.4	298	Baker, 1995
AX-21+PVDC	monolith		163 stored	3.4	298	Quinn and MacDonald, 1992
AX-21+PVA	monolith	148 stored	186 stored	3.5	298	Bose *et al.*, 1991
Mesocarbon+KOH	monolith		163 stored	3.4	298	Chen *et al.*, 1997
Maxsorb	monolith	180 stored	155 stored	3.4	298	Manzi *et al.*, 1997
Anthracite+KOH	granular	164 stored	157 delivered	4.0	298	Lozano-Castelló *et al.*, 1999

Table 8-3 Gravimetric storage capacities for hydrogen on some adsorbent carbons

Carbon*	Gravimetric capacity (wt%)	Storage pressure (bar)	Storage temperature (K)	Reference
Activated carbon	0.6	60	298	Chahine and Bose, 1994
Activated carbon	4.7	60	77	Noh *et al.*, 1987
SWCNT	5~10	0.4	273~133	Dillon *et al.*, 1997
SWCNT	4.5	~100	~298	Liu *et al.*, 1999
MWCNT	0.5	100	298	Klyamkin *et al.*, 1999
GNF tubular	11.3	120	298	Chambers *et al.*, 1998
GNF herringbone	57.9~67.5	120	298	Chambers *et al.*, 1998
GNF herringbone	0.3	100	298	Ahn *et al.*, 1998
GNF tubular	10~13	80~110	298	Fan *et al.*, 1999

*SWCNT, single walled carbon nanotube; MWCNT, multi-walled carbon nanotube; GNF, graphite nanofibre

hydrogen gravimetric capacity is more than 10 times the DOE target (Table 8-3). Several attempts have been made to duplicate this work. Although some of these reported significant hydrogen uptakes about 10~13 wt% [Fan *et al.*, 1999], others have reported very low uptakes of less than 1 wt% [Ahn *et al.*, 1998; Mellor *et al.*, 1999].

8.4.2 Theoretical and molecular simulation studies

8.4.2.1 Methane storage

Molecular simulations of methane adsorption in model pores [Aukett *et al.*, 1992; Cracknell and Gubbins, 1992] can provide insights into the effects of micropore structure on the adsorbed methane density. This kind of study can be used to predict the optimal structure of the carbon and the resultant storage and delivered methane capacities. Thus it is useful to guide the design of the carbon for methane storage. Tan and Gubbins [1990] studied the effects of pore size and temperature on methane adsorption isotherms in model slit pores. They found that the maximum adsorption occurs at a slit width of 11.2 Å. This corresponds to two layers of methane molecules being accommodated in the pore. Matranga *et al.* [1992a; 1992b] also found the optimal pore size is 11.4 Å using Monte Carlo molecular simulations, in good agreement with the results of Tan and Gubbins [1990]. They also found that the maximum delivered capacity is 220 v/v for monolithic carbon and 153 v/v for pelletised carbon with storage pressure of 35 bar and temperature of 300 K. More recently, Chen *et al.* [1997] conducted Monte Carlo molecular simulations of methane adsorption in model slit-shaped carbon pores and applied the simulation results to models of void-free microporous carbon monoliths and to model monoliths formed from activated carbon powder (hexagonal close-packed spherical particles (HCPS) model) and fibres (close packed parallel cylinder (CPPC) model). The maximum delivered volumetric capacities for void free model, the CPPC and the HCPS model are 198 v/v, 182 v/v and 153 v/v, respectively.

In contrast to methane storage in activated carbons, no simulations have been reported on methane storage in carbon nanotubes.

8.4.2.2 Hydrogen storage

Pederson and Broughton [1992] reported their theoretical calculations that suggested that adsorption forces for polarizable molecules within SWCNTs would be stronger

than that for adsorption on ordinary graphite. Thus, high hydrogen storage capacities could be achieved at relatively high temperatures and low pressures as compared to adsorption on activated carbons. This motivated the continuous study of hydrogen storage in SWCNTs by Dillon' s group since 1993 [Dillon *et al.*, 1999]. Recently, Stan and Cole [1998] performed some theoretical calculations of hydrogen adsorbed in carbon nanotubes. They found that nanotubes are a good adsorbent for hydrogen and quantum effects are not important when temperatures are higher than ~ 50 K. Darkrim and Levesque [1998] performed Monte Carlo molecular simulations of hydrogen adsorption in square arrays of SWCNTs with diameters from 7.04 to 19.57 Å at 293 K and up to 100 bar. For the 11.74 Å tube array, three tube separations, 3.334 Å, 5 Å and 7 Å, were studied. They also concluded that SWCNTs are good adsorbents for hydrogen storage and quantum effects are not important at all but very low temperatures. The capacities of hydrogen storage they found are from 100 (STP) v/v to 118 (STP) v/v at storage conditions: p_s = 100 bar and T_s = 293 K. Wang and Johnson [1999a] and Rzepka *et al.* [1998] performed molecular simulations on hydrogen storage in both activated carbons and carbon nanotubes. They found that the hydrogen storage capacities of both systems are low and only at very low pressures that carbon nanotubes adsorbs more hydrogen than activated carbons. Thus, Wang and Johnson [1999a] studied hydrogen adsorption in a 12.2 Å and a 24.4 Å carbon nanotube arrays and concluded that at ambient temperature an array of nanotubes is not suitable sorbent material for achieving DOE targets for vehicular hydrogen storage. They also found that quantum effects might be important in small interstice at 77 K. However, in a more recent study, Wang and Johnson [1999b] used classical Monte Carlo simulations to study hydrogen storage in carbon nanotube arrays. They studied three single wall tubes with diameters of 12.2 Å, 16.3 Å and 24.4 Å and tube separations from 3.2 Å to 12 Å. They found that the gravimetric storage capacities of hydrogen are less than 1 wt% at ambient temperature and less than 10 wt% at 77 K and 100 bar. The optimal array configurations for volumetric hydrogen capacities are D = 12.2 Å with tube separations G = 6 Å at 298 K and G = 9 Å at 77 K. The corresponding maximum volumetric capacities are ~ 64 (STP) v/v and 620 (STP) v/v, respectively. They concluded that carbon nanotubes do not appear to be useful adsorbents for vehicular hydrogen storage applications. Similar results were found by Gordon and Saeger [1999] by using density functional theory simulations. More recently, Simonyan *et al.* [1999] conducted molecular simulations of hydrogen adsorption in charged SWCNTs. They found that

negatively charged nanotubes with average charge of 0.1e per carbon atom will yield ~10% - ~20% higher capacities at 298 K and ~15 % - ~30% higher capacities at 77 K as compared with uncharged nanotubes. They also concluded that even charged nanotubes are not suitable sorbents for achieving the DOE target for hydrogen transportation and storage at normal temperatures. Wang and Johnson [1999c] also studied hydrogen storage in graphite nanofibres using GCEMC molecular simulations. They found that the simulated capacity is 100 times less than the capacity claimed by Chambers *et al.* [1998].

It is interesting to note that unlike in the situations of methane storage in carbon materials, simulation results to date are unable to explain the high hydrogen uptake reported experimentally. This suggests that much more work is needed to explore the fundamentals and mechanism of hydrogen adsorption in carbon nanotubes.

This study provides the first systematic study of methane and hydrogen storage in arrays of SWCNTS with tube diameters varying from 6 to 120 Å and tube separations range from 4 to 30 Å. Quantum effects were not taken into consideration (1) because the effects are of second order for temperatures greater than 50 K; (2) to save computation time. Attempts were made to correlate the simulated capacities with nanotube arrays configurational parameters, to provide possible means for the prediction of methane and hydrogen capacities of arrays of SWCNTs from some conventional parameters, such as the BET surface area and pore volume.

Chapter 9
Hydrogen Storage

Chapter 8 provides a general introduction of fuel gas storage, especially hydrogen and methane storage. This chapter presents the molecular simulations results of hydrogen storage in activated carbons and arrays of single-walled carbon nanotubes. Methane storage will be discussed in the next chapter.

9.1 Hydrogen storage at ambient temperature

9.1.1 Hydrogen capacity as a function of storage pressure

Figures 9-1 and 9-2 show the delivered volumetric and gravimetric hydrogen capacity at 298 K of several trigonal arrays of open SWCNTs with varying tube diameters and separations as a function of storage pressure. Except in the case of the smallest tube diameter with 3.2 Å separation, all delivered capacities increase with storage pressure. Generally, the capacities increase with either increasing tube separations at constant tube diameters or increasing tube diameters at constant tube separations. However, as far as the volumetric capacity is concerned, the differences between capacities of different arrays are not marked. Figure 9-1 also shows that the array with tubes of

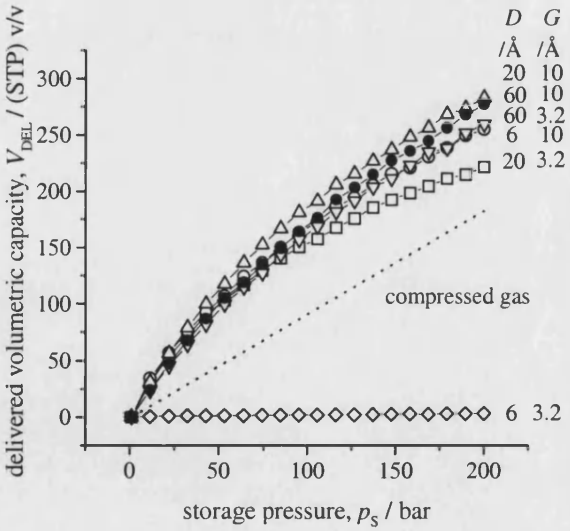

Figure 9-1. Simulated delivered hydrogen volumetric capacity at 298K of trigonal arrays of open SWCNTs as a function of storage pressure and tube diameter, D and separation, G. Also shown is delivered capacity of compressed hydrogen at 298 K. The delivery pressure is 1 bar.

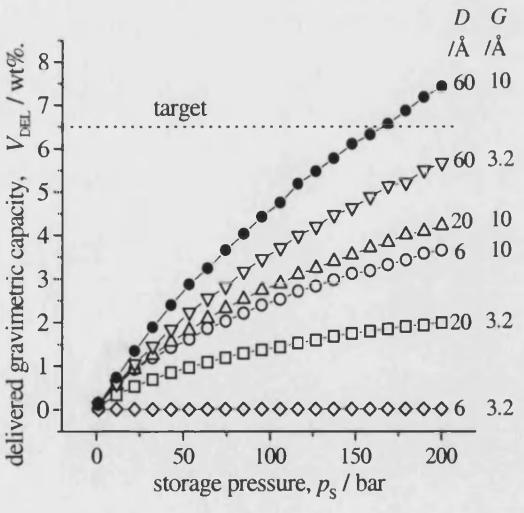

Figure 9-2. Simulated delivered hydrogen gravimetric capacity at 298 K of trigonal arrays of open SWCNTs as a function of storage pressure and tube diameter, D and separation, G. Also shown is the DOE gravimetric target of 6.5 wt%. The delivery pressure is 1 bar.

diameter 20 Å and separation 10 Å results in the highest volumetric capacity at all storage pressures. However, even at storage pressure of 200 bar, the maximum capacity is less than half of the target value. Also, the enhancement of adsorbed hydrogen over compressed gas is not marked. From this point of view, SWCNT arrays do not appear to be effective hydrogen storage media at ambient temperatures.

Similar situations can be found in the case of gravimetric capacities. However, the increases of hydrogen capacity with either increasing storage pressure or increasing tube diameter or separation are more marked. Also, the highest capacity here results from the array with tube diameter of 60 Å and separation of 10 Å and the maximum capacity is greater than the target. The reason is that in the case of volumetric capacities, increases of tube diameter or separation will result in rapid increases of the volume of the simulation cell (~ $(D+G)^2$), while in the case of gravimetric capacities, the weight of the simulation cell increases slowly with increasing D (~D) and is independent of G. Therefore, the volumetric target of 695 (STP) v/v is a stricter requirement than the gravimetric target.

9.1.2 Hydrogen capacity as a function of tube diameter

Figures 9-3 and 9-4 show the delivered hydrogen capacity as a function of tube diameter for three tube separations and two storage pressures, 70 bar and 200 bar. It is clear that the volumetric capacities increase with increasing tube diameter at small D values and then decrease. Therefore, there is an optimal diameter for each separation and pressure. Generally, the smaller the tube separation and the higher the pressure, the larger the optimal tube diameter. It is interesting to note that for larger tube diameters, the delivered capacities seem to be independent of both tube diameter and separation.

The gravimetric capacities increase with increasing tube diameter progressively, except in the case of arrays with tube separations of 20 Å, where a decrease in hydrogen capacity can be found at small tube diameters. At large D and small G values, the volume of the simulation cell is proportional to D^2 while the weight of nanotubes contained in the cell is proportional to D. Thus, the volume of the space accessible to hydrogen molecules per unit mass is proportional to D. Consequently, if the number or weight of hydrogen molecules adsorbed is mainly determined by the volume available,

the gravimetric capacity will increases linearly with increasing tube diameter. Figure 9-4 confirms this expectation.

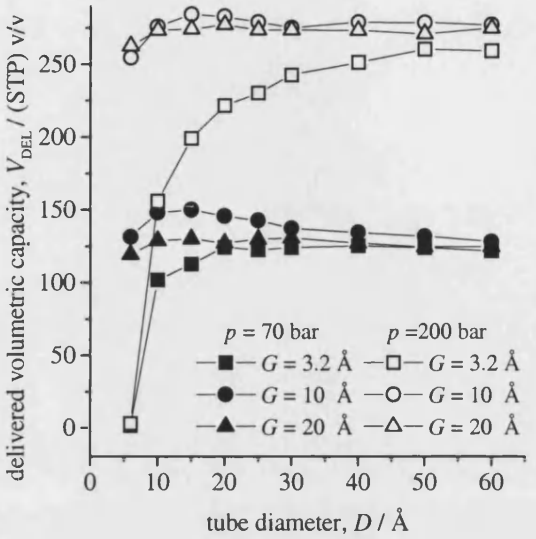

Figure 9-3. Simulated delivered hydrogen volumetric capacity at 298 K of trigonal arrays of open SWCNTs as a function of tube diameter, D, with three different separations, G, at two storage pressures, 70 bar and 200 bar. The delivery pressure is 1 bar.

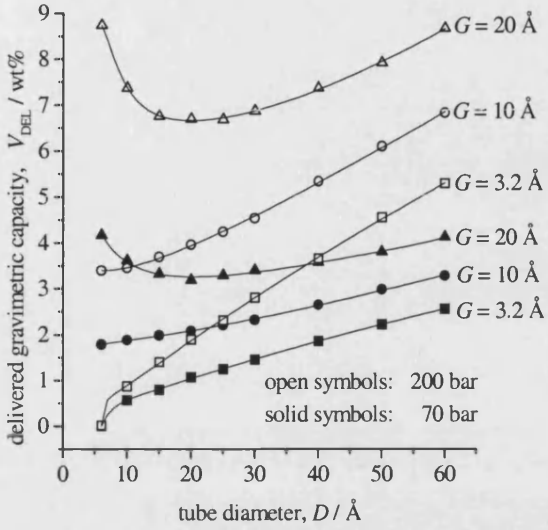

Figure 9-4. Simulated delivered hydrogen gravimetric capacity at 298 K of trigonal arrays of open SWCNTs as a function of tube diameter, D, with three different separations, G, at two storage pressures, 70 bar and 200 bar. The delivery pressure is 1 bar.

Another feature in Figure 9-4 is that the gravimetric capacities of arrays with a tube separation of 20 Å and storage pressure of 200 bar are all greater than the target value. This means that if separations can be introduced into tube arrays and can be controlled, the gravimetric target can be met at ambient temperatures. However, as shown in Figure 9-3, the volumetric capacities of such arrays are also around 270 (STP) v/v, less than 40% of the target. This once again indicates that the volumetric target is more difficult to reach. Therefore, discussions are mainly focused on volumetric capacities in the following sections.

9.1.3 Comparison with activated carbons

Figure 9-5 shows the storage hydrogen capacity in single wall carbon slit pores as a function of storage pressure for different slit widths. It is clear that these isotherms are in a good agreement with Henry's Law. The enhancement of the adsorbed phase over compressed hydrogen is not significant due to the high temperature. It is interesting that the smallest pore studied here, namely H = 6 Å, gave a volumetric capacity not far from the optimal structure, while carbon nanotube arrays with such a diameter and 3.2 Å tube

separation gave nearly zero capacity (see Figure 9-1). This means that hydrogen molecules can get into slits with width of 6 Å, but cannot get into nanotubes with the same pore size. The reason is that in such small pores, the interactions between the fluid molecules and pore walls are repulsive and they are more strongly enhanced in nanotubes than in slits. Thus these small nanotubes are more difficult for fluid molecules to be adsorbed in compared to slits.

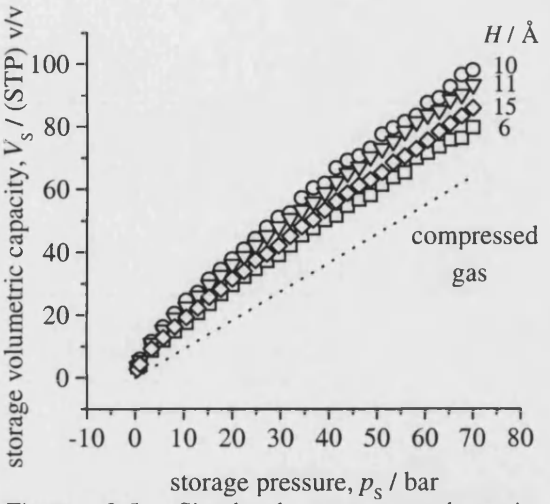

Figure 9-5. Simulated storage volumetric hydrogen capacity of single-walled slit pore carbons at 298 K as a function of storage pressure for a range of pore widths, H. Also shown is the capacity of compressed hydrogen gas at 298 K.

The capacities as functions of slit width in the micropore region are shown in Figure 9-6. It is believed that increasing slit width to mesopore region will decrease the capacity. As can be seen from Figure 9-6, the delivered capacity increases with increasing pore width at first, then reaches a maximum and finally decreases with increasing pore width. The maximum enhancement over compressed hydrogen is about twice and in other cases the enhancement is rather small.

The optimal pore width as shown in Figure 9-6 is 6.7 Å, a little larger than $\sigma_{cc} + \sigma_{ff}$ = 6.36 Å. Wang and Johnson [1999a] studied hydrogen storage in slits of width $2\sigma_{ff}$, $3\sigma_{ff}$, $4\sigma_{ff}$ and $6.67\sigma_{ff}$ and found that pores with a width of $3\sigma_{ff}$ gave the highest volumetric capacity. Carbon slit

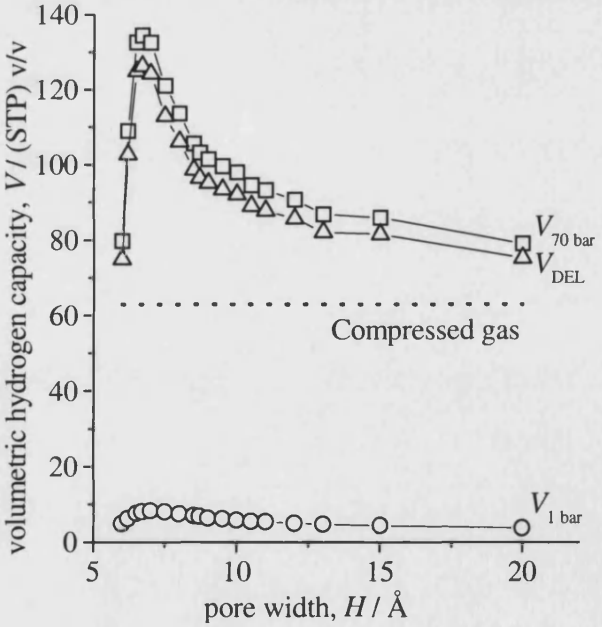

Figure 9-6. Simulated storage volumetric hydrogen capacities at 70 bar, 1 bar and delivered hydrogen capacity as a function of single-walled slit width, H, at 298 K. Also shown is the capacity of compressed hydrogen gas, ~63 (STP) v/v.

pores with a width of $3\sigma_{ff}$ had been found to give the highest methane capacity at ambient temperature, where two layers of methane can be formed between the pore walls [Tan and Gubbins, 1992; Matranga *et al.*, 1992a, 1992b]. However, this is not the case in the situation of hydrogen adsorption. At ambient temperature, even at 70 bar, no single layers of hydrogen molecules can be formed between two pore walls. For example, typically about 20-30 hydrogen molecules were found in the simulation cell of dimension $10\sigma_{ff}\times10\sigma_{ff}$ with pore width in the range from 6 to 20 Å, while a complete single layer can hold up to 100 molecules. This is due to weaker adsorption potential in the hydrogen-carbon system compared to methane-carbon and the critical temperature of hydrogen is much lower than methane. Thus the optimal pore width shifts to a lower value where the enhancement of adsorption potential is stronger. Wang and Johnson's results [1999a] did not give the optimal pore width due to the lack of results of hydrogen adsorption in pores with widths between $2\sigma_{ff}$ and $3\sigma_{ff}$, thus these authors missed the whole peak in Figure 9-6.

As far as the maximum capacity is concerned, single-walled carbon nanotube arrays are not much better than single-walled carbon slits with respect to hydrogen storage at ambient temperature (see Figures 9-1 and 9-6). However, the capacity decreases sharply when slit pore widths depart from the optimal value. This means that in practice, to achieve a capacity close to the optimal value, the pore width in activated carbons has to be controlled within a few Ås. In the case of nanotubes, except the smallest tubes, all arrays give similar capacities. This may indicate that some values of capacities are more achievable with carbon nanotube arrays.

As hydrogen storage capacities at ambient temperature are far from satisfactory, we have concentrated on hydrogen capacities at 77 K. Results from this work are reported in the following sections.

9.2 Hydrogen storage in trigonal arrays of closed SWCNTs at 77 K

9.2.1 Storage hydrogen capacity as a function of D and G

Hydrogen storage volumetric capacity of trigonal arrays of closed SWCNTs at 77 K as a function of tube diameter and separation is shown in Figure 9-7. As can be seen from Figure 9-7, the storage hydrogen volumetric capacity decreases sharply with increasing tube diameter for a certain tube separation, except at very small tube separations. This is

so because increasing tube diameter increases the volume of the simulation cell, though the interstitial space available to the adsorptive also increases, but only by a small fraction. Thus increasing tube diameter at fixed tube separation effectively decreases the open pore volume fraction. This results in a decrease in volumetric storage capacity. On the other hand, in most cases, the volumetric storage capacity increases with increasing tube separation at fixed tube diameter, except with very small tube diameters. In arrays of small tubes, if the tube separations are too large, the adsorption potential will be very weak; this reduces the packing density of adsorbed molecules considerably. Hence the storage capacity decreases. The optimal configuration for maximum storage volumetric capacity is D = 6 Å and G = 13 Å with the maximum capacity of 785 (STP) v/v. This value of capacity is more than 10% higher than the DOE target. However, as can be seen from Figure 9-7, only very limited array configurations close to the optimal configuration can yield volumetric capacities greater than the DOE target. Thus this implies that it may be very difficult to use closed trigonal SWCNT arrays to achieve the DOE target for hydrogen storage even at 77 K.

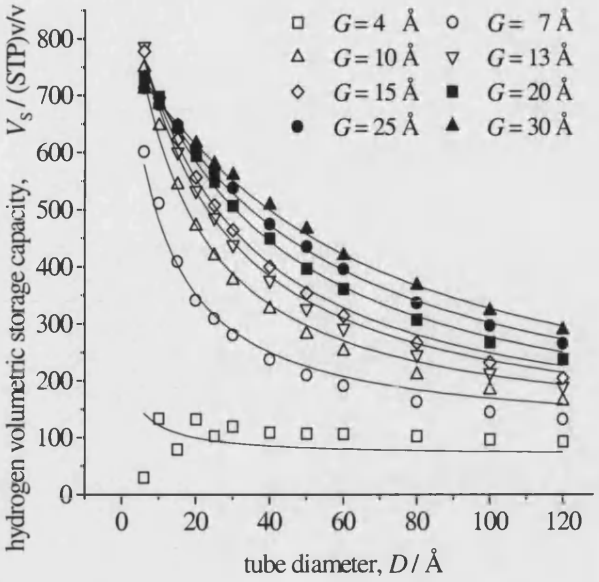

Figure 9-7. Simulated volumetric storage hydrogen capacity at 77 K and 70 bar as a function of tube diameter, D, and separation, G, for trigonal arrays of closed SWCNTs. Curves are fits of Equation (9-2) to the simulations data.

For the smallest tube separations shown in Figure 9-7, the storage volumetric capacity fluctuates with increasing tube diameters. For very small tube arrays, the interstitial space is so small that only very few molecules may be forced into the space by high external pressure. Thus the storage capacity is very low. When the tube diameter increases to around 10 Å, as shown in Figure 9-8(a), the interstitial space is wide enough to hold two columns of hydrogen molecules, one column in each trigonal section. In this case, the adsorption potential in the interstitial space is strongly enhanced. Thus these columns of molecules are closely packed and the storage capacity reaches a local maximum. Further increases of tube diameters do not increase the

number of adsorbed molecules much because the space can still only hold one column of molecules, though the molecules may be packed in a zigzag way in the column (similar to the situation shown in Figure 6-4b). On the other hand, the volume of the cell will increase as ~ $(D+G)^2$, leading to a sharp decrease in storage volumetric capacity. When the tube diameter increases to around 20 Å, the interstitial space can hold three

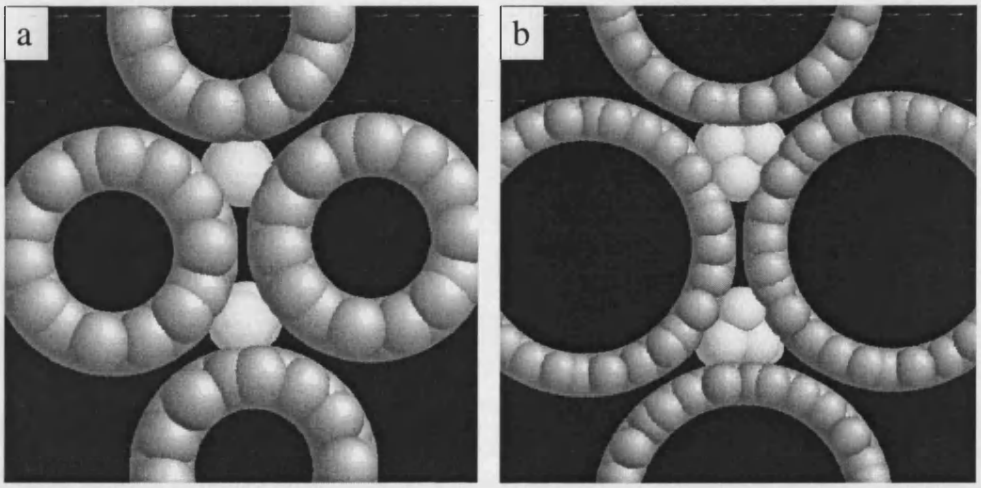

Figure 9-8. Snapshots of hydrogen molecules adsorbed at 77 K and 70 bar in the interstitial space of trigonal arrays of closed SWCNTs with tube separation G = 4 Å. The white spheres are adsorbed hydrogen molecules and the grey ones are carbon atoms. (a) Tube diameter D = 10 Å, the interstitial space is just wide enough to hold two columns of hydrogen molecules; (b) Tube diameter D = 20 Å, six columns of hydrogen molecules can be adsorbed in the interstitial space.

columns of hydrogen molecules in each trigonal section and six columns in the cell, as shown in Figure 9-8(b). Thus the storage volumetric capacity reaches another local maximum. This situation will continue to larger tube diameters, but the effects become smaller and smaller and finally smooth out. As most single-walled carbon nanotubes found experimentally have diameters less than 20 Å, this packing effect will be significant in experimental observations.

The gravimetric storage capacity for hydrogen in trigonal arrays of closed SWCNTs as a function of tube diameter and separation are shown in Figure 9-9. Similar variations in capacity with increasing tube diameter and separation are easily seen. But there are a few differences between Figures 9-7 and 9-9. Firstly, the gravimetric storage capacity increases progressively with increasing tube separation within the range studied. Thus no optimal configurations for gravimetric capacity were found. This is because increasing tube separation does not increase the weight of the solid in the cell, but

increases the volume of available space. Secondly, the largest value of gravimetric capacity shown in Figure 9-9 is about 5 times of the DOE target of 6.5 wt%. And when tube separations exceed 10 Å, all the gravimetric capacities are greater than the target. This once again shows that the gravimetric target may be easier to achieve than the volumetric one. Finally, in the case of volumetric capacities, the capacity decreases with increasing tube diameter markedly even at fairly large tube diameters. Here, when tube diameters exceed about 30 Å, there will be little change in gravimetric storage capacity upon further increase of tube diameter.

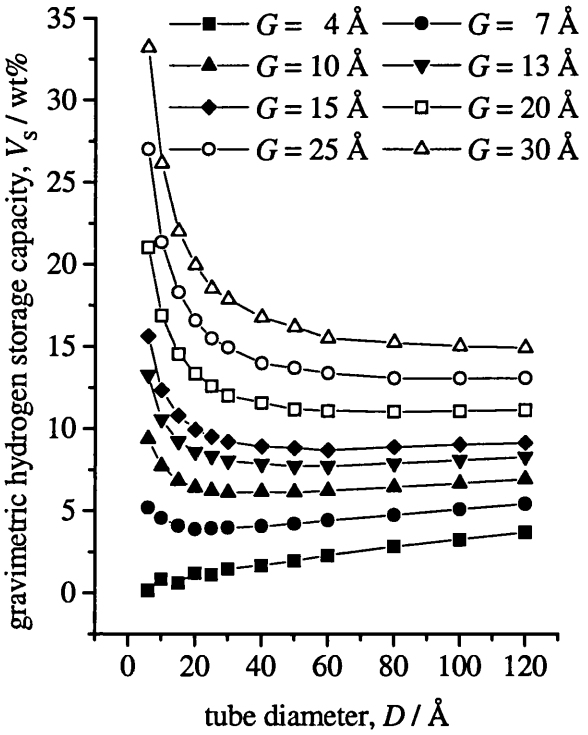

Figure 9-9. Simulated gravimetric storage capacity of hydrogen in trigonal arrays of closed SWCNTs at 77 K and 70 bar as a function of tube diameter, D, and separation, G.

9.2.2 Packing of hydrogen molecules in the interstitial space

The adsorption capacity of a porous system is mainly determined by the pore volume available to the adsorptive and the adsorption potential inside this volume. In the case of carbon nanotube arrays, these are functions of both D and G. Using simple geometrical calculations, it can be shown that the volume available to adsorbates in unit volume of trigonal nanotube arrays is:

$$V_{av} = 1 - \frac{\pi\left(D+\sigma_{cc}\right)^2}{2\sqrt{3}(D+G)^2} \tag{9-1}$$

Where σ_{cc} is the LJ distance parameter of carbon atoms. If the geometrical aspects are predominant, then storage capacities may be proportional to the volume available, that is,

$$V_S = Cf\ V_{av} = C f \left[1 - \frac{\pi (D+\sigma_{cc})^2}{2\sqrt{3}(D+G)^2} \right] \quad (9\text{-}2)$$

Where C is a conversion factor to volume at standard temperature and pressure and f is the packing factor that describes the proportion of the available volume occupied by adsorbate. f can be a function of G. C = 2739 (STP) v/v in the case of hydrogen storage. Equation (9-2) can be used to estimate the highest storage capacity possible of an adsorbent system. If all the volume of the adsorbent is occupied by adsorbate, that is the term in bracket is equal to unity, and the packing factor is 0.74, the same as the closest packing of hard spheres, then the storage capacity is 2027 (STP) v/v. However, this can only happen when $G >> D$. In closely packed arrays, where $G \sim \sigma_{cc}$, $V_S \approx \left(1 - \frac{\pi}{2\sqrt{3}}\right) Cf \approx 0.1Cf$. Thus, the maximum capacity would be ~ 203 (STP) v/v. Since this result is independent of storage conditions and tube diameter, the only way to reach the DOE target is to increase G, *i. e.* introduce gaps between tubes.

Equation (9-2) was fitted to the storage capacity data and the fitted curves are shown in Figure 9-7. As can be seen from Figure 9-7, the equation fits the data well except at the smallest tube separations, especially at small tube diameters. This indicates that the storage capacities are mainly determined by the volumes available to the adsorptive. At larger tube diameters, the fits overestimate the capacity. This is because at such tube diameters, the adsorption potential in the central region of the interstitial space becomes very weak. The packing factor determined using Equation (9-2) is shown in Figure 9-10 as a function of tube separation. First, the variation of packing factor as a function of tube

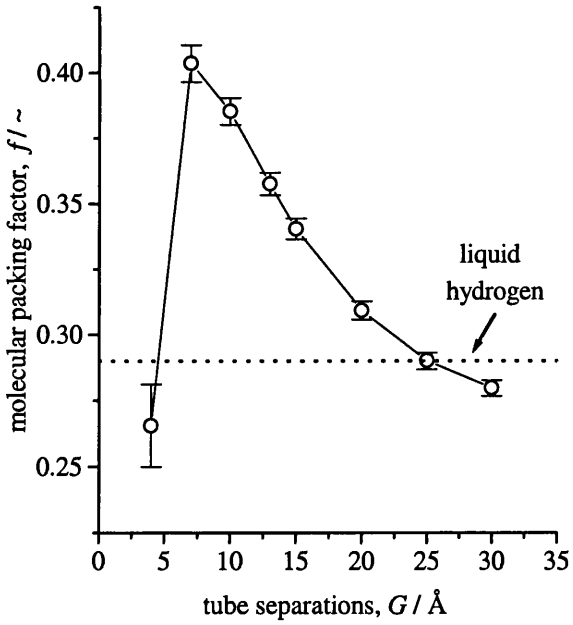

Figure 9-10. Molecular packing factor of adsorbed hydrogen molecules at 77 K and 70 bar in trigonal arrays of closed SWCNTs as a function of tube separation, G. Error bars are of ± one standard deviation. Also shown is the packing factor calculated for bulk hydrogen liquid at 20 K.

separation is generally similar to that in the case of nitrogen adsorption. But the absolute values of packing factor are lower than that of nitrogen. Second, most of the packing factors are higher than the value of liquid hydrogen that was calculated from liquid hydrogen density at 20 K (70.8 kg m^{-3}) and LJ collision diameters. Thus the adsorbed phase is denser than the liquid phase in most cases. Thirdly there is a maximum in packing factor which occurs at G = 7 Å. This corresponds to a monolayer formed between two nanotubes. Another point is that the deviations associated with packing factors determined by fitting Equation (9-2) to the data are small, indicating that packing factor is mainly determined by G rather than D. Finally, the data for G = 4 Å did not fit to Equation (9-2) at all. This is due to the packing effect shown in Figure 9-8.

9.2.3 Delivered hydrogen capacity as a function of D and G

Figure 9-11 shows volumetric delivered capacity of hydrogen in trigonal arrays of closed SWCNTs at 77 K as a function of tube diameter, D and tube separation, G.

Comparison with Figure 9-7 shows that the delivered capacity is considerably lower than the storage capacity. This indicates that a substantial amount of adsorbed hydrogen is retained in the interstitial space at the delivery pressure. The retained amount is a function of tube diameter and separation and ranges form about 10% to over 90% of the stored amount. For the largest tube diameter and separation where the retained amount is the smallest the retained amount is about 13%. While in arrays of D = 10 Å and G = 4 Å, the retained amount is about 93%. This is because even at the delivery pressure there is a considerable number of molecules adsorbed in the interstitial space due to the strong adsorption potential, especially at the corners formed by the neighbouring nanotubes (see Figure 9-12). Therefore in some

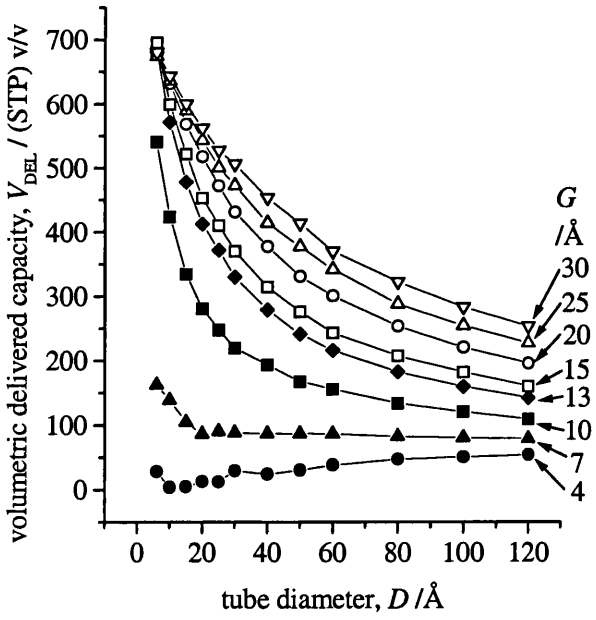

Figure 9-11. Simulated volumetric delivered capacity of hydrogen in trigonal arrays of closed SWCNTs as a function of tube diameter, D, and separation, G. The storage pressure is 70 bar, delivery pressure is 1 bar and temperature is 77 K.

cases a material may seem to have a useful storage capacity, but for vehicular applications where delivered capacity is more important the material could be no good at all. However, this retained amount can be released by heating the storage system to a higher temperature.

From Figure 9-11, it is clear that except at very small G, the delivered hydrogen capacity decrease progressively with increasing tube diameter. At certain G values, the effects of increasing D are two fold: one is to increase the volume available to the adsorptive and the other is to increase the volume of the simulation cell (that is the volume of the adsorbent and adsorbate). Therefore, the results show that the second effect is more important. At small G, especially at G = 4 Å, where tubes are nearly contacting each other, the effects are not clear. However, the effects of increasing tube separation are marked and the delivered capacity increases with increasing G at all D values. Here the main effect is the increase of the volume available to the adsorptive. It is interesting that the smallest tubes with sufficiently large separations will give the highest delivered capacities.

The optimal array configuration here is D = 6 Å and G = 15 Å with the maximum capacity of 696 (STP) v/v. Snapshots of this configuration at pressures of 1 bar and 70 bar are shown in Figure 9-12 (a) and (b) respectively. At 1 bar, there are some molecules adsorbed in the interstitial space. However, the monolayer is not complete. This means a relatively low amount of adsorbed molecules is retained at delivery pressure. At 70 bar, the interstitial space is full of adsorbed molecules, approximately two layers outside each tube and four layers between two tubes.

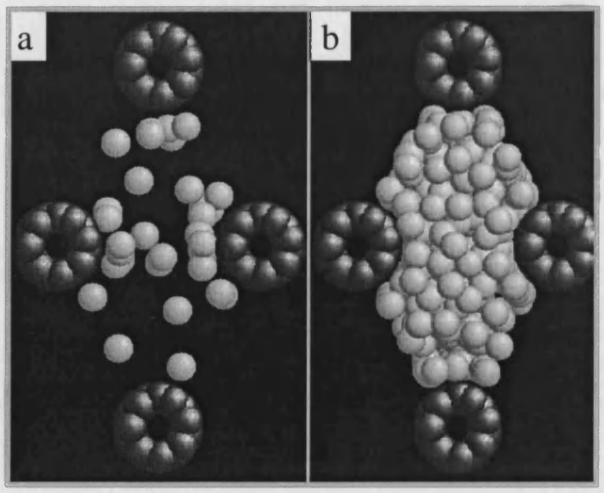

Figure 9-12. Snapshots of the optimal configuration (D = 6 Å, G = 15 Å) of hydrogen storage in trigonal arrays of closed SWCNTs at 77 K and 70 bar. The white spheres are hydrogen molecules adsorbed and the dark spheres are carbon atoms forming the four tubes in the array. (a) at 1 bar; (b) at 70 bar.

Although the optimal delivered capacity exceeds the target value of 695 (STP) v/v, all the other delivered

capacities are lower, especially at small tube separations. For the smallest tube separations, that is the closely packed arrays, the delivered capacities are extremely low, less than 1/10 of the DOE target. Even with a separation of 7 Å, the maximum capacity is still 1/3 of the target. Thus for the purpose of hydrogen storage, gaps must be introduced in between closed tubes. Another point is that only those SWCNT arrays that have similar configurations to the optimal one can yield delivered capacities close to the target. Any deviations from the optimal configuration will cause considerable decrease in delivered hydrogen capacity. Thus even if there is a narrow tube diameter distribution within an array, the capacity can be considerably reduced.

The gravimetric delivered capacity of hydrogen in trigonal arrays of closed SWCNTs as a function of tube diameter and separation are shown in Figure 9-13. The variations of the capacities with D and G are similar to the storage capacities. The maximum delivered capacity is still about five times the DOE target and if the separations between tubes are greater than 13 Å, all the capacities are greater than the target.

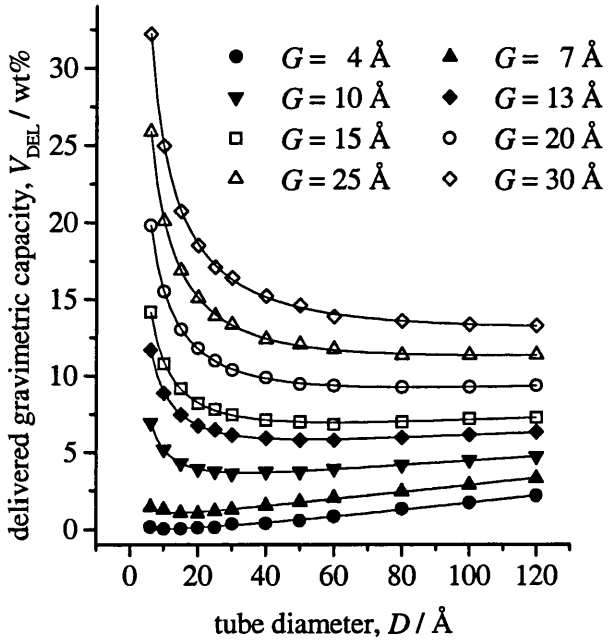

Figure 9-13. Simulated gravimetric delivered capacity of hydrogen in trigonal arrays of closed SWCNTs at 77 K as a function of tube diameter, D, and separation, G. Storage pressure 70 bar, delivery pressure 1 bar.

9.2.4 Effects of increasing storage pressure

It is well known that increasing storage pressure will increase delivered capacity. However, it may be not effective when the storage pressures are too high. Figure 9-14 shows the delivered capacity of adsorbed hydrogen in trigonal arrays of closed SWCNTs with the optimal configuration, of compressed hydrogen gas and the enhancement of adsorbed fluid over compressed gas as a function of storage pressure over a range from 1 bar to 200 bar. As can be seen from Figure 9-14, to reach the target storage pressure has to be very close to 200 bar for compressed gas, while it is only about 70 bar in the case of adsorbed fluid. The delivered capacity of adsorbed fluid increases with increasing storage pressure. However, the enhancement of adsorbed fluid

over compressed gas is no longer efficient when storage pressure is over around 100 bar and if the storage pressures are higher than 200 bar, then it is highly likely that compressed gas can reach or exceed the same capacity. Also, when storage pressure is over 100 bar, the increase of delivered capacity is not marked. Thus the main advantage of the adsorption system is to operate at lower pressures rather than higher capacities.

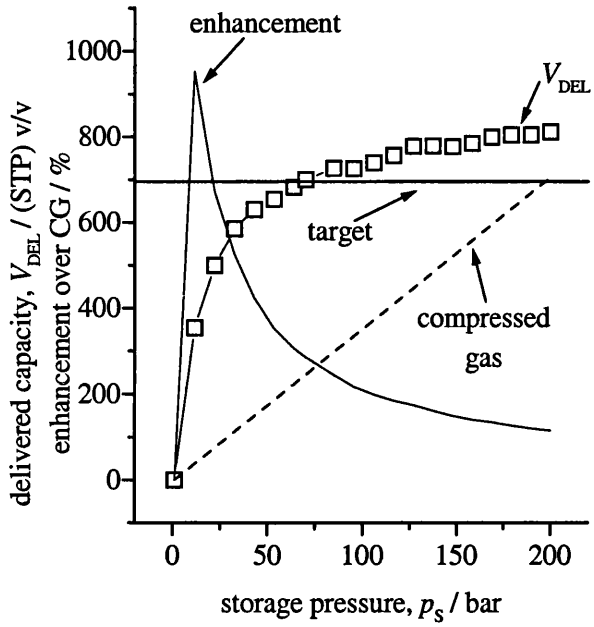

Figure 9-14. Simulated volumetric delivered capacity of hydrogen adsorbed at 77 K in trigonal arrays of closed SWCNTs with the optimal configuration, D = 6 Å and G = 15 Å, as a function of storage pressure. Delivery pressure is 1 bar. Also shown are delivered volumetric capacity of compressed hydrogen gas at 77 K and the enhancement of adsorption over compressed gas. The horizontal line shows the DOE target value.

It should be pointed out that Figure 9-14 is only an example. For different array configurations, the details (such as the pressure at which adsorption will have no enhancement over compressed gas) may vary, but the essential features (such as the higher the storage pressure, the weaker the enhancement over compressed gas) are the same.

9.3 Hydrogen storage in trigonal arrays of open SWCNTs at 77 K

9.3.1 Storage hydrogen capacity as a function of D and G

The volumetric storage capacity of hydrogen in trigonal arrays of open SWCNTs as a function of tube diameter and separation is shown in Figure 9-15. The capacities of all systems are very close, except of the smallest separations. Also, except the smallest tube separation with small diameter tubes, all capacities are above 600 (STP) v/v. Generally, volumetric storage capacities decrease with increasing tube diameter at large tube diameters, but the changes in capacities are small. For sufficiently large tube systems, the capacities are nearly independent of tube separation. Thus, the storage capacities of open tube systems are not so sensitive to array configurations compared to closed tubes. Comparison with closed tube systems also shows that opening up of the tubes improve the storage capacities markedly, especially at large D and small G, due to the

contribution of endohedral adsorption. However, the optimal configuration here is the same as is the maximum capacity.

Unlike the storage capacities of the closed tube systems, storage capacities of open tube systems do not fit to an analogue of Equation (9-2) very well.

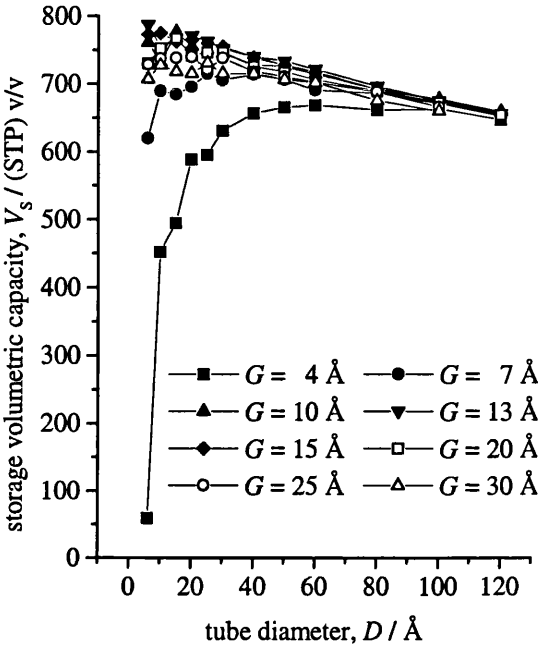

Figure 9-15. Simulated volumetric storage capacity of hydrogen at 77 K and 70 bar in trigonal arrays of open SWCNTs as a function of tube diameter, D, and separation, G.

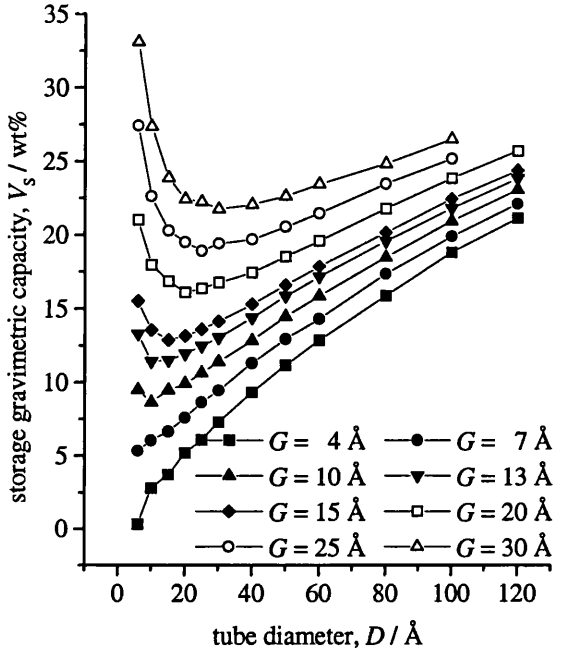

Figure 9-16. Simulated gravimetric storage capacity of hydrogen at 77 K and 70 bar in trigonal arrays of open SWCNTs as a function of tube diameter, D, and separation, G.

The gravimetric storage capacity of trigonal arrays of open SWCNTs as a function of tube configuration is shown in Figure 9-16. Compared to the capacities of closed tube systems, Figure 9-9, we can see that the gravimetric capacities at larger tube diameters and separations increase markedly and generally increase with increasing either tube diameters or tube separations. However, at small tube diameters and large tube separations, the capacities are similar in both cases. In most cases here, the storage capacities are well above the DOE gravimetric target.

9.3.2 Delivered hydrogen capacity as a function of D and G

It is expected that in open nanotube systems the delivered capacity will be higher due to the contribution of endohedral adsorption. Figure 9-17 shows volumetric delivered capacity of hydrogen in trigonal arrays of open SWCNTs as a function of tube diameter and separation. Comparison with delivered hydrogen capacities of closed trigonal arrays, Figure 9-11, shows that open tubes do improve delivered capacities significantly at large tube diameters, especially at small G values. For example, for an array of D = 120 Å and G = 4 Å, the delivered capacity of closed tube array is only 54 (STP) v/v, while that of open tube array is 554 (STP) v/v, nearly an order of magnitude increase. This is easy to understand because the larger the tube diameter, the more important the endohedral adsorption (see section 9.3.3).

However, this improvement of delivered capacity does not occur for small tube diameters. For example, for an array of D = 10 Å and G = 7 Å, the delivered capacity of a closed tube array is 138 (STP) v/v while that of an open tube array is 154 (STP) v/v. The optimal configuration here is the same as in the case of closed tube arrays as is the maximum delivered capacity. Thus, open tubes are not a necessity to obtain high delivered capacities.

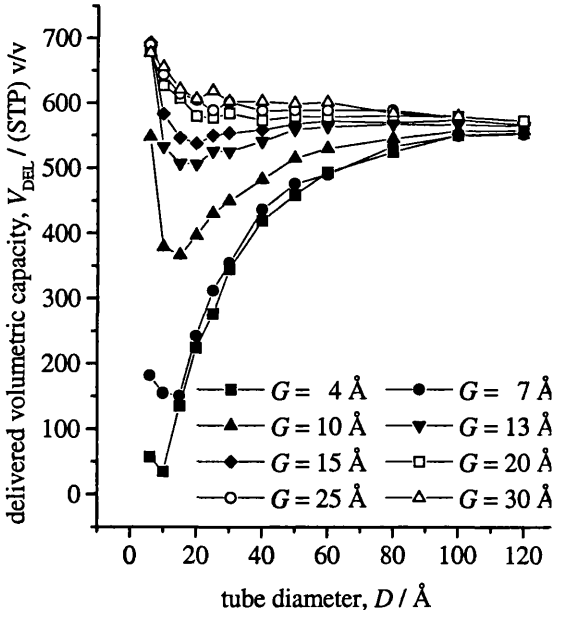

Figure 9-17. Simulated volumetric delivered capacity of hydrogen at 77 K in trigonal arrays of open SWCNTs as a function of tube diameter, D, and separation, G. The storage and delivery pressures are 70 bar and 1 bar respectively.

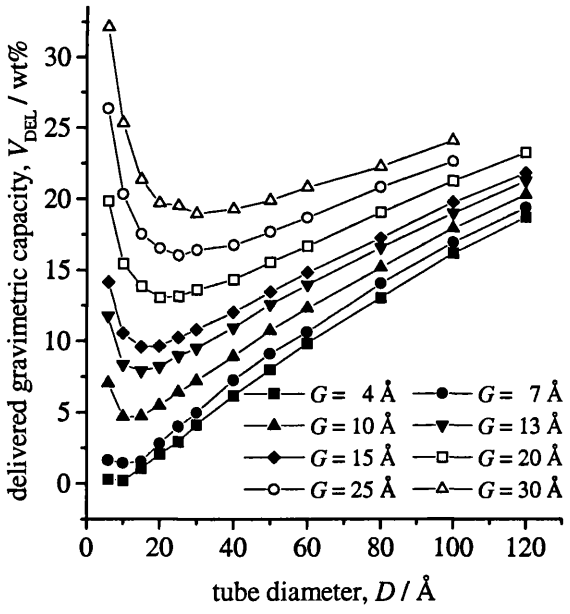

Figure 9-18. Simulated gravimetric delivered capacity of hydrogen at 77 K in trigonal arrays of open SWCNTs as a function of tube diameter, D, and separation, G. The storage and delivery pressures are 70 bar and 1 bar respectively.

The optimal configuration here is D = 6 Å and G = 15 Å with the maximum capacity of 693 (STP) v/v. The optimal configuration here shifts to larger tube separations when compared to that for the case of storage capacity. This is because that the amount retained at the delivery pressure is higher at small G than at larger G.

The gravimetric delivered capacity of hydrogen in trigonal arrays of open SWCNTs as a function of tube diameter and separation is shown in Figure 9-18. These functions are similar to those of storage capacities so need not be discussed further.

9.3.3 Comparison of exohedral and endohedral contributions to capacities

In open tube systems, both endohedral and exohedral adsorption can take place. The contributions of both to the total capacities are functions of both D and G. Figure 9-19 shows the contribution of exohedral adsorption to the total delivered capacity as a function of D and G. As can be seen from Figure 9-19, at D = 6 Å and G > 4 Å, the total delivered capacity is entirely due to exohedral adsorption; endohedral adsorption makes little contribution to the capacity. These cases give rise to the highest capacities as discussed before. However, exohedral contribution decreases sharply with increasing D at small G and increases with increasing G. The lowest contribution of exohedral adsorption can be as low as a few per cent of the total.

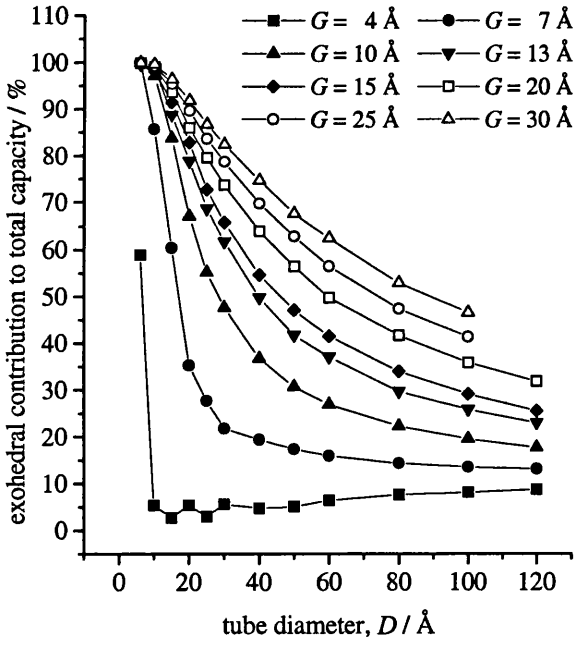

Figure 9-19. Exohedral contributions to the total delivered capacities of hydrogen at 77 K in trigonal arrays of open SWCNTs as a function of tube diameter, D, and separation, G.

At optimal configurations, the delivered capacity is mainly due to exohedral adsorption. Besides, as nanotubes are often found with large aspect ratio, that is they are very long comparing with their diameters, there might be a diffusion problem with endohedral adsorption in the application of gas storage. However, the interstitial space can form some kind of network and hence there will be no or little diffusion problems. Therefore,

a favoured nanotube array structure for storage of hydrogen as well as other gases should have high proportion of interstitial space, where exohedral adsorption will play an important or dominant role.

9.3.4 Comparison with capacities of activated carbons

Figure 9-20 shows delivered hydrogen capacity of carbon slit pore systems as a function of pore width, together with storage capacity at 70 bar, 1 bar, delivered capacity of compressed gas and the target capacity.

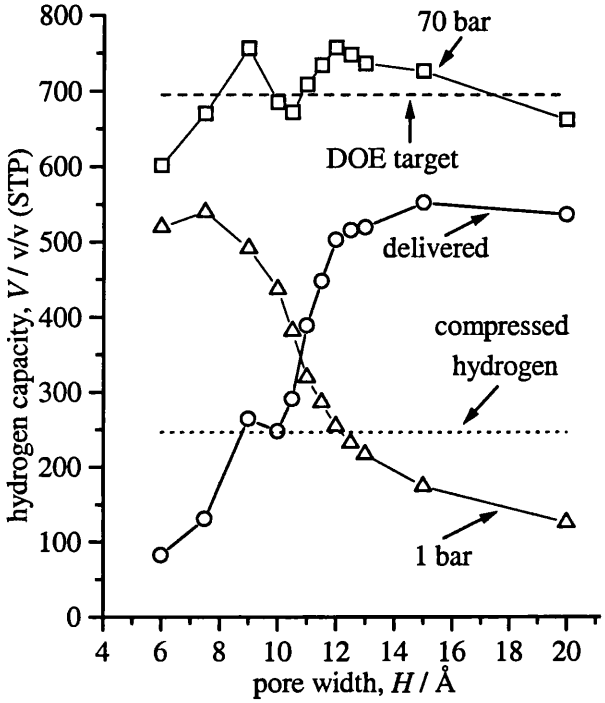

Figure 9-20. Simulated storage (at 70 bar and 1 bar) and delivered hydrogen capacities of single-walled carbon slits at 77 K as a function of pore width, *H*, together with the delivered capacity of compressed hydrogen at 77 K and the DOE target capacity. The storage and delivery pressures are 70 bar and 1 bar respectively.

As can be seen from Figure 9-20, the storage capacities are around the target. At some favourable pore widths, the storage capacity can be higher than 750 (STP) v/v. The optimal pore widths for storage capacity are about 9 and 12 Å, where the pore can hold two and three layers of adsorbed molecules respectively. However, as a high proportion of the stored hydrogen will be retained in the pore, the delivered capacity is much lower than the storage capacity. Especially at pore widths less than about 11 Å, the delivered capacities are even lower than that of compressed gas. The optimal pore width is about 15 Å with a delivered capacity of 550 (STP) v/v. In this optimal structure, about four layers of hydrogen molecules are adsorbed in the pore at 70 bar. This pore width is slightly larger than the optimal pore width for methane storage, where the optimal pore width is 11.2 Å and the pore can hold two layers of methane molecules. The reason is the lower temperature employed in the simulation of hydrogen storage here. Hence weaker adsorption potential is required to obtain the optimal delivered capacity.

It is clear that nanotube arrays will give higher optimal delivered capacity compared with activated carbons. This is in some kind of agreement with Dillon and co-workers' work [Dillon *et al.*, 1997]. Another point is that in the case of nanotube arrays, there is a wider range of array configurations that can yield higher delivered capacities. However, at present carbon nanotubes are much more expensive to make and to introduce a controlled gap between the tubes might be a difficulty.

9.3.5 Comparison with experiments

Hydrogen storage capacities reported experimentally are mostly in the gravimetric form. Thus, comparisons with simulations can only be made on the same basis.

The simulated volumetric capacities of hydrogen stored in activated carbons at 298 K and 70 bar shown in Figure 9-6 correspond to a gravimetric capacity range from ~0.5 wt% to ~1.9 wt% in the smallest and the largest pore respectively. The experimental results, 0.6 wt%, of Chahine and Bose [1994] at 298 K and 60 bar are within this range (Table 8-3). Considering that the storage pressure employed is lower than in the simulation and experiments are not so idealised, we can conclude that the simulation results are in a good agreement with experimental data. Similar conclusions are found for the results at 77 K. The gravimetric capacity corresponding to the simulated hydrogen capacities of activated carbons shown in Figure 9-20 is in the range from ~ 4.2 wt% to ~15.3 wt%. These figures are also in a good agreement with experimental results, such as those reported by Noh *et al.* [1987], 4.7 wt% (Table 8-3). Thus, it is concluded that simulations of hydrogen storage in activated carbons at 77 K are also in a good agreement with experimental studies.

Figure 9-2 shows that for closely packed trigonal arrays of open SWCNTs with D = 20 Å, the gravimetric capacity is about 1 wt% at 100 bar and 298 K. This value is much lower than the experimental capacity reported by Liu *et al.* [1999] (Table 8-3) for nanotubes with an average diameter of 18.5 Å at similar storage conditions. To reach the reported capacity of 4.2 wt%, gaps larger than 10 Å must be introduced between the nanotubes (Figure 9-2). Similarly, to reach a capacity of 8.25 wt% reported by Ye *et al.* [1999] at 80 K, gaps larger than 10 Å must also be introduced when tube diameters are less than 20 Å. In fact, Ye *et al.* [1999] reported a phase transition at pressures higher than 40 bar during their experimental studies of hydrogen adsorption on crystalline

ropes of SWCNTs, where individual SWCNTs were separated and hydrogen was physisorbed on their exposed surfaces. Taking this into consideration, the simulation results are also in a good agreement with the experimental data.

9.4 Hydrogen storage in square arrays of SWCNTs at 77 K

Figures 9-21 to 9-24 show the delivered hydrogen capacity of square arrays of closed and open SWCNTs as a function of tube diameter and tube separation. Comparison with Figures 9-11, 9-13, 9-17 and 9-18 shows that the curves are generally the same. This means that the delivered capacity is not very sensitive to array configuration. However, as there is more interstitial space available in the case of square arrays than in the case of trigonal arrays, square arrays result in higher capacities in some cases. For example, at D = 6 Å and G = 7 Å, the delivered capacity of an open square array is about 260 (STP) v/v, but is 180 (STP) v/v in the case of open trigonal arrays, an increase of more than 40%. This improvement does not exist for larger tube diameters or larger tube separations. The maximum delivered capacity here is similar to that in the case of trigonal arrays, though the optimal configuration changes to D = 6 Å and G = 20 Å. The optimal parameters for volumetric capacity are summarised in Table 9-1.

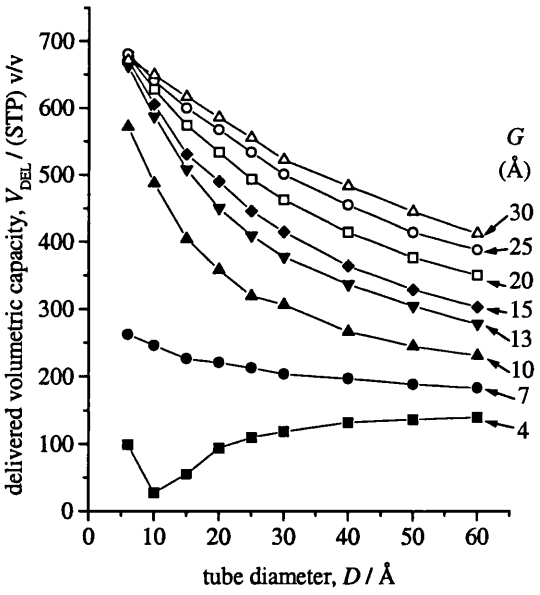

Figure 9-21. Simulated volumetric delivered capacity of hydrogen in square arrays of closed SWCNTs at 77 K as a function of tube diameter, D, and separation, G. The storage and delivery pressures are 70 bar and 1 bar respectively.

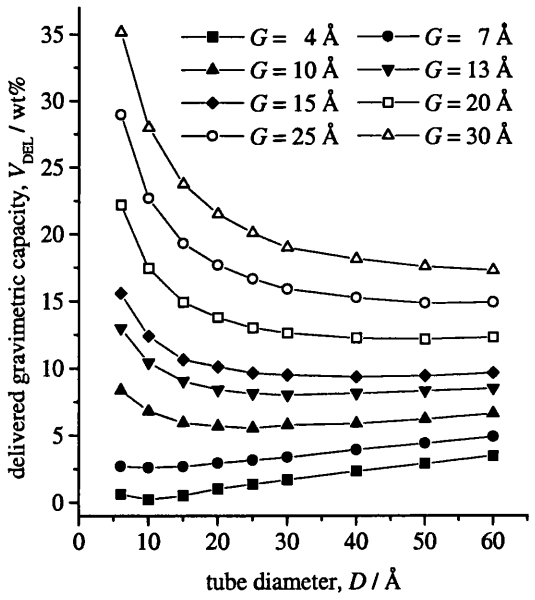

Figure 9-22. Simulated gravimetric delivered capacity of hydrogen in square arrays of closed SWCNTs at 77 K as a function of tube diameter, D, and separation, G. The storage and delivery pressures are 70 bar and 1 bar respectively.

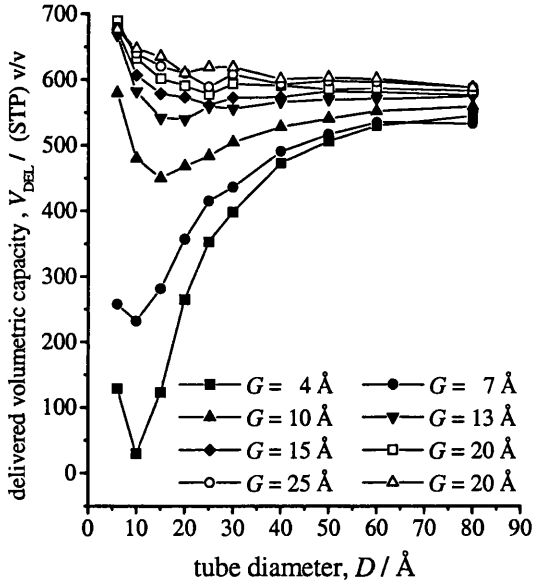

Figure 9-23. Simulated volumetric delivered capacity of hydrogen in square arrays of open SWCNTs at 77 K as a function of tube diameter, D, and separation, G. The storage and delivery pressures are 70 bar and 1 bar respectively.

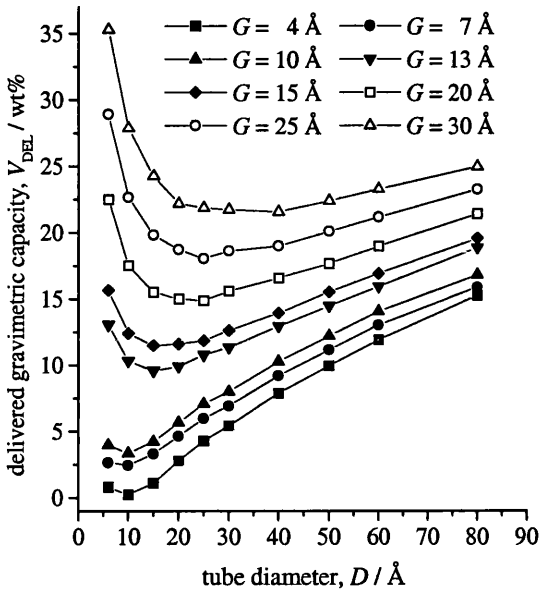

Figure 9-24. Simulated gravimetric delivered capacity of hydrogen in square arrays of open SWCNTs at 77 K as a function of tube diameter, D, and separation, G. The storage and delivery pressures are 70 bar and 1 bar respectively.

Table 9-1. Optimal parameters for volumetric hydrogen capacities at 77 K

Arrays	Tubes	Optimal D (Å)		Optimal G (Å)		Capacity ((STP)v/v)	
		storage	delivered	storage	delivered	storage	delivered
Trigonal arrays	Closed	6	6	13	15	785	696
	Open	6	6	13	15	787	693
Square arrays	Closed	6	6	13	25	749	681
	Open	6	6	13	20	754	689

Storage pressure = 70 bar, delivery pressure = 1 bar.

At small tube diameters and larger tube separations, square arrays give higher gravimetric delivered capacities than trigonal arrays due to more space available. On the other hand, at larger tube diameters, square arrays yield lower gravimetric capacities than trigonal arrays due to weaker interactions.

9.5 Summary and Conclusions

From the above results, the following conclusions may be drawn:

(1) At ambient temperature (298 K), volumetric storage and delivered hydrogen capacities of SWCNT arrays are well below the DOE target. Even with storage pressures up to 200 bar, the capacities are only a little higher than 1/3 of the DOE target and are no better than for activated carbons in similar conditions. Thus from the volumetric point of view, carbon nanotubes are not good for hydrogen storage at ambient temperature. In the case of gravimetric capacities, delivered capacities in excess of the DOE target may be obtained with pressures up to 200 bar and with some favourable SWCNT array configurations.

(2) At 77 K and 70 bar, the volumetric storage capacities of some favourable configurations of SWCNTs can be as high as 800 (STP) v/v. However, as a considerable amount of the adsorbed hydrogen is retained in the material at the delivery pressure, the highest delivered capacity with a storage pressure of 70 bar and delivery pressure of 1 bar is only 696 (STP) v/v, just above the DOE target. The gravimetric capacities can be as high as several times the DOE target. Thus in hydrogen storage, the volumetric target is a more demanding requirement.

(3) Increasing storage pressure can increase storage and delivered capacities. However, if the storage pressure is above 200 bar, then the enhancement of adsorption over compressed gas will be small or even negative in some array configurations. In addition, the increase of capacities with increasing pressure up to such a high level will be very slow in most the cases, because adsorption is close to saturation.

(4) The capacities of SWCNT arrays are related to their configuration. They are mainly determined by the volume of the accessible space available in the array. Generally, arrays consisting of small tubes but with sufficiently large tube separations yield high capacities. In most cases, the density of the adsorbed hydrogen is higher than that of liquid hydrogen.

(5) Exohedral adsorption plays a very important role in hydrogen storage. In all optimal configurations, more than 99% of the maximum delivered capacities are due to exohedral adsorption. To reach the DOE target, exohedral adsorption must be brought into play and gaps between the tubes are necessary. Thus, the introduction of gaps into between the tubes may be vital if carbon nanotubes are to be used as hydrogen storage media.

(6) Square · arrays may give higher capacities than trigonal arrays for some configurations, but generally they do not improve the capacity to an appreciable degree. This may indicate that some arrays of trigonal and square arrays or even randomly arranged nanotubes will give similar capacities, provided the diameters of the tubes and the average gaps are similar.

(7) Carbon nanotubes are better than activated carbons for hydrogen storage at 77 K as far as the maximum capacities are concerned. Also, a large range of array configurations can yield capacities higher than 550 (STP) v/v, which is the maximum capacity of single-walled slit carbons. However the production of carbon nanotubes is at the present not so easy as activated carbons.

(8) Simulated hydrogen storage capacities of activated carbons are in good agreement with experimentally reported results both at room temperature and 77 K. Hydrogen capacities of closely packed arrays of SWCNTs are much lower than experimental results at both 298 K and 77 K. When sufficiently large gaps are introduced between nanotubes, simulation results can match the experimental ones. This suggests that nanotubes are not closely packed in experiments.

Chapter 10
Methane Storage

Chapter 9 presented simulation results of hydrogen storage in arrays of single-walled carbon nanotubes. This chapter reports the simulation results of methane storage in arrays of SWCNTs. As some features are common to both hydrogen and methane storage, the discussion here may be sometimes rather brief.

10.1 Methane storage in trigonal arrays of closed SWCNTs at 298 K

10.1.1 Storage methane capacity as a function of D and G

The volumetric storage capacity for methane in trigonal arrays of closed SWCNTs at 298 K and 34 bar as a function of tube diameter and separation is shown in Figure 10-1. Similar to hydrogen volumetric storage capacity, methane volumetric capacity decreases sharply with increasing tube diameter for a given tube separation, except at very small tube separations. The reasons for this have been discussed in section 9.2.1.

As can be seen from Figure 10-1, for a given tube diameter, the capacity increases with increasing tube separation at small G, reaches a maximum at a critical separation G_c, and then decreases with further increases of G. This is because at a given tube diameter, increasing G increases the accessible volume, but reduces the average potential in the interstitial space. On volume per volume basis, the interstitial space decreases with increasing tube diameter, but increases with increasing tube separation. Therefore, the larger the tube diameter, the larger the critical separation, G_c (Figure 10-1). In fact, this behaviour is also observed for

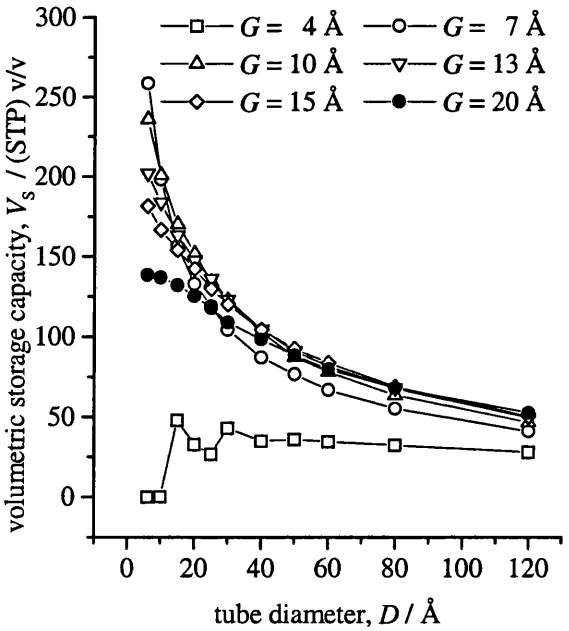

Figure 10-1. Simulated volumetric storage capacity for methane in trigonal arrays of closed SWCNTs at 298 K and 34 bar as a function of tube diameter, D, and tube separation, G.

hydrogen. But the G_c value is larger for hydrogen for the same tube diameter. Therefore G_c is only observed at very small tube diameters where the corresponding G_c values are within the range of tube separations studied (see Figure 9-7). Possible reasons for this difference are (1) The storage pressure for methane storage is less than half of that for hydrogen storage; (2) For methane storage at 298 K, the temperature is much higher than for hydrogen storage at 77 K, therefore the optimal pore size should be smaller. For the same reasons, the optimal configuration here is D = 6 Å and G = 7 Å (compared with D = 6 Å and G = 13 Å for hydrogen storage at 77 K and 70 bar) with the maximum capacity of ~260 (STP) v/v.

The maximum simulated methane storage capacity is more than 90% higher than the target capacity of 137 (STP) v/v (section 8.3.2). However, as can be seen from Figure 10-1, only a few array configurations close to the optimal one can have volumetric capacities greater than the target. For the closely packed tube arrays, the maximum capacity is less than 50 (STP) v/v. Thus this may imply that it is very difficult to use trigonal arrays of closed SWCNTs to achieve the target for methane storage. For the same geometrical packing effects as explained in Figure 9-8, the volumetric storage capacities of the closely packed arrays fluctuate with increasing tube diameters.

The gravimetric storage capacity for methane in trigonal arrays of closed SWCNTs as a function of tube diameter and separation is shown in Figure 10-2. As for gravimetric hydrogen storage capacities, the storage gravimetric capacity for methane increases progressively with increasing tube separation within the range studied. Thus no optimal configurations for gravimetric capacity were found. Also, when tube diameters exceed about 30 Å, there will be little change in gravimetric storage capacities upon further increase of tube

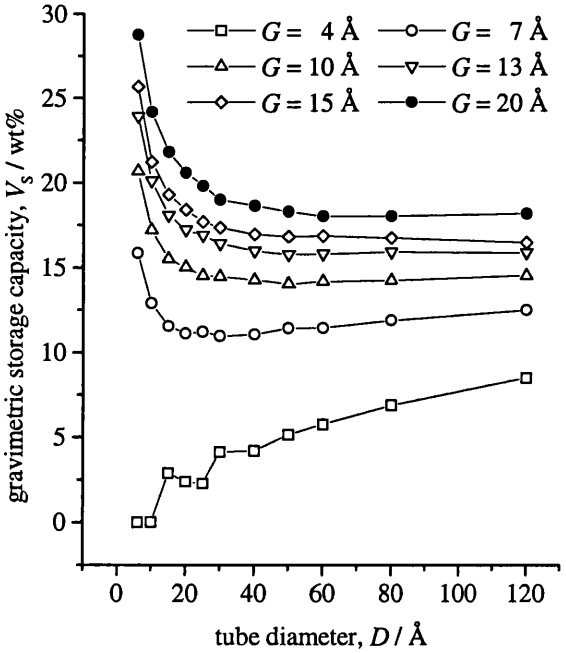

Figure 10-2. Simulated gravimetric storage capacity for methane at 298 K and 34 bar in trigonal arrays of closed SWCNTs as a function of tube diameter, D, and separation, G.

diameter except for closely packed arrays.

One interesting point is that the volumetric methane capacities are much lower than volumetric hydrogen capacities, while gravimetric methane capacities are higher than gravimetric hydrogen capacities even though the temperature for methane adsorption is much higher than that for hydrogen adsorption. This is simply because the molecular mass of methane is about eight times of that of hydrogen.

10.1.2 Delivered methane capacity as a function of D and G

Figure 10-3 shows volumetric delivered capacity for methane in trigonal arrays of closed SWCNTs at 298 K as a function of tube diameter, D and separation, G. Generally, volumetric delivered capacity decreases sharply with increasing tube diameter, except for the closely packed arrays. The volumetric delivered capacities of the closely packed arrays are extremely low with a maximum value about only 30 (STP) v/v. The optimal configuration here is D = 6 Å and G = 10 Å with the maximum capacity of 210 (STP) v/v. This optimal configuration is illustrated in Figure 10-4 in the form of snapshots at 1 bar and 34 bar. It is clear that, at 34 bar, there are two adsorbed methane layers between two tubes, a monolayer on each tube. This is in a

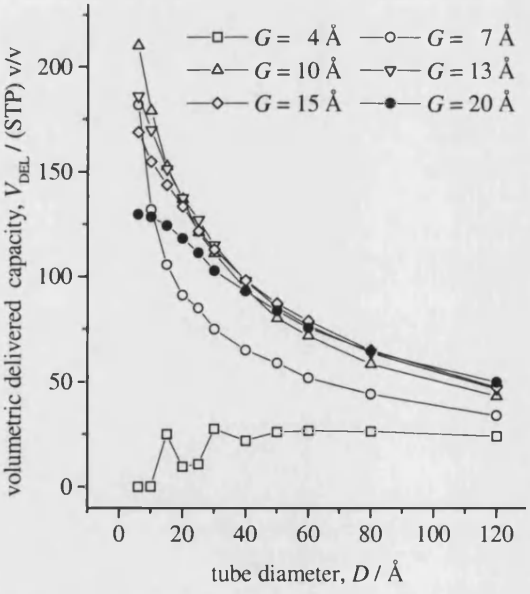

Figure 10-3. Simulated volumetric delivered capacity for methane at 298 K in trigonal arrays of closed SWCNTs as a function of tube diameter, D, and tube separation, G. The storage and delivery pressures are 34 bar and 1 bar respectively.

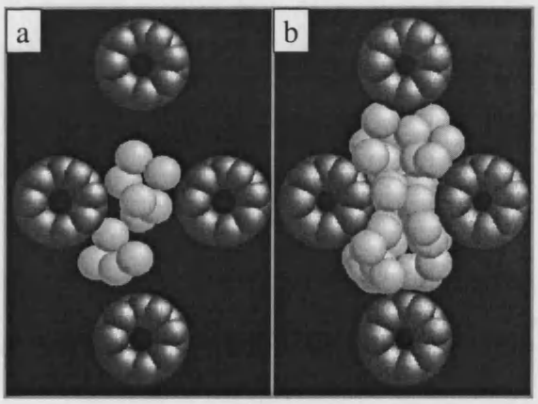

Figure 10-4. Snapshots of the optimal configuration (D = 6 Å, G = 10 Å) of methane storage in trigonal arrays of closed SWCNTs. The white spheres are methane molecules adsorbed and the dark spheres are carbon atoms forming the tubes. (a) at 1 bar; (b) at 34 bar.

good agreement with simulation results of methane adsorption in carbon slit pores where the optimal pore width is ~11.2 Å and two layers of methane are adsorbed between the two pore walls [Tan and Gubbins, 1992; Matranga *et al.*, 1992a, 1992b]. In this optimal configuration, about 1/5 of the adsorbed molecules are retained in the material at 1 bar. From Figure 10-3, the delivered methane capacities at larger tube separations are not sensitive to tube separations compared with in the case of delivered hydrogen capacities (*cf.* Figure 9-11).

The gravimetric delivered capacity for methane in trigonal arrays of closed SWCNTs as a function of tube diameter and separation is shown in Figure 10-5. The variation of capacity with D and G is similar to the storage capacities and also similar to that of hydrogen. Except for the closely packed arrays, the gravimetric delivered methane capacity is not sensitive to tube diameter when D exceeds about 30 Å. However, the gravimetric capacities are still sensitive to tube separations even at very large tube diameters.

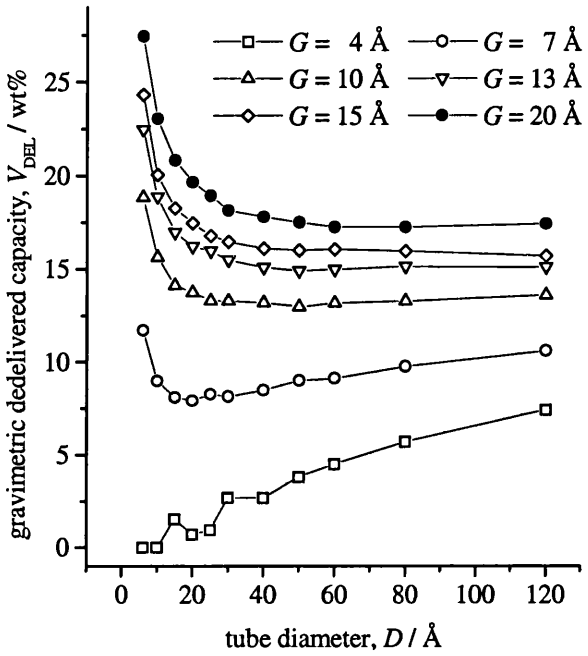

Figure 10-5. Simulated gravimetric delivered capacity for methane at 298 K in trigonal arrays of closed SWCNTs as a function of tube diameter, D, and separation, G. The storage and delivery pressures are 34 bar and 1 bar respectively.

10.2 Methane storage in trigonal arrays of open SWCNTs at 298 K

10.2.1 Storage methane capacity as a function of D and G

The volumetric storage capacity for methane at 298 K in trigonal arrays of open SWCNTs as a function of tube diameter and separation is shown in Figure 10-6. Generally, the capacity increases with increasing tube diameter at small tube diameters, though there are some fluctuations due to the packing effects similar to those shown in Figure 9-8. Storage capacity reaches a maximum for diameters between 15 and 20 Å. Finally, capacity decreases with further increasing tube diameter.

The optimal configuration here is D = 15 Å and G = 7 Å with the maximum storage capacity of about 290 (STP) v/v, which is more than twice the target. The optimal configuration here is different from both that of hydrogen storage at 77 K and of closed tube arrays for methane storage, where the optimal configurations are all with the smallest tube diameters and intermediate tube separations. In closed tube arrays, the available volume (on volume per volume basis) decreases with increasing tube diameter. But in open tube arrays, the available volume increases with increasing tube diameter when $D > G$. Thus the optimal configuration might shift to larger tube diameters, as compared to closed tube arrays. The difference between methane storage at 298 K and hydrogen storage at 77 K is due to more important endohedral contribution to the capacity at higher temperatures, as indicated by comparing hydrogen storage at 298 K and 77 K. As shown in Figure 9-3, arrays with D = 6 Å do not yield the highest hydrogen capacity at 298 K. The optimal array configuration for hydrogen storage at 298 K also shifts to larger tubes when compared with at 77 K. The possible reason is that endohedral potential is generally more enhanced than exohedral potential.

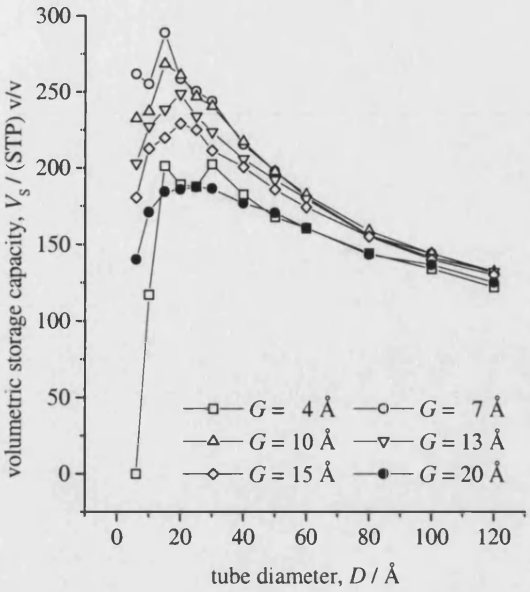

Figure 10-6. Simulated volumetric storage capacity of methane at 298 K in trigonal arrays of open SWCNTs as a function of tube diameter, D, and separation, G. Storage pressure is 34 bar.

Due to similar reasons, opening up of the tubes improves storage capacity more considerably than in the case of hydrogen storage at 77 K, as can be seen from Figures 10-6 and 10-1. At large tube diameters, storage capacity is more than doubled. Even the maximum capacity is increased by more than 10% compared to the case of hydrogen, where they are essentially the same for both closed and open tube arrays.

There is a wide range of array configurations that can give methane storage capacities greater than the target. From Figure 10-6, it is clear that if the tube diameters are within the range of about 11-90 Å, all the storage capacities are above the target, for all values

of D and G. Thus, a storage capacity of more than 137 (STP) v/v should be not too difficult to achieve, if all the tubes can be opened and the tubes are purified.

The gravimetric storage capacity of methane in trigonal arrays of open SWCNTs as a function of tube configuration is shown in Figure 10-7. Compared with the capacities of closed tube systems, Figure 10-2, gravimetric capacities at larger tube diameters increase markedly with increasing tube diameter. This is different from closed tube arrays, where gravimetric storage capacities are nearly independent of tube diameters. At very small D, gravimetric storage capacity decreases with increasing D, except for G = 4 Å. However, this decrease of capacity at small D is not so marked as for hydrogen storage at 77 K, Figure 9-16. As we know that increasing tube diameter will increase the weight of the nanotubes in the cell as well as increase the number of fluid molecules adsorbed into the simulation cell. In the case of hydrogen, the increased weight of adsorbed hydrogen due to increasing D at small tube diameters may not overcome the increased weight of nanotubes because hydrogen is very light. On the other hand, methane is eight times as heavy as hydrogen. Therefore adsorbing one more methane molecule will cause the same effect to the gravimetric capacity as adsorbing eight more hydrogen molecules.

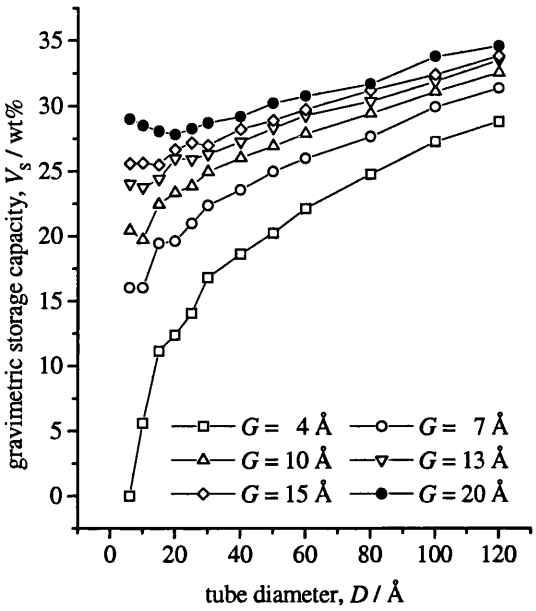

Figure 10-7. Simulated gravimetric storage capacity of methane at 298 K in trigonal arrays of open SWCNTs as a function of tube diameter, D, and separation, G. Storage pressure is 34 bar.

10.2.2 Delivered methane capacity as a function of D and G

Figure 10-8 shows that the volumetric delivered capacity of methane at 298 K in trigonal arrays of open SWCNTs first increases with tube diameter, D, to a maximum, then decreases. This is similar behaviour to that for storage capacity, Figure 10-6. It is also clear that increasing tube separation will not always increase delivered capacity and separations greater than 10 Å will lead to a considerable decrease in delivered capacity. The optimal configuration here is D = 20 Å and G = 10 Å with the maximum capacity

of 233 (STP) v/v. These values are larger than those for storage capacity, because larger D and G will give rise to less adsorbed methane retained at the delivery pressure. The snapshots of this optimal configuration are shown in Figure 10-9. As can be seen, at the delivery pressure, there are some molecules adsorbed, but even monolayers both inside and outside the tubes are incomplete, indicating a relative lower retention of adsorbed methane at the delivery pressure. At the storage pressure, the endohedral and exohedral spaces are filled with adsorbed methane, though the packing of the molecules is not very tight. In this optimal configuration, there are two layers of methane adsorbed between two tubes, a monolayer on each tube, and roughly two layers of methane inside each tube. This is also in good agreement with simulation results of methane storage in activated carbons [Tan and Gubbins, 1992; Matranga *et al.*, 1992a, 1992b].

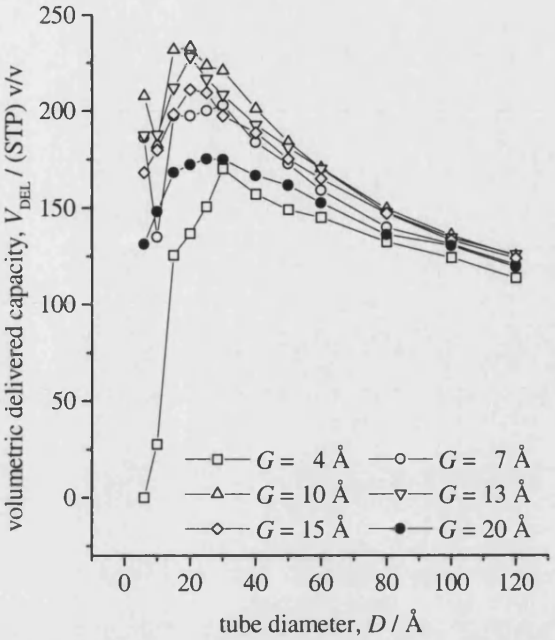

Figure 10-8. Simulated volumetric delivered capacity of methane at 298 K in trigonal arrays of open SWCNTs as a function of tube diameter, D, and separation, G. Storage pressure is 34 bar, delivery pressure is 1 bar.

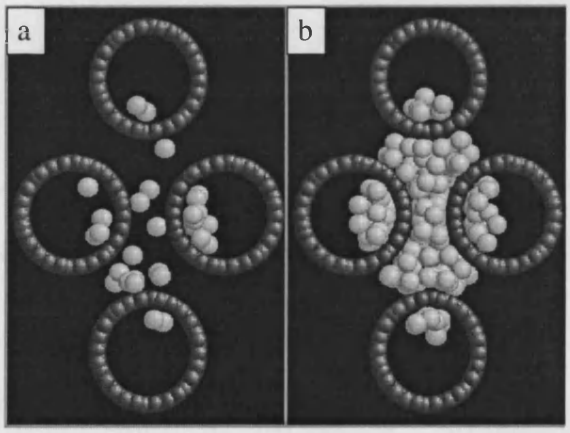

Figure 10-9. Snapshots of the optimal configuration (D = 20 Å, G = 10 Å) for methane storage at 298 K in trigonal arrays of open SWCNTs. White spheres are methane molecules and dark spheres are carbon atoms. (a) at 1 bar; (b) at 34 bar.

Compared with closed tube arrays, not only do the structural parameters of the optimal configuration change, but also the delivered methane capacities are improved markedly, especially with large tube arrays. When tube diameters are in the range from 25 Å to 50 Å, all the arrays will meet the target value of delivered capacity. Unfortunately, most experimentally observed SWCNTs to date have diameters less than 20 Å. For these nanotube arrays, gaps must

be introduced in between the tubes to achieve the target. For arrays with tube diameters larger than 80 Å, it is impossible to reach the target.

The gravimetric delivered capacity of methane at 298 K in trigonal arrays of open SWCNTs as a function of tube diameter and separation is shown in Figure 10-10. The capacities are improved markedly when comparing with closed tube arrays due to endohedral adsorption. These functions are similar to those of storage capacities and have been discussed in the previous section.

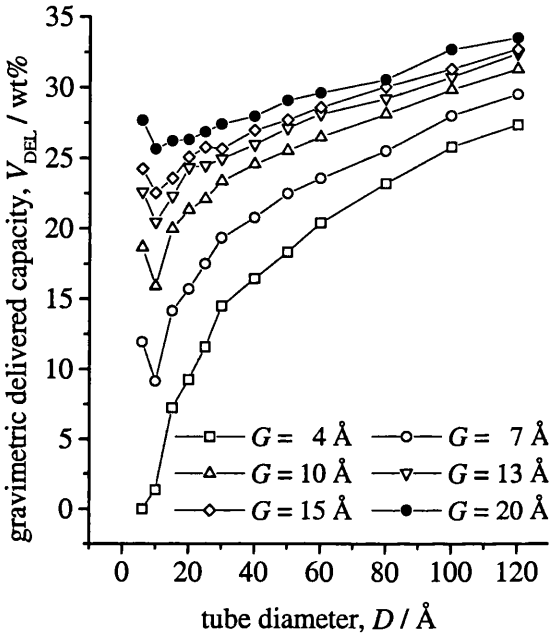

Figure 10-10. Simulated gravimetric delivered capacity of methane at 298 K in trigonal arrays of open SWCNTs as a function of tube diameter, D, and separation, G. Storage pressure is 34 bar, delivery pressure is 1 bar.

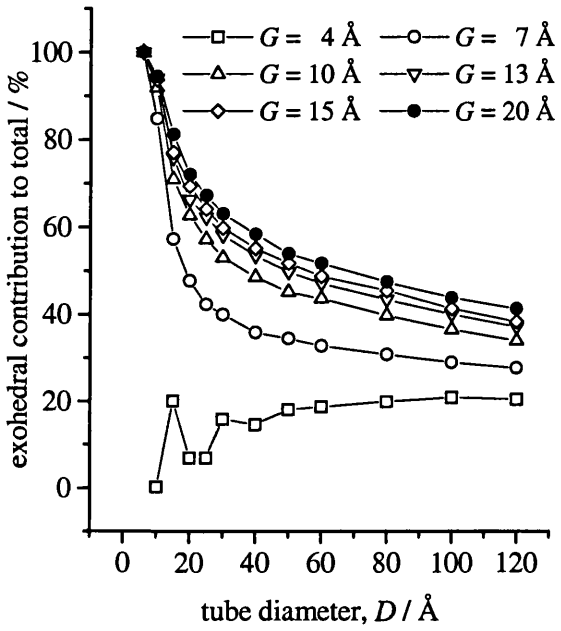

Figure 10-11. Contribution of exohedral adsorption to the total delivered capacity of methane at 298 K in trigonal arrays of open SWCNTs as a function of tube diameter, D, and separation, G.

10.2.3 Comparison of exohedral and endohedral contributions to capacity

Figure 10-11 shows the contribution of exohedral adsorption to the total delivered capacity as a function of D and G. As for hydrogen adsorbed in open trigonal arrays, exohedral adsorption plays a predominant role in arrays with small tube diameters and large separations. This is because fluid molecules either cannot enter then endohedral space or the endohedral potential is so strong that most of the adsorbed fluid will be retained inside the tubes. However, in larger tube arrays endohedral adsorption plays the main role, and in closely packed tube array, exohedral adsorption contributes no more than 20% to the total delivered capacity. At the optimal configuration, the contribution

of exohedral adsorption is about 62%. Thus, to obtain a higher delivered capacity full advantage of the interstitial space must be taken.

Compared to hydrogen storage at 77 K, exohedral contribution decreases more sharply at small tube diameters (*cf.* Figure 9-19). For example, when D = 15 Å and G = 10 Å, the exohedral contributions are ~ 84% and ~ 70% for hydrogen storage at 77 K and methane storage at 298 K respectively. This confirms the argument that endohedral adsorption may be more important at high temperatures made in section 10.2.1. However, this only occurs for a small range of D and G values.

10.2.4 Effects of increasing storage pressure

Typical methane adsorption isotherms at 298 K for trigonal arrays of open SWCNTs with two different tube separations, 4 and 10 Å, are shown in Figures 10-12 and 10-13 respectively, together with the target capacity and the storage capacities of compressed methane at the same temperature. The amount adsorbed is expressed in volumetric capacity, (STP) v/v. As it is expected, the smaller the tube, the lower the pressure at which the isotherms saturate. Generally the enhancement of adsorbed methane over compressed methane is most marked at lower pressures. For small tubes and closely packed arrays, increasing pressure may not be an efficient way to increase the storage capacity. For larger tubes and / or larger tube separations, the increase of storage capacity with increasing pressure and the enhancement of adsorbed methane over compressed methane are still remarkable even at high pressures.

As shown in Figures 10-12 and 10-13, all the isotherms can be fitted to the Tóth equation [Tóth, 1981] which is widely used in high pressure and temperature adsorption isotherm analysis:

$$w = \frac{ab^{1/c}p}{\left(1+bp^{c}\right)^{1/c}}$$

where w is the amount adsorbed, a, b, and c are constants and p the pressure. This may indicate that it is possible to predict higher-pressure behaviour of the isotherms from limited experimental data. However, care must be taken in doing so because

considerable errors may be introduced, especially if the highest pressure of the experimental data is well below the saturation pressure. The same approach also appears to be useful for analysing hydrogen adsorption.

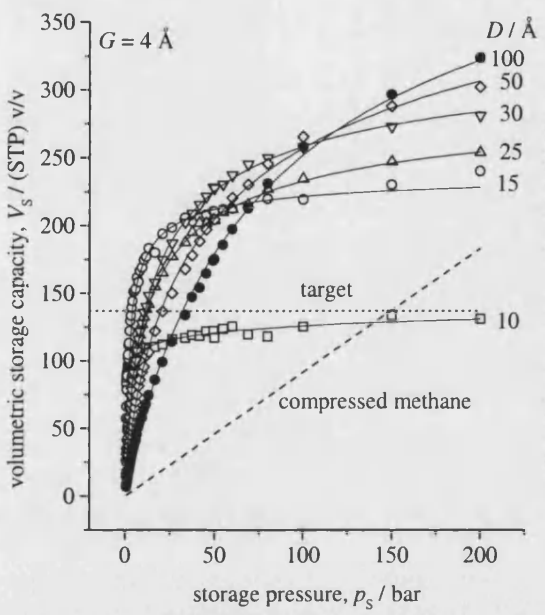

Figure 10-12. Methane adsorption isotherms of closely packed (G = 4 Å) trigonal arrays of open SWCNTs at 298 K. The amount adsorbed is expressed in (STP) v/v. The solid lines are Tóth fits to the data. The target capacity and the storage capacity of compressed methane are also shown in the figure.

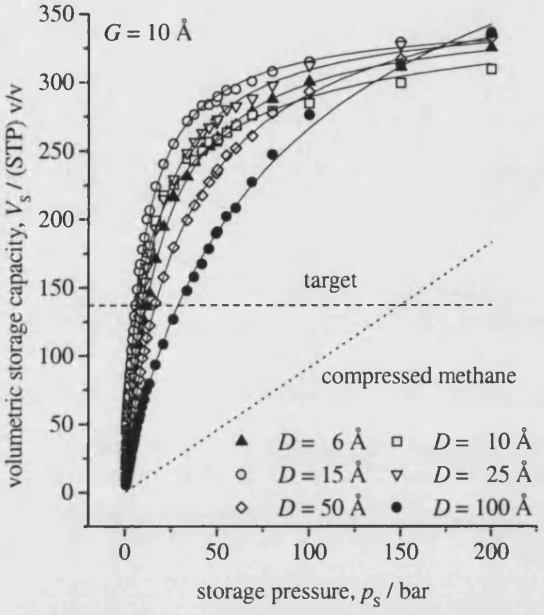

Figure 10-13. Methane adsorption isotherms of trigonal arrays of open SWCNTs with G = 10 Å at 298 K. The amount adsorbed is expressed in (STP) v/v. The solid lines are Tóth fits to the data. The target capacity and the storage capacity of compressed methane are also shown in the figure.

10.2.5 Comparison with capacities of activated carbons

Figure 10-14 shows delivered and storage methane capacity of single-walled carbon slit pore systems at 298 K as a function of pore width, H. The storage pressure is 34 bar and delivery pressure is 1 bar.

As can be seen from Figure 10-14, the storage capacities are above the target when pore width is in the range from 7 to 17 Å. The maximum capacity is about 250 (STP) v/v and is corresponding to a pore width of 7 Å. At this optimal pore width, only one layer of methane is adsorbed in the pore. Due to the strong adsorption potential, a large amount of methane is adsorbed (hence retained) in pores with this size at 1 bar. Thus a large portion (~ 40%) of the adsorbed methane is retained in the material at delivery, resulting in a much lower delivered capacity. The optimal pore with for maximum delivered capacity is 11.2 Å with the maximum capacity of 214 (STP) v/v. At this pore

width, two layers of methane are adsorbed in the pore. As can be seen from Figure 10-14, the amount adsorbed at 1 bar is considerably lower here, resulting in a higher delivered capacity.

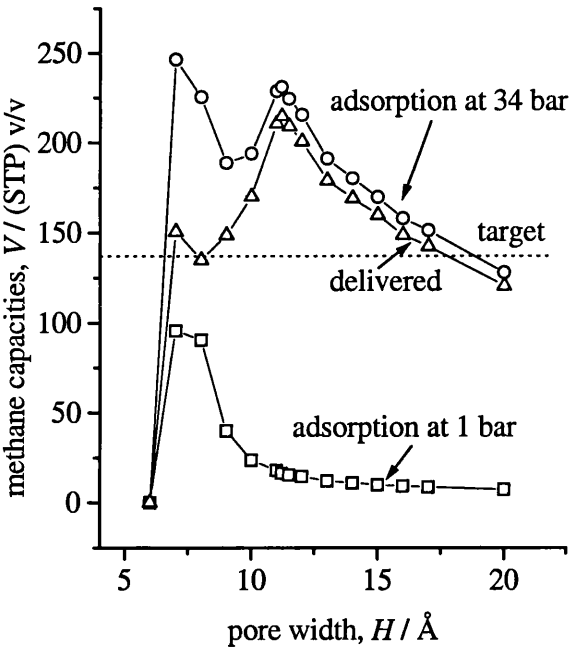

Figure 10-14. Simulated methane storage and delivered capacities of single-walled carbon slit pores at 298 K as a function of pore width, H. The storage and delivery pressures are 34 bar and 1 bar respectively.

Compared with slit carbons, SWCNT arrays are advantageous in the following two aspects: (1) The maximum capacity of 233 (STP) v/v for trigonal arrays of open SWCNTs is about 10% higher than that for slit carbons. (2) There is a wide range of array configurations that can give delivered capacities greater than the target, while in slit carbons the pore width is limited to a 10 Å range. This implies that if gaps can be introduced in between carbon nanotubes, the target is more achievable. On the other hand, activated carbons have the advantages of being cheap and easy to produce.

10.3 Methane storage in square arrays of SWCNTs at 298 K

Figures 10-15 to 10-18 show the delivered methane capacity of square arrays of open and closed SWCNTs as a function of tube diameter and separation. The variations of the capacities with varying tube diameter and separation and the optimal configurations are generally the same as in the case of trigonal arrays, though the maximum capacities are different, as shown in Table 10-1.

At small tube diameters and separations, there are marked increases in delivered volumetric capacities compared with trigonal arrays. For example, at D = 10 Å and G = 4 Å, the delivered capacity of the open square array is about 70 (STP) v/v, but is less than 30 (STP) v/v in the case of open trigonal array. That is, the capacity is more than doubled as more space is available. However, this improvement does not occur for larger tube diameters or larger tube separations. In fact, the maximum delivered

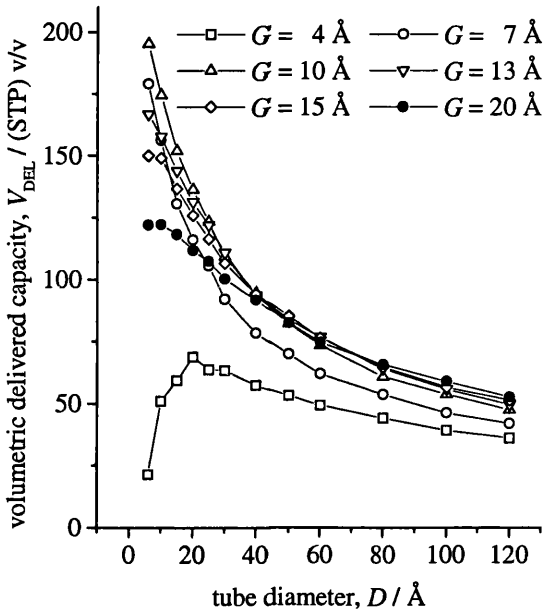

Figure 10-15. Simulated volumetric delivered capacity of methane at 298 K in square arrays of closed SWCNTs as a function of tube diameter, D, and separation, G. Storage and delivery pressures are 34 bar and 1 bar respectively.

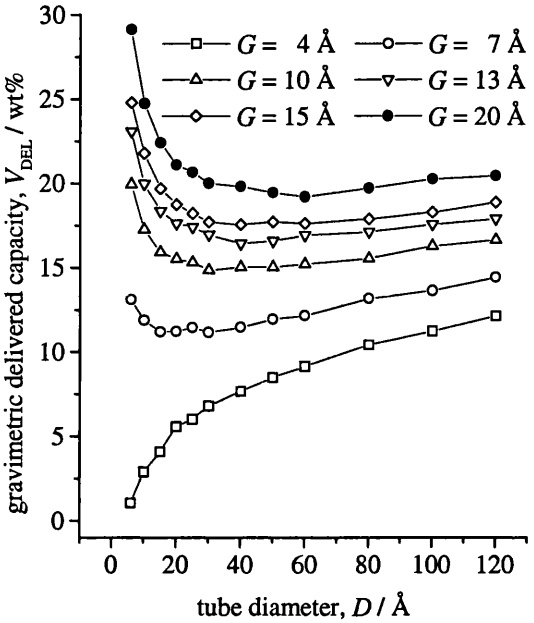

Figure 10-16. Simulated gravimetric delivered capacity of methane at 298 K in square arrays of closed SWCNTs as a function of tube diameter, D, and separation, G. Storage and delivery pressures are 34 bar and 1 bar respectively.

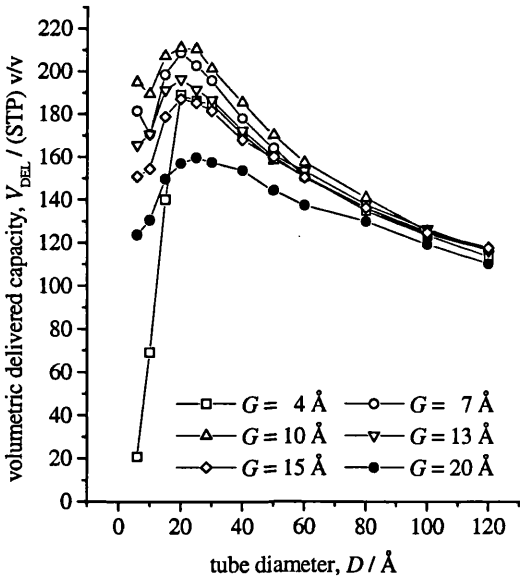

Figure 10-17. Simulated volumetric delivered capacity of methane at 298 K in square arrays of open SWCNTs as a function of tube diameter, D, and separation, G. Storage and delivery pressures are 34 bar and 1 bar respectively.

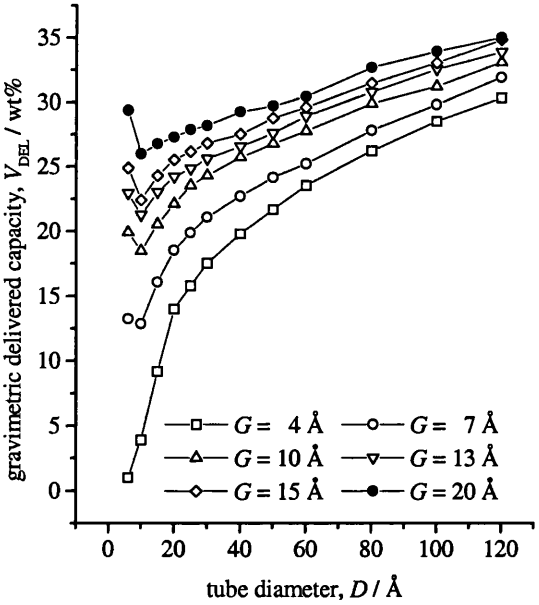

Figure 10-18. Simulated gravimetric delivered capacity of methane at 298 K in square arrays of open SWCNTs as a function of tube diameter, D, and separation, G. Storage and delivery pressures are 34 bar and 1 bar respectively.

volumetric capacity of open square arrays is 211 (STP) v/v, about 10% lower than that of open trigonal arrays. The reason is that in square arrays, adsorption potentials are less enhanced than in trigonal arrays.

Table 10-1. Optimal parameters for volumetric methane capacities at 298 K

arrays	tubes	Optimal D / Å		Optimal G / Å		Capacity / (STP)v/v	
		storage	delivered	storage	delivered	storage	delivered
Trigonal arrays	Closed	6	6	7	10	259	210
	Open	15	20	7	10	289	233
Square arrays	Closed	6	6	7	10	229	195
	Open	15	20	7	10	254	211

Storage pressure = 34 bar, Delivery pressure = 1 bar.

Different from volumetric capacities, gravimetric capacities of square arrays are generally higher than that of trigonal arrays. For example, the volumetric delivered capacity of an array with tubes of diameter of 6 Å and separation of 7 Å, the gravimetric capacity changes from 12 wt% for trigonal array to 13 wt% for square array. Generally, square arrays yield 6~10 wt% higher gravimetric capacities than trigonal arrays. Thus, from the gravimetric point of view, square arrays are better than trigonal arrays.

10.4 Summary and Conclusions

In summary, the following conclusions may be drawn from the above discussions:

(1) The maximum volumetric storage and delivered methane capacities are in trigonal arrays of open SWCNTs. At 34 bar, the maximum capacity is 289 (STP) v/v, nearly double the target. As a large amount of adsorbed methane is retained in the material at 1 bar, the delivered capacity is much lower than the storage capacity. If delivery pressure is 1 bar, then the maximum delivered capacity is 233 (STP) v/v, which is 10% higher than the maximum of single-walled carbon slit systems.

(2) Arrays of open tubes yield higher storage and delivered capacities than arrays of closed tubes. The increase is about 10% as far as the maximum capacities are concerned. Square arrays yield about 10% lower maximum volumetric capacities than trigonal arrays due to weaker intermolecular interactions in them. This means that any deviation from trigonal packing of tubes may result in a decrease in volumetric methane capacities. On the other hand, square arrays are better than trigonal arrays if gravimetric capacities are the main concern.

(3) Increasing storage pressure can increase storage and delivered capacities. However, the efficiency of increasing storage pressure is largely dependent on array configuration. The smaller the tube and tube separation, the lower the efficiency.

Adsorption isotherms can be fitted to the Tóth equation, which may be a useful empirical method to represent simulation data.

(4) The capacities of SWCNT arrays are related to their configuration. Capacities are mainly determined by array geometry. Thus, it is highly possible to predict methane storage and delivered capacities using characteristic parameters of the material, such as tube size and separation.

(5) Most features of methane storage in arrays of SWCNTs are similar to those of hydrogen storage, though there are some differences due to different storage conditions used and differences in the nature of the systems.

Chapter 11
Correlating Capacities of Nanotube Arrays

As discussed in Chapter 10, it is possible to use the Tóth or similar empirical equations to predict storage and delivered capacities of nanotube arrays, provide the parameters in these equations are determined either by previous experiments or a limited set of adsorption data. From an engineering point of view, it is highly desirable to predict the capacities using a few characteristic quantities that are easily determined by experiment. BET surface areas and pore volumes are examples of such quantities. In this chapter, efforts are made to correlate both methane and hydrogen capacities with such quantities.

11.1 Capacities as functions of pore volume

The pore volume here is defined as the volume of the space within the adsorbent open to the adsorptive per unit mass of the solid and is conveniently expressed in $cm^3\ g^{-1}$. More specifically, it is the open pore volume, as opposed to the closed pore volume which is inaccessible to fluids penetrating from external surfaces. This quantity is determined directly from the array parameters.

Simulated hydrogen and methane capacities of arrays of single-walled carbon nanotubes as functions of pore volume are shown in Figures 11-1 to 11-4. The storage and delivery pressures for methane are 34 bar and 1 bar respectively, and the temperature is 298 K. The storage pressure, delivery pressure and temperature for hydrogen are 70 bar, 1 bar and 77 K respectively. Large scatter exists at small values of pore volume, though there are correlations between volumetric capacities and pore volume (Figures 11-1 and 11-3). The volumetric capacities increase with increasing pore volume at small pore volumes, then reach a maximum and finally decrease with further increase of pore volume. This is because at small pore volumes, increasing pore volume increases the space available to the adsorptive while the adsorption potential is still strongly enhanced. The increase in the volume of adsorbed fluid exceeds the increase in pore volume. This results in increased capacity. On further increase of pore volume, the average adsorption potential weakens and the increase in the volume of adsorbed fluid is less than the increased pore volume. Hence volumetric capacities decrease.

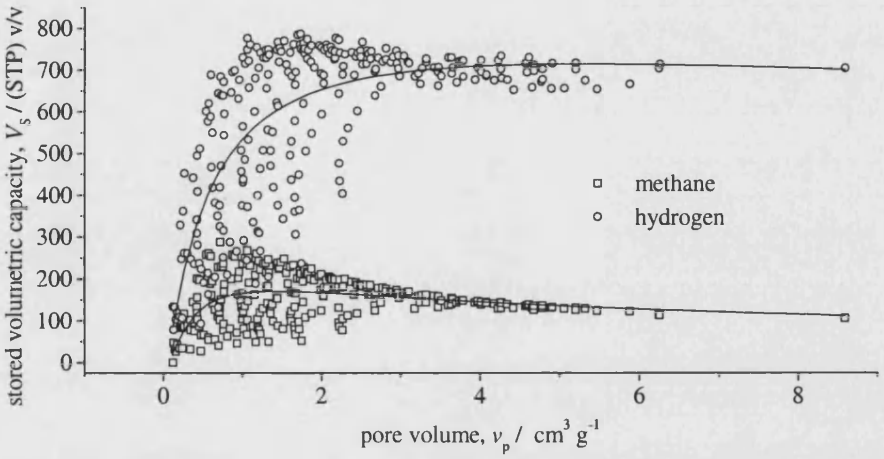

Figure 11-1. Simulated volumetric stored methane (square) and hydrogen (circle) capacities as functions of pore volume of SWCNT arrays. The curves are best fits of Equation (11-1) to the capacity data and are represented by Equations (11-2) and (11-4). The storage pressure for methane is 34 bar and the temperature is 298 K. The storage pressure and temperature for hydrogen are 70 bar and 77 K respectively.

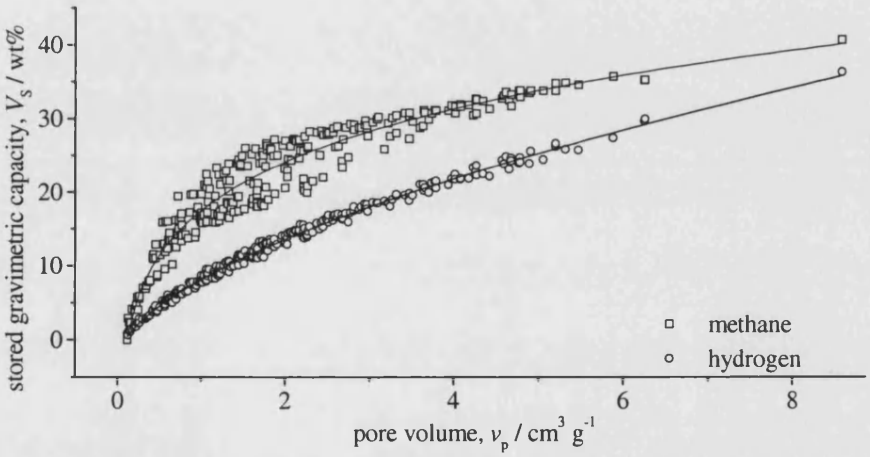

Figure 11-2. Simulated gravimetric stored methane (square) and hydrogen (circle) capacities as functions of pore volume of SWCNT arrays. The curves are best fits of Equation (11-6) to the capacity data and are represented by Equations (11-7) and (11-9). The storage pressure for methane is 34 bar and the temperature is 298 K. The storage pressure and temperature for hydrogen are 70 bar and 77 K respectively.

For convenience, an empirical equation has been chosen to correlate the volumetric capacities with pore volume. The equation is as follows:

$$y = A\left(\frac{x}{x_P}\right)^C e^{-\left(\frac{x}{x_P}\right)^C} \qquad (11\text{-}1)$$

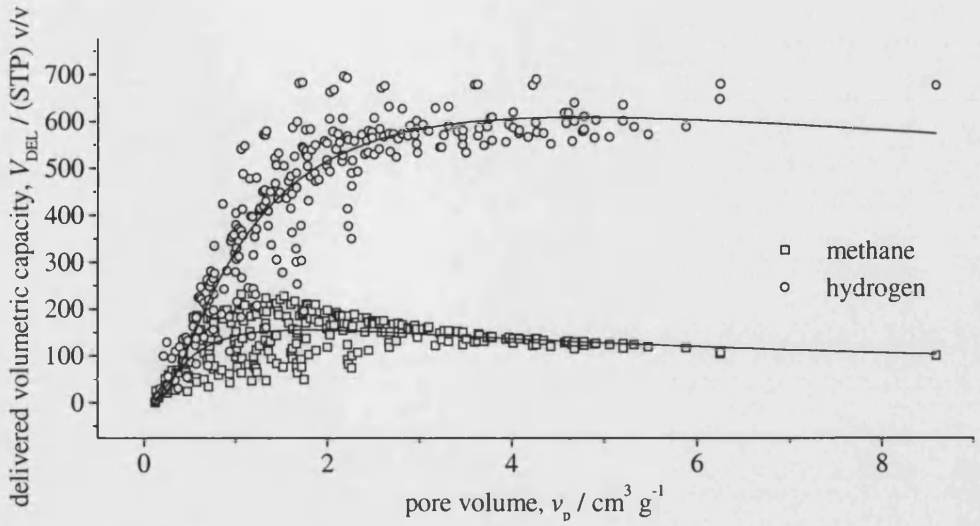

Figure 11-3. Simulated volumetric delivered methane (square) and hydrogen (circle) capacities as functions of pore volume of SWCNT arrays. The curves are best fits of Equation (11-1) to the capacity data and are represented by Equations (11-3) and (11-5). The storage and delivery pressures for methane are 34 bar and 1 bar respectively and the temperature is 298 K. The storage and delivery pressures and temperature for hydrogen are 70 bar, 1 bar and 77 K respectively.

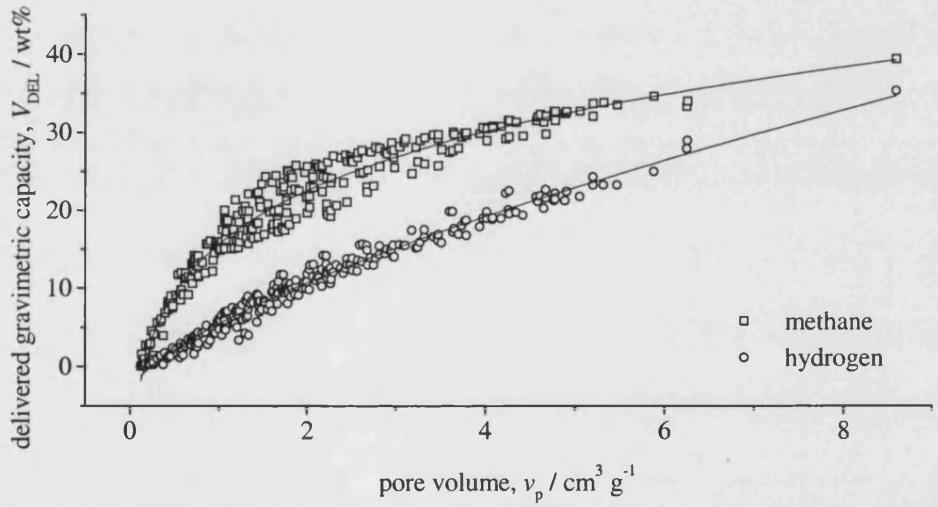

Figure 11-4. Simulated gravimetric delivered methane (square) and hydrogen (circle) capacities as functions of pore volume of SWCNT arrays. The curves are best fits of Equation (11-6) to the capacity data and are represented by Equations (11-8) and (11-10). The storage and delivery pressures for methane are 34 bar and 1 bar respectively and the temperature is 298 K. The storage and delivery pressures and temperature for hydrogen are 70 bar, 1 bar and 77 K respectively.

where y stands for the capacity ((STP) v/v), x stands for the independent variable and is pore volume here (v_p). A, C and x_p are three parameters. This equation was chosen because of its simplicity. In Equation (11-1), the maximum value of y will be A/e and the value of the independent variable corresponding to y_{max} is x_p. Equation (11-1) was fitted to the capacity data in Figures 11-1 and 11-3 and the results are:

$$V_S = 463\left(\frac{v_P}{1.44}\right)^{-0.605} e^{-\left(\frac{v_P}{1.44}\right)^{-0.605}} \quad (11\text{-}2)$$

$$V_{DEL} = 422\left(\frac{v_P}{1.77}\right)^{-0.673} e^{-\left(\frac{v_P}{1.77}\right)^{-0.673}} \quad (11\text{-}3)$$

for stored and delivered methane volumetric capacities respectively. Equation (11-2) shows that the maximum storage methane capacity of ~ 170 (STP) v/v occurs at v_p = 1.44 m^3 g^{-1}. However, the deviation of simulated data from the best fit around this part is huge, ranging from 50 to 250 (STP) v/v. At high pore volumes, the best fit seems to be a good estimate of the simulation data. The maximum delivered capacity of ~ 155 (STP) v/v can be obtained from Equation (11-3) at v_p = 1.77 m^3 g^{-1}, which is lower than the predicted maximum of stored capacity. Also, the optimal pore volume for delivered capacity is larger than that for stored capacity, as expected.

For hydrogen, the corresponding equations are as follows:

$$V_S = 1942\left(\frac{v_P}{5.25}\right)^{-0.407} e^{-\left(\frac{v_P}{5.25}\right)^{-0.407}} \quad (11\text{-}4)$$

$$V_{DEL} = 1653\left(\frac{v_P}{4.73}\right)^{-0.609} e^{-\left(\frac{v_P}{4.73}\right)^{-0.609}} \quad (11\text{-}5)$$

The values of *C* parameters for hydrogen are smaller than for methane. The maximum stored and delivered capacities of 714 and 608 (STP) v/v occur at v_p = 5.25 and 4.73 m^3 g^{-1} respectively. These values are much higher than those for methane. Curves corresponding to Equations (11-2) to (11-5) are plotted in Figures (11-1) and (11-3). Generally, Equation (11-1) fits the data fairly well, but there is considerable scatter around the fitted lines. The fits are better for hydrogen than for methane and are better for delivered capacities than for storage capacities. The discrepancy exists mainly at small pore volumes, where the same pore volume corresponds to a number of array configurations that may have marked difference in the adsorption potentials. However,

as the pore volume is defined on a per unit mass of solid basis while the volumetric capacity is defined on a per unit volume of solid basis, these scatter are acceptable.

Gravimetric capacities are much better correlated with pore volume, as can be seen from Figures 11-2 and 11-4. Compared with volumetric capacities, gravimetric capacities increase progressively with increasing pore volume, rapidly at first then less so at large pore volumes. In order to predict the gravimetric capacities, the following empirical equation was used to correlate the capacities with pore volume:

$$y = A + Bx^C \tag{11-6}$$

where y stands for the gravimetric capacity (wt%), x stands for the independent variable and is pore volume here (v_p), and A, B and C are constants. This equation fits the data very well as shown in Figures 11-2 and 11-4 by the solid lines. The fitted equations for stored and delivered methane capacities are:

$$V_S = -52.5 + 70.0 v_P^{0.130} \tag{11-7}$$

$$V_{DEL} = -54.8 + 70.5 v_P^{0.134} \tag{11-8}$$

The corresponding equations for hydrogen are:

$$V_S = -2.59 + 10.7 v_P^{0.593} \tag{11-9}$$

$$V_{DEL} = -3.23 + 8.67 v_P^{0.686} \tag{11-10}$$

Comparison with Figures 11-1 and 11-3 shows that the scattering here is much smaller, especially in the case of hydrogen. This is because both gravimetric capacities and pore volume are defined on the same basis, that is per unit mass of solid carbon. Therefore, it is more accurate to predict gravimetric capacities rather than volumetric capacities from pore volume. When density of the adsorbent is known, volumetric capacity can be derived from the density and the predicted gravimetric capacity. Equations (11-7) to (11-10) show that A parameters in all cases are negative, indicating that non-zero capacity only can be obtained with adsorbents with pore volumes larger than a critical

value. This value for methane storage, delivery, hydrogen storage and delivery capacities are 0.11, 0.15, 0.09 and 0.24 $m^3 g^{-1}$ respectively.

11.2 Capacities as functions of fractional porosity

From the above discussion, it is better to predict gravimetric capacities of SWCNT arrays from pore volume because the same basis is used to define both quantities. Thus, it is natural to think that it may be better to predict volumetric capacities from some parameter that is defined on a volumetric basis. One parameter of this kind is the fractional open porosity which is defined as the ratio of the volume of open pores divided by the total volume of the material (including pores). This parameter is determined directly from the array geometry. The four capacities as functions of fractional porosity are shown in Figures 11-5 to 11-8.

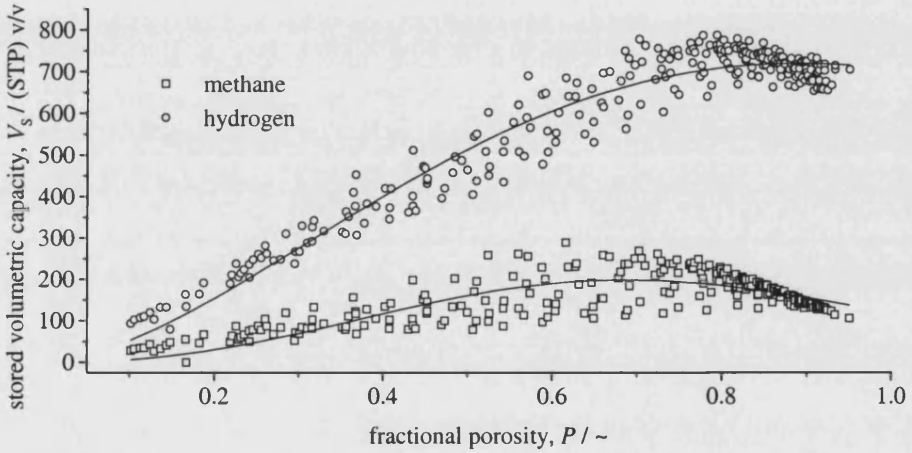

Figure 11-5. Simulated volumetric stored methane (square) and hydrogen (circle) capacities as functions of fractional porosity of SWCNT arrays. The curves are best fits of Equation (11-1) to the capacity data and are represented by Equations (11-11) and (11-13). The storage pressure for methane is 34 bar and the temperature is 298 K. The storage pressure and temperature for hydrogen are 70 bar and 77 K respectively.

As can be seen from Figures 11-5 to 11-8, there is some correlation between the capacities and fractional porosity, though with some scatter. The variations of these capacities with varying fractional porosity are similar to the variations with changing pore volume. Thus, Equations (11-1) and (11-6) were used to fit the data and the curves in Figures 11-5 to 11-8 are plotted according to the best fits. The best fits to the methane volumetric data are:

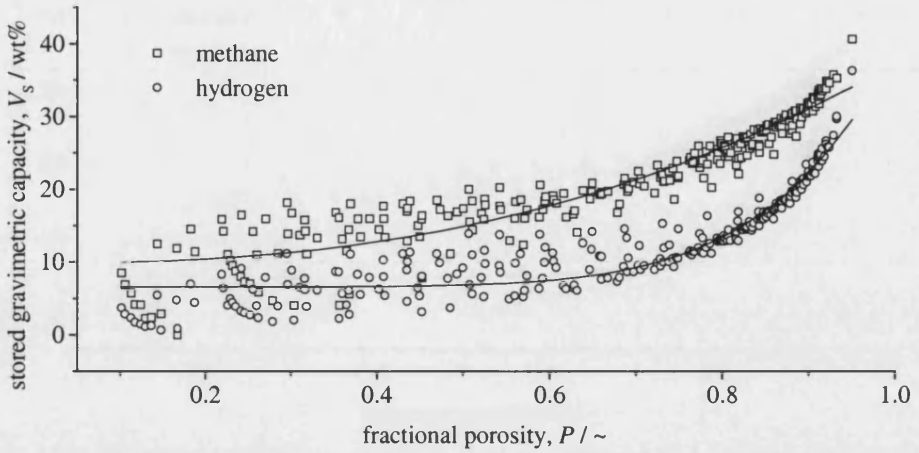

Figure 11-6. Simulated gravimetric stored methane (square) and hydrogen (circle) capacities as functions of fractional porosity of SWCNT arrays. The curves are best fits of Equation (11-6) to the capacity data and are represented by Equations (11-15) and (11-17). The storage pressure for methane is 34 bar and the temperature is 298 K. The storage pressure and temperature for hydrogen are 70 bar and 77 K respectively.

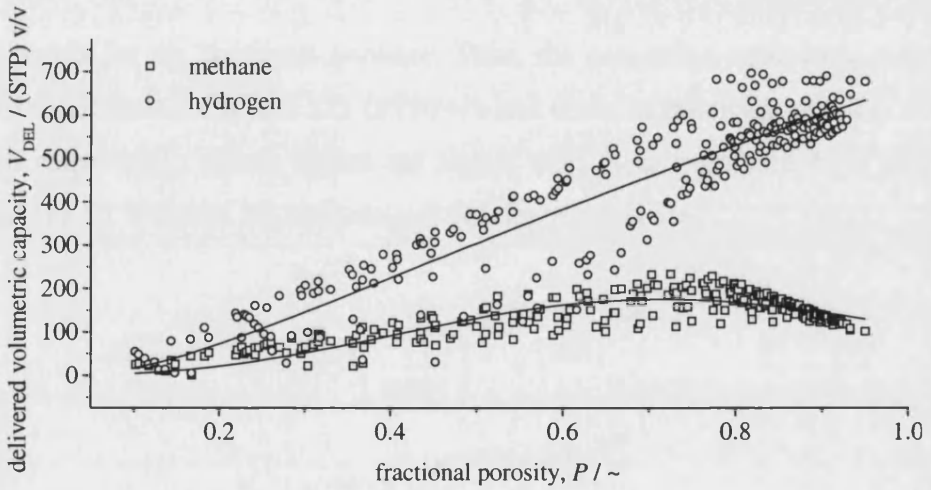

Figure 11-7. Simulated volumetric delivered methane (square) and hydrogen (circle) capacities as functions of fractional porosity of SWCNT arrays. The curves are best fits of Equation (11-1) to the capacity data and are represented by Equations (11-12) and (11-14). The storage and delivery pressures for methane are 34 bar and 1 bar respectively and the temperature is 298 K. The storage and delivery pressures and temperature for hydrogen are 70 bar, 1 bar and 77 K respectively.

$$V_S = 538\left(\frac{P}{0.686}\right)^{2.30} e^{-\left(\frac{P}{0.686}\right)^{2.30}} \qquad (11\text{-}11)$$

$$V_{DEL} = 475\left(\frac{P}{0.715}\right)^{2.42} e^{-\left(\frac{P}{0.715}\right)^{2.42}} \qquad (11\text{-}12)$$

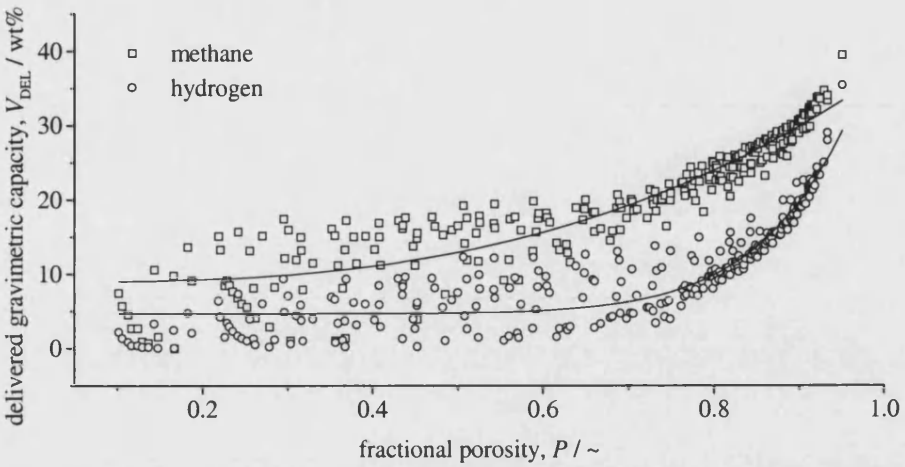

Figure 11-8. Simulated gravimetric delivered methane (square) and hydrogen (circle) capacities as functions of fractional porosity of SWCNT arrays. The curves are best fits of Equation (11-6) to the capacity data and are represented by Equations (11-16) and (11-18). The storage and delivery pressures for methane are 34 bar and 1 bar respectively and the temperature is 298 K. The storage and delivery pressures and temperature for hydrogen are 70 bar, 1 bar and 77 K respectively.

where P stands for the fractional porosity. Thus, the maximum volumetric stored and delivered capacities are 198 and 175 (STP) v/v and occur at fractional porosity of 0.686 and 0.715 respectively. These values are higher than those predicted from Equations (11-2) and (11-3). The best fits to hydrogen volumetric data are:

$$V_S = 1954\left(\frac{P}{0.891}\right)^{1.647} e^{-\left(\frac{P}{0.891}\right)^{1.647}} \quad (11\text{-}13)$$

$$V_{DEL} = 2922\left(\frac{P}{2.21}\right)^{1.46} e^{-\left(\frac{P}{2.21}\right)^{1.46}} \quad (11\text{-}14)$$

From Equation (11-13), the maximum hydrogen stored capacity is 719 (STP) v/v and occurs at $P = 0.891$. The delivered volumetric capacity does not correlate very well with fractional porosity. However, if $P \sim 0.9$, the delivered capacity from Equation (11-14) is 601 (STP) v/v, which is in a good agreement with the maximum predicted from Equation (11-5). The best fits of Equation (11-6) to gravimetric data are presented in Equations (11-15) and (11-16) for methane and in Equations (11-17) and (11-18) for hydrogen:

$$V_S = 9.86 + 27.3P^{2.44} \quad (11\text{-}15)$$

$$V_{DEL} = 8.92 + 28.1P^{2.81} \quad (11\text{-}16)$$

$$V_S = 6.58 + 33.0P^{7.05} \quad (11\text{-}17)$$

$$V_{DEL} = 4.68 + 38.8P^{9.01} \quad (11\text{-}18)$$

From Figures 11-6 and 11-8, there is large scatter around the best fit curves, especially at small porosities. At high porosities, there is less scatter and Equations (11-15) to (11-18) give similar up limits for gravimetric capacities of about 40 wt%.

The volumetric capacities are better correlated to fractional porosity rather than gravimetric capacities as it is expected. It is believed that Equation (11-13) can be used to predict volumetric storage capacities for hydrogen quite well, though the equation does not describe the correlation very well (Figure 11-5).

11.3 Capacities as functions of BET surface areas

BET surface area is a commonly used parameter to characterise porous materials. Here, low pressure part of simulated nitrogen adsorption isotherms is fitted with the linear form of the BET Equation and BET surface area is then calculated from the intercept and slope (section 6.1.4). The methane and hydrogen capacities as functions of BET surface areas are shown in Figures 11-9 to 11-12. Generally, the volumetric capacities are fairly well correlated to BET surface areas and can be described by the following two empirical equations for methane:

$$V_S = 499\left(\frac{A}{3987}\right)^{0.304} e^{-\left(\frac{A}{3987}\right)^{0.304}} \quad (11\text{-}19)$$

$$V_{DEL} = 494\left(\frac{A}{8117}\right)^{-0.406} e^{-\left(\frac{A}{8117}\right)^{-0.406}} \quad (11\text{-}20)$$

where A is the BET surface area. Corresponding equations for hydrogen are:

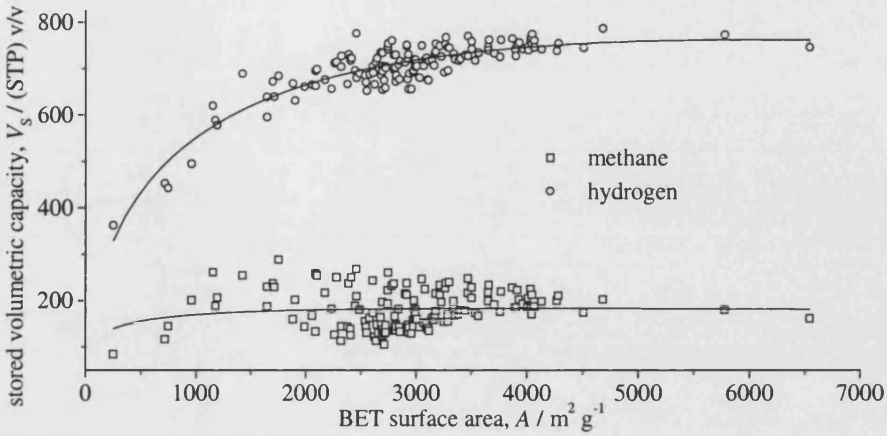

Figure 11-9. Simulated volumetric stored methane (square) and hydrogen (circle) capacities as functions of BET surface area of SWCNT arrays. The curves are best fits of Equation (11-1) to the capacity data and are represented by Equations (11-19) and (11-21). The storage pressure for methane is 34 bar and the temperature is 298 K. The storage pressure and temperature for hydrogen are 70 bar and 77 K respectively.

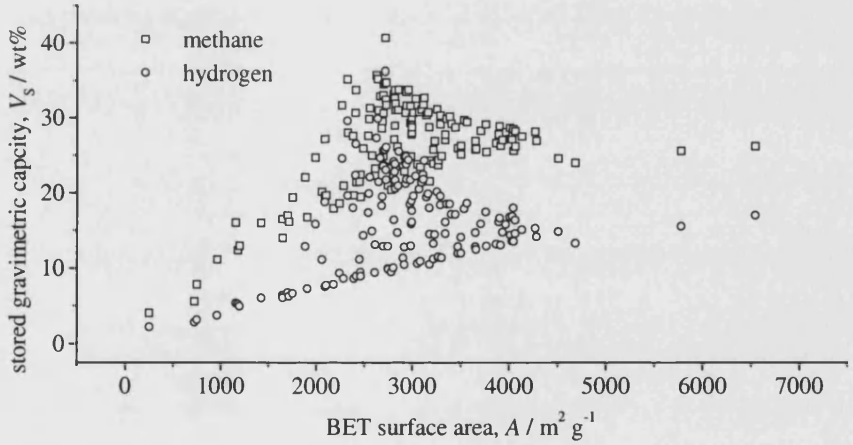

Figure 11-10. Simulated gravimetric stored methane (square) and hydrogen (circle) capacities as functions of BET surface area of SWCNT arrays. The storage pressure for methane is 34 bar and the temperature is 298 K. The storage pressure and temperature for hydrogen are 70 bar and 77 K respectively.

$$V_S = 2071\left(\frac{A}{6028}\right)^{0.517} e^{-\left(\frac{A}{6028}\right)^{0.517}} \qquad (11\text{-}21)$$

$$V_{DEL} = 1605\left(\frac{A}{4185}\right)^{-1.02} e^{-\left(\frac{A}{4185}\right)^{-1.02}} \qquad (11\text{-}22)$$

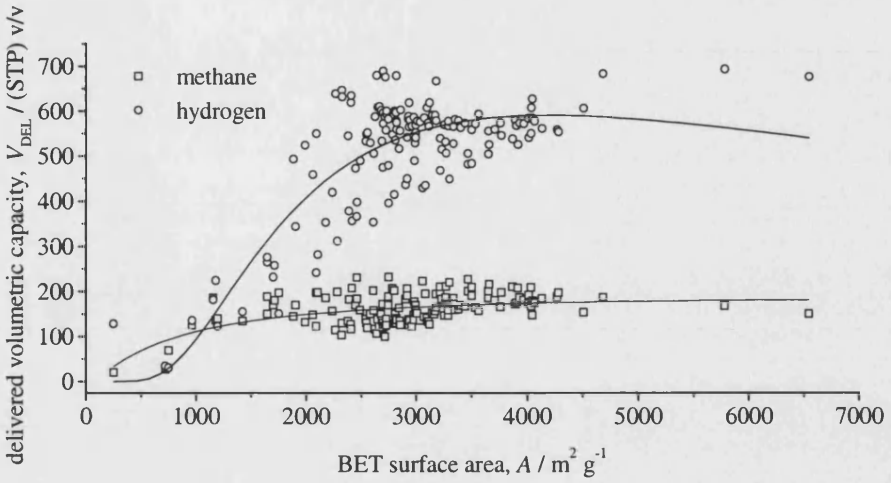

Figure 11-11. Simulated volumetric delivered methane (square) and hydrogen (circle) capacities as functions of BET surface area of SWCNT arrays. The curves are best fits of Equation (11-1) to the capacity data and are represented by Equations (11-20) and (11-22). The storage and delivery pressures for methane are 34 bar and 1 bar respectively and the temperature is 298 K. The storage and delivery pressures and temperature for hydrogen are 70 bar, 1 bar and 77 K respectively.

The maximum capacities predicted from Equations (11-19) to (11-22) are 184, 182, 762 and 590 (STP) v/v and occur at BET surface areas of 3987, 8117, 6028 and 4185 m^2 g^{-1} respectively. However, gravimetric capacities are complicated functions of BET surface area. The graphs are interesting and more studies are required to explain them.

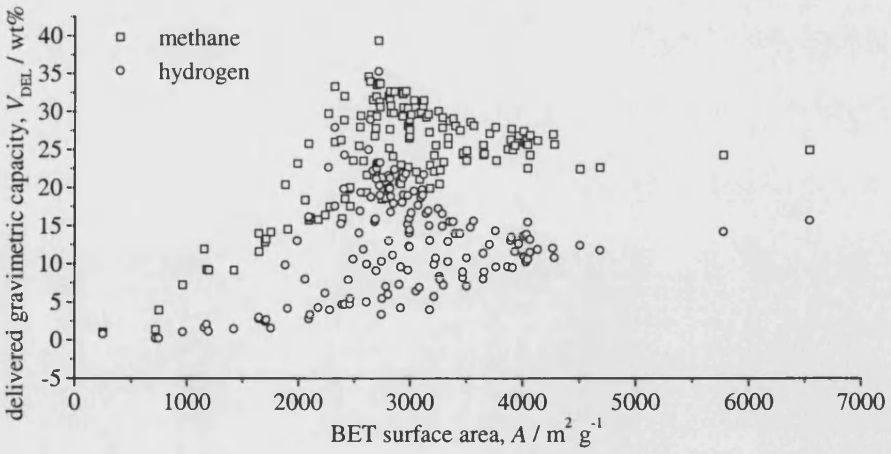

Figure 11-12. Simulated gravimetric delivered methane (square) and hydrogen (circle) capacities as functions of the BET surface area of SWCNT arrays. The storage and delivery pressures for methane are 34 bar and 1 bar respectively and the temperature is 298 K. The storage and delivery pressures and temperature for hydrogen are 70 bar, 1 bar and 77 K respectively.

11.4 Summary and conclusions

Stored and delivered capacities for methane and hydrogen are correlated with pore volume, fractional porosity and the BET surface areas. From this study, the gravimetric capacities can be best estimated from the pore volume, while the volumetric capacities may be better estimated from BET surface areas and / or fractional porosity. However, further studies are required to establish better means of predicting gas storage capacities in carbon nanotubes and to validate these by means of experimental measurements.

Section 4

Conclusions and Future Work

Chapter 12
Conclusions

12.1 Conclusions

The following conclusions may be drawn from the present work:

(1) Marked enhancement of adsorption potentials only can be found in small slit micropores in carbons, but can be found in carbon cylinders as wide as 50 Å. This enhancement of potential in cylindrical pores compared to slit pores, indicates that carbon nanotubes might be a good adsorbent compared to active carbons. Pore wall thickness has marked influence on the adsorption potentials (The thicker the pore wall, the deeper the potential well) in thin wall pores and pore walls with five or more carbon layers can be effectively regarded as infinitely thick. Interstitial potentials in nanotube arrays can be very strong due to the overlap of potentials from different tubes, indicating that interstitial adsorption can make a marked contribution to adsorption in carbon nanotube arrays.

(2) Simulated nitrogen adsorption at 77 K in slit-shaped pores, which model pores in activated carbons is strongly dependent on pore size. Adsorption in small micropores shows type I adsorption behaviour, while that in larger micropores and small mesopores shows type IV adsorption behaviour with clear monolayer formation and condensation steps. The density of the adsorbed phase at saturation is around that of bulk liquid nitrogen. Pore wall structures have marked effects on the adsorption behaviour of activated carbons in thin wall pores and walls with five or more graphene sheets can be effectively regarded as infinitely thick. The defects in pore walls mainly affect the monolayer formation pressure. The effects of the interlayer spacing are small and can be neglected in most cases. In thin walled small pores, the interaction between fluid molecules adsorbed in neighbouring slits and the contribution of neighbouring pore walls to the adsorption potential have marked effects on the low pressure part of adsorption isotherms. In large and thick-walled pores, this influence is small and can be neglected. The value of the Lennard-Jones (LJ) energy and length parameters used in the simulation, have very marked

influence on the results, especially on the pore filling pressures. The effects of changing the LJ length parameter are much more marked than that of changing the LJ energy parameter. Therefore, the selection of LJ parameters for molecular simulations should be made with care and possible errors in these parameters and their effects on the simulation results should be considered.

(3) Simulated endohedral adsorption isotherms of small isolated carbon nanotubes are of type I, while those of large tubes are of type IV. The adsorbed nitrogen density is higher than that of liquid nitrogen and is also higher than that in carbon slits. Tube wall thickness has significant effects on the adsorption of thin wall tubes. When the number of graphene sheets in the walls exceeds five, the wall can be effectively regarded as infinitely thick. The amount adsorbed exohedrally increases with increasing tube diameter. In open tubes, the molecules adsorbed inside and outside the tubes interact with each other, and thus both endohedral and exohedral adsorption are enhanced. Adsorption in isolated open tubes starts with the formation of the endohedral monolayer, and is then followed by the formation of the exohedral monolayer and finally condensation of endohedral adsorption and building up of further exohedral layers. Exohedral adsorption might be more important than endohedral adsorption in applications such as gas storage.

(4) Adsorption isotherms of nitrogen adsorbed at 77 K in arrays of SWCNTs with small tube diameters and separations are of type I, showing microporous behaviour. Isotherms of arrays with large tube separations or large tube diameters are of type IV, showing both monolayer formation and saturation. The amount adsorbed is dominated by geometrical factors, *i.e.* tube diameter and separation. At saturation, the packing density of the adsorbed phase is close to that of bulk liquid nitrogen. In arrays with intermediate tube separations, the packing density is higher than that of bulk liquid nitrogen. Endohedral packing density does not change much with chaging tube separations, G, while exohedral packing density is sensitive to G and shows a maximum at $G \sim 10$ Å.

(5) Close packed nanotube arrays with tube diameters that correspond to structures observed experimentally have very low adsorption capacities. Introducing gaps between the tubes forming the arrays can markedly improve the capacities and the

highest capacities come from the arrays with the smallest tubes but with sufficiently large tube separations. In such arrays, interstitial adsorption is predominant and opening up the tubes is not necessary to improve capacities. This indicates that dispersed nanotube materials may have capacities higher than close packed aligned nanotube materials.

(6) Very high BET surface areas and very high amounts adsorbed can be reached with certain array configurations. BET surface areas can even be higher than most experimentally found values of activated carbons. This suggests that carbon nanotubes could be a good adsorbent, provide that gaps can be introrduced between the tubes.

(7) Simulated nitrogen adsorption isotherms are in reasonable agreement with experimental adsorption data.

(8) At ambient temperature, volumetric stored and delivered hydrogen capacities of SWCNT arrays are well below the DOE target for transport (695 (STP) v/v). Even with storage pressures up to 200 bar, the capacities are only a little higher than 1/3 of the DOE target and are no better than activated carbons. Thus from the volumetric point of view, carbon nanotubes are not good for hydrogen storage at room temperature. In the case of gravimetric capacities, delivered capacities in excess of the DOE target (6.5 wt%) may be obtained with pressures up to 200 bar and with some favourable SWCNT array configurations. This indicates that carbon nanotubes as a hydrogen storage medium are more promising on a gravimetric basis than on a volumetric basis.

(9) At 77 K and 70 bar, the volumetric stored capacities of hydrogen in some favourable configurations of SWCNTs can be as high as 800 (STP) v/v. However, the highest delivered capacity with storage pressure of 70 bar and delivery pressure of 1 bar is only 696 (STP) v/v, just above the DOE target. Gravimetric capacities can be as high as several times the DOE target, thus in hydrogen storage the volumetric target is a more demanding requirement. Favourable arrays for high hydrogen capacities comprise small tubes and intermediate tube separations, where exohedral adsorption

plays a dominant role. Thus, introducing gaps into between the tubes may be vital to the application of carbon nanotubes as a hydrogen storage medium.

(10) Carbon nanotubes are better than activated carbons for hydrogen storage at 77 K as far as maximum capacities are concerned. Also, a large range of array configurations can yield capacities higher than 550 (STP) v/v that is the maximum capacity of single-walled slit carbons. However the experimental production of carbon nanotubes needs to be optimised to explore this further.

(11) Simulated hydrogen storage capacities of activated carbons are in good agreement with experimentally reported results both at room temperature and 77 K. Hydrogen capacities of close packed arrays of SWCNTs are much lower than experimental results at both 298 K and 77 K. When sufficiently large gaps are introduced between nanotubes, simulation results can match experimental results. This suggests that experimentally nanotubes either are not closely packed or are dispersed at high pressures.

(12) Maximum stored and delivered methane volumetric capacities are in open trigonal SWCNT arrays. At 34 bar, the maximum stored capacity is 289 (STP) v/v, more than double the target (137 (STP) v/v). If delivery pressure is 1 bar, then the maximum delivered capacity is 233 (STP) v/v, that is 10 % higher than the maximum for single-walled carbon slit systems.

(13) Methane and hydrogen stored and delivered capacities are correlated with pore volume, fractional porosity and BET surface area. From this study, the gravimetric capacities can be best predicted from the pore volume, while the volumetric capacities may be better predicted from BET surface areas and / or fractional porosity. The adsorption isotherms of both methane and hydrogen can be fitted to the Tóth equation very well, thus provide another way to predict capacities of carbon nanotubes, though more study is required. The Tóth isotherm Equation is a good fit to simulated adsorption data in SWCNT arrays, and might be a useful tool in predicting adsorption for experimental systems.

12.2 Publications arising from this work

(1) **Yin, Y. F.**, Mays, T. J. and McEnaney, B. (1997). Adsorption potentials and simulations in carbon slits and cylinders. *Carbon '97*, Penn State, USA, 66-67.

(2) McEnaney, B., Mays, T. J., **Yin, Y. F.**, Chen, X. and Rodriguez-Reinoso, F. (1997). Estimating the dimensions of ultramicropores using molecular probes. In McEnaney *et al.* (eds.) *Characterisation of Porous Solids IV*, 125-132.

(3) **Yin, Y. F.**, McEnaney, B. and Mays, T. J. (1998). Dependence of GCEMC simulations of nitrogen adsorption on activated carbons on input parameters. *Carbon* **36**(10), 1425-1432.

(4) **Yin, Y. F.** and Mays, T. J. (1998). Adsorption in carbon nanotubes. *Carbon '98*, Strasbourg, France, 831-832.

(5) **Yin, Y. F.**, Mays, T. J. and McEnaney, B. (1998). Adsorption potentials and simulations in carbon slits and cylinders. In Francis Meunier (ed.) *Fundamentals of adsorption 6,* 261-266.

(6) McEnaney, B., Mays, T. J., and **Yin, Y.F.** (1998). Microporosity and its characterisation. *Extended Abstracts, NATO Advanced Study Institute on Advanced Carbon Materials*, Anatalya, Turkey, 17-21.

(7) McEnaney, B., Chen, X.S., Mays, T.J., Tennison, S., and **Yin, Y.F.** (1998). Porous carbons for gas storage and gas separation. *Extended Abstracts, NATO Advanced Study Institute on Advanced Carbon Materials*, Anatalya, Turkey, 54-58.

(8) **Yin, Y. F.**, Mays, T. J. and McEnaney, B. (1999). Nitrogen adsorption in carbon nanotube arrays. *Carbon '99.* Charleston, South Carolina, USA, 90-91.

(9) **Yin, Y. F.**, Mays, T. J. and McEnaney, B. (1999). Hydrogen storage in carbon nanotube arrays. *Carbon '99.* Charleston, South Carolina, USA, 784-785.

(10) **Yin, Y.F.**, Mays, T.J. and McEnaney, B. (1999). Adsorption of nitrogen in carbon nanotube arrays, *Langmuir* **15**, 8714-8718.

(11) Alain, E., **Yin, Y. F.**, Mays, T. J. and McEnaney, B. (2000). Molecular simulation and measurement of adsorption in porous carbon nanotubes. *Studies in Surface Science and Catalysis* **128**, 313-322.

(12) McEnaney, B., Alain, E., **Yin, Y. F.** and Mays, T. J. (2000). Porous carbons for gas storage and separation. NATO, in press.

(13) **Yin, Y. F.**, Mays, T. J. and Alain, E. (2000). Measurements and simulations of gas adsorption in arrays of single-walled carbon nanotubes. *Carbon '2000*, Berlin, Germany, in press.

(14) **Yin, Y. F.**, Mays, T. J., Alain, E. and McEnaney, B. (2000). Carbon nanotube adsorbents. ACS proceedings, in press.

(15) **Yin, Y. F.**, Mays, T. J. and McEnaney, B. (2000). Molecular simulations of hydrogen storage in carbon nanotube arrays. *Langmuir*, submitted.

Chapter 13
Future Work

The suggested future work is as follows.

(1) *Modifications to the model carbons.* Although the present models represent activated carbons and carbon nanotubes fairly well and modifications will probably not make dramatic changes to the simulation results, more work is required to make the models more representative of the real material. This includes (a) defects in carbon sheets, such as missing carbon atoms; (b) finite size effects; (c) non-parallel pore wall; (d) surface chemical heterogeneity, such as H, O, N and S in carbon layers and (e) structural heterogeneity, such as non-uniform tube diameter. Models taking all these into consideration at the same time based on experimental observations will virtually rebuild the microstructure of the material. Molecular simulations based on such models may yield much more informative results.

(2) *Modifications to the interatomic potential.* Whilst the Lennard-Jones potential is one of the most popular potential expressions for simple intermolecular forces, other potentials may be used to calculate both the fluid-fluid and fluid-solid interactions. Some modifications to the approach to the interaction potential employed in this study can be made: (a) pair-wise summation rather than integration; (b) three-body interactions; (c) site-site interactions and (d) quantum mechanical effects. These effects could be significant in small pores and at low temperatures and / or high pressures.

(3) *Enhanced molecular simulations.* A number of parameters are used to control the simulation cycle and these may have marked effects on the results. Therefore, the actual effects of varying these parameters are of interest. These parameters include (a) number of runs; (b) size of simulation cells; (c) ratio of creation, destruction and translation moves and (d) the cut-off distance in potential calculations.

(4) *Adsorption kinetics.* Monte Carlo molecular simulations only provide equilibrium properties of the adsorbent-adsorbate system, but does not provide any information

on the kinetics of adsorption processes. This is particularly important in the case of carbon nanotubes, where the material has a very high aspect ratio. Thus, molecular dynamics study of diffusion in nanotube arrays of gases, especially fuel gases, is of great interest. The importance of this kind of study with respect to gas storage is that some kind of nanotube arrays with high capacities may have very low diffusion rates, so that it may take an unacceptably long time to fill the storage tank and to release the gas. It is also interesting to research whether the diffusion in interstitial spaces is faster than inside tubes.

(5) *Comparison with experiment.* Although simulation results presented in this study are in a good agreement with experimental observations, more experimental measurements on adsorption of different gases in carbon nanotubes are required to make a thorough comparison with simulations. This requires purer nanotube samples and the better characterisation of the structure of the nanotube samples.

(6) *Molecular sieving.* As diameters of carbon nanotubes are thought to be controllable and the interstitial and endohedral space may have different properties, carbon nanotubes could act as molecular sieve materials. Therefore, study of the possible molecular sieve effects of carbon nanotube bundles with different tube diameters would be of interest. Also, the possibility of carbon nanotubes as gas separation materials might be studied by using similar techniques employed in this study.

(7) *Adsorption of different gases in carbons at different temperatures.* Molecular simulations can be applied to adsorption of different gases in activated carbons and carbon nanotubes at high temperatures and pressures to reveal the high pressure and high temperature adsorption properties of these materials. The advantage of this kind of work is that molecular simulations do not have the limitations of experimental observations, where the equipment available restricts achievable temperatures and pressures. The importance of this kind of study is two fold: (a) to validate existing theoretical and empirical adsorption isotherm equations for these materials and gases, and hence make better interpretations of these equations in terms of the properties of the adsorption systems, and (b) to provide possible means of predicting adsorption isotherms of these systems and hence to predict capacities of certain gas storage systems at given storage and delivery condition.

(8) *Nanotube array structures.* As gaps must be introduced between carbon nanotubes to obtain high fuel gas storage capacities and separation of individual carbon nanotubes in close packed nanotube bundles has only been indirectly observed, it will be helpful to calculate the separation conditions, *i.e.* temperatures and pressures, and the size of the possible gaps. This will give supportive information to the experimental observations and supply guidance to the optimal gas storage conditions. It may be possible to control tube separation by adding molecules or functional groups to external tube surfaces. This is an exciting possibility that should be explored further.

Chapter 14
References

Adams, D. J. (1974). Chemical potential of hard sphere fluids by Monte Carlo methods. *Mol. Phys.* **28**, 1241-52.

Adams, D. J. (1975). Grand canonical ensemble Monte Carlo for a Lennard-Jones fluid. *Mol. Phys.* **29**, 307-11.

Atlanta Gas & Light Adsorbent Research Group (AGLARG)(1994). Final report on adsorbed natural gas research, GR1-95/0068, Gas Research Institute, USA.

Ahn, C. C., Ye, Y., Ratnakumar, B. V., Witham, C., Bowman Jr., R. C. and Fultz, B. (1998). Hydrogen desorption and adsorption measurements on graphite nanofibers. *Appl. Phys. Lett.* **73** (23), 3378-3380.

Ajayan, P. M., Ebbesen, T. W., Ichihashi, T., Iijima, S., Tanigaki, K. and Hiura, H. (1993). Opening carbon nanotubes with oxygen and implications for filling. *Nature* **362**, 522-525.

Ajayan, P. M. and Iijima, S. (1993). Capillarity-induced filling of carbon nanotubes. *Nature* **361**(6410), 333-334.

Alain, E., McEnaney, B. and Mays, T. J. (1999). Experimental measurements of nitrogen adsorption in carbon nanotubes. Carbon '99. American Carbon Society, Charleston, SC, USA, 88-89.

Alain, E., Yin, Y. F., Mays, T. J. and McEnaney, B. (2000). Molecular simulation and measurement of adsorption in porous carbon nanotubes. *Studies in Surface Science and Catalysis* **128**, 313-322.

Alcaniz-Monge, J., de la CasaLillo, M. A., Cazorla-Amoros, D. and Linares-Solano, A. (1997). Methane storage in activated carbon fibres. *Carbon* **35**(2), 291-297

Allen, M. P. and Tildesley, D. J. (1987). Computer Simulation of Liquids. Clarendon Press, Oxford, 127.

Amankwah, A. G., Noh, J. S. and Schwarz, J. A.(1989). Hydrogen storage on superactivated carbon at refrigeration temperatures. *Int. J. Hydrogen Energy* **14** (7), 437-447.

Aukett, P. N., Quirke, N., Riddiford, S. and Tennison, S. R. (1992). Methane adsorption on microporous carbons—a comparison of experiment, theory, and simulation. *Carbon* **30**(6), 913-924.

Ayappa, K. G. (1998). Simulations of binary mixture adsorption in carbon nanotubes: transition in adsorbed fluid composition. *Langmuir* **14**, 880-890.

Baker, F. S. (1995). Production of a highly microporous activated carbon product. *US Patent* 5416056.

Bansal, R. C., Donnet, J. and Stoeckli, F. (1988). Active Carbon. Dekker, New York.

Bethune, D. S., Kiang, C. H., Devries, M. S., Gorman, G., Savoy, R., Vazquez, J. and Beyers, R. (1993). Cobalt-catalysed growth of carbon nanotubes with single-atomic-layerwalls. *Nature* **363**(6430), 605-607.

Bose, T. K., Chahine, R. and St. Arnaud, J. M. (1991). High density adsorbent and method of producing same, *US Patent* 4999330.

Breton, J., Gonzalez-Platas, J. and Girardet, C. (1994). Endohedral adsorption in graphitic nanotubules. *J. Chem. Phys.* **101**(4), 3334-3340.

Byrne, J. F. and Marsh, H. (1995). Introductory Overview, in *Porosity in Carbons*, Patrick, J. W. Ed, Edward Arnold, London, 1-48.

Carpetis, C. and Peschka, W. (1980). A study on hydrogen storage by use of cryoadsorbents. *International Journal of Hydrogen Energy* **5**, 539-554

Chahine, R. and Bose, T. K. (1994). Low-pressure adsorption storage of hydrogen. *Int. J. Hydrogen Energy* **19** (2), 161-164.

Chambers, A., Park, C., Baker, R. T. K. and Rodriguez, N. M. (1998). Hydrogen storage in graphite nanofibers, *J. Phys. Chem. B* **102** (22), 4253-4256.

Chaudron, G. (1989). Natural gas for vehicles adsorption storage tanks. Intercom, Belgium.

Chauvet, O., Forro, L., Zuppiroli, L. and DeHeer, W. A. (1997). Electronic properties of aligned carbon nanotubes. *Synthetic metals* **86**(1-3), 2311-2312.

Chen, P., Wu, X., Lin, J. and Tan, K. L. (1999). High H_2 uptake by alkali-doped carbon nanotubes under ambient pressure and moderate temperatures. *Science* **285**(5424), 91-93

Chen, X. S., McEnaney, B., Mays, T. J., Alcaniz-Monge, J., Cazorla-Amoros, D. and Linares-Solano, A. (1997). Theoretical and experimental studies of methane adsorption on microporous carbons, *Carbon* **35** (9), 1251-1258.

Chen, Y. K., Green, M. L. H., Griffin, J. L., Hammer, J., Lago, R. M. and Tsang, S. C. (1996). Purification and opening of carbon nanotubes via bromination. *Advanced Materials* **8** (12), 1012-1015.

Chopra, N. G., Benedict, L. X., Crespi, V. H., Cohen, M. L., Louie, S. G. and Zettl, A. (1995). Fully collapsed carbon nanotubes. *Nature* **377**(6545), 135-138.

Cook, T. L., Komodromos, C., Quinn, D. F. and Ragan, S. (1999). Adsorbent storage for natural gas vehicles, in T. D. Burchell (ed.), *Carbon Materials for Advanced Technologies*, Elsevier Science, Oxford, 269-302.

Cracknell, R. F., Gubbins, K. E. (1992). A Monte Carlo study of methane adsorption in aluminophosphates and porous carbons. *J. Molecular Liquids* **54**, 261-271.

Cracknell, R. F., Gubbins, K. E. (1993). Molecular simulation of adsorption and diffusion in VPI-5 and other aluminophosphates. *Langmuir* **9**(3), 824-830.

Cracknell, R. F., Gubbins, K. E., Maddox, M. and Nicholson, D. (1995). Modeling fluid behaviour in well-characterised porous materials. *Accounts of Chemical Research* **28**, 281-288.

Cracknell, R. F., Koh, C. A., Thompson, A. M. and Gubbins, K. E. (1993). *Mat. Res. Soc. Symp. Proc.* **290**, 135.

Darkrim, F. and Levesque, D. (1998). Monte Carlo simulations of hydrogen adsorption in single-walled carbon nnaotubes. *Journal of Chemical Physics* **109**(12), 4981-4984.

Derbyshire, F., Jagtoyen, M. and Thwaites, M. (1995). Activated Carbons—Production and Applications, in J. W. Patrick (ed.), *Porosity in Carbons*, Edward Arnold, London, 227-252.

Dillon, A. C., Jones, K. M., Bekkedahl, T. A., Kiang, C. H., Bethune, D. S. and Heben, M. J. (1997). Storage of hydrogen in single-walled carbon nanotubes. *Nature* **386**(6623), 377-379.

Dillon, A. C., Gennett, T., Alleman, J. L., Jones, K. M., Parilla, P. A. and Heben, M. J. (1999). Carbon nanotube materials for hydrogen storage. *Proceedings of the 1999 DOE/NREL hydrogen program review*. National Renewable Energy laboratory, Golden, CO8041-3393, USA

Dresselhaus, M. S., Dresselhaus, G. and Saito, R. (1995). Physics of carbon nanotubes. *Carbon* **33**(7), 883-891.

Dujardin, E., Ebbesen, T. W., Krishnam, A. and Treacy, M. M. J. (1998). Purification of single-shell nanotubes. *Advanced Materials* **10**(8), 611-613.

Ebbesen, T. W. (1994). Carbon nanotubes. *Annual Review of Materials Science* **24**, 235-264.

Ebbesen, T. W. (1996). Carbon nanotubes. *Physics Today* **49** (6), 26-32.

Ebbesen, T. W. and Ajayan, P. M. (1992). Large-scale synthesis of carbon nanotubes. *Nature* **358**(6383), 220-222.

Ebbesen, T. W. and Ajayan, P. M., Hiura, H. and Tanigaki, K. (1994). Purification of nanotubes. *Nature* **367**(6463), 519.

Ebbesen, T. W. , Hiura, H., Fujita, J., Ochiai, Y. Matsui, S. and Tanigaki, K. (1993). Patterns in the bulk growth of carbon nanotubes. *Chem. Phys. Lett.* **209**(1-2), 83-90.

Endo, M. and Kroto, H. W. (1992). Formation of carbon nanofibers. *Journal of Physical Chemistry* **96**(17), 6941-6944.

Everett, D. H. and Powl, J. C. (1976). Adsorption in slit-like and cylindrical micropores in the Henry's Law region. A model for the microporosity of carbons. *J.C.S. Faraday Trans I* **72**, 619-636.

Fan, Y. Y., Liao, B., Liu, M., Wei, Y. L., Lu, M. Q., and Cheng, H. M. (1999). Hydrogen uptake in vapor-grown carbon nanofibers. *Carbon* **37**, 1649-1652.

Fryer, J. R. (1981). The micropore structure of disordered carbons determined by high resolution electron microscopy. *Carbon* **19**(6), 431-439.

Gaucher, H., Pellenq, R. J. M., Grillet, Y., Bonnamy, S. and Beguin, F. (1997). Gas adsorption by catalytic carbon nanotubes. *Carbon '97*, Pen State, USA, 388-389.

Ge, M. H. and Sattler, K. (1993). Vapor-condensation generation and STM analysis of fullerene tubes. *Science* **260**(5107), 515-518.

Gordon, P. A. and Saeger, R. B. (1999). Molecular modelling of adsorptive energy storage: hydrogen storage in single-walled carbon nanotubes. *Ind. Eng. Chem. Res.* **38**, 4647-4655.

Gradshteyn, I. S. and Ryzhik, I. M. (1965). Table of Integrals, Series and Products. Academic Press, New York.

Gregg, S. and Sing, K. S. W. (1982). Adsorption, Surface Area and Porosity. Academic Press, London, UK.

Gubbins, K. E. and Quirke, N. (1996). Molecular simulation and industrial applications: methods, examples and prospects, in K. E. Gubbins and N. Quirke (ed.), *Molecular Simulation and Industrial Applications: Methods, Examples and Prospects*. Gordon and Breach Science Publishers, Amsterdam, 1-69.

Hiura, H., Ebbesen, T. W. and Tanigaki, K. (1995). Opening and purification of carbon nanotubes in high yields. *Advanced Materials* **7**(3), 275-276.

Hynek, S., Fuller, W. and Bentley, J. (1997). Hydrogen storage by carbon sorption. *Int. J. Hydrogen Energy* **22** (6), 601-610.

Iijima, S. (1991). Helical microtubules of graphitic carbon. *Nature* **354**(6348), 56-58.

Iijima, S. and Ichihashi, T. (1993). Single-shell carbon nanotubes of 1-nm diameter. *Nature* **363**(6430), 603-605.

Ingersoll, J. G. (1996). Natural Gas Vehicles. The Fairmont Press, Inc., New York.

Issi, J. P., Langer, L., Heremans, J. and Olk, C. H. (1995). Electronic properties of carbon nanotubes—experimental results. *Carbon* **33**(7), 941-948.

IUPAC (1982). International Committee for Characterisation and Terminology of Carbon. 1st publication of 30 tentative definitions. *Carbon* **20**(5), 445-449.

IUPAC (1983). International Committee for Characterisation and Terminology of Carbon, 1st publication of further 24 tentative definitions. *Carbon* **21**(5), 517-519.

IUPAC (1985). International Committee for Characterisation and Terminology of Carbon, 1st publication of further 14 tentative definitions. *Carbon* **23**(5), 601-603.

Kelly, B. T. (1981). Physics of Graphite. Applied Science Publishers, London and New Jersey.

Khan, I. A. and Ayappa, K. G. (1998). Density distributions of diatoms in carbon nanotubes: A grand canonical Monte Carlo study. *Journal of Chemical Physics* **109**(11), 4576-4586

Kiang, C. -H., Endo, M., Ajayan, P. M., Dresselhaus, G and Dresselhaus, M. S. (1998). Size effects in carbon nanotubes. *Physical Review Letters* **81**(9), 1869-1872.

Kihara, T. (1978). *Intermolecular forces.* John Wiley & Sons, New York.

Klyamkin, S. N., Metenier, K., Sklovsky, D. E., Bonnamy, S. and Béguin, F. (1999). Multiwall carbon nanotubes under high hydrogen pressure. *Carbon '99*, American Carbon Society, Charleston, SC, USA, 94-95.

Kroto, H. W., Heath, J. R., O'Brien, S. C., Curl, R.F. and Smalley, R.E. (1985). C-60 - Buckminsterfullerene. *Nature* **318**(6042), 162-163.

Lastoskie, C., Gubbins, K. E. and Quirke, N. (1993). Pore size distribution analysis of microporous carbons: A density functional theory approach. *J. Phys. Chem.* **97**, 4786-4796.

Lipman, T. E. and DeLucchi (1996). Hydrogen-fuelled vehicles. *Int. J. of Vehicle Design 17* (5/6) (Special Issue), 562-589.

Liu, C., Fan, Y. Y., Liu, M., Cong, H. T., Cheng, H. M. and Dresselhaus, M. S. (1999). Hydrogen storage in single-walled carbon nanotubes at room temperature, *Science* **286**, 1127-1129.

Lozano-Castelló, D., de la Casa Lillo, M. A., Cazorla-Amorós, D. and Linares-Solano, A. (1999). Methane storage at commercially attractive levels in superactivated carbons and commercial activated carbon fibers, *Extended Abstracts 'Carbon '99'*, American Carbon Society, Charleston, SC, USA, 626-627.

Lu, J. P. (1997). Elastic properties of single and multilayered nanotubes. *J. Phys. Chem. Solids* **58** (11), 1649-1652.

Mackie, E. B., Wolfson, R. A., Arnold, L. M., Lafdi, K. and Migone, A. D. (1997). Sorption studies of methane films on catalytic carbon nanotubes and carbon filaments. *Langmuir* **13**, 7197-7201.

Maddox, M. W. and Gubbins, K. E. (1994). Molecular simulation of fluid adsorption in Buckytubes and MCM-41. *International Journal of Thermophysics* **15**(6), 1115-1123.

Maddox, M. W. and Gubbins, K. E. (1995). Molecular simulation of fluid adsorption in Buckytubes. *Langmuir* **11**, 3988-3996.

Maddox, M. W., Sowers, S. L. and Gubbins, K. E. (1996). Molecular simulation of binary mixture adsorption in buckytubes and MCM-41. *Adsorption* **2**, 23-32.

Maddox, M. W., Ulberg, D. and Gubbins, K. E. (1995). Molecular simulation of simple fluids and water in porous carbons. *Fluid Phase Equilibria* **104**, 145-158.

Maitland, G.C., Rigby, M., Smith, E.B. and Wakeham, W.A. (1981). *Intermolecular Forces*, Clarendon Press, Oxford.

Manzi, S., Valladares, D., Marchese, J. and Zgrablich, G. (1997). Characterization of Maxsorb activated carbons and their evaluation for gas storage. *Adsorption Sci. Tech.* **15**, 301-309.

Marsh, H. and Crawford, D. (1982). Carbons of high surface area. A study by adsorption and high resolution electron microscopy. *Carbon* **20**(5), 419-426.

Matranga, K. B., Myers, A. L. and Glandt, E. D. (1992a). Storage of natural gas by aadsorption on activated carbon. *Chem. Eng. Sci.* **47** (7), 1659-1679.

Matranga, K. B., Stella, A., Myers, A. L. and Glandt, E. D. (1992b). Molecular simulation of adsorbed natural gas. *Separation Science and Technology* **27** (14),1837-1856.

Mays, T. J. (1996). Simulations of adsorption and the design of activated carbons. *Fundamentals of adsorption*, LeVan, M. D. (Ed.). Kluwer Academic Publishers, Boston, Massachusetts.

McEnaney, B., Mays, T. J. and Chen, X. (1998). Computer simulations of adsorption processes in carbonaceous adsorbents. *Fuel* **77**(6), 557-562.

McEnaney, B., Mays, T. J., Yin, Y. F., Chen, X. and Rodriguez-Reinoso, F. (1997). Estimating the dimensions of ultramicropores using molecular probes. In B. McEnaney et al (eds.) *Characterisation of Porous Solids IV*, Royal Society of Chemistry, Cambridge, 125-132.

Mellor, I. M., Mortimer, R. J. and Turpin, M. (1999). The Use of Carbon Nanofibers as Hydrogen Storage Materials. *Carbon '99*. Charleston, USA, 622-623

Mintmire, J. W. and White, C. (1995). Electronic and structural-properties of carbon nanotubes. *Carbon* **33**(7), 893-902.

Noh, J. S., Agarwal, R. K. and Schwarz, J. A. (1987). Hydrogen storage-systems using activated carbon. *Int. J. Hydrogen Energy* **12** (10), 693-700.

Norman, G. E. and Filinov, V. S. (1969). Investigations of phase transitions by a Monte Carlo method. *High Temp. (USSR)* **7**, 216-22.

Park, C., Anderson, P. E., Chambers, A., Tan, C. D., Hidalgo, R. and Rodriguez, N. M. (1999). Further studies of the interaction of hydrogen with graphite nanofibers. *J. Phys. Chem. B* **103**, 10572-10581.

Parkyns, N. D. and Quinn, D. F. (1995). Natural gas adsorbed on carbon, In J. W. Patrick (ed.), *Porosity in Carbons*, Edward Arnold, London, 291-325.

Pederson, M. R. and Broughton, J. Q. (1992). Nanocapillarity in fullerene tubules. *Phys. Rev. Lett.* **69**(18), 2689-2692.

Peng, D.Y. and Robinson, D.B. (1976). A new two-constant equation of state, *Ind. Eng. Chem. Fundam.* **15**, 59-64.

Peterson, D. L., Helfferich, F. and Carr, R. J. (1966). Measurement of phase equilibria at high pressures by Tracer-Pulse Chromatography. *AIChE J.* **12** (5), 903-905.

Qin, L. C. and Iijima, S. (1997). Structure and formation of raft-like bundles of single-walled helical carbon nanotubes produced by laser evaporation. *Chemical Physics Letters* **269** (1-2), 65-71

Quinn, D. F. and MacDonald J. A. (1992). Natural gas storage. *Carbon* **30**, 1097-1103.

Quirke, N and Tennison, S. R. (1996). The interpretation of pore size distributions of microporous carbons. *Carbon* **34**(10), 1281-1286.

Rao, C. N. R., Sen, R., Satishkumar, B. C. and Govindaraj, A. (1998). Large aligned nanotube bundles from ferrocene pyrolysis. *Chemical Communications* **15**, 1525-1526.

Ray, G. C. and Box, E. O. (1950). Adsorption of gases on activated charcoal. *Ind. Eng. Chem.* **42** (7), 1315-1318.

Rinzler, A. G., Hafner, J. H., Nikolaev, P., Lou, L., Kim, S. G., Tomanek, D., Nordlander, P., Colbert, D. T. and Smalley, R. E. (1995). Unraveling nanotubes—field emission from an atomic wire. *Science* **269**(5230), 1550-1553.

Rodriguez, N. M. and Baker, R. T. K. (1997). Storage of hydrogen in layered nanostructures. *US Patent* 5653951.

Ruoff, R. S. and Lorents, D. C. (1995). Mechanical and thermal-properties of carbon nanotubes. *Carbon* **33**(7), 925-930.

Rzepka, M., Lamp, P. and de la Casa-Lillo, M. A. (1998). Physisorption of hydrogen on microporous carbon and carbon nanotubes. *J. Phys. Chem. B* **102**, 10894-10898.

Saito, R., Dresselhaus, G. and Dresselhaus, M. S. (1998). Physical Properties of Carbon Nanotubes. Imperial College Press, London, UK.

Saito, Y., Yoshikawa, T. , Bandow, S. , Tomita, M. and Hayashi, T. (1993). Interlayer spacings in carbon nanotubes. *Physical Review B —Condensed Matter* **48**(12), 1907-1909.

Samios, S., Stubos, A. K., Kanellopoulos, N. K., Cracknell, R., Papadopoulos, G. and Nicholson, D. (1997). Micropore size distributions from experimental isotherm data and Grand Canonical Monte Carlo simulaitons, in B. McEnaney et al (ed.), *Characterisation of Porous Solids IV*, The Royal Society of Chemistry, Cambridge, UK, 141-148.

Seaton, N. A., Walton, J. P. R. B. and Quirke, N. (1989). A new analysis method for the determination of the pore size distribution of porous carbons from nitrogen adsorption measurements. *Carbon* **27**(6), 853-861.

Shelimov, K. B., Esenaliev, R. O., Rinzler, A.G., Huffman, C. B. and Smalley, R. E. (1998). Purification of single-wall carbon nanotubes by ultrasonically assisted filtration. *Chemical Physics Letters* **282** (5-6), 429-434.

Simonyan, V.V., Diep, P. and Johnson, J. K. (1999). Molecular simulation of hydrogen adsorption in charged single-walled carbon nanotubes. *Journal of Chemical Physics* **111**(21), 9778-9783.

Sing, K. S. W., Everett, D. H., Haul, R. A. W., Moscou, L., Pierotti, R. A., Rouquerol, J. and Siemieniewska, T. (1985). Reporting physisorption data for gas solid

systems with special reference to the determination of surface-area and porosity (recommendations 1984). *Pure and Applied Chemistry* **57**(4), 603-619.

Sklovsky, D. E., Gaucher, H., Bonnamy, S., Beguin, F and Nalimova, V. A. (1997). Elastic properties of multiwall carbon nanotubes. *Carbon '97.* Pen State, USA, 392-393.

Somers, S. A., Ayappa, K. G., McCormick, A V. and Davis, H. T. (1996). Binary fluids in planar nanopores: adsorptive selectivity, heat capacity and self-diffusitivity. *Adsorption* **2**, 33-40.

Stan, G. and Cole, M. W. (1998). Hydrogen adsorption in nanotubes. *Journal of Low Temperature Physics* **110**(1/2), 539-544.

Steele, W. A. (1974). *The Interaction of Gases with Solid Surface*, Pergamon Press, Oxford.

Stoeckli, H. F. (1995). Characterisation of microporous carbons by adsorption and immersion techniques, in *Porosity in Carbons*, Patrick, J. W. Ed, Edward Arnold, London, 67-92.

Suzuki, T., Kaneko, K., Setoyama, N., Maddox, M. and Gubbins, K. (1996). Grand canonical Monte Carlo simulation for nitrogen adsorption in graphitic slit micropores: effect of interlayer distance. *Carbon* **34**(7), 909-912.

Tan, Z. and Gubbins, K. E. (1990). Adsorption in carbon micropores at supercritical temperatures. *J. Phys. Chem.* **94**, 6061-6069.

Terrones, M., Grobert, N., Zhang, J. P., Terrones, H., Olivares, J., Hsu, W. K., Hare, J. P., Cheetham, A. K., Kroto, H. W. and Walton, D. R. M. (1998). Preparation of aligned carbon nanotubes catalysed by laser-etched cobalt thin films. *Chemical Physics Letters* **285** (5-6), 299-305.

Thess, A., Lee, R., Nikolaev, P., Dai, H., Petit, P., Robert, J., Xu, C., Lee, Y. H., Kim, S. G., Rinzler, A. G., Colbert, D. T., Scuseria, G. E., Tománek, D., Fischer, J. E. and Smalley, R. E. (1996). Crystalline ropes of metallic carbon nanotubes. *Science* **273** (5274), 483-487.

Tóth, J. A. (1981). A uniform interpretation of gas/solid adsorption. *J. Coll. Int. Sci.* **79**(1), 85-95.

Tsang, S. C., Harris, P. J. F. and Green, M. L. H. (1993). Thinning and opening of carbon nanotubes by oxidation using carbon dioxide. *Nature* **362**, 520-521.

Tsang, S. C., Chen, Y.K., Harris, P. J. F. and Green, M. L. H. (1994). A simple chemical method of opening and filling carbon nanotubes. *Nature* **372**, 159-162.

Walton, J. P. R. B. and Quirke, N. (1989). Capillary condensation: a molecular simulation study. *Molecular Simulation* **2**, 361-391.

Wang, Q. and Johnson, J. K. (1999a). Molecular simulation of hydrogen adsorption in single-walled carbon nanotubes and idealized carbon slit pores. *Journal of Chemical Physics* **110**(1), 577-586.

Wang, Q. and Johnson, J. K. (1999b). Optimization of carbon nanotube arrays for hydrogen adsorption. *J. Phys. Chem. B* **103**, 4809-4813.

Wang, Q. and Johnson, J. K. (1999c). Computer simulations of hydrogen adsorption on graphite nanofibers. *The Journal of Physical Chemistry B* **103**(2), 277-281.

Whitehouse, J. S., Nicholson, D., and Parsonage, N. G. (1983). A grand ensemble Monte Carlo study of krypton adsorbed on graphite, *Mol. Phys.* **49**, 829-47.

Yamabe, T. (1995). Recent development of carbon nanotube. *Synthetic metals* **70** (1-3), 1511-1518.

Ye, Y., Ahn, C. C., Witham, C., Fultz, B., Liu, J., Rinzler, A. G., Colbert, D., Smith, K. A. and Smalley, R. E. (1999). Hydrogen adsorption and cohesive energy of single-walled carbon nanotubes. *Applied Physics Letters* **74** (16), 2307-2309.

Yin, Y. F., Mays, T. J. and McEnaney, B. (1998). Adsorption potentials and simulations in carbon slits and cylinders. In Francis Meunier (ed.) *Fundamentals of adsorption 6,* Elsevier, Paris, France, 261-266.

Yin, Y. F., McEnaney, B. and Mays, T. J. (1998). Dependence of GCEMC simulations of nitrogen adsorption on activated carbons on input parameters. *Carbon* **36**(10), 1425-1432.

Zhou, L. and Zhou, Y. (1996). A comprehensive model for the adsorption of supercritical hydrogen on activated carbons. *Ind. Eng. Chem. Res.* **35**, 4166-4168.

Acknowledgements

The author would like to thank Dr Tim Mays for supervision; Professor Brian McEnaney for many things; Members of the Bath Carbon and Graphite Group for help, discussion and co-operation; Technicians at the university, mostly Peter Taylor, Simon Bowman, Robert Perkins and Ian Trussler, and member of the Department Office for their assistance; My wife and daughter for their support; BUCS for enormous computing time; and those who helped knowingly or unknowingly during the author's study here. Finally, the author acknowledges the University of Bath for sponsorship.